



Ecole Doctorale "Sciences de la Matière, du Rayonnement et de l'Environnement" (EDSMRE)

## **Thèse**

Pour l'obtention du grade de

**Docteur de L'Université de Lille**

Discipline : Chimie des Matériaux

Filière : Molécules et Matière Condensée

Présentée et soutenue publiquement par

**Anastasiia ZADOIA**

Le 7 avril 2021

---

*Vers de nouvelles architectures oxo-centrés obtenues par  
synthèses HP-HT*

---

**Dirigée par :** M<sup>me</sup> Marie COLMONT, Maître de Conférence, ENSCL, Lille.

**Co-dirigée par :** M<sup>me</sup> Marielle HUVE, Professeur, UCCS, Lille.

**Membres du Jury :**

**Rapporteurs :**

M. François GOUTENOIRE, Professeur, Université du Maine, Le Mans.

M<sup>me</sup> Christine MARTIN, Directeur de Recherche, CNRS, CRISMAT, Caen.

**Examineur :**

M<sup>me</sup> Céline DARIE, Professeur, INP, Université Grenoble Alpes.

M. Angel AREVALO-LOPEZ, Charge de Recherche, CNRS, UCCS, Lille.



---

*Towards new oxo-centered architectures  
obtained by HP-HT syntheses*

---



## Acknowledgement

*In the beginning, I would like to express my grateful acknowledgment to my supervisor Dr. Marie COLMONT for the continuous support on each step of my Ph.D study and related research. Her patience and motivation helped me in all the time of research and writing of this thesis. I was immensely glad to be under her tactful and professional guidance.*

*I would like to thank my co-supervisor Pr. Marielle HUVÉ for fair adjustments and helpful recommendation during my work. I am infinitely grateful to Angel M. AREVALO-LOPEZ and Olivier MENTRE who spend a lot of time explaining the most difficult concepts for me.*

*I wish to express my profound gratitude to Céline DARIE from Neel Institute, Javier SANCHEZ-BENITEZ from Madrid University, and Oleg SIIDRA from St. Petersburg University for the supervision during my internships.*

*I am deeply grateful to members of Ph.D committee: Christine MARTIN, François GOUTENOIRE who accepted to review my work.*

*I am very thankful to be a part of the lab, for the invaluable experience of working in such a well-organized and professional team. I am grateful to Nora for helping me with hydrothermal synthesis, thermogravimetric and EDS analysis, Laurence and Florent for XRD measurements, Maxence and Fred for single crystal diffraction.*

*Finally, I would like to thank my family and all friends for supporting me during the compilation of this dissertation.*



## Abstract

This work is dedicated to the investigation of crystal structural features and physical properties of oxo-centered compounds obtained or modified under high-temperature and high-pressure conditions. During the work on this thesis, Bi –, Ln – and Pb – based chemical systems were investigated due to the keen interest of UCCS (Unité de Catalyse et de Chimie du Solide) in Lille, and particularly the team MISSP (Matériaux inorganiques, structures, systèmes et propriétés).

Within the framework of this work, various methods of applying high pressure were used, often accompanied by the use of high temperatures to stabilize the substance. So, experiments on hydrothermal synthesis were carried out, as well as some experiments using Large Anvil Cells press – Piston Cylinder apparatus. Another part of high-pressure high-temperature experiments were realized at the Neel Institute in Grenoble using a Belt type press allowing to reach higher pressure-temperature conditions. Experiments at ambient temperature and higher pressure (up to 20 GPa) conditions were performed using Diamond Anvil Cells equipment during a stage at Madrid University.

A significant part of this work is devoted to practical experiments aimed to synthesis of new compounds and modification of already known phases. The main methods of the crystal structures study are monocrystal and powder X-Ray diffraction, usually coupled with Raman spectroscopy or UV-visible diffuse reflectance analysis. Special attention is paid to the description of crystal structures, since most of the compounds are new. Of great importance is the measurement and description of some physical properties of the studied materials: ionic conductivity or magnetic measurements.

## Résumé

Ce travail est dédié à l'étude des structures cristallines et des propriétés physiques de composés oxo-centrés obtenus ou modifiés dans des conditions de hautes température et pression. Au cours des travaux de cette thèse, des composés oxo-centrés à base de bismuth, de lanthanides ou de plmob ont été étudiés en raison de l'intérêt porté par l'UCCS (Unité de Catalyse et de Chimie du Solide) à Lille, et en particulier l'équipe MISSP (Matériaux Inorganiques, structures, systèmes et propriétés) à ce type de composés. Dans le cadre de ce travail, différentes méthodes d'application de hautes pressions ont été utilisées, souvent accompagnées de l'utilisation de températures élevées pour stabiliser les composés. Des expériences de synthèse hydrothermale ont également été réalisées, ainsi que des expériences utilisant des presses multi-enclumes ou un piston cylindre. Une autre partie des expériences à hautes pression et température a été réalisée à l'Institut Néel de Grenoble en utilisant une presse de type Belt permettant des conditions de pression-température plus élevées. Des expériences à température ambiante et dans des conditions de pressions plus élevées (jusqu'à 20 GPa) ont été réalisées à l'aide de l'équipement Diamond Anvil Cells lors d'un stage réalisé à l'Université de Madrid. Les échantillons ont été analysés par diffraction des rayons X sur monocristal et sur poudre, par spectroscopie Raman ou par analyse de réflectance diffuse UV-visible. Une attention particulière a été portée à la description des structures cristallines des nouveaux composés obtenus. Certaines propriétés physiques des matériaux obtenus ont été étudiées : la conductivité ionique ou mesures magnétiques en fonction des matériaux.

## Table of content

I.	General introduction.....	15
I.1.	State of the art.....	19
I.1.1.	Crystal structure descriptions using the Anion-centered approach.....	19
a.	History .....	20
b.	Crystal chemistry .....	21
I.2.	A good knowledge of these systems at UCCS .....	22
I.2.1.	Bi-based materials .....	22
a.	Design approach.....	22
b.	Disorder phases .....	23
c.	Towards multi-dimensional open frameworks .....	24
I.2.2.	Ln-based materials .....	26
I.3.	Towards new oxo-centered architectures obtained by HPHT syntheses .....	27
I.3.1.	High-Pressure Apparatus.....	28
a.	High-pressure equipment used in current research .....	31
I.3.2.	Anion-centered architectures obtained by HP-HT .....	36
a.	Samples from hydrothermal synthesis .....	37
b.	HP-HT Polymorphs of simple oxides .....	38
c.	Rare-earth borates .....	41
I.4.	References .....	43
II.	Pressure induced new crystal structures in the Bi-based oxo-centered systems.....	49
II.1.	High-Pressure modification of $\text{BiCu}_2\text{XO}_6$ ( $X = \text{P}, \text{V}$ ) solid solution .....	51
II.1.1.	State of the Art .....	51
a.	On the interest in using $\text{BiM}_2\text{XO}_6$ compounds .....	51
II.1.2.	The case of $\text{BiCu}_2\text{PO}_6$ , an interesting spin ladder system .....	54
II.1.3.	On the solid solution $\text{BiCu}_2\text{P}_{1-x}\text{V}_x\text{O}_6$ .....	57

a.	Crystal structures.....	57
-	Magnetic properties .....	58
II.1.4.	HP-HT experiments on $\text{BiCu}_2(\text{P}_{1-x}\text{V}_x)\text{O}_6$ .....	59
a.	HP- $\text{BiCu}_2\text{VO}_6$ .....	59
-	Synthesis .....	59
-	Rietveld refinement of High-Pressure form of $\text{BiCu}_2\text{VO}_6$ .....	60
-	TEM.....	62
-	High-Temperature X-ray Diffraction .....	62
b.	Determination of HP phase stability area of $\text{BiCu}_2(\text{P}_{1-x}\text{V}_x)\text{O}_6$ .....	63
-	Identification of the synthesis conditions .....	63
-	Rietveld refinement of High-Pressure form of $\text{BiCu}_2(\text{P}_{1-x}\text{V}_x)\text{O}_6$ .....	72
-	Magnetic Measurements.....	75
II.1.5.	Conclusion .....	79
II.2.	Investigation of the HP- $\text{BiNiPO}_5$ polymorph.....	80
II.2.1.	State of the Art .....	80
a.	On the interest in $\text{BiMXO}_5$ compounds.....	80
II.2.2.	Ambient-pressure $\text{BiNiPO}_5$ phase (AP-BNPO).....	81
II.2.3.	The new HP-polymorph .....	81
a.	Synthesis of the raw $\text{BiNiPO}_5$ .....	81
b.	HP-HT synthesis .....	82
c.	Rietveld refinement of new high pressure $\text{BiNiPO}_5$ phase.....	83
II.2.4.	Crystal structures comparison between HP- $\text{BiNiPO}_5$ and AP- $\text{BiNiPO}_5$ .....	85
a.	Lone Pair activity .....	86
b.	High-temperature X-ray Diffraction .....	87
-	HTXRD of ambient-pressure $\text{BiNiPO}_5$ phase .....	88
-	HTXRD of high-pressure $\text{BiNiPO}_5$ phase. ....	89
c.	AP- and HP $\text{BiNiPO}_5$ magnetic properties .....	92

II.2.5.	Conclusion .....	94
II.3.	Oxo-centered architectures obtained by Supercritical Steam .....	95
II.3.1.	Synthesis .....	95
II.3.2.	Crystal structures of the new compounds obtained by Supercritical Steam .....	96
a.	The new $\text{Bi}_3(\text{VO}_4)\text{O}_3$ .....	96
b.	The new $\text{Bi}_{3.5}\text{O}_4(\text{AsO}_4)\text{H}_{0.5}$ .....	98
c.	Solid-state synthesis of the new phases .....	100
II.3.3.	Structural complexity .....	101
II.3.4.	Conclusion .....	103
II.4.	Conclusion and perspectives .....	104
II.5.	Supplementary information .....	105
II.6.	References .....	112
III.	High-pressure exploration in the lanthanide-based oxo-centered systems .....	119
III.1.	High-pressure exploration in the Li – Ln – V – O system .....	121
III.1.1.	Evidence of phase transition by in situ high-pressure Raman spectroscopy .....	122
III.1.2.	Synthesis using High-Pressure High-Temperature experiments .....	125
III.1.3.	Investigation of the new compounds .....	128
a.	The new HP form of $\text{LiLa}_5\text{O}_5(\text{VO}_4)_2$ .....	128
-	Single crystal XRD .....	128
-	High-angle annular dark-field imaging (HAADF) .....	131
b.	$\text{LiNd}_5\text{O}_5(\text{VO}_4)_2$ characterization .....	133
-	Single crystal XRD .....	133
-	Magnetic measurements .....	134
c.	The new $\text{LiLa}_2\text{O}_2\text{VO}_4$ .....	135
-	Single crystal XRD .....	135
III.1.4.	Conclusion .....	138
III.2.	Ln-V-O system investigation .....	139

III.2.1.	Context.....	139
a.	From $\text{La}_7\text{V}_3\text{O}_{18}$ .....	139
b.	Bibliography of $\text{Ln}_8\text{V}_2\text{O}_{17}$ phases .....	140
III.2.2.	A new 3D framework: $\text{Gd}_8\text{V}_2\text{O}_{17}$ .....	142
a.	Synthesis of the powder.....	142
b.	Crystal structure of $\text{Gd}_8\text{V}_2\text{O}_{17}$ phase .....	142
c.	Magnetocaloric properties of $\text{Gd}_8\text{V}_2\text{O}_{17}$ phase .....	146
III.2.3.	Reduction of $\text{Gd}_8\text{V}_2\text{O}_{17}$ .....	150
a.	Synthesis routes.....	150
b.	Crystal structure of reduced phase .....	154
c.	Confirmation of reduction of vanadium by XPS .....	155
III.2.4.	Comparison between the two crystal structures.....	156
a.	Magnetic properties of $\text{Gd}_8\text{V}_2\text{O}_{16.92}$ .....	159
-	First measurements done in Madrid .....	159
-	Magnetic measurements on $\text{Gd}_8\text{V}_2\text{O}_{16.92}$ .....	160
b.	Optical Measurements .....	161
III.2.5.	HP-HT investigation of $\text{Gd}_8\text{V}_2\text{O}_{17}$ .....	162
III.3.	Conclusion and perspectives .....	163
III.3.1.	Summary.....	163
III.3.2.	Perspectives .....	163
III.4.	Supplementary information .....	164
III.5.	References .....	182
IV.	Crystal chemistry of Pb-based oxo-centered compounds.....	190
IV.1.	$\text{Pb}_4\text{Ln}_2\text{O}_7$ (Ln= Nd, Sm and Gd).....	191
IV.1.1.	Investigation of samples stability .....	193
a.	$\text{Pb}_4\text{Nd}_2\text{O}_7$ .....	194
-	HP-HT experiments.....	194

b.	$\text{Pb}_4\text{Sm}_2\text{O}_7$ .....	197
c.	$\text{Pb}_4\text{Gd}_2\text{O}_7$ .....	197
IV.1.2.	Magnetic measurement .....	199
IV.1.3.	Diffuse reflectance spectroscopy .....	201
IV.1.4.	IR investigation .....	202
IV.1.5.	HP Raman investigation .....	202
IV.1.6.	Conclusion and perspectives .....	204
IV.2.	From $\text{Bi}_{4.65}\text{La}_{1.36}\text{O}_9$ to $\text{Pb}_4\text{La}_2\text{O}_7$ .....	205
IV.2.1.	Bibliography note on $\text{Bi}_{4.65}\text{La}_{1.36}\text{O}_9$ .....	205
IV.2.2.	Investigation of the solid solution .....	206
a.	$\text{Pb}_4\text{La}_2\text{O}_7$ .....	210
b.	Conductivity measurements .....	211
IV.2.3.	Conclusion .....	215
IV.3.	Toward new oxo-centered crystal structures in lead containing systems .....	216
IV.3.1.	A description based on the structure hierarchy hypothesis .....	218
IV.3.2.	Pb – Ge – Al – O/F chemical system .....	220
a.	$\text{Pb}_{14}\text{Ge}_8\text{Al}_7\text{O}_{31}\text{F}_{19}$ .....	220
b.	$[\text{Pb}_{12}\text{O}_6]\text{Ge}_7\text{Al}_4\text{O}_{26}$ .....	222
IV.3.3.	Pb – Si – Al – O chemical system .....	227
a.	$[\text{Pb}_{13}\text{O}_8]\text{Si}_8\text{Al}_2\text{O}_{24}$ .....	227
-	Structure comparison of $[\text{Pb}_{12}\text{O}_6]\text{Ge}_7\text{Al}_4\text{O}_{26}$ and $[\text{Pb}_{13}\text{O}_8]\text{Si}_8\text{Al}_2\text{O}_{24}$ .....	230
b.	$[\text{Pb}_6\text{CaO}_2](\text{Al}/\text{Si})_8\text{O}_{17}$ .....	231
-	Structure comparison of $\text{Pb}_2[\text{O}_2\text{Pb}_7](\text{Al}_8\text{O}_{19})$ .....	234
IV.4.	Perspectives and conclusion .....	235
IV.4.1.	Perspectives .....	235
IV.5.	Supplementary information .....	236
IV.6.	References .....	246

V. Summary and Outlook.....250

---

## I. *General introduction*

---

At UCCS (Unité de Catalyse et de Chimie du Solide) in Lille, the team MISSP (Matériaux inorganiques, structures, systèmes et propriétés) is developing a fundamental research mainly based on the investigation of innovative inorganic materials for their magnetic, optical or magnetic properties with potential applications in broad fields like luminescence, spintronics or photocatalysis enabling hydrogen production, a hot topic of today's research. Even if our research is widened to different kind of compounds like mixed anions, it mainly remains based on inorganic oxides. Historically in the solid-state chemistry lab of Lille, compounds based on bismuth are largely investigated since the discovery of the BiMeVO<sub>x</sub> series which are high performances oxide ion conductors. One thing leading to another, the oxide transition metal phosphate family and oxo-centered materials were deeply investigated. The strategy developed so far goes over the traditional shake and bake method and used design and rational approach to predict and the synthesise new phases.

To do so, many innovative tools have been developed and are available locally, involving diffraction (electron, X-Ray, neutron) on powder or single crystals, electron microscopy (electron crystallography, TEM, TITAN...) or measurement of magnetic properties.

More recently, many efforts have been devoted to the development of new synthesis tools in order to increase the chances to target new structures. Some of them are based on the modification of thermodynamic conditions through the use of high-pressure and high-temperature since the installation of a Piston-Cylinder at the university of Lille.

The work of this thesis is based on the use of pressure to synthesise new phases and/or modify already synthesized crystal structures. To do so, many tools were tried involving various process changing the pressure itself (low pressure to high pressure), the temperature (from Room temperature to high temperature) or the media (gaz, liquid...) changing drastically the reactivity. To do so, I have the chance to spend two months with Dr. Javier Sanchez Benitez at the Complutense University of Madrid doing in situ high-pressure Raman spectroscopy in diamond anvil cells and two weeks in the Néel Institute, working with Belt press at the Néel Institute under the supervision of Pr. Céline Darrie.

The oxo-centered materials investigated during this thesis were not only based on bismuth but also on lanthanides and lead. Lead samples were fully characterized at the University of Saint Petersburg with Pr. Oleg Siidra where I spent four months during the rehabilitation works of the lab.

This thesis is divided in three different chapters.

The **first chapter** is dedicated to the synthesis of  $\text{Bi}_3(\text{VO}_4)\text{O}_3$  and  $\text{Bi}_{3.5}\text{O}_4(\text{AsO}_4)\text{H}_{0.5}$  using supercritical hydrothermal pressure, mimicking the procedure of synthesis of  $\text{Bi}_3(\text{PO}_4)\text{O}_3$ . All these three phases will be discussed and compared especially in terms of complexity. Secondly, HP-HT modifications of several terms of the solid solution  $\text{BiCu}_2\text{P}_{1-x}\text{V}_x\text{O}_6$  and of  $\text{BiNiPO}_5$  are presented. In the case of copper samples, a full investigation of the stability of the different phases is done. The magnetic properties are also measured and discussed in correlation with what was done at ambient pressure.

The **second chapter** gathered results on two chemical systems:  $\text{Li/Ln/V/O}$  and  $\text{Ln/V/O}$ . The first one presents the full story of evidence and synthesis and two three new phases through the combined use of in situ Raman spectroscopy in diamond anvil cells and the piston cylinder. In a second time, the new  $\text{Gd}_8\text{V}_2\text{O}_{17}$  phase and its reduced form are detailed. The crystal structures are complex and required synchrotron data.

The **third chapter** involved Pb-based oxo-centered materials. The first part is related to the study of several 2D Van de Waals materials characterized and modified to study its ionic conductivity. The mechanism structure-property is discussed. Finally, new oxo-centered Pb-based compounds were isolated and studied. They present  $[\text{PbO}_4]$  oxo-centered units connecting together giving various dimensionalities but, in that case, the funny point is the addition of a complex anionic subgroup described using the formalism developed by Franck Hawthorne which highlight the modularity of the anionic counterpart.

All this work led to the publication of the following articles:

1. “High-pressure exploration in the Li-Ln-V-O system”, Zadoya, A.I., Arévalo-López, Á.M., Sánchez-Benítez, J., ...Chantel, J., Colmont, M., Dalton Transactions, 2020, 49(39), pp. 13663–13670;

2. “Original Oxo-Centered Frameworks in  $\text{Bi}_3(\text{VO}_4)\text{O}_3$  and  $\text{Bi}_{3.5}(\text{AsO}_4)(\text{OH})_{0.5}\text{O}_{3.5}$  by Supercritical Steam”, Colmont, M., Zadoya, A., Daviero-Minaud, S., Djelal, N., Mentré, O., Inorganic Chemistry, 2020, 59(14), pp. 9486–9490;

3. “Pure and  $\text{RE}^{3+}$ -Doped  $\text{La}_7\text{O}_6(\text{VO}_4)_3$  (RE = Eu, Sm): Polymorphism Stability and Luminescence Properties of a New Oxyvanadate Matrix”, Gómez Torres, M.A., Gauthier, G.H., Kaczmarek, A.M., ...Zadoya, A., Colmont, M., Inorganic Chemistry, 2020, 59(9), pp. 5929–5938;

4. “Origin of Luminescence in  $\text{La}_2\text{MoO}_6$  and  $\text{La}_2\text{Mo}_2\text{O}_9$  and Their Bi-Doped Variants”, Colmont, M., Boutinaud, P., Latouche, C., ...Zadoya, A., Jobic, S., Inorganic Chemistry, 2020, 59(5), pp. 3215–3220;

*And another one is submitted: “Short Bi-Bi contacts in the HP-  $\text{BiNiO}(\text{PO}_4)$  polymorph”, Colmont, M. Zadoya, A. Darie, C., Domingos, C., Leclercq, B. and Mentré, O., Chemical Communications, submitted.*

## I.1. State of the art

### I.1.1. Crystal structure descriptions using the Anion-centered approach

All the crystal structures described in this thesis are based on the anion centered theory. Usually, in inorganic chemistry there is a basic principle description based on assignment of coordination polyhedrons centered on cations and coordinated by anions. This situation is characteristic for cation-centered approach which is the most applicable and extensively used, enabling interpretation of physical properties through the establishment of structure-properties relation.

Nevertheless, in particular cases, this approach is not possible. In that case, the anion-centered approach is used, based on polyhedrons centered on anions and coordinated by cations, the opposite.

One of the examples to show differences between the two approaches is a crystal structure description of georgbokiite,  $\text{Cu}_5\text{O}_2(\text{SeO}_3)_2\text{Cl}_2$ . [1] For the first time the crystal structure was described in terms of cation-centered approach. In that case there are strongly distorted polyhedrons with Cu atoms at the centers of the  $[\text{Cu}(1)\text{O}_3\text{Cl}_2]$  trigonal bipyramids and at  $[\text{Cu}(2)\text{O}_4\text{Cl}_2]$  and  $[\text{Cu}(3)\text{O}_5\text{Cl}]$  octahedrons. The strongest structural unit is a chain made from the strong bonds of Cu(3)-O (fig 1.a).

After a while, a high-temperature X-ray diffraction study was conducted. [2] It indicated thermal expansion values are anisotropic being maximal along *b*, minimal along *c* and intermediate along *a* axis. Proceeding from this evaluation the discrepancy between thermal expansion and structure of compound was revealed. Using an anion centered approach to describe this structure, the presence of “additional” oxygen atom was recognized. These atoms are the centers of  $(\text{OCu}_4)$  tetrahedrons shared to each other alternately by common corners or edges forming the  $[\text{O}_2\text{Cu}_5]$  chains extended along the *c* axis (Figure 1(b)). At that point  $[\text{O}_2\text{Cu}_5]$  chain can be described as strongest structural units with the shortest bond lengths and correlates perfectly with the minimum of thermal expansion value.

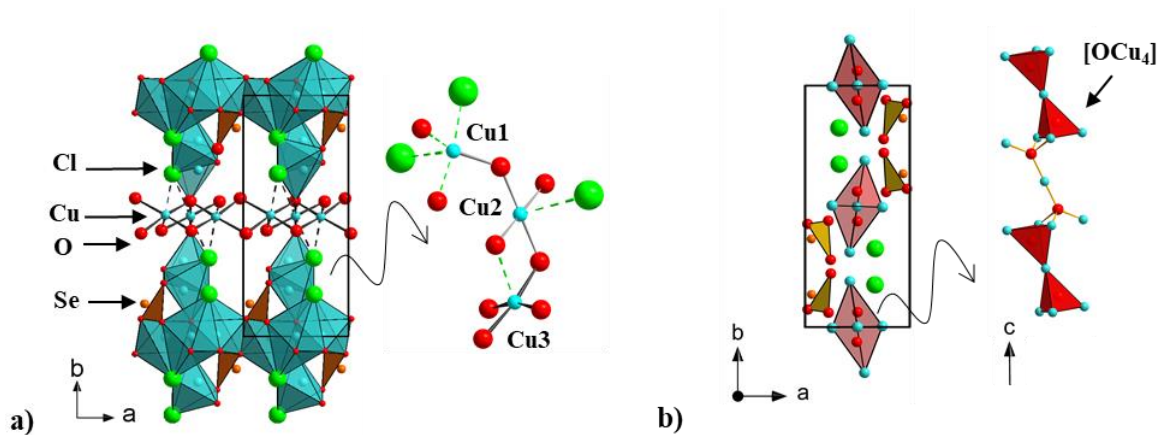


**Figure 1.** Crystal structure of georgbokiite,  $\text{Cu}_5\text{O}_2(\text{SeO}_3)_2\text{Cl}_2$ . a) It is shown in terms of cation-centered approach, where Cu atoms and polyhedrons  $[\text{Cu}(1)\text{O}_3\text{Cl}_2]$ ,  $[\text{Cu}(2)\text{O}_4\text{Cl}_2]$  and  $[\text{Cu}(3)\text{O}_5\text{Cl}]$  are given in blue, chlorine atoms in green,  $\text{SeO}_3$  in orange. b) Oxygen atoms and polyhedrons formed around are given in red using oxo-centered approach.

This example demonstrates the benefits of the anion-centered approach in the case under consideration. Foremost that approach gives better description of thermal expansion anisotropy. On the other hands it leads to reduction of crystal structure description complexity or may be powerful in the case of structural disorders as detailed later.

### *a. History*

For the first time in 1968 Bergerhoff, G and Paeslack, J. revised large a group of structures where the central atom of coordination polyhedra is in the negative state of oxidation. They proposed to consider a crystal structures of some compounds where there is a combination of both strongly bounded complexes of “acid residues” such as sulfate, silicate, germanate, chloride, fluoride, etc. and the “additional” oxygen atoms. To confirm the reasoning and regularity of new approach they provided the examples of a structures like dolerophanite [3],  $\text{Cu}_2\text{O}(\text{SO}_4)$ , where oxygen atoms are associated with either a sulphate group or copper. Using this approach, tetrahedral complexes  $[\text{OCu}_4]$  where oxygen atom is coordinated by four copper atoms were defined. These tetrahedrons form positively charged 2D  $[\text{OCu}_2]^{2+}$  layers share edges and corners whereas the negatively charged tetrahedral  $(\text{SO}_4)^{2-}$  anions contribute to the electro neutrality of the structure.

Bergerhoff, G. and Paeslack, J. [4] also showed the applicability of this method to describe the crystal structures of some other compounds:  $\text{Zn}_4\text{O}(\text{BO}_2)$  and  $\text{Be}_4\text{O}(\text{CH}_3\text{COO})$  (both containing isolated  $[\text{OM}_4]$  tetrahedra), kyanite,  $\text{Al}_2\text{O}(\text{SiO}_4)_4$  (containing double  $[\text{OAl}_2]^{4+}$  chains),  $\text{Bi}_2\text{O}_2(\text{GeO}_3)$ ,  $\text{La}_2\text{O}_2\text{S}_6$  (based upon the layers of edge-sharing  $[\text{OM}_4]$  tetrahedra ( $\text{M} = \text{Bi}^{3+}$  or

La<sup>3+</sup>), and Pb<sub>2</sub>OF<sub>2</sub> (containing [OPb<sub>2</sub>]<sup>2+</sup> or [OPb<sub>4</sub>] tetrahedra with F<sup>-</sup> ions in framework cavities).

Around the same time Caro while working on MOCl and A-M<sub>2</sub>O<sub>3</sub> systems (M = rare-earth metal) made a conclusion that oxo-centered tetrahedra can be identified in rare earth oxide and oxysalt structures. [5]

In the next more than decade, a systematic study of this oxo-centered structural units was not commonly elaborated. Sixteen years later, Carre et al. published a paper [6] on the investigations of compounds containing lanthanum oxo-centered complexes and derive various new types of complexes from [OLa] layer. In the following research scientists focused on the study contained in both crystalline and amorphous media. Consecutive review of Bengtsson and Holmberg was aimed at the study of oxo-centered [OPb<sub>4</sub>] tetrahedra containing both in the crystalline and amorphous media. [7] Damodaran and Rao moved far forward in-depth study of glasses containing [OPb<sub>4</sub>] tetrahedra performs a similar function as the [SiO<sub>4</sub>] tetrahedra in silicate glasses. [8] In 1982, Keller launched the beginning of a series of papers devoted to comprehensive investigation of Pb oxyhalides made up of [OPb<sub>4</sub>] structural units. Aside from this, Schleid and co-workers undertook a crystal chemistry study of compounds involve rareearth elements and “additional” oxygen and nitrogen atoms as the centers of metal tetrahedrons. In 2000 Magarill with colleagues developed the structural classification of Hg<sup>+</sup> and Hg<sup>2+</sup> oxysalts.

### ***b. Crystal chemistry***

To be more precise, some parameters should be clarified. In crystal structures, the strong complexes [T<sub>m</sub>O<sub>n</sub>] of high-valent cations of Si, Ge, B, S, P, V, As, Se, etc. (T) can be distinguished. Anions that do not involved in the formation of these strong complexes and forming strong bonds to other atoms consider as “additional” atoms. In terms of anion-centered approach “additional” anions may be perceived as a coordination centers of anion-centered complexes. Oxygen is the most common anion acting as a coordination center due to its high electronegativity [9] (3.44) and high hardness [10] (6.08). N<sup>3-</sup> anion is also well sorted (electronegativity: 3.04, hardness: 7.23) to enter these units whereas F<sup>-</sup> or Cl<sup>-</sup> are barely rare (electronegativity: F; 3.98 and Cl; 4.68, hardness: F; 3.16 and Cl; 4.68) also because of their low charge which is a limiting parameter.

The nature of cations is also limited. In 2001, Krivovichev and Filatov [11] have published their scientific treatise in which they reviewed minerals and inorganic compounds containing

anion-centered tetrahedra. They extracted general principles under which conditions the formation of these complexes may be occurred giving clues on cations nature.

The first principle is based on bond valence calculations [12], where the valence unit is a decisive parameter. The first principle reads as follows that anion-centered tetrahedra  $[X^nM_4]$  may exist if cation M may form an M–X bond with the bond valence of  $n/4$ . By inference from that the oxo-centered tetrahedra  $[OM_4]$  may exist if cation M may form an M–O bond with the bond valence of 0.5 valence units.

The second principle states that the presence of anion-centered unit can be confirmed if M–X bonds are the strongest bonds in the  $[MX_m]$  coordination polyhedra. The combination of these principles makes it easy to choose the most appropriate method for describing crystal structures. According to the results of a global study of anion-centered compounds, this approach is the most efficient for  $Cu^{2+}$ ,  $Pb^{2+}$  and  $REE^{3+}$ , more rarely for  $Bi^{3+}$ . In terms of anion-centered approach anion, tetrahedral  $[XA_4]$  coordination occurs more often than triangles  $[XA_3]$  or octahedra  $[XA_6]$  in antiperovskites or inverse perovskites structures [13], where (A cations; X = anions). In our lab, we have a strong experience on the Bi-based oxo-centered compounds and recently opened a new route of research, working with lanthanides.

## **I.2. A good knowledge of these systems at UCCS**

### **I.2.1. Bi-based materials**

The lab has a strong experience in the isolation of new oxo-centered materials, mainly based on bismuth.

#### *a. Design approach*

A large part of the story started with the investigation of the bismuth transition metal phosphate family of compounds. Most of these compounds are built of 1D ribbons of variable width, built on  $[O(Bi,M)_4]$  (M= Cu, Zn, Mg, Cd...) tetrahedra sharing edges. The ribbons are surrounded by isolated phosphate groups and also showing sometimes tunnels with variable number of cations. A deep investigation of these systems allowed to establish structural rules which enabled the design, formulation, synthesis and full characterization of new members of the family. Several examples exist and are presented in ref [14]. Also, these structural rules were

also successfully used to give a formulation to defects observed on High-resolution electron microscopy (HREM) images. [15]

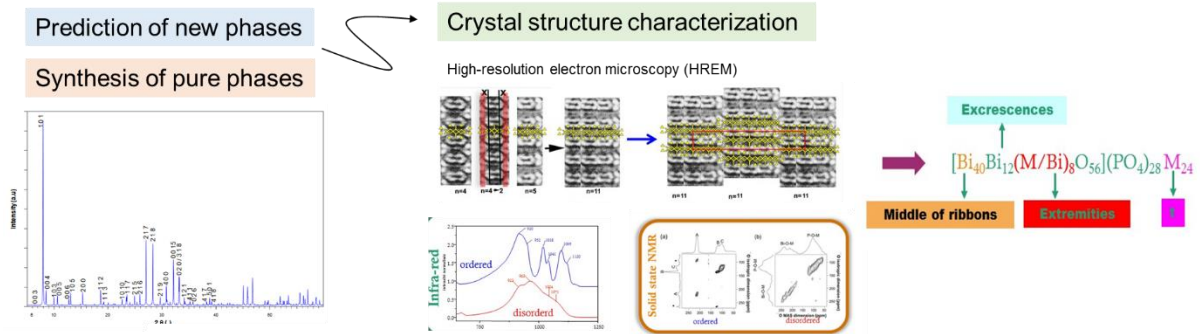


**Figure 2. General overview on strategy, enabling of new compounds design from observation on HREM images going through identification of types of ribbons, formulation to the synthesis of the pure phase.**

### *b. Disorder phases*

Most of these compounds show a disorder easily observed using infra-red, NMR or also single crystal X-Ray diffraction. During long time, it remains questionable and without precise explanation. Recently, a study was performed to characterize all the levels of disorder in these crystalline/glassy intermediates. Three different intermediate cases were isolated [16]:

- a full disorder observed in  $[Bi_2(Bi_{1.5}K_{0.44})^{dis}O_3]K_{0.88}^{dis}(PO_4)_2$  related to the arrangement of K in the tunnels as well as a mixed position Bi/K at the edges of the ribbons. These disorders were observed at nano and micro-size of domains.
- a partial cationic ordering was evidenced in  $[Bi_{10}(Bi_{\approx 0.5}Cd_{\approx 0.5})_8^{dis}O_{16}](Bi_{0.6}Cd_{0.8})_2^{ord}(PO_4)_8$ . That time, it shows a Bi/Cd ordering in the cationic channels whereas the extremities of ribbons remain fully disordered,
- finally a total ordering in  $[Bi_{18}Zn_{10}O_{21}]^{ord}Zn_5^{ord}(PO_4)_{14}$  with all terms of the crystal structure perfectly ordered.

All these terms are explained in Figure 3.

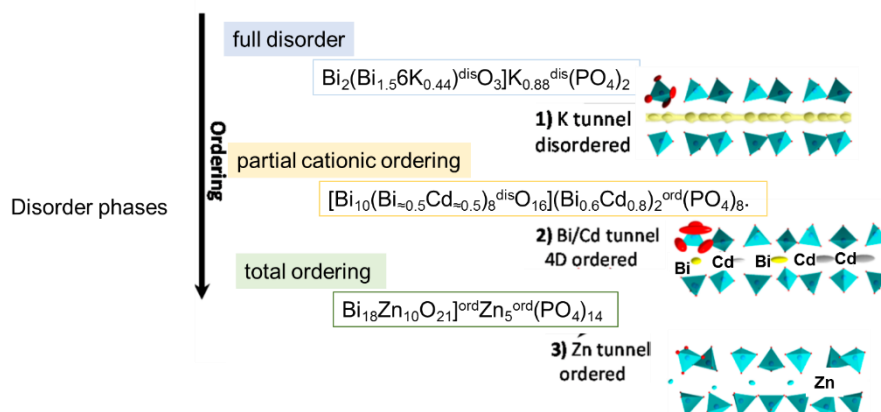
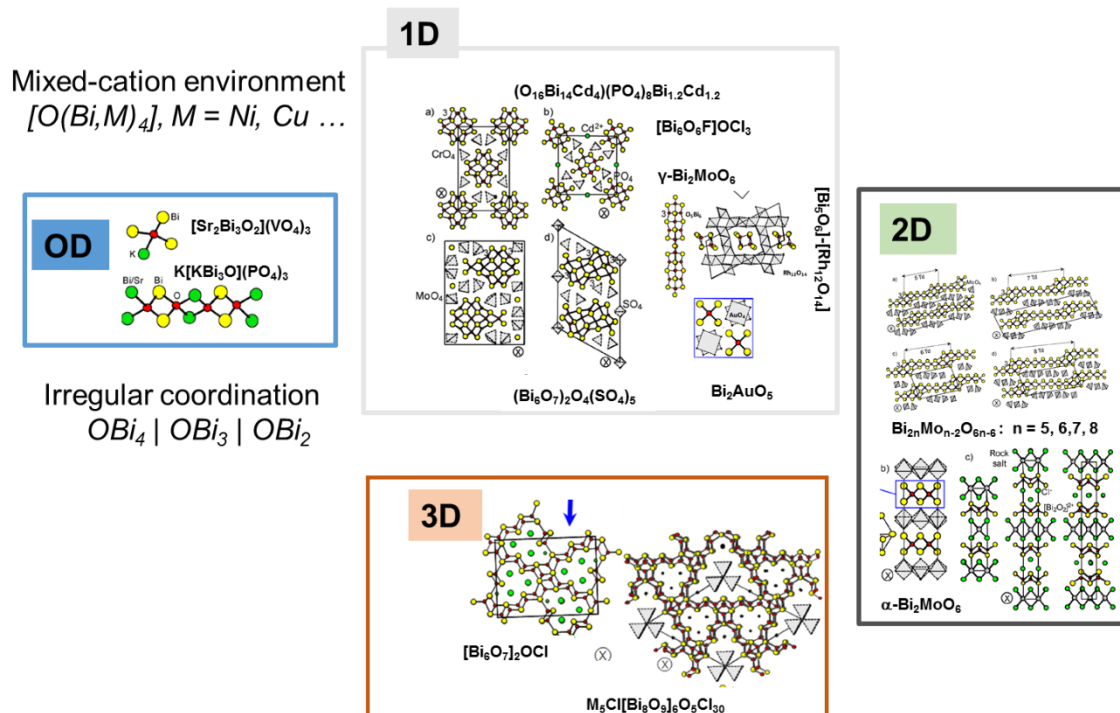


Figure 3. Representation of order and disorder in tunnels of three crystal structures.

### c. Towards multi-dimensional open frameworks

The  $\text{Bi}^{3+}$  cation and its lone pair are very efficient and prompt to the flexibility of structural units. Several examples are listed below about the dimensionalities of the building units available:

- 0D: the number of structures showing 0D units remains rare because of bond valence effects and because the charge is finally too high to be compensated. For example  $[\text{Sr}_2\text{Bi}_3\text{O}_2](\text{VO}_4)_3$  [17], is built on association of  $[\text{O}_4(\text{Bi}_2(\text{Bi}/\text{Sr})_2)]$  tetrahedra sharing edges;
- 1D chains and ribbons: this includes 1D single chains presented in the case of the bismuth oxide phosphate family. Most of the units presented are ribbon-like polycations  $[\text{O}(\text{Bi},\text{M})_2]^{n+}$  built on the edge sharing of  $[\text{O}(\text{Bi},\text{M})_4]$  tetrahedra. To date, the observed width varies from 1 to 11, with a unit cell parameter ranging up to  $58\text{\AA}$ . In other cases, the 1D units look like column more or less distorted as shown on Figure 4;
- 2D units: the extension of the 1D units gives rise to 2D layers, planar or like Cresnel function again surrounded by isolated  $[\text{XO}_4]$  entities ( $\text{X} = \text{Mo}, \text{V}, \text{P}, \text{As}, \text{W}, \dots$ );
- 3D-units: frameworks: finally, some 3D-networks of connected tetrahedra are also observed, sometimes showing open structures with tunnels of variable size and width.



**Figure 4. The examples of Bi-based oxo-centered units of different dimensionality**

It was recently shown that the modification of the anionic counterpart has important effects on the dimensionality of the crystal structure. Many 2D layered compounds are referenced with  $Cl^-$  as counterpart, for example in the Sillen-Aurivillius [18] series of compounds. Times to times,  $Cl^-$  anions take place in 1D tunnels built in a bismuth framework as it is observed in  $Bi_{12}O_{15}Cl_6$  [19],  $[Bi_6O_6F]OCl_3$  [20]) or  $(Ag_{4.78}Cl_{1.5})(Bi_{48}O_{58.64}Cl_{30})$ . [21] These three structures show these 1D channels with triangular structures of variable width. Also the use of Bi is very powerful, the Bi-O bond valence of 0.596 v.u. compared with 0.5 v.u. in the case of a regular tetrahedra. This implies a flexibility of the  $[OBi_4]$  tetrahedra and the possibility to replace Bi by other cations as  $Na^+$ ,  $Mn^{2+}$ ,  $Pb^{2+}$  in small amounts. [22]

Combining that, multi-dimensionnal open frameworks were successfully obtained as shown on Figure 5.

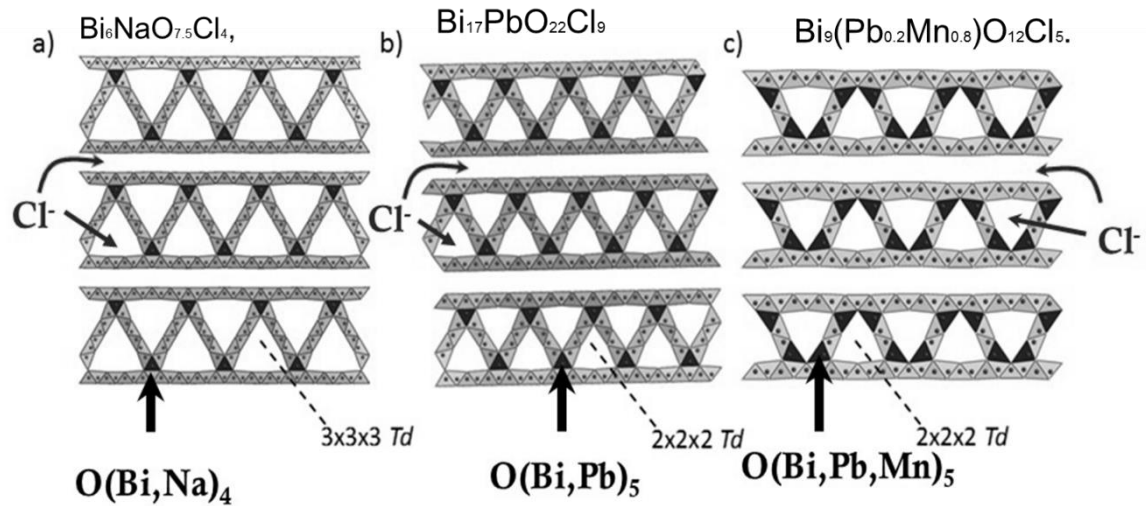


Figure 5. Examples of multi-D open frameworks: a)  $\text{Bi}_6\text{NaO}_{7.5}\text{Cl}_4$ , b)  $\text{Bi}_{17}\text{PbO}_{22}\text{Cl}_9$  and c)  $\text{Bi}_9(\text{Pb}_{0.2}\text{Mn}_{0.8})\text{O}_{12}\text{Cl}_5$ . [figure borrowed from 22]

### 1.2.2. Ln-based materials

More recently, new investigations were performed, using lanthanides instead of bismuth. It induced adaptation of the synthesis routes as lanthanides are naturally more refractive and  $\text{Ln}^{3+}$  cations go into very regular tetrahedra which limit the possibilities. Several new materials were isolated  $\text{Pb}_4\text{La}_2\text{O}_7$  [23], an interesting 2D Van der Waals material, the series of  $\text{ALa}_5\text{V}_2\text{O}_{13}$  (A= Li, Na, Rb, K) [24] and two polytypes of  $\text{La}_7\text{V}_3\text{O}_{18}$  [25]. All of them will be presented later but for the moment, it is important to mention the difficulties encountered to study them: in front of big unit cell parameters and volume, heavy elements in the unit cell and in absence of the possibility to obtain single crystals, the PEDT was successfully developed and used. Of course, for the moment we don't yet have the benefit of hindsight concerning these chemical systems but at least it enabled to figure the points that have to be clarified and the technological barriers to be settle. Also, the properties measured are different, mainly dedicated to the study of magnetic properties after doping the phosphors by emitters as  $\text{Eu}^{3+}$ ,  $\text{Sm}^{3+}$  or  $\text{Tb}^{3+}$ .

Whatever the system investigated is, the synthesis routes were mainly centered on usual conditions, involving various synthesis process as solid-solid synthesis or hydrothermal synthesis under classical range of temperature or pressure. Nevertheless, for the moment, nothing was tried working at higher pressures also it may be interesting to stabilize metastable phases or phases with transition metal with unusual high oxidation rate. This is a more and more used nowadays after its efficiency on Perovskites mainly.

In the next part, a review of the technical aspects enabling the application of pressure and in some times temperature also will be presented as well as an overview of the oxo-centered phases obtained by HP-HT synthesis.

### **I.3. Towards new oxo-centered architectures obtained by HPHT syntheses**

The synthesis of new inorganic compounds that cannot exist under normal conditions can be efficiently obtained under high-pressure conditions. New compounds synthesized under high-pressure conditions may have different valences, unusual structures, and sometimes unexpected physical and chemical properties due to variations of interatomic distances and other changes. The effect of applying high pressure on the crystal structure may be reversible when the pressure is unloaded. In order to stabilize the structure, the high temperatures are in routine using together in high-pressure synthesis. Conditions for high-pressure high-temperature synthesis should comply the pressure range  $1.01 - 10^9$  Pa at temperature ranging from ambient to 3000°C.

The most widely used method of synthesis in high-pressure field is **hydrothermal**. Hydrothermal technology has a historical connection with development geological sciences in the mid-nineteenth century. Initially the term "hydrothermal" was used by Geologist Sir Roderick Murchison (1792-1871) to describe the crystallization mechanism of some minerals from fluids related with magma. The operating pressure-temperature range for hydrothermal method is 100-1000°C and 1-100 MPa. The era of true high pressures began with work of P.W. Bridgman. The field of high pressures came under the scrutiny of the scientific world after he received the Nobel Prize in 1946. The technology of using direct synthesis or modification of chemical compounds by the method of high pressures is not widespread like other methods of synthesis. There are several reasons for this, but the main one is the sufficient complexity of the process itself. For a successful experiment, in addition to choosing the right one type of high-pressure apparatus (detailed below) a substantial number of variable parameters must be chosen: Pressure Transmitting Media, Pressure and temperature calibrant, way of high-temperature generation etc. The second significant problem is the high cost of equipment and related materials. The next important amendment is the dependence of the decrease in the volume of a substance with the pressure increase (Figure 6) which can be a significant problem to study the sample and/or to measure any physical properties. [26]

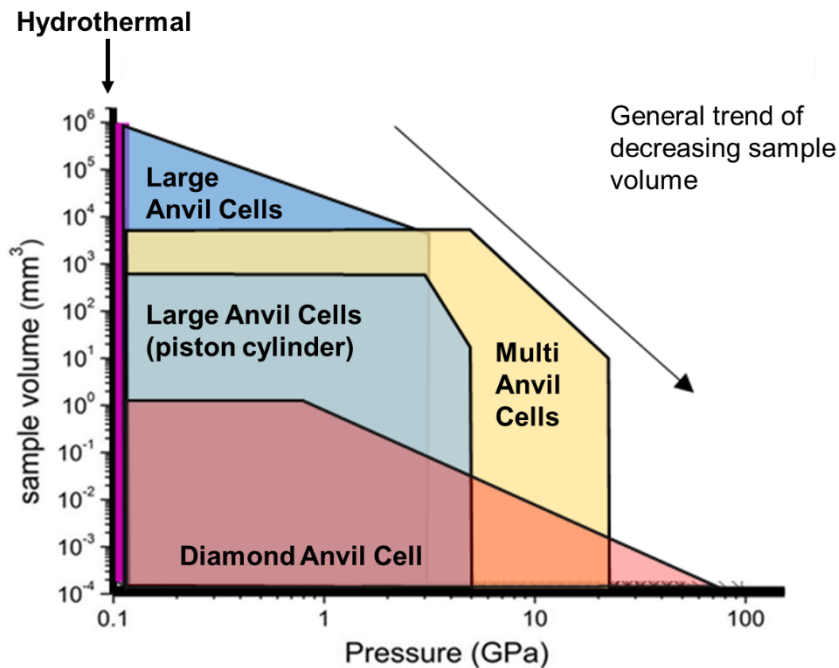


**Figure 6. General trend of sample volume dependence on the pressure increase using different types of HP-HT apparatus.**

In the next part, the main types of high-pressure devices and their operation principle are considered. The variety of working conditions and purposes for high-pressure application are demonstrated.

### I.3.1. High-Pressure Apparatus

Hydrostatic high-pressure synthesis can be broadly divided into static and dynamic technologies.

Static-type pressure devices can be performed by gas containers and autoclave presses. For example, in lab **the Paterson apparatus** can be used. That is a special high-pressure high-temperature internally-heated pressure vessel aimed at performing dynamic experiments (i.e., deformation). It is a triaxial cell capable of pressures of up to 500 MPa (approximately 20 km depth in the Earth's mantle) using Argon gas as pressurizing medium and up to a maximum of 1300 °C. The equipment can be fitted with either a standard axial deformation piston (for pure shear deformation) or a torsion actuator (for simple shear deformation). **Ultrasonic Rig** - Internally heated hydrostatic pressure vessel (oil confining medium), equipped with piezoelectric elements to transmit and receive waveforms through rock samples (Birch's method) allowing P and S seismic velocities measurements, up to 400 MPa and 150°C. The

**Geneva rig** is also equipped with a hydraulic circuit to vary the pore pressure up to 50 MPa. **Broad Band Attenuation Vessel** allows maximum size of the sample is 76 mm in diameter and 250 mm in length. The sample can be confined up to 25 MPa. The BBAV has a hydraulic circuit to saturate the sample. **Uniaxial Cold Press** [26] - This apparatus is used for sample deformation and powder compaction at room temperature and atmospheric confining pressure. **Hot Isostatic Press** is a large capacity industrial internally-heated pressure vessel used for high-pressure and high-temperature synthesis. The pressure range for all these devices is 0.1–1GPa and a volume of sample can be  $\sim 0.01\text{--}1\text{m}^3$ . Pressures  $\sim 0.1\text{GPa}$  are extremely intensively used industrially. These values of pressure are considered rather low compared to the latest technologies.

Another type of high-pressure equipment is **Bridgman-anvils** [28] devices (flat, profiled, toroidal, double-toroidal). [29] This apparatus was made to create pressure between two anvils. To create a hydrostatic pressure, the sample is loaded in pressure medium and surrounded by gasket between two opposed hard anvils. When the anvils draw together, the gasket uniformly distorts and contributes to the equal pressure distribution on the sample. For hard alloy anvils maximum pressure is around 15–20GPa; for SiC anvils – 20–70 GPa; and for diamond anvils – 100–300 GPa. But the volume of sample decreases from  $10^{-1}$  to  $10^{-6}$  mm<sup>3</sup>.

Depending on the purpose of the study, it may be necessary to apply uniaxial strains, for example, to study the rheological properties. The **D-DIA** or **deformation-DIA** is an apparatus used for high-pressure and/or high-temperature deformation experiments. [30] The advantage of this apparatus is the ability to apply pressures up to approximately 15 GPa while independently creating uniaxial strains up to 50%. To investigate plastic deformation in crystalline materials, **Griggs apparatus** [33] is used, where temperatures of up to 1600 K along with pressures of approximately 3 GPa can be achieved. The most extreme non hydrostatic P–T conditions currently available are developed in dynamic environments permits reaching pressures  $\sim 100\text{--}1000$  GPa using Ultrasonic or Shock wave techniques. That allow sampling of deep planetary interiors including the gas giants and small stars. The products and reaction mechanisms of shock-induced chemical reactions are quite different than those produced under ambient conditions or static high pressure.

To create a higher pressure is necessary to use equipment with moving parts- dynamic technologies. The **piston-cylinder** [34] type devices can accommodate a sufficiently large sample volume and reaches pressures up to 3 GPa. Small-volume piston-cylinder apparatus

allow reaching pressures 5–7GPa. In these devices the piston and the cylinder parts are constructed of ram driven cemented tungsten carbide, being very high compressive strength material. Carbide cylinder is surrounded by massive alloy-steel binding rings. The principle of the instrument is to generate pressure by compressing a sample assembly, which includes a resistance furnace, inside a pressure vessel.

**Belt Apparatus** [36] is used to create and maintain high pressure and temperature for a long time. Two conical pistons squeeze the chamber where the sample is located. The tube in which the sample is located serves as a heating element. The current flows to the sample by touching the conductive parts of the system. Thermal insulation is provided by pyrophyllite parts.

More than two anvils are used for samples from 1 mm<sup>3</sup>. They are classified based on geometry of pressure chamber. The first type of multianvil cell was represented by tetrahedral geometry. In a cubic press six sides of the cube are pressed together creating pressure on the sample and transmitting medium. In contradistinction to previous types octahedral cell is multistaging. First stage presented by multianvil cell of cubic type. Second is an assembly of eight cubes truncated at one corner forming cavity in the center filled by solid pressure transmitting medium and the sample.

The **Diamond Anvil Cell** (DAC) is similar in pressure build-up with Bridgman-anvils cell and enters into group of devices with opposed anvil configuration. Considering the unique hardness of the diamond they are used as anvils. To avoid a contact between two diamonds they are protected by a metal gasket, which is deformed over the course of the experiment. The sample is placed inside the through hole in the gasket, the remaining space is filled with transmitted media. There are several types of experiments available using this technology- hydrothermal DAC, Resistively Heated DAC, Laser-heated DAC, Double-stage DAC for highest pressure.

To conclude with a classification of the high-pressure techniques are useful for the solid-state chemistry, the Table 1 was prepared to summarize the principal values of pressure, temperature and average sample volume. The basic parameter to divide the high-pressure equipment is a sample volume capacity. [39] The high-pressure devices can be roughly divided according to anvil cell size. [43] The Large anvil cells (LACs) presses have a sample capacity between the mm<sup>3</sup> and cm<sup>3</sup> scales, compared to extremely small just noticeable amount in case of Diamond anvil cells (DACs). A compromise in sample size can be found by the use of Multi Anvil Cells (MACs) devices.

**Table 1. The operating pressure-temperature range of high-pressure equipment.**

	<b>Apparatus</b>	<b>Average sample volume</b>	<b>Pressure limit</b>	<b>Temperature limit, C(°)</b>
<b>Diamond Anvil Cells (DACs)</b>	Diamond anvil cells	To micrograms	beyond 500 GPa	To 4000 °C
<b>Multi Anvil Cells (MACs)</b>	Walker type press	To few milligrams	To 25 GPa	To 2000 °C
<b>Large Anvil Cells (LACs)</b>	Belt-type press	To 1 gram	To 2-8 GPa	To 1500 °C
<b>Hydrothermal</b>	Novaswiss autoclave	To few grams	To 2,5 Kbar	To 700 °C

#### *a. High-pressure equipment used in current research*

While working on my thesis, I used several of the methods presented above. The first experiments were done in Lille University on hydrothermal equipment with the support of Nora Djelal. Novaswiss autoclave was used to provide a series of experiments under counter supercritical water pressure. The sample was placed in a gold tube, that was subsequently sealed. The disassembled High-Pressure Vessel is given on Figure 7 (a). The equipment is ready for the experiment when the gold tube is placed inside the container filled with water and tightly closed, as is shown on Figure 7 (b). A photo of the device with the designation of High-Pressure Vessel location is shown on Figure 7 (c). Successful results of these experiments are described in II.3 chapter.

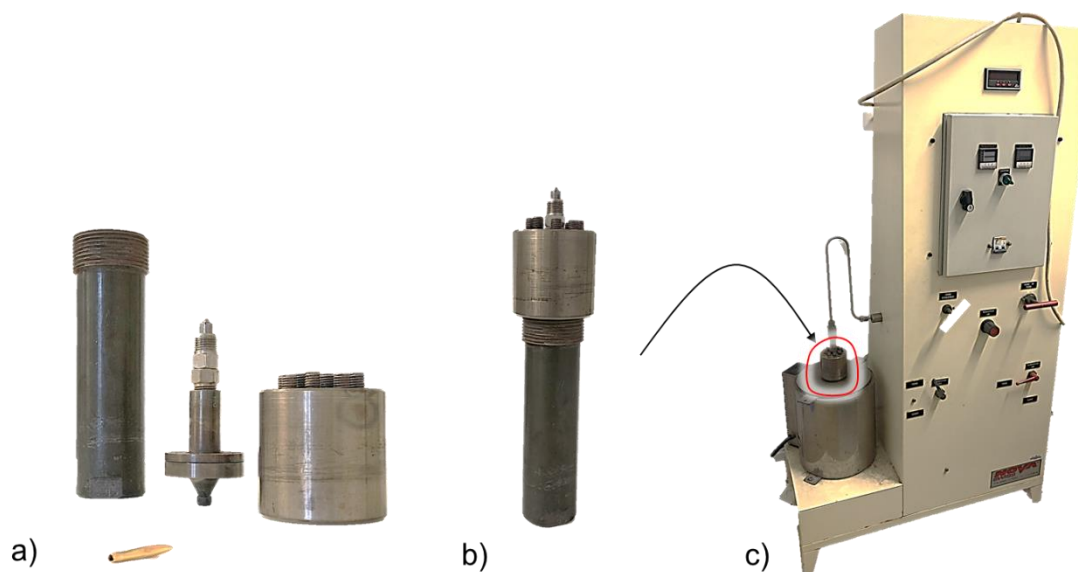


**Figure 7. High Pressure Vessel in disassembled (a) and assembled (b) view. General photo of the Novaswiss autoclave device (c).**

My acquaintance with the topic of real high pressures for the purpose of the synthesis and modification of new materials occurred during an internship in Grenoble under the supervision of Céline Darie. In order to provide series of experiments during my work, the BELT X type and Konak type high-pressure chamber were used during the one-week stage at the Neel Institute. The inner pressure chamber is composed by assembly of metal sample container, two halves of pyrophyllite gaskets and graphite parts (Figure 8(a)). In order to avoid sample container interactions with an initial powder, the Au or Pt capsules can be used. Since the capsule is only 2-3 mm in diameter and 5-6 mm in high, the powdered sample needs to be slightly compressed inside the capsule to be more compact. Onwards the capsule was placed inside the graphite oven where the pyrophyllite cylinder used as insulator. In the next step this construction placed inside the doubly concave double-sided pyrophyllite gasket which act as the pressure transmitting medium. Two polytetrafluoroethylene (PTFE) gaskets were placed at the last step of pressure chamber loading. Two conical Carboloy pistons pushed into each side of a specially shaped Carboloy chamber. The sample was pressed by tapering of binding rings around tungsten carbide pistons that forms a toroidal belt (Figure 8(b)). During the experiment the High temperature was achieved by applying a high intensity electric current through the graphite cylinder in the pressure chamber.

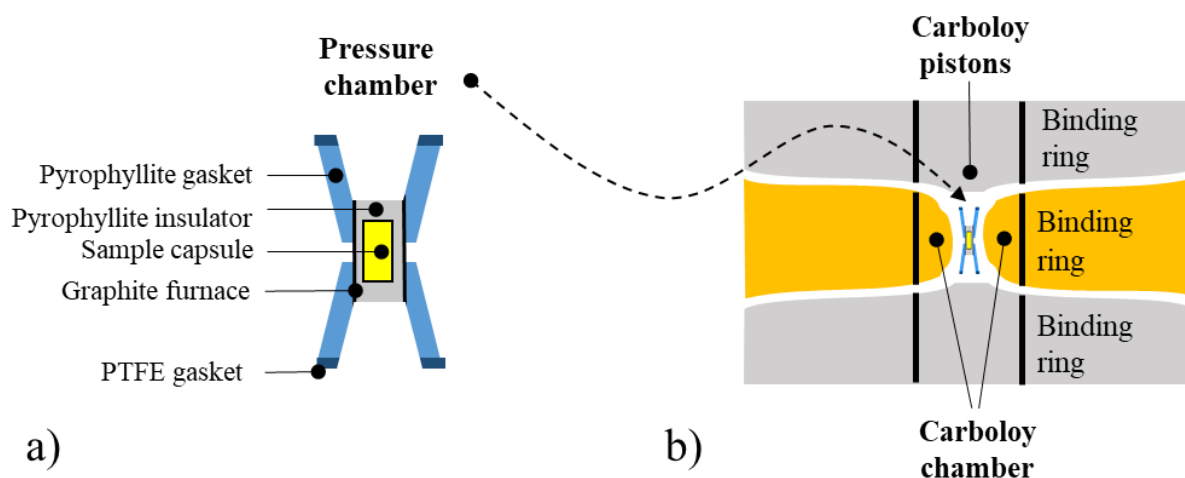


**Figure 8. a) Cut through the pressure cell of the BELT type press; b) The "belt", ultrahigh-pressure, high-temperature assembly.**

The BELT X type of press has a water-cooling system, that is constructed into the toroidal belt. The HT-HP conditions were controlled through the applied force (to the pistons) and power supplied (to the oven). Due to technical limitations there is no possible way to provide direct measurements of applied conditions on the sample. Related force to pressure and wattage to temperature graphs were used. These graphs were obtained by press calibration procedure. In order to provide this experiment, the induced phase transitions of bismuth were investigated with a thermocouple loaded in the pressure cell. After the experiment the capsules was cleaned from the destroyed disposable chamber. The use of this equipment has led to the successful modification of some compounds, that will be described in II.1 and II.2 chapters.

Before starting independent use of Diamond Anvil Cell equipment, I was trained by Sébastien Merkel - Professeur Université de Lille from Unité Matériaux et Transformations. Over the course of several weeks, I learned how to align the diamonds, drill the gasket and load the cell. After training, he kindly lent me two cells for further experiments. Next two months (from 1<sup>st</sup> October 2018 till 1<sup>st</sup> December 2018) I did an internship at University of Madrid, Department of Physical Chemistry, Faculty of Chemical Sciences under supervision of Dr. Javier Sanchez-Benitez. The main purpose of this work was to detect changes in the crystal structure of the starting compound or phase transition under the influence of high pressure using XRD. Unfortunately, the equipment was out of order and I focused on Raman spectrometry.

During the internship, I worked with two technical aids to achieve high-pressure conditions, that are not available in Lille:

1. High-pressure high-temperature experiments were provided by Belt-type press (similar was use during the stage at the Neel Institute). Only a few experiments were performed, which did not lead to the production of new phases;
2. High-pressure experiments were provided using Diamond Anvil Cell equipment.

The Screw Driven Plate Diamond Anvil Cells (Figure 9(a)) with 300  $\mu\text{m}$  cullet size were used during the stage. We chose steel gaskets that allowed to reach pressure up to 20 Gpa and silicone oil as for pressure transmitting medium. For each experiment the gaskets were pre-indented manually to reach 30  $\mu\text{m}$  thickness of 100  $\mu\text{m}$  diameter hole. Thereafter the hole was drilled using Betsa Electric Discharge Machine. The Figure 9 (b) shows the structure of the inner part of the cell, as seen through binocular at 60x magnification. This is what a real sample (contoured yellow) looks like lodged between the two diamonds. Ruby is shown in red, placed as an indicator for pressure control.

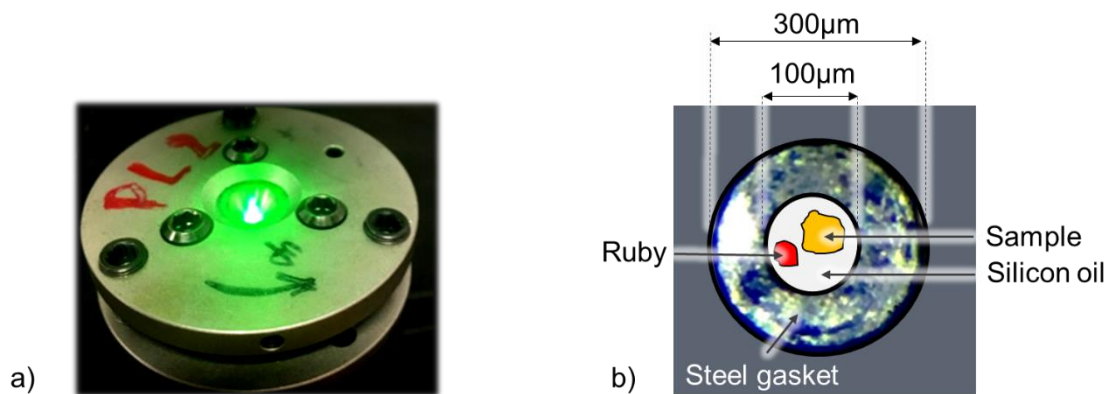


**Figure 9. Schematic representation of loaded DAC ready for the experiment.**

Raman spectra were collected at room temperature on a backscattering confocal micro-Raman spectrometer (Voyage<sup>TM</sup> BWS435-532SY, BW&Tek) equipped with a CCD detector. The excitation was a 532 nm line from a solid-state laser, collected on the sample through an Olympus BX51 microscope with a 20x objective. Laser power was limited to 2 mW to avoid sample degradation. In order to determine the pressure inside the DAC, ruby spheres were placed next to the sample. Raman spectra were registered in the 100-1500  $\text{cm}^{-1}$  range of Raman-

shift. The Raman spectra were registered in the 100-1500  $\text{cm}^{-1}$  range of Raman-shift. At the end of the study, the sample cannot be recovered.

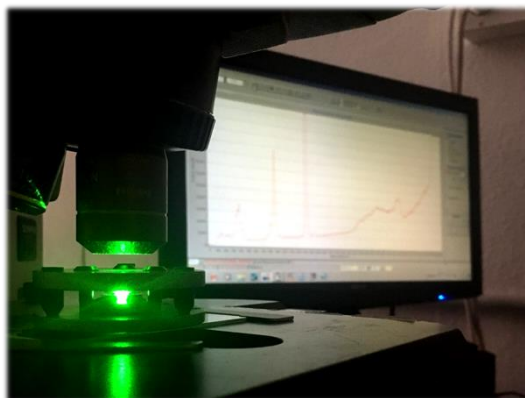


**Figure 10.** The photo was taken during the experiment of Raman spectra collection.

The positions of Raman peaks versus pressure can be obtained by two methods using Origin 2018b software. First way implies detection of peak position using second order derivative curve, whereas another way uses to operate with Multiple peak fit Analysis. Both of them show experimental reproducibility.

In total, more than 15 high-pressure experiments were performed using DAC equipment. Some of them turned out to be promising and will be described in

Another type of instrument that I actively used during my theses is a piston-cylinder apparatus in Lille University (Produced by Rockland Research Corporation, USA). This type of press, allows experiments at pressures up to 4 GPa and temperatures of 1800°C on millimeter to centimeter-scale samples. Photos of this device are shown on Figure 11. The press consists of pressure vessel, stack components and associated hydraulic control systems. The end load ram and main hydraulic ram are the parts of the press. The pressure vessel contains a tungsten carbide core, accompanied by rings of hardened steel. The sample assembly is also multicomponent. For the experiments we used platinum capsules around 3mm in diameter and 5mm in height. It is loaded in a graphite furnace, and a remain space inside the heater is filled with ceramics (MgO). At the final step the cell is wrapped around by Pb foil and inserted into pressure vessel. The thermocouple assembly inserts through the hole in the top plate.

In total, about 15 experiments were done on this equipment for different chemical systems. Some of them have given promising results and will be considered in chapter III, dedicate to High-pressure exploration in the lanthanide-based oxo-centered systems.

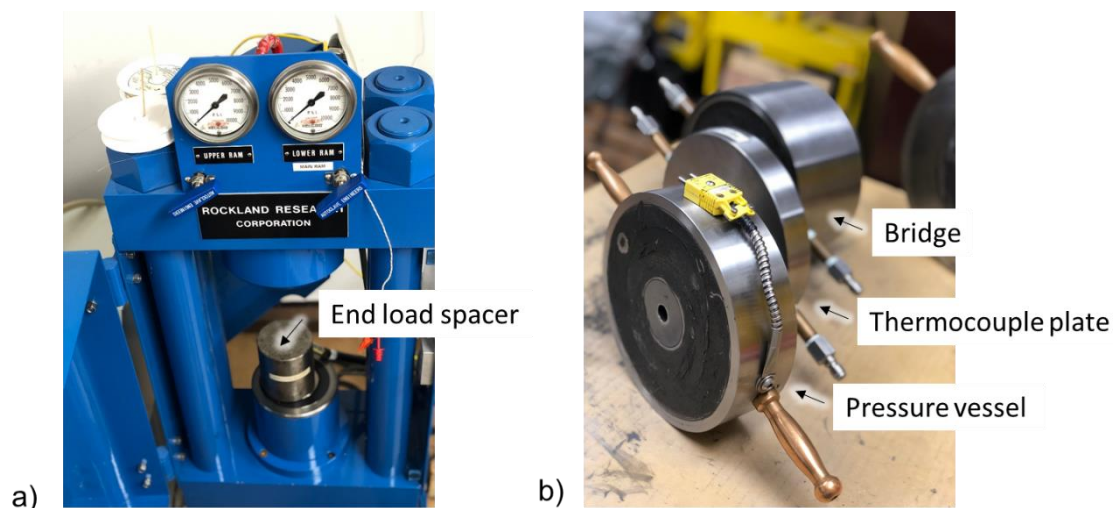


**Figure 11. (a) Photo of the piston-cylinder apparatus without a pressure vessel. (b) The components of apparatus.**

There are new oxo-centered compounds were obtained using this type of press. All of them will be described below. I have used the most common types of presses in my work. The only multi-anvil type of press was not used.

In the range of inorganic materials and oxides, the most studied phases are perovskites. Nevertheless, some studies, in a relatively low number, were done on anion-centered compounds.

### **I.3.2. Anion-centered architectures obtained by HP-HT**

This part is devoted to take a brief tour of the anion-centered structures diversity obtained by high-pressure high-temperature methods of synthesis. For the nonce there is no consistent review of inorganic compounds obtained by this method. That is a tough proposition to provide a literature survey targeted on both anion-centered compounds and their HP-HT modifications or synthesis. This is a consequence of several factors, in the first instance it is a double natured way of crystal structure description (anion- or cation-centered) according to the purpose of

investigation and authors own opinion. Also, the HP-HT conditional range is quite wide – from almost imperceptible to ultimate values. On this basis it was suggested to roughly divide all known compound according to the conditions of their synthesis.

#### *a. Samples from hydrothermal synthesis*

According to the general search in crystallographic database it was established that the majority of compounds described in anion-centered approach were obtained applying pressure less than 2 GPa and by hydrothermal route. A feature of the hydrothermal method of synthesis in comparison with other high-pressure methods is the ability to lengthen the time of the experiment and the impact of the media (pH, redox, ...). It allows to avoid the temperature and pressure gradient during the experiment and results in quite pure samples. Homogenization of the initial reagents throughout the chamber volume favors to provide the experiments with multicomponent systems.

This method of synthesis is an excellent simulator of natural processes leading to the growth of mineral-like compounds. The hydrothermal technique is one of the most applied and applicable in geology and other related disciplines. [38] Actually, even the term *hydrothermal* has a purely geology origin. It was embedded by Sir Roderick Murchison in 19<sup>th</sup> century in order to describe the affection of water on earth's crust, that driving the formation of various rocks and minerals. [44]

This method is widespread in order reproduce the original mineral in laboratories to provide the exhaustive analysis, that is frequently impractical if using the natural samples. Another advantage is to simulate the natural environmental conditions in order to understand the behavior of chemical system in dynamic and detect metastable phases, for example. The consequent way to use hydrothermal method is developing a new composition, derived from minerals or be absolutely new.

A scientific work performed by Aksenov et al. (2017) is an excellent example of successful synthesis of namibite-like crystal structure compared with its natural analogue. [45]  $\text{Ni}(\text{BiO})_2\text{PO}_4(\text{OH})$  was synthesized using Cu-lined stainless steel autoclave of 16 ml capacity at the general pressure of 480-500 atm in the temperature range from 690 K to 700 K. The crystal structure of new compound is similar to the structure of natural namibite  $\text{Cu}(\text{BiO})_2\text{VO}_4(\text{OH})$  and is made up from infinite chains  $\{\text{MOH}(\text{TO}_4)\}_\infty^n$  of corner shared octahedrons of  $\text{Ni}^{2+}$  or  $\text{Cu}^{2+}$  and tetrahedrons of  $\text{P}^{5+}$  and  $\text{V}^{5+}$  long c axis. These chains alternate

with layers of Bi atoms in terms of cation-centered approach. Both crystal structures of  $\text{Ni}(\text{BiO})_2\text{PO}_4(\text{OH})$  and namibite have the ‘additional’ oxygen atoms that make them possible to be described in the terms of anion-centered approach. The oxo-centered polyhedrons are forming by two types of cations. In  $\text{Ni}(\text{BiO})_2\text{PO}_4(\text{OH})$  it contains one  $\text{Ni}^{2+}$  and three  $\text{Bi}^{3+}$  atoms and form  $[\text{ONiBi}_3]$  elemental building units, whereas Ni is replaced by Cu in parent mineral. Tetrahedrons shared common edges and form double *einer* chain of C3-Type.

In the course of literature survey on application of extreme HP-HT conditions it was revealed that there is tendency towards decreasing of components complexity in experiments. Most of the work was done on the study of fairly simple compounds. This is primarily due to the difficulty of analyzing polyphase systems. Even so HP-HT method was applied to synthesize the analogue of mineral of rather complex Lead Oxychloride Borate system. The aim of [69] work was to synthesize the Mereheadite,  $\text{Pb}_{47}\text{O}_{24}(\text{OH})_{13}\text{C}_{125}(\text{BO}_3)_2(\text{CO}_3)$ . This compound was forms at high-temperature and high-pressure conditions in natural environments. The “rapid quenching route” and high-temperature hydrothermal way of synthesis were unsuccessful. Direct synthesis way from precursors using the piston cylinder module of a Vöggenreiter Model LP 1000-540/50 system at 3.5 GPa and 750°C resulted in obtaining of two novel lead oxychloride borates  $[\text{Pb}_{10}\text{O}_4]\text{Pb}_2(\text{B}_2\text{O}_5)\text{Cl}_{12}$  and  $[\text{Pb}_{18}\text{O}_{12}]\text{Pb}(\text{BO}_2\text{OH})_2\text{Cl}_{10}$

#### ***b. HP-HT Polymorphs of simple oxides***

It is worthwhile noting that studies of substances under more extreme conditions are carried out less frequently. A significant proportion of the material under study is the substance of the earth's interior or related compositions and simple systems. Nevertheless, some demonstrative examples of successful experiments show the significant changes in the crystal structure under higher pressures are listed hereinbelow.

Simple oxides like lead oxide PbO and bismuth trioxide  $\text{Bi}_2\text{O}_3$  are important in industry due to their ability to form different types of glasses and especially transparent. Their properties and phase transition under extreme conditions were deeply investigated. At ambient-pressure conditions, lead monoxide occurs in two polymorphs: tetragonal  $\alpha$ -PbO and transforms into orthorhombic  $\beta$ -PbO at 540°C. Adams et al [50] detected a second-order phase transition (to *Pm21n* orthorhombic  $\gamma$ -phase) at room temperature at around 0.7 GPa, that transforms to  $\beta$ -PbO at 2.5 GPa. The crystal structure of HP phase has an orthorhombic distortion of the litharge structure. The structure refinement is absented in this work, but proposed model for  $\gamma$ -PbO at 2.0 GPa is given on Figure 12 (c), where the  $\alpha$ -PbO is given on (a), and  $\beta$ -PbO – on (b). In

crystal structures of all polymorphs, oxygen atoms are tetrahedrally coordinated by four lead cations, resulted in  $[\text{OPb}_4]$  tetrahedrons. Structures are based on infinite  $[\text{OPb}]$  layers and differ in the degree of distortion of the layers.

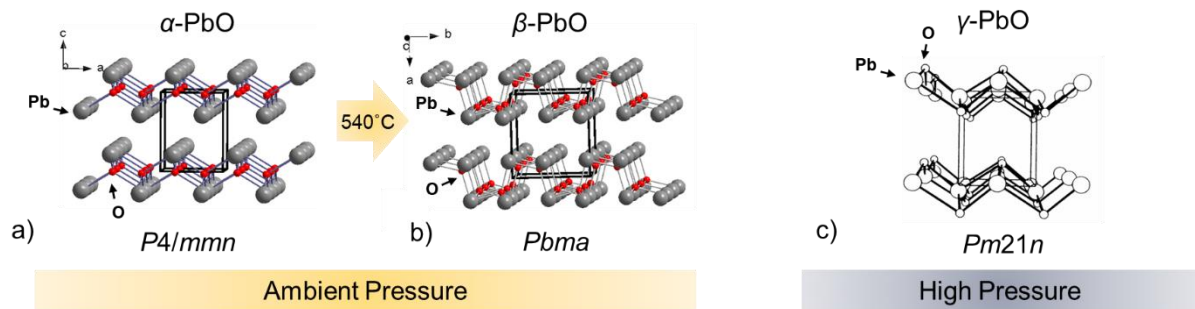


**Figure 12.** General representation of distortion of  $[\text{OPb}]$  layers in crystal structure of tetragonal (a) and monoclinic (b) polymorphs of lead monoxide. (c) Proposed model for  $\gamma$ -PbO at 2.0 GPa borrowed from [50]. Oxygen atoms are in small circles, whereas lead atoms are the in big circles.

At ambient-pressure conditions  $\text{Bi}_2\text{O}_3$  exists in several stable and metastable polymorphs. In nature it can be founded as stable bismite mineral.  $\alpha$ - $\text{Bi}_2\text{O}_3$  crystallizes in monoclinic  $P2_1/c$ , space group. Heating of  $\alpha$ - $\text{Bi}_2\text{O}_3$  above  $730^\circ\text{C}$  resulted into formation of cubic  $Fm-3m$  fluorite-type  $\delta$ - $\text{Bi}_2\text{O}_3$ . On cooling of high-temperature phase two intermediate metastable, tetragonal  $P-42_1c$   $\beta$ -phase (sphaerobismoite) and cubic  $I23$   $\gamma$ -phases can be obtained. The diversity of  $\text{Bi}_2\text{O}_3$  polymorphs at ambient-pressure conditions is shown on (Figure 13). The fifth metastable  $\varepsilon$ - $\text{Bi}_2\text{O}_3$  polymorph has been obtained using hydrothermal treatment of mixture form number of precursors in a highly concentrated KOH solution. [70]

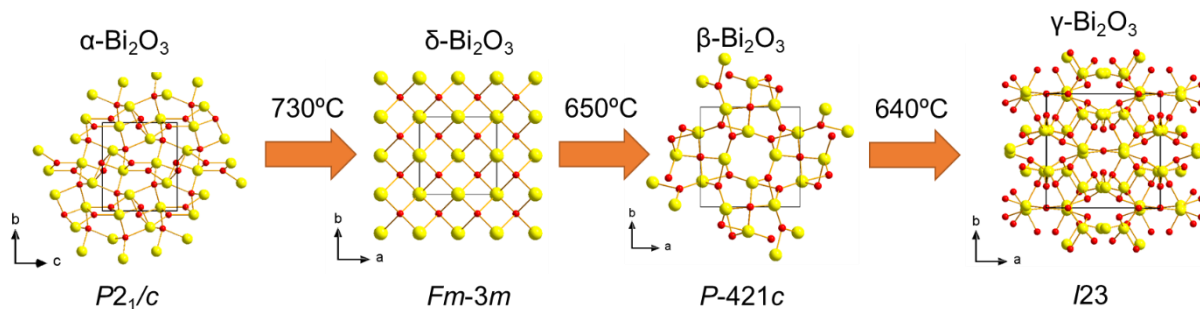


**Figure 13.** Diversity of  $\text{Bi}_2\text{O}_3$  polymorphs at ambient-pressure conditions, where Bi atoms are given in yellow circles and O – in red.

Solid-solid structural transformation induced by high-pressure conditions are efficient in  $\text{Bi}_2\text{O}_3$ . High-pressure form of  $\text{Bi}_2\text{O}_3$  obtained at 6 PGa and  $880^\circ\text{C}$  is metastable at ambient conditions. This hexagonal polymorph (HPC- $\text{Bi}_2\text{O}_3$ ) has an A-type structure crystallizes in  $P-3m1$  space group. [51] This experiment was repeated by Ghedia et al [52], and lead to formation of two different metastable polymorphs of  $\text{Bi}_2\text{O}_3$  (HP- $\text{Bi}_2\text{O}_3$  and R- $\text{Bi}_2\text{O}_3$ ). HP- $\text{Bi}_2\text{O}_3$  has a noncentrosymmetric  $P31c$  trigonal symmetry that transforms into monoclinic  $P2_1/c$  after few months.

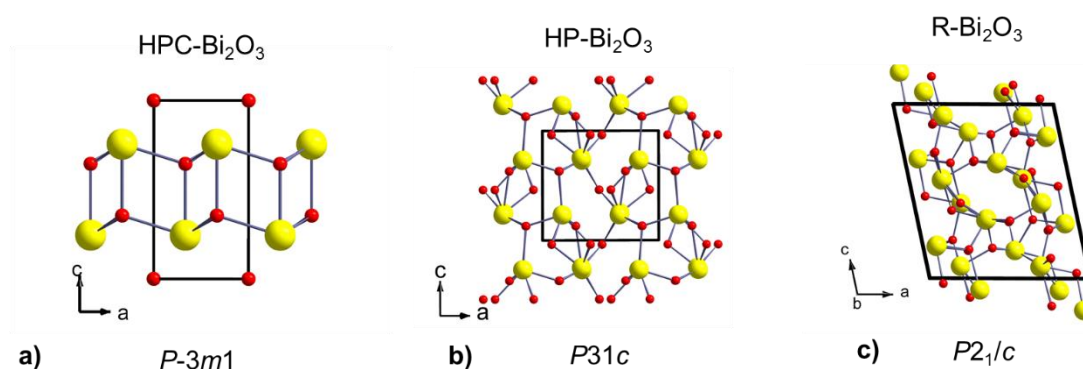


**Figure 14. Diversity of  $\text{Bi}_2\text{O}_3$  polymorphs at high-pressure conditions, where Bi atoms are given in yellow circles and O – in red.**

Amorphisation of bismite  $\alpha$ - $\text{Bi}_2\text{O}_3$  phase occurred at 20 GPa. It was proposed after high-pressure Raman investigation. [53] High-pressure behavior of the  $\alpha$  phase has been deeply investigated up to 45 GPa in work of Pereira et al in 2013. [54]

Rare-Earth (RE) metals have been the object of systematic high-pressure investigation. [71] The investigation of ceramics  $(\text{Eu}_{1-x}\text{La}_x)_2\text{O}_3$  solid solution at high-pressure conditions was recently provided by Irshad et al. [72] They reported the compressibility behavior of RES ceramics with dissimilar structure and significant difference in cationic radii. The anomalous lattice compression of the hexagonal  $\text{La}_2\text{O}_3$  compound was reported in ref. [73]

Unprecedented phenomenon of  $[\text{HLa}_4/\text{OLa}_4]$  anion-centered tetrahedral transformation was predicted and reported by Broux et al. [47] Reversal anion coordination obtained in the High-Pressure Polymorph of LaHO is shown on Figure 15. At ambient-pressure  $\alpha$ -LaHO crystallized in  $P4/nmm$  group in fluorite structure with  $\text{LaO}_4\text{H}_4$  local coordination. At 3GPa structure

changed into  $\gamma$ -LaHO with Pnma space group and  $\text{LaO}_4\text{H}_5$  coordination. In structure of  $\delta$ -LaHO ( $\text{P6}\overline{2}\text{m}$ ) at 5 GPa reversal coordination geometry was observed.

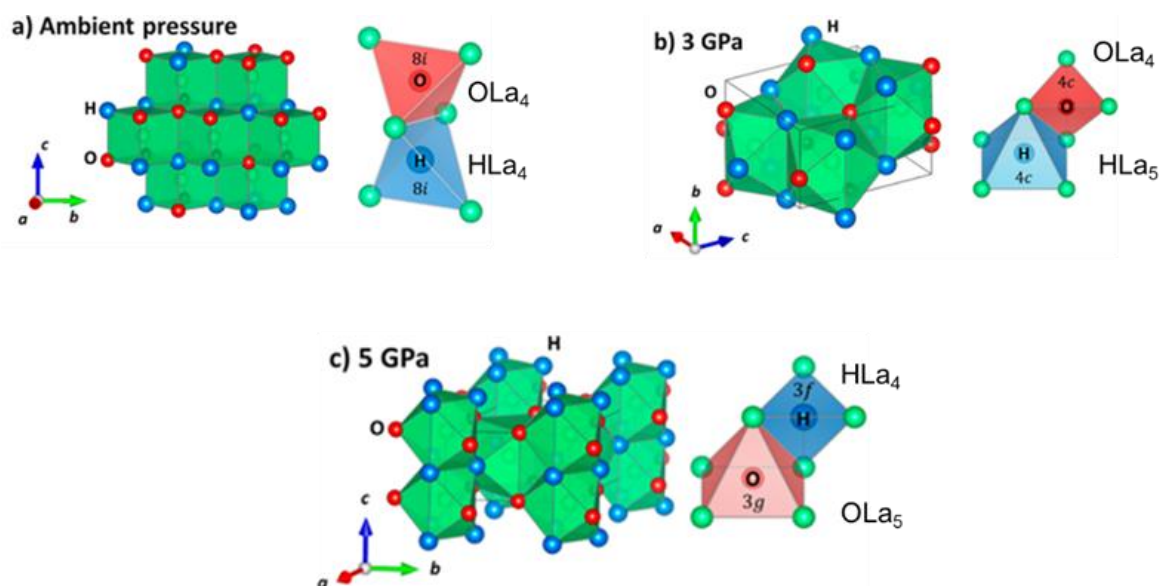


Figure 15. Crystal structures of  $\alpha$ -LaHO (a),  $\gamma$ -LaHO (b) and  $\delta$ -LaHO polymorph of LaHO. This figure was borrowed from original source from ref [47].

### c. Rare-earth borates

There is a keen interest to rare-earth borates under HP-HT conditions, because of remarkable luminescent properties [60] and photocatalytic activity. [61] It was noted they use to form a glass in general, whereas there is a tendency to crystallize under pressure. From the classical crystal chemistry point of view, this class of compounds is of the utmost interest. Triangular and tetrahedral coordination of borate groups capable to share the vertices are forming a variety of diverse structures. Two different structure types of  $\text{RE}_4\text{B}_4\text{O}_{11}\text{F}_2$  were obtained by high-pressure high-temperature syntheses.  $\text{La}_4\text{B}_4\text{O}_{11}\text{F}_2$  [62] is the only crystallizes in the monoclinic space group P21/c, whereas other RE = Pr, Nd, Eu, Gd, Dy, Sm, Tb, Ho, Er in C2/c. [63, 64] Experiments with other elements (RE = Tm, Yb, Lu) were not yielded results.

Both of structure types were obtained using Walker-type multianvil apparatus from the corresponding rare earth oxides and fluorides with boron oxide. Crystal structures of  $\text{RE}_4\text{B}_4\text{O}_{11}\text{F}_2$  family of compounds are based on boron polyhedrons shared corners in different order. First structure type of  $\text{La}_4\text{B}_4\text{O}_{11}\text{F}_2$  shows a wave-like modulation of  $\text{BO}_3$ -groups and  $\text{BO}_4$ -tetrahedra. According to the Burns et al. [66] approach of fundamental building blocks

(FBB) descriptions  $\text{BO}_3$ -groups have a ( $\Delta$ ) symbol and  $\text{BO}_4$ -tetrahedra ( $\square$ ). In this structure a part of  $\text{BO}_3$  groups is isolated and within share common vertices. They were assigned the designation of  $\Delta\Delta$ . The rest of  $\text{BO}_3$  groups are connected via the  $\text{BO}_4$ -tetrahedron forming fundamental building blocks  $2\Delta\square:\Delta\square\Delta$ . The  $[\text{FLa}_3]$  and  $[\text{FLa}_4]$  anion-centered units can be found in the structure.

The crystal structure of  $\text{Gd}_4\text{B}_4\text{O}_{11}\text{F}_2$  is the first described among the variety compounds in second type of  $\text{RE}_4\text{B}_4\text{O}_{11}\text{F}_2$ . The fundamental building blocks consist of two  $\text{BO}_3$ -groups ( $\Delta$ ) and two  $\text{BO}_4$ -tetrahedra ( $\square$ ) have been labelled as  $2\Delta 2\square:\Delta\square\square\Delta$ . Another example of rare-earth borate contains anion-centered units is ytterbium fluoride borate  $\text{Yb}_5(\text{BO}_3)_2\text{F}_9$ . [67] It was also synthesized under high-pressure high-temperature conditions in a Walker-type multianvil apparatus at 7.5 GPa and 1100°C. The structure of  $\text{Yb}_5(\text{BO}_3)_2\text{F}_9$  consists of  $\text{BO}_3$ -groups, ytterbium cations, and fluoride anions. Three different ytterbium cations can be identified in the crystal structure. Each one of the five fluoride ions in  $\text{Yb}_5(\text{BO}_3)_2\text{F}_9$  is coordinated by three ytterbium ions. Such complex can be described as the formal composition of “ $\text{YbF}_3$ ”.  $\text{BO}_3$  groups are isolated and alternate with ytterbium cations construct the layer with formal composition of  $(\text{Yb}_2)\text{BO}_3$ . Conversely,  $\text{Yb}_5(\text{BO}_3)_2\text{F}_9$  can be compared to structures of other rare-earth fluoride borates  $\text{RE}_3(\text{BO}_3)_2\text{F}_3$  ( $\text{RE} = \text{Sm}, \text{Eu}, \text{Gd}$ ) and  $\text{Gd}_2(\text{BO}_3)\text{F}_3$ . Both of them have similar alternating layers with formal composition of “ $\text{REBO}_3$ ” and “ $\text{REF}_3$ ”.

This is not a complete list of compounds obtained or modified by the HP-HT method of synthesis. Only the most representative in their group were presented above with the aim of showing the conditions used and employ them as starter. It is also important to see the possibilities offered by the application of high pressure. The field of investigation is broad and opens a wide range of investigations started in this thesis. Next chapter is dedicated to investigation of pressure induced new crystal structures in the Bi-based oxo-centered systems, where the  $\text{Bi}_2\text{O}_3$  used as a precursor.

## I.4. References

1. Krivovichev, S. V.; Shuvalov, R. R.; Semenova, T. F.; Filatov, S. K. (1999). *Crystal structure of georgbikiite*. Z. Kristallogr. 214, 135;
2. Krivovichev, S. V.; Semenova, T. F.; Filatov, S. K. (1998) Crystallogr. Rep., 43, 1061;
3. Effenberger, H. (1985). *Cu<sub>2</sub>O(SO<sub>4</sub>), dolerophanite: Refinement of the crystal structure, with a comparison of [OCu(II)<sub>4</sub>] tetrahedra in inorganic compounds*. Monatshefte Fur Chemie Chemical Monthly, 116(8-9), 927–931. doi:10.1007/bf00809186;
4. Bergerhoff, G., & Paeslack, J. (1968). *Sauerstoff als Koordinationszentrum in Kristallstrukturen*. Zeitschrift Für Kristallographie, 126(1-3), 112–123. doi:10.1524/zkri.1968.126.1-3.112;
5. Caro, P. E. (1968). *OM<sub>4</sub> Tetrahedra linkages and the cationic group (MO)<sub>n</sub><sup>n+</sup> in rare earth oxides and oxysalts*. Journal of the Less Common Metals, 16(4), 367–377. doi:10.1016/0022-5088(68)90134-3;
6. Carré, D., Guittard, M., Jaulmes, S., Mazurier, A., Palazzi, M., Pardo, M. P., Laurelle, P., and Flahaut J. (1984). *Oxysulfides formed by a rare earth and a second metal. II. Shear structures*. J. Solid State Chem. 55, 287–292;
7. Bengtsson, L. and Holmberg, B. (1990). *Cationic lead(II) hydroxide complexes in molten alkali-metal nitrate*. J. Chem. Soc., Faraday Trans. 86, 351–359;
8. Damodaran, K. V. and Rao, K. J. (1988). *A molecular dynamics investigation of the structure of PbO-PbF<sub>2</sub> glasses*. Chem. Phys. Lett. 148, 57–61;
9. Pauling, L. (1960). *The Nature of the Chemical Bond and the Structure of Molecules and Crystals: An Introduction to Mode* (3rd ed.). Cornell University Press; Jensen, William B. (1996). *Electronegativity from Avogadro to Pauling: Part I: Origins of the Electronegativity Concept*. J. Chem. Educ. 73, 1. 11;
10. Pearson, R. G. (n.d.). *Chemical hardness — A historical introduction. Structure and Bonding*, 1–10. doi:10.1007/bfb0036796;
11. Krivovichev, S. V. and Filatov, S. K. (2001). *Crystal chemistry of minerals and inorganic compounds with complexes of anion-centered tetrahedra*. St. Petersburg University Press, St. Petersburg;
12. Brese N. E., O'Keeffe, M. (1991). *Bond-valence parameters for solids*. Acta Cryst.. B47, 192-197;
13. Krivovichev, S.V. (2008) *Minerals with antiperovskite structure: a review*. Z. Kristallogr. 223 109–113;
14. Endara, D., Colmont, M., Huvé, M., Tricot, G., Carpentier, L., & Mentré, O. (2012). *Novel Tailormade Bi<sub>4</sub>MO<sub>4</sub>(PO<sub>4</sub>)<sub>2</sub> Structural Type (M = Mg, Zn)*. Inorganic Chemistry, 51(8), 4438–4447. doi:10.1021/ic201572y;
15. Huvé, M., Colmont, M., Lejay, J., Aschehoug, P., & Mentré, O. (2009). *Building Units and Intergrowths: Toward the Design of an Extended Family of Acentric Bi-Based Materials with Second Harmonic Generacy*. Chemistry of Materials, 21(17), 4019–4029. doi:10.1021/cm901466e;
16. Aliev, A., Endara, D., Huvé, M., Colmont, M., Roussel, P., Delevoye, L., ... Mentré, O. (2013). *Labile Degree of Disorder in Bismuth-Oxophosphate Compounds: Illustration through Three New Structural Types*. Inorganic Chemistry, 53(2), 861–871. doi:10.1021/ic402930d;
17. Boje, J., & Muller-Buschbaum, H. (1992). *Zur Kenntnis von Sr<sub>2</sub>Bi<sub>3</sub>V<sub>3</sub>O<sub>14</sub>*. Zeitschrift Fur Anorganische Und Allgemeine Chemie, 618(12), 39–42. doi:10.1002/zaac.19926180108;
18. Fujito, H., Kunioku, H., Kato, D., Suzuki, H., Higashi, M., Kageyama, H., & Abe, R. (2016). *Layered Perovskite Oxychloride Bi<sub>4</sub>NbO<sub>8</sub>Cl: A Stable Visible Light Responsive*

- Photocatalyst for Water Splitting*. Journal of the American Chemical Society, 138(7), 2082–2085. doi:10.1021/jacs.5b11191;
19. Hopfgarten, F. (1976). *The crystal structure of Bi<sub>12</sub>O<sub>15</sub>Cl<sub>6</sub>*. Acta Crystallographica Section B Structural Crystallography and Crystal Chemistry, 32(9), 2570–2573. doi:10.1107/s0567740876008285;
  20. Hopfgarten, F. (1975). *The crystal structure of Bi<sub>6</sub>O<sub>7</sub>FCl<sub>3</sub>*. Acta Crystallographica Section B Structural Crystallography and Crystal Chemistry, 31(4), 1087–1092. doi:10.1107/s0567740875004554;
  21. Aurivillius, B. (1990). *Crystal structures of (M(I)<sub>5</sub>Cl)(Bi<sub>48</sub>O<sub>59</sub>Cl<sub>30</sub>), M(I)=Cu, Ag*. Acta Chemica Scandinavica 44, 111. doi:10.3891/acta.chem.scand.44-0111;
  22. Lü, M., Aliev, A., Olchowka, J., Colmont, M., Huvé, M., Wickleder, C., & Mentré, O. (2013). *Multidimensional Open-Frameworks: Combinations of One-Dimensional Channels and Two-Dimensional Layers in Novel Bi/M Oxo-Chlorides*. Inorganic Chemistry, 53(1), 528–536. doi:10.1021/ic402578m;
  23. Colmont, M., Lemoine, K., Roussel, P., Kabbour, H., Olchowka, J., Henry, N., ... Mentré, O. (2019). *Identification and optical features of the Pb<sub>4</sub>Ln<sub>2</sub>O<sub>7</sub> series (Ln = La, Gd, Sm, Nd), genuine 2D-van der Waals oxides*. Chemical Communications. doi:10.1039/c8cc07707j;
  24. Colmont, M., Saitzek, S., Katelnikovas, A., Kabbour, H., Olchowka, J., & Roussel, P. (2016). *Host-sensitized luminescence properties of KLa<sub>5</sub>O<sub>5</sub>(VO<sub>4</sub>)<sub>2</sub>:Eu<sup>3+</sup> for solid-state lighting applications*. Journal of Materials Chemistry C, 4(30), 7277–7285. doi:10.1039/c6tc02258h;
  25. Gómez Torres, M. A., Gauthier, G. H., Kaczmarek, A. M., Huvé, M., Roussel, P., Dupray, V., ... Colmont, M. (2020). *Pure and RE<sup>3+</sup>-Doped La<sub>7</sub>O<sub>6</sub>(VO<sub>4</sub>)<sub>3</sub> (RE = Eu, Sm): Polymorphism Stability and Luminescence Properties of a New Oxyvanadate Matrix*. Inorganic Chemistry. doi:10.1021/acs.inorgchem.9b03689;
  26. Hull, S. (2014). *Techniques in High Pressure Neutron Scattering*, by Stefan Klotz. Contemporary Physics, 1–1. doi:10.1080/00107514.2014.983171;
  27. Tisato N. & Madonna C. (2012) *Attenuation at low seismic frequencies in partially saturated rocks. Measurements and description of a new apparatus*. Journal of Applied Geophysics, 86, 44-53;
  28. Bridgman, P. W. (1952). *Physics of high pressure*. Proc. Am. Acad. Arts Sci. 81, 165;
  29. Fang, J., Bull, C. L., Loveday, J. S., Nelmes, R. J., & Kamenev, K. V. (2012). *Strength analysis and optimization of double-toroidal anvils for high-pressure research*. Review of Scientific Instruments, 83(9), 093902;
  30. Wang, Y., Durham, W. B., Getting, I. C., & Weidner, D. J. (2003). *The deformation-DIA: A new apparatus for high temperature triaxial deformation to pressures up to 15 GPa*. Review of Scientific Instruments, 74(6), 3002–3011;
  31. Green, Harry; R.S. Borch (1990). *High pressure and Temperature deformation experiments in a liquid confining medium*. Geophysical Monograph Series. 56: 195–201;
  32. Chang, Z. P., & Graham, E. K. (1977). *Elastic properties of oxides in the NaCl-structure*. Journal of Physics and Chemistry of Solids, 38(12), 1355–1362. doi:10.1016/0022-3697(77)90007-5;
  33. Précigout, J., Stünitz, H., Pinquier, Y., Champallier, R., & Schubnel, A. (2018). *High-pressure, High-temperature Deformation Experiment Using the New Generation Griggs-type Apparatus*. Journal of Visualized Experiments, (134). doi:10.3791/56841;
  34. Dunn T. (1993) – The piston-cylinder apparatus. In: Luth R. W. (Ed.) *Experiments at High Pressure and Applications to the Earth's Mantle*, MAC Short Course Handbook, 21, Mineralogical Association of Canada, pp. 39-94;

35. S.N. Vaidya, V. Vijay Kumar, C. Karunakaran, BARC, Reports 102, 1 (1981);
36. Hall, H. T. (1960). *Ultra- High- Pressure, High- Temperature Apparatus: the "Belt"*. Review of Scientific Instruments, 31(2), 125–131;
37. Mao, H.-K., Chen, B., Chen, J., Li, K., Lin, J.-F., Yang, W., & Zheng, H. (2016). *Recent advances in high-pressure science and technology*. Matter and Radiation at Extremes, 1(1), 59–75;
38. Byrappa, K. Yoshimura. (2013) M. Handbook of Hydrothermal Technology (Second Edition);
39. Badding, J. V. (1998). *High-pressure synthesis, characterization, and tuning of solid state materials*. Annual Review of Materials Science, 28(1), 631–658. doi:10.1146/annurev.matsci.28.1.631;
40. Bundy, F. P. (1977). *Designing tapered anvil apparatus for achieving higher pressures*. Review of Scientific Instruments, 48(6), 591–596. doi:10.1063/1.1135115;
41. Zhong-Zhu, L., Jing-Qiu, L., & Xiao-Peng, J. (2009). *Effects of NaN<sub>3</sub> Added in Fe—C System on Inclusion and Impurity of Diamond Synthesized at High Pressure and High Temperature*. Chinese Physics Letters, 26(3), 038104. doi:10.1088/0256-307x/26/3/038104;
42. Kawai, N., & Endo, S. (1970). *The Generation of Ultrahigh Hydrostatic Pressures by a Split Sphere Apparatus*. Review of Scientific Instruments, 41(8), 1178–1181. doi:10.1063/1.1684753;
43. Holzapfel, W. B. (1996). *Physics of solids under strong compression*. Reports on Progress in Physics, 59(1), 29–90. doi:10.1088/0034-4885/59/1/002;
44. Labachev, A.N. (Ed.), (1971) *Hydrothermal Synthesis of Crystals*, Nauka, Moscow;
45. Aksenov, S. M., Mironov, V. S., Borovikova, E. Y., Yamnova, N. A., Gurbanova, O. A., Volkov, A. S., ... Deyneko, D. V. (2017). *Synthesis, crystal structure, vibrational spectroscopy and expected magnetic properties of a new bismuth nickel phosphate Ni(BiO)<sub>2</sub>(PO<sub>4</sub>)(OH) with a namibite-type structure*. Solid State Sciences, 63, 16–22;
46. Filatov, S., Bendeliani, N., Albert, B., Kopf, J., Dyuzeva, T., & Lityagina, L. (2005). *Highpressure synthesis of  $\alpha$ -PbO<sub>2</sub> and its crystal structure at 293, 203, and 113 K from single crystal diffraction data*. Solid State Sciences, 7(11), 1363–1368;
47. Broux, T., Ubukata, H., Pickard, C. J., Takeiri, F., Kobayashi, G., Kawaguchi, S., ... Kageyama, H. (2019). *High-Pressure Polymorphs of LaHO with Anion Coordination Reversal*. Journal of the American Chemical Society, 141(22);
48. Miletich, R., Allan, D. R., & Angel, R. J. (1998). *Structural control of polyhedral compression in synthetic braunite, Mn<sup>2+</sup>Mn<sup>3+</sup><sub>6</sub>O<sub>8</sub>SiO<sub>4</sub>*. Physics and Chemistry of Minerals, 25(3), 183–192;
49. Winter, J.K. and Ghose, S. (1979). *Thermal expansion and high temperature crystal chemistry of the Al<sub>2</sub>SiO<sub>5</sub> polymorphs*. Am. Mineral 64, 573-586;
50. Adams, D. M., Christy, A. G., Haines, J., & Clark, S. M. (1992). *Second-order phase transition in PbO and SnO at high pressure: Implications for the litharge-massicot phase transformation*. Physical Review B, 46(18), 11358–11367;
51. Atou, T., Faqir, H., Kikuchi, M., Chiba, H., & Syono, Y. (1998). *A New High-Pressure Phase of Bismuth Oxide*. Materials Research Bulletin, 33(2), 289–292;
52. Ghedia, S., Locherer, T., Dinnebier, R., Prasad, D. L. V. K., Wedig, U., Jansen, M., & Senyshyn, A. (2010). *High-pressure and high-temperature multianvil synthesis of metastable polymorphs of Bi<sub>2</sub>O<sub>3</sub>: Crystal structure and electronic properties*. Physical Review B, 82(2). doi:10.1103/physrevb.82.024106 6/s0025-5408(97)00216-x;
53. Chouinard, C., Desgreniers, S. (1999). *Bi<sub>2</sub>O<sub>3</sub> under hydrostatic pressure: observation of a pressure-induced amorphization*. Solid State Communications, 113(3), 125–129;

54. Pereira, A. L. J., Errandonea, D., Beltrán, A., Gracia, L., Gomis, O., Sans, J. A., ... Popescu, C. (2013). *Structural study of  $\alpha$ -Bi<sub>2</sub>O<sub>3</sub> under pressure*. *Journal of Physics: Condensed Matter*, 25(47), 475402;
55. Pereira, A. L. J., Santamaría-Pérez, D., Ruiz-Fuertes, J., Manjón, F. J., Cuenca-Gotor, V. P., Vilaplana, R., ... Sans, J. A. (2018). *Experimental and Theoretical Study of Bi<sub>2</sub>O<sub>2</sub>Se Under Compression*. *The Journal of Physical Chemistry C*, 122(16), 8853–8867. doi:10.1021/acs.jpcc.8b02194;
56. Wu, J.; Yuan, H.; Meng, M.; Chen, C.; Sun, Y.; Chen, Z.; Dang, W.; Tan, C.; Liu, Y.; Yin, J.; et al. (2017). *High Electron Mobility and Quantum Oscillations in Non-Encapsulated Ultrathin Semiconducting Bi<sub>2</sub>O<sub>2</sub>Se*. *Nat. Nanotech*, 12, 530-534;
57. Demchyna, R., Leoni, S., Rosner, H., & Schwarz, U. (2006). *High-pressure crystal chemistry of binary intermetallic compounds*. *Zeitschrift Für Kristallographie - Crystalline Materials*, 221(5-7);
58. Brock, S. L., & Kauzlarich, S. M. (1995). *Pnictide Oxides: A Unique Class of Compounds*. *Comments on Inorganic Chemistry*, 17(4), 213–238.
59. Heymann, G., Riecken, J. F., Johrendt, D., Rayaprol, S., Pöttgen, R., & Huppertz, H. (2013). *Ce<sub>4</sub>Ag<sub>3</sub>Ge<sub>4</sub>O<sub>0.5</sub> – chains of oxygen-centered [OCe<sub>2</sub>Ce<sub>2</sub>] tetrahedra embedded in a [CeAg<sub>3</sub>Ge<sub>4</sub>] intermetallic matrix*. *Dalton Transactions*, 42(42);
60. Vitzthum, D., Wurst, K., Pann, J. M., Brüggeller, P., Seibald, M., & Huppertz, H. (2018). *Exploration into the Syntheses of Gallium- and Indiumborates under Extreme Conditions: M<sub>5</sub>B<sub>12</sub>O<sub>25</sub>(OH): Structure, Luminescence, and Surprising Photocatalytic Properties*. *Angewandte Chemie International Edition*, 57(35), 11451–11455;
61. Vitzthum, D., Schauerl, M., Strabler, C. M., Brüggeller, P., Liedl, K. R., Griesser, U. J., & Huppertz, H. (2015). *New High-Pressure Gallium Borate Ga<sub>2</sub>B<sub>3</sub>O<sub>7</sub>(OH) with Photocatalytic Activity*. *Inorganic Chemistry*, 55(2), 676–681;
62. Haberer, A., Kaindl, R., Oeckler, O., & Huppertz, H. (2010). *A new structure type of RE<sub>4</sub>B<sub>4</sub>O<sub>11</sub>F<sub>2</sub>: High-pressure synthesis and crystal structure of La<sub>4</sub>B<sub>4</sub>O<sub>11</sub>F<sub>2</sub>*. *Journal of Solid State Chemistry*, 183(9), 1970–1979;
63. Haberer, A., Kaindl, R., & Huppertz, H. (2010). *Gd<sub>4</sub>B<sub>4</sub>O<sub>11</sub>F<sub>2</sub>: Synthesis and crystal structure of a rare-earth fluoride borate exhibiting a new “fundamental building block” in borate chemistry*. *Journal of Solid State Chemistry*, 183(2), 471–478;
64. Glätzle, M., & Huppertz, H. (2016). *RE<sub>4</sub>B<sub>4</sub>O<sub>11</sub>F<sub>2</sub> (RE = Sm, Tb, Ho, Er): four new rare earth fluoride borates isotypic to Gd<sub>4</sub>B<sub>4</sub>O<sub>11</sub>F<sub>2</sub>*. *Zeitschrift Für Naturforschung B*, 71(11), 1105–1113. doi:10.1515/znb-2016-0123;
65. Haberer, A., Kaindl, R., & Huppertz, H. (2010). *The first praseodymium fluoride borate Pr<sub>4</sub>B<sub>3</sub>O<sub>10</sub>F – High-pressure synthesis and characterization*. *Solid State Sciences*, 12(4), 515–521. doi:10.1016/j.solidstatesciences.2009.12.017;
66. Burns, P.C. Grice, J.D. Hawthorne, F.C. (1995). *Can. Miner.* 33 1131;
67. Haberer, A., & Huppertz, H. (2009). *High-pressure synthesis, crystal structure, and structural relationship of the first ytterbium fluoride borate Yb<sub>5</sub>(BO<sub>3</sub>)<sub>2</sub>F<sub>9</sub>*. *Journal of Solid State Chemistry*, 182(4), 888–895;
68. Ortner, T. S., Vitzthum, D., Heymann, G., & Huppertz, H. (2017). *High-Pressure Synthesis and Single-Crystal Structure Elucidation of the Indium Oxide-Borate In<sub>4</sub>O<sub>2</sub>B<sub>2</sub>O<sub>7</sub>*. *Zeitschrift Für Anorganische Und Allgemeine Chemie*, 643(24), 2103–2109;
69. Siidra, O. I., Kabbour, H., Mentre, O., Nazarchuk, E. V., Kegler, P., Zinyakhina, D. O., ... Depmeier, W. (2016). *Lead Oxychloride Borates Obtained under Extreme Conditions*. *Inorganic Chemistry*, 55(17), 9077–9084;
70. Cornei, N., Tancret, N., Abraham, F., & Mentré, O. (2006). *New  $\epsilon$ -Bi<sub>2</sub>O<sub>3</sub> Metastable Polymorph*. *Inorganic Chemistry*, 45(13), 4886–4888. doi:10.1021/ic0605221;

71. McWhan, D. B., & Stevens, A. L. (1965). *Effect of Pressure on the Magnetic Properties and Crystal Structure of Gd, Tb, Dy, and Ho*. *Physical Review*, 139(3A), A682–A689. doi:10.1103/physrev.139.a682;
72. Irshad, K. A., Srihari, V., Kalavathi, S., & Shekar, N. V. C. (2020). *Structural phase transition, equation of state and phase diagram of functional rare earth sesquioxide ceramics (Eu<sub>1-x</sub>La<sub>x</sub>)<sub>2</sub>O<sub>3</sub>*. *Scientific Reports*, 10(1). doi:10.1038/s41598-020-68400-9;
73. Irshad, K. A., Anees, P., Rajitha, R., Ravindran, T. R., Srihari, V., Kalavathi, S., & Shekar, N. V. C. (2020). *Anomalous lattice compression in the hexagonal La<sub>2</sub>O<sub>3</sub>— A high pressure X-ray diffraction, Raman spectroscopy and first principle study*. *Journal of Alloys and Compounds*, 153657. doi:10.1016/j.jallcom.2020.153657;
74. Abraham, F.; Thomas, D. (1975). *Structure cristalline de Bi<sub>3</sub>Ru<sub>3</sub>O<sub>11</sub>*. *Bull. Soc. Franc. Mineral. Cristallogr.* 98, 25.



---

II. *Pressure induced new crystal structures in the  
Bi-based oxo-centered systems*

---

Our lab is internationally recognized for its study of Bi-based materials. Historically, since the discovery of  $\text{Bi}_4\text{V}_2\text{O}_{11}$ , [1] ionic conductors were deeply investigated and as a matter of fact the BiMeVO<sub>x</sub> series of materials. [2] Step by step and with the ulterior motive of designing new materials using an exploratory approach, the chemical systems were widened as well as the targeted properties: energy, optic or catalysis... To date, the obtention of innovative phases was ensured by the use of a rationalization approach assorted with a strong expertise in crystallography.

Concerning the rationalization approach, it was accurately used to develop series of materials of the bismuth transition metal phosphate family. New materials with various building units size and shapes starting from isolated units ( $\text{Bi}_3\text{O}_2$ ) $\text{Ru}_3\text{O}_9$  [74], going through 1D and 2D layers [3] were designed and synthesized, making possible the tuning of the properties.

Concerning the crystallographic tools, big developments were reached through the use of:

- transmission electron microscopy, first working from images (observation of defects, formulation of new phase, synthesis and characterization) [4] and secondly from electron diffraction patterns in order to solve crystal structures at the nanoscale;
- X-Ray and neutron diffraction [6] in case of complex crystal structures (twins, modulation...);
- or NMR in particular systems. [7]

Until this thesis, all the strategy developed never used other thermodynamical parameters than temperature. As a consequence, the diversification of synthesis routes opened a wide field of investigation. Three examples are given in this chapter: the first two are dedicated to the HPHT modification of materials with interesting magnetic properties, the full solid solution of  $\text{BiCu}_2\text{P}_{1-x}\text{V}_x\text{O}_6$  and  $\text{BiNiPO}_5$ . The last one is based on the use of hydrothermal pressure on relatively simplest systems.

## II.1. High-Pressure modification of BiCu<sub>2</sub>XO<sub>6</sub> (X = P, V) solid solution

### II.1.1. State of the Art

#### a. On the interest in using BiM<sub>2</sub>XO<sub>6</sub> compounds

Among the number of Bi<sup>3+</sup>/M<sup>2+</sup> vanadophosphate isolated so far, most of them show ordered frameworks where the variety of Bi<sup>3+</sup>/M<sup>2+</sup> arrangements drives the following optical/electric/magnetic properties. For example, the BiM<sub>2</sub>XO<sub>6</sub> family (M= Cu, Mg, Pb, Zn, Mn, Cd... / X= V, As, P) was deeply investigating, since the initial discovery and investigation of BiMg<sub>2</sub>VO<sub>6</sub>. [52] A lot of isotopic compounds were further characterized providing interesting examples in various field of research (see Table 2). The nature of both M and X cations has impacts on the crystal structure in terms of crystal system and/or space group. It also impacts the versatility of the physical properties. For example, BiCa<sub>2</sub>VO<sub>6</sub> has a ferroelectric behavior, [54] BiCd<sub>2</sub>VO<sub>6</sub> and BiCd<sub>2</sub>AsO<sub>6</sub> crystalized in NCS space groups and provide second harmonic generation, [53] optical properties of BiM<sub>2</sub>XO<sub>6</sub> (M= Cd, Mg, Zn and X= P, As and V) show interesting Room Temperature Bi<sup>3+</sup> luminescence although the concentration of Bi<sup>3+</sup> in the structure is quite high. [34] To finish, let's mention BiCu<sub>2</sub>PO<sub>6</sub> and BiCu<sub>2</sub>VO<sub>6</sub>. These two compounds show interesting exotic magnetism, deeply investigated, that will be discussed further.

**Table 2. Crystalline characteristics of BiM<sub>2</sub>XO<sub>6</sub> phases**

Compound	Space Group	a (Å)	b (Å)	c (Å)	β (°)	Z	Ref	Studied properties
BiZn <sub>2</sub> PO <sub>6</sub>	<i>P nma</i>	11.8941(3)	5.2754(2)	7.8161(2)		4	[45, 59]	Magnetic, thermal
BiMg <sub>2</sub> PO <sub>6</sub>	<i>B bmm</i>	11.888(3)	5.273(2)	7.801(2)		4	[50, 49]	Luminescence
BiMg <sub>2</sub> VO <sub>6</sub>	<i>P nma</i>	12.2475(3)	5.4431(2)	7.9160(2)		4	[52]	Luminescence
BiMg <sub>2</sub> AsO <sub>6</sub>	<i>B bmm</i>	12.1637(8)	5.3898(4)	7.9142(5)		4	[50]	IR, Raman, luminescence
BiCd <sub>2</sub> PO <sub>6</sub>	<i>B b2<sub>1</sub>m</i>	11.952(10)	5.374(10)	8.505(10)		4	[34]	Luminescence
BiCd <sub>2</sub> VO <sub>6</sub>	<i>B b2<sub>1</sub>m</i>	11.4611	5.6455	8.6451		4	[48]	Optical
BiCd <sub>2</sub> AsO <sub>6</sub>	<i>B b2<sub>1</sub>m</i>	11.949(2)	5.4407(7)	8.618(1)		4	[53]	Optical
BiCa <sub>2</sub> VO <sub>6</sub>	<i>B b2<sub>1</sub>m</i>	11.9608(1)	5.5459(5)	8.8932(7)		4	[54]	Magnetic
BiCa <sub>2</sub> AsO <sub>6</sub>	<i>B b2<sub>1</sub>m</i>	11.9723(11)	5.5453(5)	8.8848(8)		4	[50]	
BiCu <sub>2</sub> PO <sub>6</sub>	<i>P nma</i>	11.776(1)	5.1730(6)	7.7903(6)		4	[3]	Magnetic

<b>BiCu<sub>2</sub>VO<sub>6</sub></b>	<i>P 2<sub>1</sub>/n</i>	13.471(1)	7.812(1)	15.760(1)	113.10(1)	12	[51]	
<b>BiCu<sub>2</sub>AsO<sub>6</sub></b>	<i>P nma</i>	12.253(1)	5.280(1)	7.577(1)		4	[41]	Photocatalytic
<b>BiPb<sub>2</sub>PO<sub>6</sub></b>	<i>P bnm</i>	11.473(6)	5.930(4)	9.079(10)		4	[55]	Elastic anisotropy, thermodynamics
<b>BiPb<sub>2</sub>VO<sub>6</sub></b>	<i>P 2<sub>1</sub>/m</i>	15.0501(5)	5.9011(3)	7.5355(5)	101.5657	4	[56,60]	Thermal
<b>BiPb<sub>2</sub>AsO<sub>6</sub></b>	<i>P 2<sub>1</sub>/c</i>	8.2662(4)	5.6274(3)	14.3152(7)	106.663(2)	4	[58]	Luminescence
<b>BiMn<sub>2</sub>PO<sub>6</sub></b>	<i>P nma</i>	12.031(1)	5.3652(5)	8.1225(7)		4	[59]	Magnetic, thermal
<b>BiMn<sub>2</sub>VO<sub>6</sub></b>	<i>P nma</i>	12.002(1)	5.4421(5)	8.2378(7)		4	[57, 58]	Luminescence
<b>BiMn<sub>2</sub>AsO<sub>6</sub></b>	<i>P nma</i>	12.009(1)	5.3734(4)	8.2092(7)		4	[57, 58]	Luminescence

As already discussed, BiM<sub>2</sub>XO<sub>6</sub> phases are described using the antiphase approach. They are all built on association of oxo-centered O(Bi<sub>2</sub>M<sub>2</sub>) tetrahedra that share edges, leading to infinite  $[\text{BiM}_2\text{O}_2]^{+3}$  1D ribbons (see on Figure 16(a)) surrounded by isolated  $[\text{XO}_4]^{3-}$  tetrahedra. All ribbons are running along *b*-axis ( $b \approx 5.5 \text{ \AA}$  corresponding to the height of two tetrahedra sharing edges) but their respective orientation is related to the crystal structure and nature of M<sup>2+</sup> and X<sup>5+</sup>. For example, Figure 16 presented orientations of the  $[\text{XO}_4]$  groups in different polymorphs: BiCa<sub>2</sub>VO<sub>6</sub> Figure 16(b), BiMg<sub>2</sub>PO<sub>6</sub> Figure 16(c), BiPb<sub>2</sub>VO<sub>6</sub> Figure 16(d) and BiZn<sub>2</sub>PO<sub>6</sub> Figure 16(e). All of them are shown in the (a,c) plane, that help to highlight rotation/tilting/twisting of  $[\text{XO}_4]$  groups compared with the ribbons. The nature of the cations has also a tendency to distort the ribbons which was largely used in the investigation of the optical properties of BiM<sub>2</sub>XO<sub>6</sub> (X= Zn, Mg, Cd and X= P, V and As). [34]

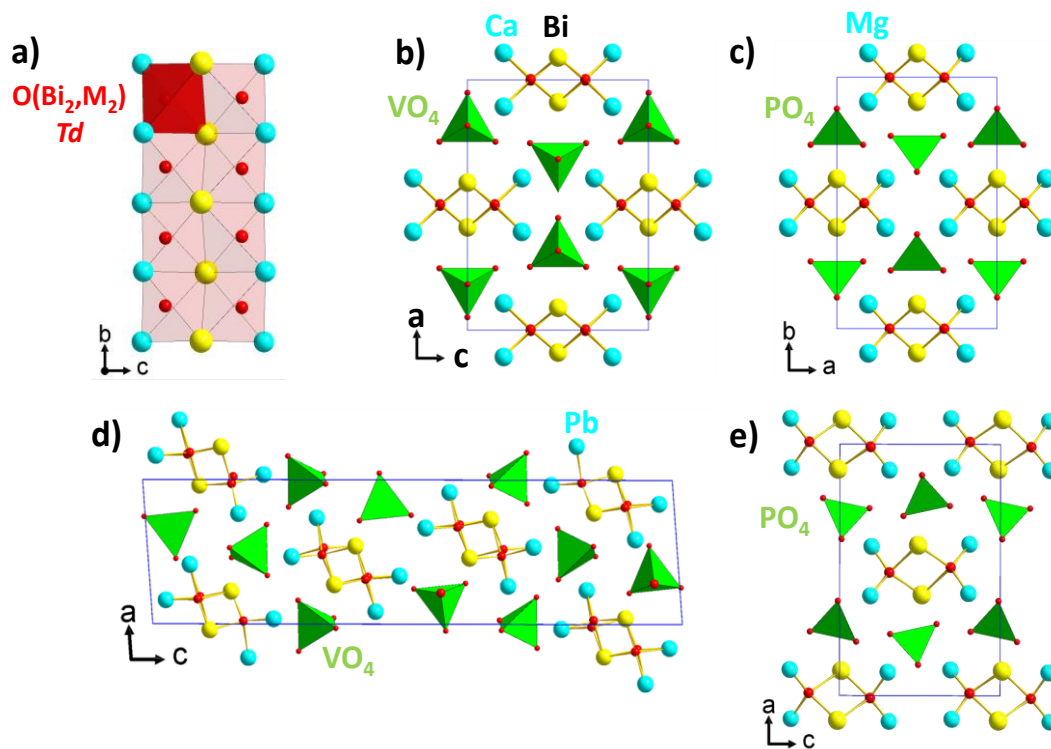


Figure 16. (a) The infinite  $[\text{BiM}_2\text{O}_2]^{+3}$  1D ribbon representation. The orientation of ribbons in crystal structures of (b)  $\text{BiCa}_2\text{VO}_6$ , (c)  $\text{BiMg}_2\text{PO}_6$ , (d)  $\text{BiPb}_2\text{VO}_6$  and (e)  $\text{BiZn}_2\text{PO}_6$ , where  $[\text{XO}_4]^{3-}$  tetrahedrons are shown in green.

The possibility to isolate one particular polymorph is strongly related:

- 1) To the nature of the cation introduced in the matrix applying thus a chemical pressure;
- 2) To the temperature used during the synthesis as it is shown for the transition  $\alpha \rightarrow \beta \rightarrow \gamma$  in  $\text{BiPb}_2\text{VO}_6$ ; [60]
- 3) to the use of physical pressure as done for  $\text{BiCu}_2\text{PO}_6$ . [36]

$\text{BiCu}_2\text{PO}_6$ , as well as its homologous vanadate, is a rare example of  $\text{BiM}_2\text{XO}_6$  phases including a transition metal able to induce magnetic properties. In the case of these phases, they are particularly interesting and that is why  $\text{BiCu}_2\text{PO}_6$  was recently modified under pressure, to be able to induce changes in the related magnetic properties.

## II.1.2. The case of BiCu<sub>2</sub>PO<sub>6</sub>, an interesting spin ladder system

BiCu<sub>2</sub>PO<sub>6</sub> crystallized in an orthorhombic unit cell with parameters  $a=11.776(1)$  Å,  $b=5.1730(6)$  Å and  $c=7.7903(6)$  Å (S.G. *Pnma*). The crystal structure is similar to BiZn<sub>2</sub>PO<sub>6</sub> Figure 16(e). Especially, the association of [BiCu<sub>2</sub>O<sub>2</sub>]<sup>3+</sup> ribbons is at the origin of particular S=½ ladder system at the origin of frustration of spin ladders along their legs. The ladders are formed by Cu<sup>2+</sup> localized at edges of ribbons (Figure 17(a)). The frustration between Cu<sup>2+</sup> spins along the rungs drives BiCu<sub>2</sub>PO<sub>6</sub> into a gapped quantum singlet ground state with excited magnetic states. The ladders are defined by  $J_1$  (legs) and  $J_4$  (rungs), the NNN (next nearest neighbor) frustration correspond to  $J_2$  and  $J_2'$ . The couplings between the ladders ( $J_3$ ) is not negligible but of small importance, as observed reading the relative values on Figure 17(c).

Recently, the magnetic ladders were interestingly modified under pressure. High-pressure/high-temperature (HP/HT) treatment of BiCu<sub>2</sub>PO<sub>6</sub> compound was applied, probing the possibility of reorganization of the ribbons in a denser polymorph. The modified BiCu<sub>2</sub>PO<sub>6</sub> was investigated through a collaboration with the NEEL Institute and the University of Augsburg [36] before I joined the MISSP research group. The initial AP phase (AP-BCPO) [35] was used as a precursor. The experiment was provided in mentioned BELT X type of press at 5 GPa/800°C. After the pressure release, the new HP-BCPO is stable and its crystal structure was refined using a Rietveld refinement method. HP-BiCPO was indexed in an orthorhombic unit cell, with respect to *Pnma* symmetry inclined to BiCu<sub>2</sub>AsO<sub>6</sub> (BCAO) composition. [41] HP-BCPO is obtained as a pure phase. Comparing the two BCPO forms (AP and HP) presented on Figure 17 it is obvious that:

- the ratio between the cell volumes of AP-BCPO and HP-BCPO is 1.02, i.e.,  $474.56 \text{ \AA}^3 / 465.67 \text{ \AA}^3$ , which confirms the HP transformation into a denser crystal arrangement;
- the <sup>∞</sup>[BiCu<sub>2</sub>O<sub>2</sub>]<sup>3+</sup> ribbons are unchanged which suggest the conservation of basic features of the magnetic lattice;
- the orientation of <sup>∞</sup>[BiCu<sub>2</sub>O<sub>2</sub>]<sup>3+</sup> units is deeply different. In the AP form, the <sup>∞</sup>[BiCu<sub>2</sub>O<sub>2</sub>]<sup>3+</sup> magnetic ladders grow parallel, whereas in HP-BCPO, they are rotated by ca. 100° and arranged in a cross path pattern. The general projections of crystal structures and the magnetic ladders of both AP and HP polymorphs are presented on Figure 17 (c) and (d);
- concerning the coupling of the magnetic ladders,  $J_3$  is again weak due to the almost orthogonal orbital overlapping related to the Cu-O-Cu angle equal to 92.1°. Again,  $J_4$  (SSE coupling) is

important because the  $\angle\text{Cu-O}\cdots\text{O-Cu}$  dihedral angle is relatively small (around  $10.1^\circ$ ) and the oxygen-oxygen distances of  $2.749\text{\AA}$  fit with the van der Waals distance.

To conclude, the two ladder topologies of AP- and HP-BCPO exhibit similar features through conservation of the main polycationic units.

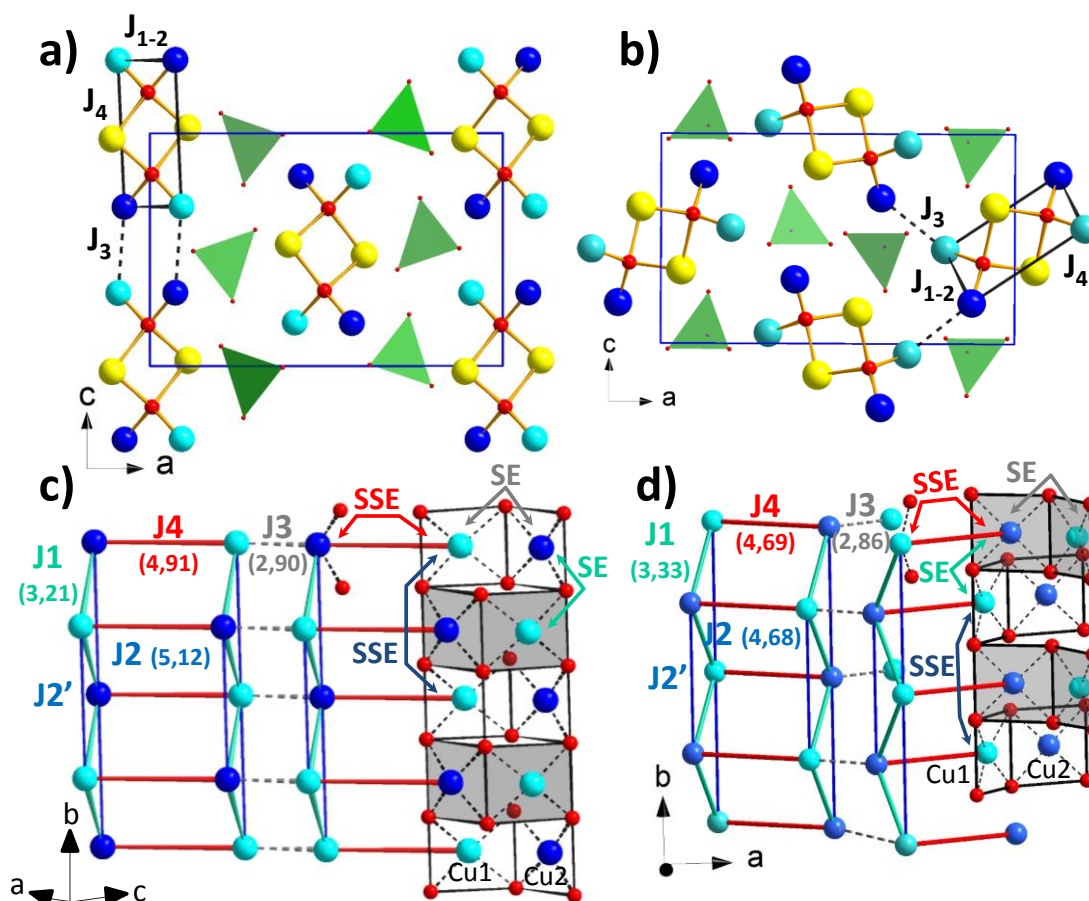
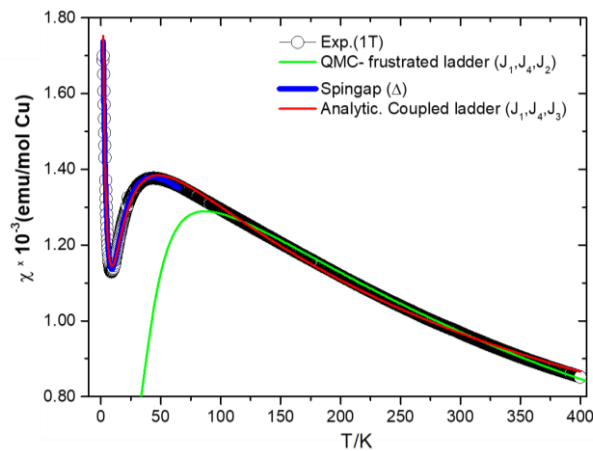


Figure 17. Projection along the  $b$  axis of the BCPO crystal structure with evidence of polycationic ribbons surrounded by  $[\text{PO}_4]$  groups and views of the magnetic ladders with main distances and  $J$  labels for (a and c) AP-BCPO and (b and d) HP-BCPO [36].

A Magnetic susceptibility  $\chi(T)$  measurement performed on HP-BCPO resulted in a significant field-dependent upturn below 10 K typical of defect paramagnetism. The absence of a magnetic ordering transition and the sharp decrease of the magnetic susceptibility below  $T_{\max} = 43$  K indicate a spin gap, similar to that of initial AP-BCPO compound.

Several calculations/fits were performed to fully understand the magnetic behavior. It is fully detailed in ref. [36] The main result is that the coupling is calculated to be stronger in HP-BCPO although the Cu-Cu distances are longer which reinforce the role of SE and SSE mechanisms. To summarize, due to geometrical reasons:

- $J_1$ , the leg coupling is enhanced;
- $J_4$  is reduced;
- $J_2$  and  $J_2'$  are smaller, modified by the O-O distance in the two possible paths: Cu–O–(P)–O–Cu and Cu–O–(Bi)–O–Cu;
- finally,  $J_3$  is necessary to properly fit the size of the spin gap, especially at low temperature (see Figure 18.).



**Figure 18.** Experimental magnetic susceptibility under 1 T. Several fit were performed and proved the importance of  $J_3$ , especially at low temperature. [36]

Also to finish, it is interesting to remind that the HP-BCPO form switch to the AP-BCPO one after heating at 690°C under air. [36] A 2D image of XRD patterns evolution with temperature is shown on Figure 19 (a). Selected 13 to 15  $2\theta$  range is given in 1D view mode on Figure 19 (b) to show the HP-BCPO transformation into the AP form. The XRD patterns of HP-BCPO sample at room temperature (RT), heated at 800°C and cooled down are shown.

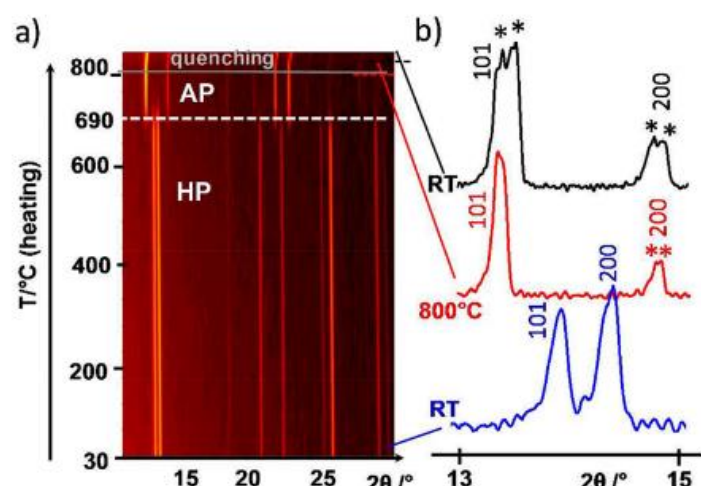


**Figure 19.** 2D view on XRD patterns evolution with temperature (a). The XRD patterns of HP-BCPO sample at room temperature (RT) (in blue), heated at 800°C (in red) and cooled down (in black) are compared (b).

This system is powerful in the production of novel frustrated ladder systems. The obtained magnetic couplings are of high interest for exotic magnetic fundamental states. In that sense, the story was continued through the HP/HT investigation of the whole  $\text{BiCu}_2\text{P}_{1-x}\text{V}_x\text{O}_6$  solid solution.

### II.1.3. On the solid solution $\text{BiCu}_2\text{P}_{1-x}\text{V}_x\text{O}_6$

#### a. Crystal structures

The  $x = 0$  term is discussed above.

The term  $x = 1$  crystallized in a triple monoclinic supercell by comparison with the already discussed  $\text{BiCu}_2\text{PO}_6$ . The unit cell parameters are  $a = 13.471(1) \text{ \AA}$ ,  $b = 7.812(1) \text{ \AA}$ ,  $c = 15.760(1) \text{ \AA}$  and  $\beta = 113.10(1)^\circ$ . The crystal structure shows the same kind of double ribbons surrounded by isolated vanadates but this time, the initial motif is splitting into two others.

Concerning the rest of the solid solution, there are several parts that are shown on Figure 20:

-for  $0 < x < 0.7$ , a solid solution exists and the crystal structures were refined in the same unit cell than the pure phosphate;

-for  $0.7 < x \leq 0.96$ , the presence of additional set of satellite spots on diffraction patterns is observed, yielding to incommensurate modulated structures. The refinement using the 4D formalism highlight deep positional modulation effects inside the polycationic  $[\text{BiCu}_2\text{O}_2]^{3+}$

ribbons (especially in terms of Cu-Cu distances) with three different  $[XO_4]$  configurations along the fourth dimension (see Figure 20);

-for  $0.96 < x < 1$ , there is a competition between two phases, one of the previous domain and a second one corresponding to the term  $x = 1$ .

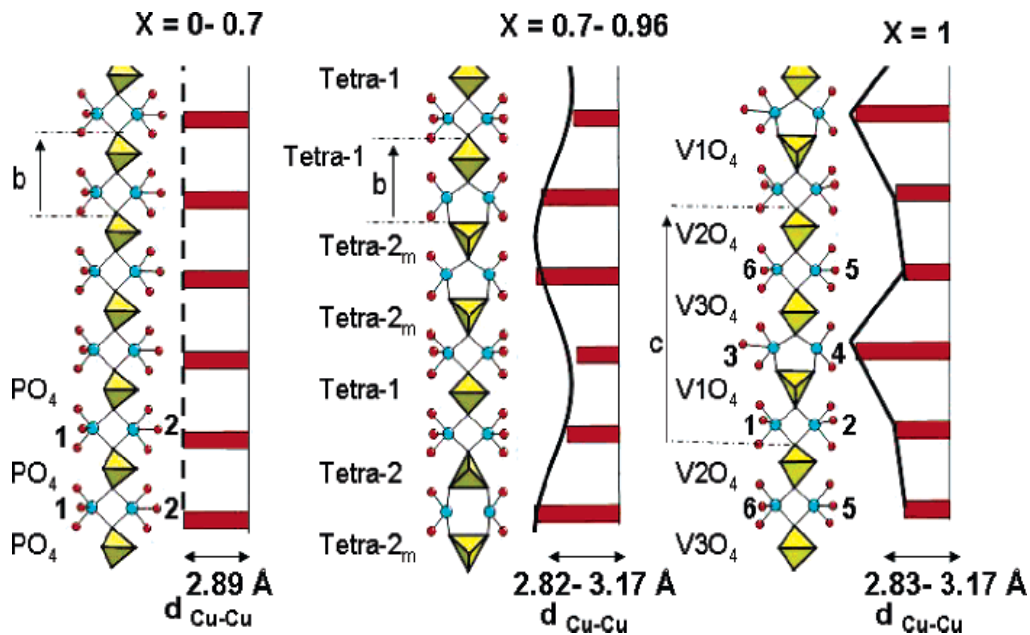


Figure 20. Orientation of the  $P/VO_4$  groups between the Cu-Cu ladder rungs in the three subsequent domains along  $x$ . For the second domain, the most probable tetrahedra are reported by analogy with tetra-1, tetra-2, and tetra-2m occupancies versus  $t$ . The bar graph shows the Cu-Cu separation along the  $b$  axis. Its smooth sinusoidal envelope pictures the modulated feature for  $x = 0.87$ , while the commensurate tripling for  $x = 1$  is shown by straight lines and sharp angles. [40]

The full system shows ordering between the flexible ribbons and the surrounding tetrahedral groups.

- Magnetic properties

All these compounds show exciting  $S = \frac{1}{2}$  spin ladders particularly interesting in the field of low-dimensional quantum materials. The thermal susceptibility was investigated for compositions  $x = 0$ ,  $x = 0.2$ ,  $x = 0.8$  and  $x = 1$  along the solid solution by O. Mentré *et al.* in 2006.

[40] The main results arising are:

- for  $x = 0, 0.2$  and  $1$ , a spin gap behavior is observed;
- for  $x = 0.8$ , there is no finite gap but a chain magnetism.

To conclude, this series of compounds show a continuous evolution from ladder to gapless systems. This is correlated to the phosphate versus vanadate substitution which impact the Cu neighbors in the zig-zag ladder and inside the polycationic ribbons.

#### II.1.4. HP-HT experiments on $\text{BiCu}_2(\text{P}_{1-x}\text{V}_x)\text{O}_6$

As far as structural changes of  $\text{BiCu}_2(\text{P}_{1-x}\text{V}_x)\text{O}_6$  family is well investigated under AP conditions, a series of HP experiments were performed. Since the members of this family demonstrate different magnetic ladders interactions, their further investigation is interesting in regard to their magnetic properties keeping in mind that small structural modifications may induce radical changes on the magnetic behavior. A series of HP-HT experiments were planned on selected members of  $\text{BiCu}_2(\text{P}_{1-x}\text{V}_x)\text{O}_6$  ( $x = 0, 0.2, 0.3, 0.4, 0.5, 0.6, 0.7, 0.8, 0.9$ ) at Neel Institute during an internship period.

To characterize the synthesized samples, in a first instance, the X-Ray powder diffraction method was used. A Search/Match Operation was performed for resulted powders, they were matched with a PDF2 database using DIFFRAC.SUITE EVA (by Bruker) to determine the phase(s) in presence. According to preliminary powder patterns investigation, some of them were selected to provide high quality measurements necessary to perform further Rietveld refinement.

##### *a. HP-BiCu<sub>2</sub>VO<sub>6</sub>*

###### *- Synthesis*

The investigation was started from the pure vanadium compound ( $\text{BiCu}_2\text{VO}_6$ ), reproducing the exact experimental conditions used for the pure phosphorous phase:  $\text{BiCu}_2\text{PO}_6$ . [36] A Pressure of 5GPa and a Temperature of 800°C were applied on a polycrystalline powder sample of  $\text{BiCu}_2\text{VO}_6$  using BELT X type of press. After recuperated from platinum crucible, a dense dark pellet was grained and studied by X-Ray powder diffraction. The data were collected in a range of 5 to 70 2theta degree in order to provide phase identification. The resulted powder diffraction pattern is presented on Figure 21. A matching with two phases of PDF database was evidenced:

the clinobisvanite -  $\text{BiVO}_4$  (PDF card № 14-0688) [42] and tenorite –  $\text{CuO}$  (PDF card № 48-1548). [43] It was thus concluded with confidence that the sample was totally decomposed.

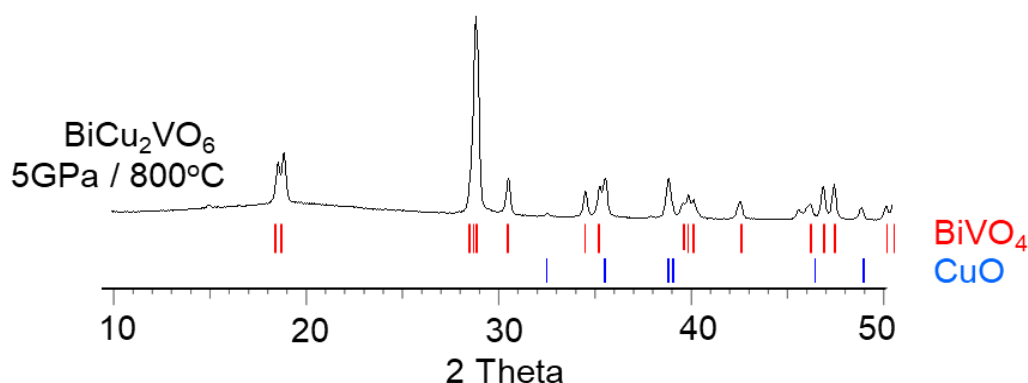


**Figure 21.** X-Ray powder diffraction of  $\text{BiCu}_2\text{VO}_6$  modified at 5GPa and 800°C.

As a consequence, the experimental conditions were changed. At this step of the study, it is possible to modify two parameters: pressure and/or temperature. The decomposition is related to too high pressure and temperature. In the following experiment, the values of both variables were decreased to 2GPa and 400°C. The duration of experiment was left the same (30 minutes).

The resulted powder was satisfactory compared to the HP-BCPO. The cell parameters of HP-BCVO were preliminary refined by LeBail method using JANA2006 software. [24] At the end, some peaks were still not explained. The careful analysis using PDF database established that these additional peaks are due to two impurities:  $\text{BiVO}_4$  [42] and  $\text{Bi}_4\text{Cu}_3\text{V}_2\text{O}_{14}$ . [44]

- Rietveld refinement of High-Pressure form of  $\text{BiCu}_2\text{VO}_6$

In order to provide Rietveld refinement, the new powder data was collected again. The low quantity of material imposed the use of another type of diffractometer. The Rigaku diffractometer is equipped with a rotating anode giving much power/intensity and able to host Si-oriented sample holder which is more accurate for small amount of samples. The powder sample was further analyzed at higher  $2\theta$  angles (5-120°) so as to comply with the requirements of Rietveld refinement.

The refinement was done in Fullprof Suite software. [61] This first step is devoted to the LeBail pattern in order to refine cell parameters of all phases and a profile functions. The peak profile was performed using a Pseudo-Voigt function, which is a convolution of a Gaussian and a Lorentzian function. For the second step of refinement the structural model is required. A structural model of known HP- BCPO was inserted. The Rietveld refinement fit of HP-BCVO is given on the Figure 22. The detailed crystallographic data and refinement parameters are given in Table 5. Atom parameters are given in Table 10. Reliability R-factor for points with Bragg contributions for pattern is 1.85, Bragg R-factor = 3.33 and RF-factor = 2.07. The relative phase amounts in mass are 82.4(2) % for the HP form of  $\text{BiCu}_2\text{VO}_6$ , 13.42(15)% for  $\text{BiVO}_4$  and 4.2(2)% for  $\text{Bi}_4\text{Cu}_3\text{V}_2\text{O}_{14}$ .

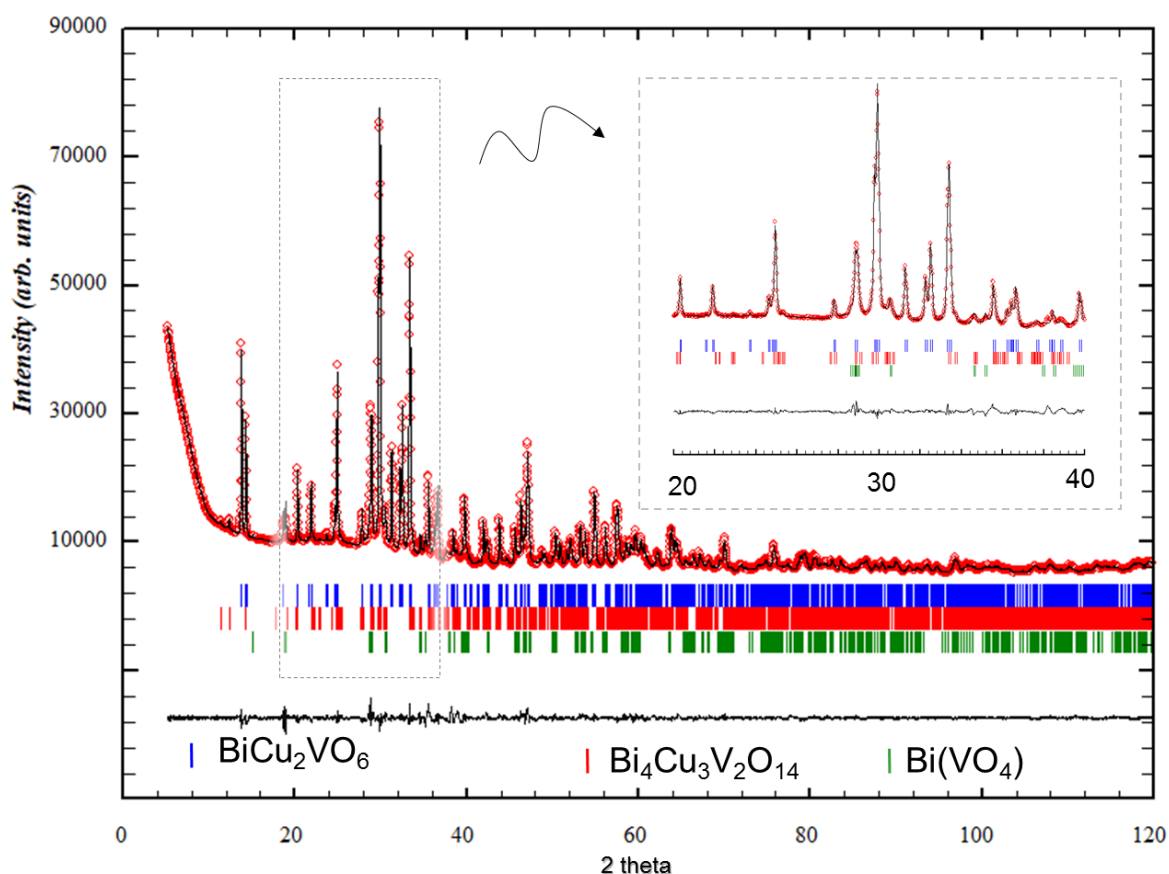


Figure 22. The Rietveld refinement fit of HP-BCVO. The colored ticks correspond to Bragg position of  $\text{BiCu}_2\text{VO}_6$  in blue,  $\text{Bi}_4\text{Cu}_3\text{V}_2\text{O}_{14}$  in red and  $\text{Bi}(\text{VO}_4)$  in green. Difference between experimental (red circles) and calculated (black line) curve is shown in black line.

As expected, the crystal structure is the same as the HP-BCPO (Figure 17(b)). The average interatomic distances were calculated in order to compare the respective HP forms of the phosphate and the vanadate. The resulted values are shown in Table 3.

**Table 3. Average interatomic distances in crystal structures of High-Pressure forms of BiCu<sub>2</sub>PO<sub>6</sub> and BiCu<sub>2</sub>VO<sub>6</sub>.**

Average bond length, Å	BiCu <sub>2</sub> PO <sub>6</sub>	BiCu <sub>2</sub> VO <sub>6</sub>
Bi – O	2.304(1)	2.375(1)
Cu – O	1.924(1)	1.905(1)
P / V – O	1.479(1)	1.674(1)

- TEM

Bearing in mind that incommensurate modulated structure was obtained at some x values in solid solution of BiCu<sub>2</sub>P<sub>1-x</sub>V<sub>x</sub>O<sub>6</sub> compound [40], a TEM investigation was provided. It makes possible to see the presence of tiny additional set of satellite spots on diffraction patterns that yields to incommensurate modulated structures. In the case of the current sample, no modulation was observed.

We investigated the possibility to synthesize polymorph of all terms of the solid solution depending on high-temperature and high-pressure conditions. This helped us to rationalize the conditions route and limit the number of synthesis starting with pertinent/adapted conditions.

- High-Temperature X-ray Diffraction

In order to determine the HP-BCVO form transformation into initial AP, the High-temperature XRD experiment was provided. The temperature stability of compound was checked in the 10-60 2θ range, with a heating step of 25 °C. 2D view on XRD patterns evolution with temperature are shown on Figure 23(a). The XRD patterns of HP-BCVO sample at room temperature and heated at 750°C compared on Figure 23 (b). We can see the appearing of AP phase at around 700°C and can expect full transition at higher temperature. Another remarkable note is full disappearing of BiVO<sub>4</sub> impurity with increasing of temperature.

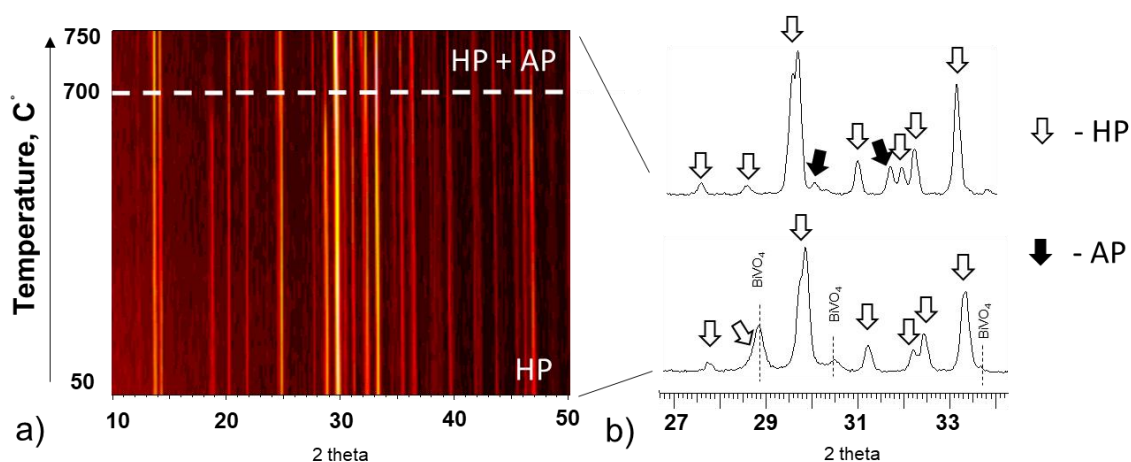


Figure 23. 2D view on XRD patterns evolution of HP-BCVO form with temperature (a). The XRD patterns at the start of the experiment and heated at 750 °C (b).

#### b. Determination of HP phase stability area of $\text{BiCu}_2(\text{P}_{1-x}\text{V}_x)\text{O}_6$

##### - Identification of the synthesis conditions

In order to establish the dependence of the desired **HP-BCVO** phase formation under different conditions and to obtain the conditions to synthesize the pure phase, a series of experiments was carried out. The XRD patterns are shown on Figure 24.

The experiment provided at 400 °C and 2 GPa became the starting point for further research. On Figure 24, it is indicated as (a) - point. This experiment resulted in appearance of **HP-BCVO** phase assorted with two impurities  $\text{BiVO}_4$  and  $\text{Bi}_4\text{Cu}_3\text{V}_2\text{O}_{14}$  in amount of 13% for  $\text{BiVO}_4$  and 4% for  $\text{Bi}_4\text{Cu}_3\text{V}_2\text{O}_{14}$ . The relative phase amounts in mass are given in Table 4 for each component.

Since the new phase was successfully obtained at sufficiently low temperature (400 °C) and pressure (2 GPa), it was decided to change one of the variable parameters. The next experiment took place at the same temperature, whereas pressure was increased to 3 GPa. Following the arrow in the figure, the second point is called (b). Based on the results of a preliminary comparison of two diffraction patterns, no evidence of differences was found between them. Thus sample obtained at 3 GPa and 400 °C corresponds mainly to HP targeted phase. The relative phase amounts in mass are 76.6(3)% for main phase, 14.70(16)% for  $\text{BiVO}_4$  and 8.7(3)% for  $\text{Bi}_4\text{Cu}_3\text{V}_2\text{O}_{14}$ . At the same time the amount of  $\text{Bi}_4\text{Cu}_3\text{V}_2\text{O}_{14}$  impurity doubled compared with previous experiment.

From this point, the sequence of experiments was divided in two directions: Decrease in temperature (to 350°C) while maintaining the pressure (3GPa) and increase pressure (to 5GPa) while maintaining the temperature (400°C). On the Figure 24 the corresponding points are named (c) and (d), respectively. According to X-Ray diffraction powder analysis of both samples, they consist mostly of unreacted initial AP phase and a small impurity content. Since a significant jump in pressure (from 3 to 5GPa) did not affect the formation of the desired phase, it has been concluded that temperature has more control over the course of the reaction. To prove this provision, the only one direction was chosen for further study: to increase the temperature. In two further experiments, pressure was fixed at 5GPa. At the same time the temperature increased by 50 degrees to reach 450°C in case of point (e) and by 100°C to reach 500°C (f - point). A comparative analysis of the two obtained diffraction patterns showed similarity with the starting (a) point of the study - they both contain a new HP polymorph of  $\text{BiCu}_2\text{VO}_6$  compound and two impurities:  $\text{BiVO}_4$  and  $\text{Bi}_4\text{Cu}_3\text{V}_2\text{O}_{14}$ . According to powder pattern analysis, the following relative amounts of main HP phase (68.8(3)%) and  $\text{BiVO}_4$  and  $\text{Bi}_4\text{Cu}_3\text{V}_2\text{O}_{14}$  (27.17(19)%) impurities were estimated for sample obtained at 5GPa and 450°C (e).

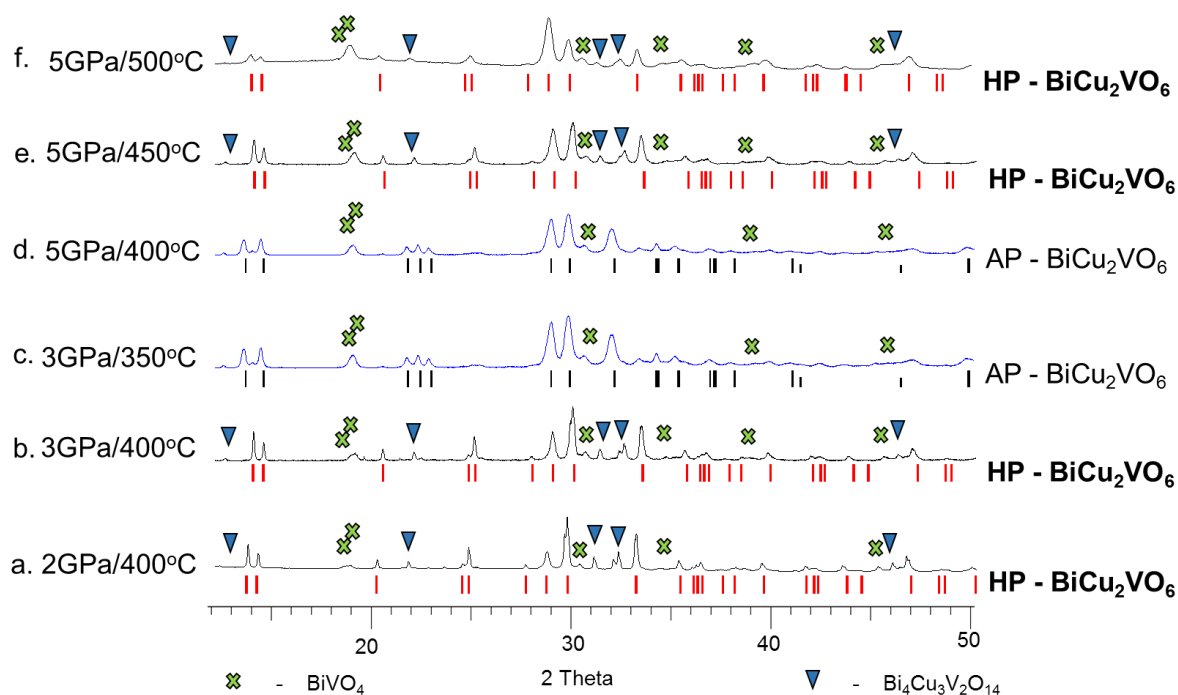


**Figure 24. Powder X-ray diffraction patterns of HP -BCVO series of experiments at different experimental conditions.**

For a visual representation of the sequence of further experiments, a diagram was drawn on Figure 25. The graph is a simple temperature versus pressure plot. The figure shows the points corresponding to the experiments and their sequence. The very first experiment that degraded to the formation of two impurities belongs to “decomposition” area. This experimental step is marked as a black circle on the mentioned figure. Comparing the results of the HP-HT experiments of starting (a) and end points (f) a slight difference may be detected. The approximate impurity contents were estimated by analyzing the diffraction patterns. The content of impurities in the initial sample (a) turned out to be lower than in the last one (f) according to roughly quick look at peak intensities.

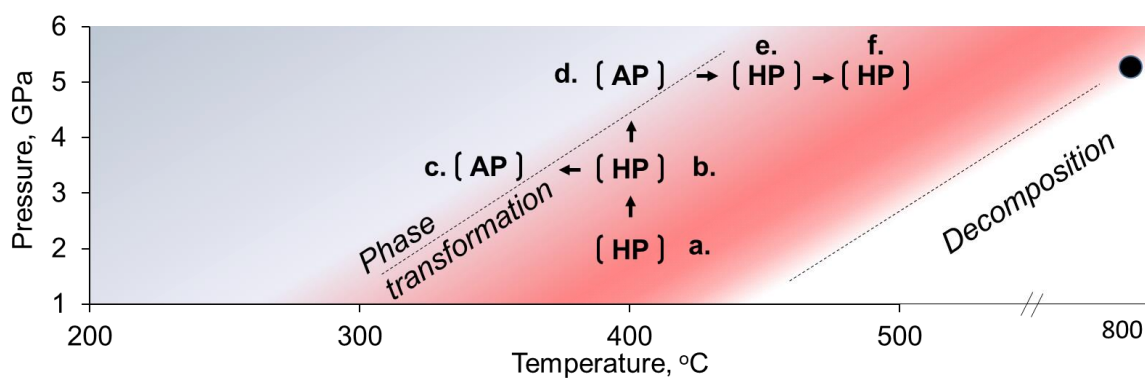


**Figure 25.** A sequence of provided experiments to establish the phase transition boundaries between ambient-pressure (AP), high-pressure (HP) forms of  $\text{BiCu}_2\text{VO}_6$  or decomposed sample (●).

Based on the obtained data, several conclusions can be drawn:

1. 3 areas can be selected on the phase diagram: stability of ambient-pressure (AP) phase, stability of high-pressure (HP) phase and area of decomposed compound;
2. Applying of HP-HT method to modify the existing phase, the result is mostly controlled by temperature;
3. An increase in pressure leads to an increment in the total impurity content;
4.  $\text{BiCu}_2\text{PO}_6$  was synthesized at 5GPa and 800°C so a substitution of V by P could start with an increase of temperature, keeping pressure constant and equal to 5GPa.

After getting an insight about the general dependence of HP phase formation for the two extreme members of  $\text{BiCu}_2(\text{P}_{1-x}\text{V}_x)\text{O}_6$  family, the study was continued for others. A series of

HP-HT experiments was provided on a selected members of  $\text{BiCu}_2(\text{P}_{1-x}\text{V}_x)\text{O}_6$  ( $x = 0.2, 0.3, 0.4, 0.5, 0.6, 0.7, 0.8, 0.9$ ) family.

In order to expand our knowledge of the represented area boundaries, the nearest to pure vanadium composition was taken:  $\text{BiCu}_2(\text{P}_{0.1}\text{V}_{0.9})\text{O}_6$ . It was proposed to carry out three syntheses at a fixed pressure (5GPa) and different temperatures with a step of 100°C. This series of experiments started from 500°C as concluded above. Figure 26 (a) and (b) demonstrates powder patterns that were obtained at 500°C and 600°C, respectively. They both succeed in the formation of HP -  $\text{BiCu}_2(\text{P}_{0.1}\text{V}_{0.9})\text{O}_6$  composition, according to identification of both powders confirming the deduced synthesis route. One can easily guess that working at lower temperatures would not result in the stabilization of the HP targeted phase.

Besides confirming the existence of the desired phase, the amount of impurities was estimated. The sample obtained at 5GPa and 500°C has a 86.1(3)% of HP-BCVO, 11.27(19)% of  $\text{BiVO}_4$  and 2.6(3)% of  $\text{Bi}_4\text{Cu}_3\text{V}_2\text{O}_{14}$ . At the same time the sample obtained at 600°C demonstrates the increased amount of impurities. Last experiment at 700°C was intended to confirm the collapse of HP-phase (Figure 26(c)). Based on the results of diffraction pattern analysis, almost complete absence of HP – phase was recorded with a relevance of  $\text{BiVO}_4$  and  $\text{CuO}$  compounds. This series of experiments clarified the boundaries of the highlighted AP, HP and decomposition areas.

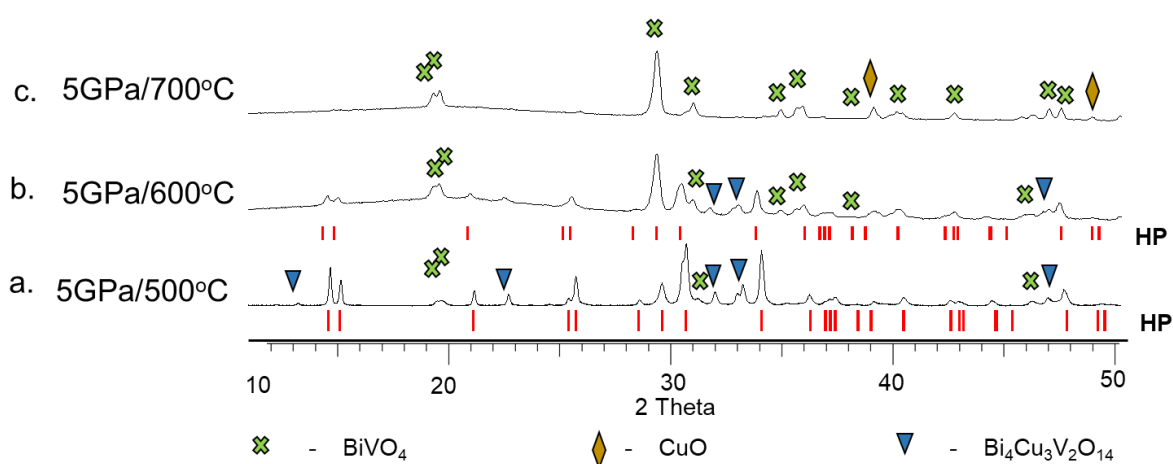


**Figure 26. Powder diffraction patterns of HP -  $\text{BiCu}_2(\text{P}_{0.1}\text{V}_{0.9})\text{O}_6$  series at different experimental conditions.**

With the same goal, four experiments were scheduled for  $\text{BiCu}_2(\text{P}_{0.2}\text{V}_{0.8})\text{O}_6$  composition. It was decided to start a new experiment in unexplored point of HP-HT condition range. First

experiment was provided at 550°C and 5 GPa (Figure 27(a)). Next two experiments were carried out at fixed temperature (500°C) and different pressure values - 3 and 5GPa (Figure 27(b, d)). The investigation of resulted powder patterns of these samples confirmed the existence of HP polymorph and two expectative impurities of BiVO<sub>4</sub> and Bi<sub>4</sub>Cu<sub>3</sub>V<sub>2</sub>O<sub>14</sub> in all three samples. The fourth experiment in this series aimed to establish the applicability of another press modification in the case of our systems (Figure 27(c)). The Conac anvil-type apparatus was used to reproduce HP-HT conditions at 500°C and 5GPa and compare with Belt type press. It allows to provide experiments on larger sample volume to 1 cm<sup>3</sup>. The duration of experiment was extended to 90 minutes. According to X-Rays powder diffraction analysis the resulted sample demonstrates significant increase in rate of impurity comparing to other samples in this series.

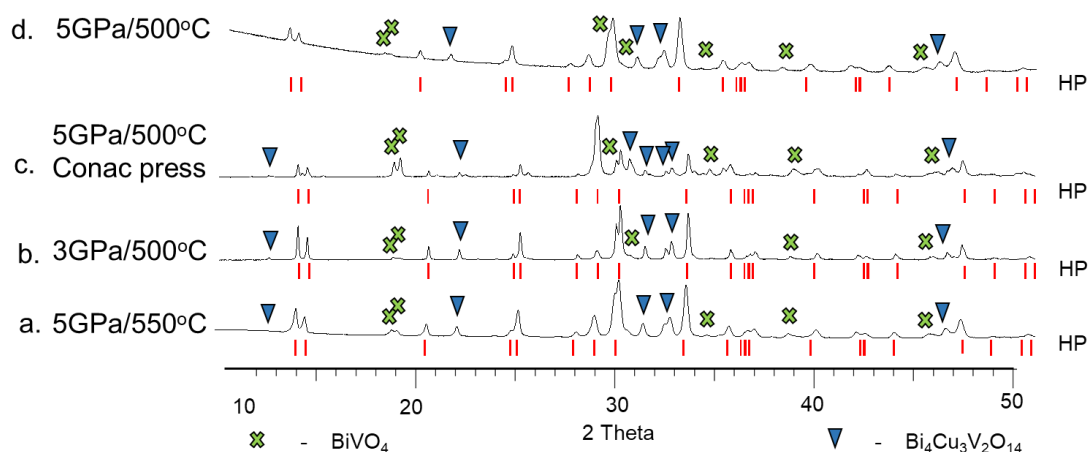


**Figure 27. Powder diffraction patterns of HP - BiCu<sub>2</sub>(P<sub>0.2</sub>V<sub>0.8</sub>) series at different experimental conditions.**

The revision of phase composition of impurities was provided at this step of experiments. The presence of their phosphorous analogues was suggested. It was decided to work on sample obtained at 500°C and 5GPa in Conac type press contains the highest amount of unexplained by HP-phase peaks. The additional examination of this sample confirmed the presence of only BiVO<sub>4</sub> and Bi<sub>4</sub>Cu<sub>3</sub>V<sub>2</sub>O<sub>14</sub> impurities.

As following from abovementioned the provided experiment in Belt type press at 550°C and 5GPa led to formation of the purest sample, but the estimated amount of impurities increased: 7.55(3)% for BiVO<sub>4</sub> and 30.7(3)% Bi<sub>4</sub>Cu<sub>3</sub>V<sub>2</sub>O<sub>14</sub>.

The aim of further research was to obtain a HP phase for other members of  $\text{BiCu}_2(\text{P}_{1-x}\text{V}_x)\text{O}_6$  family. The composition with  $x$  equal to 0.6, demonstrates a trend that wasn't so obvious earlier: increasing of phase transition temperature. The application of 500°C and 5GPa conditions on  $\text{BiCu}_2(\text{P}_{0.4}\text{V}_{0.6})\text{O}_6$  lead to formation of a mixture including initial AP and HP phases. However, an increase in temperature of 100°C leads to the successful formation of desired HP phase with several peaks of impurities again attributed to  $\text{BiVO}_4$  and  $\text{Bi}_4\text{Cu}_3\text{V}_2\text{O}_{14}$ . Both experiments are shown on Figure 28, where (a) corresponds to experiment provided at 5GPa and 500°C and (b) - to 5GPa and 600°C.

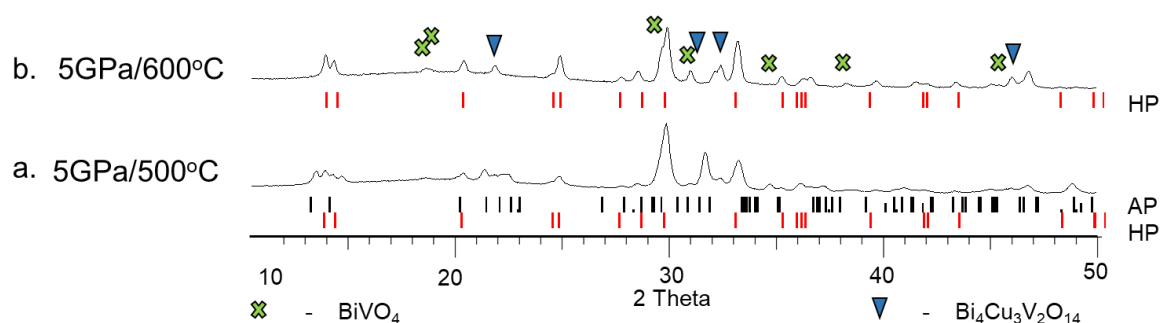


**Figure 28. Powder diffraction patterns of HP -  $\text{BiCu}_2(\text{P}_{0.4}\text{V}_{0.6})$  series at different experimental conditions.**

For a sample in which the vanadium and phosphorus elements are in equal parts, the following experiment conditions were assigned – 650°C and 5GPa. According to analysis of X-Ray powder diffraction patterns, the presence of HP phase of  $\text{BiCu}_2(\text{P}_{0.5}\text{V}_{0.5})\text{O}_6$  compound was confirmed. Formation of this compound is not possible without  $\text{BiVO}_4$  and  $\text{Bi}_4\text{Cu}_3\text{V}_2\text{O}_{14}$  impurities. The preliminary Bragg peaks distribution of three phases are shown on Figure 29 (a).

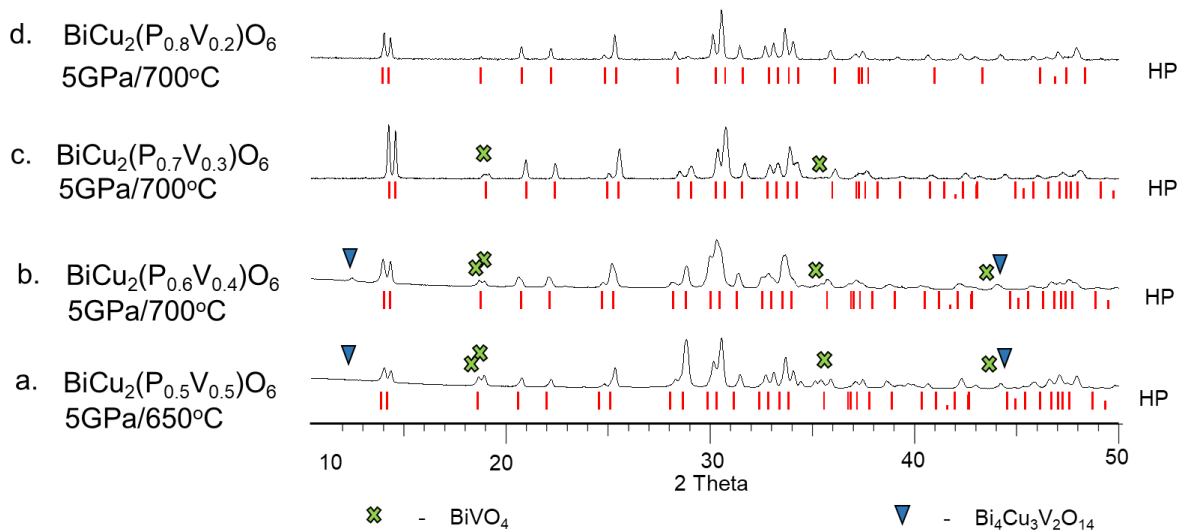


**Figure 29. Powder diffraction patterns of  $\text{BiCu}_2(\text{P}_{1-x}\text{V}_x)\text{O}_6$  series, where (a) corresponds to HP -  $\text{BiCu}_2(\text{P}_{0.5}\text{V}_{0.5})\text{O}_6$  composition, (b) to HP -  $\text{BiCu}_2(\text{P}_{0.6}\text{V}_{0.4})\text{O}_6$ , (c) to HP -  $\text{BiCu}_2(\text{P}_{0.7}\text{V}_{0.3})\text{O}_6$  and (d) to HP -  $\text{BiCu}_2(\text{P}_{0.8}\text{V}_{0.2})\text{O}_6$ .**

For the rest unmentioned members of  $\text{BiCu}_2(\text{P}_{1-x}\text{V}_x)\text{O}_6$  family, where  $x$  is equal to 0.4, 0.3, and 0.2, it was suggested to raise the temperature with a step of 50°C. HP-HT experiments on  $\text{BiCu}_2(\text{P}_{0.6}\text{V}_{0.4})\text{O}_6$  and  $\text{BiCu}_2(\text{P}_{0.7}\text{V}_{0.3})\text{O}_6$  compounds were provided at a pressure of 5GPa and 700°C. Whereas temperature was increased to 750°C in case of  $\text{BiCu}_2(\text{P}_{0.8}\text{V}_{0.2})\text{O}_6$  compound. The experiments were successful and led to the formation of the desired HP- phase in all three cases as shown on Figure 29. Some differences are noticed between all the patterns. The main difference consists in estimated amount of impurities; it decreases concurrently with increasing of phosphorus content. Thus, the  $\text{BiCu}_2(\text{P}_{0.8}\text{V}_{0.2})\text{O}_6$  compound factually contains just a traces of  $\text{BiVO}_4$  impurity. The estimated amount of impurities in percent is given in Table 4.

The final HP-HT experiment for the entire series of  $\text{BiCu}_2(\text{P}_{1-x}\text{V}_x)\text{O}_6$  family was provided on pure phosphorous  **$\text{BiCu}_2\text{PO}_6$** . [36] To roughly indicate a bottom line of AP to HP transition, the experiment at 5GPa and 600°C was carried out. Resulted sample revealed unreacted initial mixture, corresponding to AP phase that is shown on Figure 30 (a). The Figure 30 (b) demonstrates the powder pattern of pure high-pressure phase that was obtained at 5GPa, 800°C.

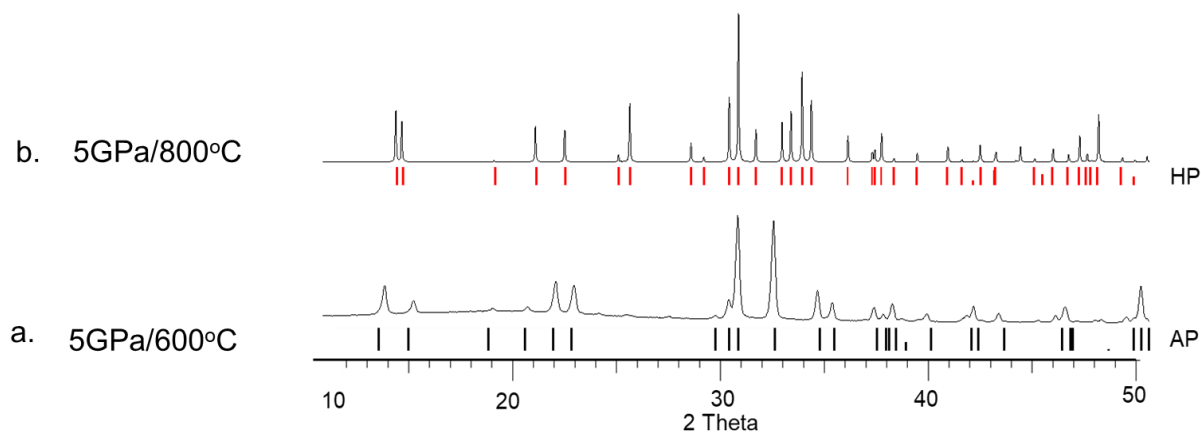


**Figure 30. Powder diffraction patterns of HP -  $\text{BiCu}_2\text{PO}_6$  compound at different experimental conditions.**

In order to bring together and link all information about the HP-HT experiments carried out and their results, the following table was compiled (Table 4). First of all, the data in the table are sorted by stoichiometry of V *versus* P, where V value is equal to x in general formula of  $\text{BiCu}_2(\text{P}_{1-x}\text{V}_x)\text{O}_6$  family. Each line of table corresponds to single experiment and has an information about target conditions. The table also contains information about the results of X-Rays powder diffraction analysis done by comparing with PDF database or by matching with reference **HP-  $\text{BiCu}_2\text{VO}_6$**  phase.

In addition, the table has the last column with symbols. These symbols will be found further in the text and on the summarizing figure dedicated to depiction of AP to HP transition and AP to decomposition area. According to investigation of the X-Ray powder patterns and comparison between them, all powders after experiment can be divided in three groups: corresponding to unreacted sample ( $\diamond$ ), related with HP form of initial compound ( $\circ$ ) or to decomposed mixture ( $\times$ ). The filling color of these forms will depend on the pressure at which the experiment was carried out. The blue color corresponds to the experiments carried out at 5GPa, the red color – at 3GPa, and green color – at 2GPa. Also one exception is made in case of Conac-type press used, this experiment corresponds to grey color.

For example, during the investigation, only one experiment has been performed at 2GPa resulted in formation of high-pressure phase. In table this experiment will have the “o” character filled with a green color.

**Table 4. Table of High-Pressure High-Temperature experiment conditions.**

Stoichiometry				Target conditions		Result after powder X-Ray analysis						Symbol
Bi	Cu	V (x)	P	Pressure	T (°C)/ duration	Main phase	%	Impurity 1	%	Impurity 2	%	
1	2	0	1	5GPa	800°C/ 30 min	HP form						●
				5GPa	600°C/ 30 min	AP form						◆
1	2	0.2	0.8	5GPa	750°C/ 30 min	HP form		BiVO <sub>4</sub>	<1			●
1	2	0.3	0.7	5GPa	700°C/ 30 min	HP form		BiVO <sub>4</sub>		Bi <sub>4</sub> Cu <sub>3</sub> V <sub>2</sub> O <sub>14</sub>		●
1	2	0.4	0.6	5GPa	700°C/ 30 min	HP form		BiVO <sub>4</sub>		Bi <sub>4</sub> Cu <sub>3</sub> V <sub>2</sub> O <sub>1</sub>		●
1	2	0.5	0.5	5GPa	650°C/ 30 min	HP form	71.3	BiVO <sub>4</sub>	26.9	Bi <sub>4</sub> Cu <sub>3</sub> V <sub>2</sub> O <sub>14</sub>	1.8	●
1	2	0.6	0.4	5GPa	600°C/ 30 min	HP form		BiVO <sub>4</sub>		Bi <sub>4</sub> Cu <sub>3</sub> V <sub>2</sub> O <sub>14</sub>		●
					500°C/ 30 min	AP form		HP form			◆	
1	2	0.8	0.2	5GPa	550°C/ 30 min	HP form	61.8	Bi <sub>4</sub> Cu <sub>3</sub> V <sub>2</sub> O <sub>14</sub>	30.7	BiVO <sub>4</sub>	7.5	●
				5GPa	500°C/ 30 min	HP form		Bi <sub>4</sub> Cu <sub>3</sub> V <sub>2</sub> O <sub>14</sub>		BiVO <sub>4</sub>		●
				3GPa	500°C/ 30 min	HP form		Bi <sub>4</sub> Cu <sub>3</sub> V <sub>2</sub> O <sub>14</sub>		BiVO <sub>4</sub>		●
				5GPa	500°C/ 90 min	HP form		BiVO <sub>4</sub>		Bi <sub>4</sub> Cu <sub>3</sub> V <sub>2</sub> O <sub>14</sub>		●
1	2	0.9	0.1	5GPa	700°C/ 30 min	BiVO <sub>4</sub>		CuO		Bi <sub>4</sub> Cu <sub>3</sub> V <sub>2</sub> O <sub>14</sub>		⊗
				5GPa	600°C/ 30 min	HP form		BiVO <sub>4</sub>		Bi <sub>4</sub> Cu <sub>3</sub> V <sub>2</sub> O <sub>14</sub>		●
				5GPa	500°C/ 30 min	HP form	86.1	BiVO <sub>4</sub>	11.9	Bi <sub>4</sub> Cu <sub>3</sub> V <sub>2</sub> O <sub>14</sub>	2.0	●
				5GPa	400°C/ 30 min	AP form					◆	
1	2	1	0	5GPa	800°C/ 30 min	BiVO <sub>4</sub>		CuO				⊗
				5GPa	500°C/ 30 min	HP form		BiVO <sub>4</sub>		Bi <sub>4</sub> Cu <sub>3</sub> V <sub>2</sub> O <sub>14</sub>		●
				5GPa	450°C/ 30 min	HP form		BiVO <sub>4</sub>		Bi <sub>4</sub> Cu <sub>3</sub> V <sub>2</sub> O <sub>14</sub>		●
				5GPa	400°C/ 30 min	AP form		BiVO <sub>4</sub>			◆	
				3GPa	400°C/ 30 min	HP form	76.3	BiVO <sub>4</sub>	14.7	Bi <sub>4</sub> Cu <sub>3</sub> V <sub>2</sub> O <sub>14</sub>	9.0	●
				2GPa	400°C/ 30 min	HP form	82.4	BiVO <sub>4</sub>	13.4	Bi <sub>4</sub> Cu <sub>3</sub> V <sub>2</sub> O <sub>14</sub>	4.2	●
				3GPa	350°C/ 30 min	AP form		BiVO <sub>4</sub>				◆

In order to make the results of the experiments more visually compelling and easier to understand, it was decided to create a drawing, where the above-mentioned characters would meet the conditions of the experiment. Points corresponding to the parameters of the experiment were put on the ordinary diagram of the temperature on composition dependence. Each point in this Figure 31 corresponds to a line from the Table 4.

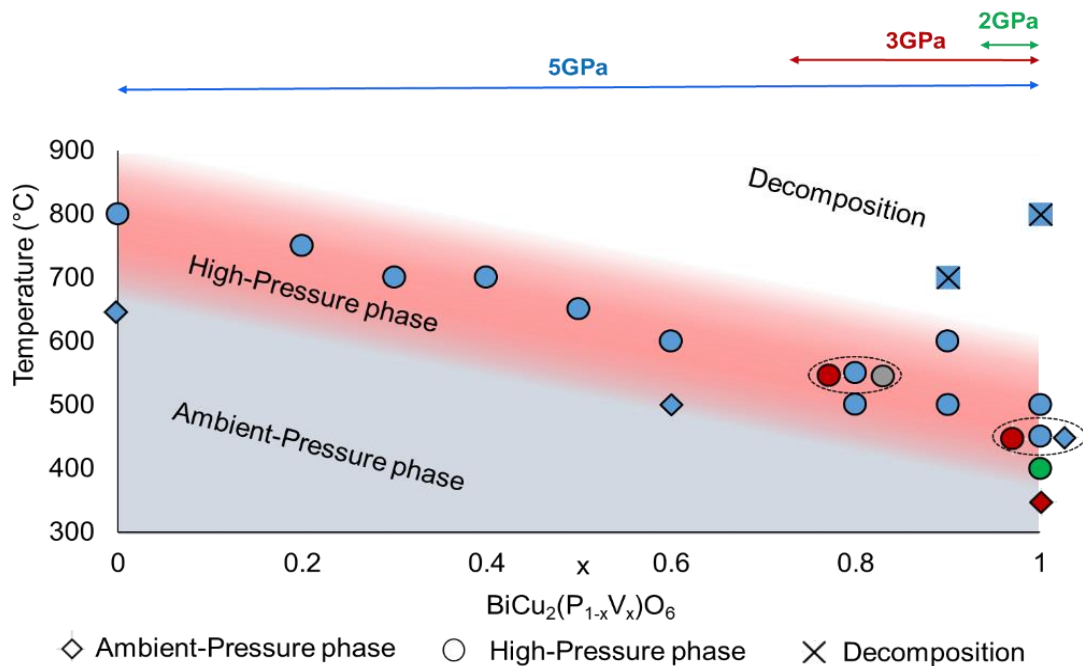


**Figure 31. Graphical presentation of results on series of HP-HT experiments.**

- Rietveld refinement of High-Pressure form of  $\text{BiCu}_2(\text{P}_{1-x}\text{V}_x)\text{O}_6$

Rietveld refinement on selected members of  $\text{BiCu}_2(\text{P}_{1-x}\text{V}_x)\text{O}_6$  family was provided following the same procedure as was detailed in case of refinement of HP form of  $\text{BiCu}_2\text{VO}_6$ .  $\text{BiCu}_2(\text{P}_{0.8}\text{V}_{0.2})\text{O}_6$ ,  $\text{BiCu}_2(\text{P}_{0.5}\text{V}_{0.5})\text{O}_6$  and  $\text{BiCu}_2(\text{P}_{0.2}\text{V}_{0.8})\text{O}_6$  compounds were chosen. For these compounds, a high-quality data collection was provided in a range from 5 to 120  $2^\circ$ theta degree, using the Rigaku diffractometer. Rietveld Refinement was performed using JANA2006 software. The structural data from refined High-Pressure form of  $\text{BiCu}_2\text{VO}_6$  was inserted as a model. During the refinement the asymmetry correction was applied. Split of atomic positions was used to create a mixed site for P and V elements. Relative occupancy of the splitted atom was kept according to V/P stoichiometry in compound. Resulted pictures of  $\text{BiCu}_2(\text{P}_{0.8}\text{V}_{0.2})\text{O}_6$ , refinement are shown on Figure 32(a), of  $\text{BiCu}_2(\text{P}_{0.5}\text{V}_{0.5})\text{O}_6$  - on (b), and of  $\text{BiCu}_2(\text{P}_{0.2}\text{V}_{0.8})\text{O}_6$  - on (c).

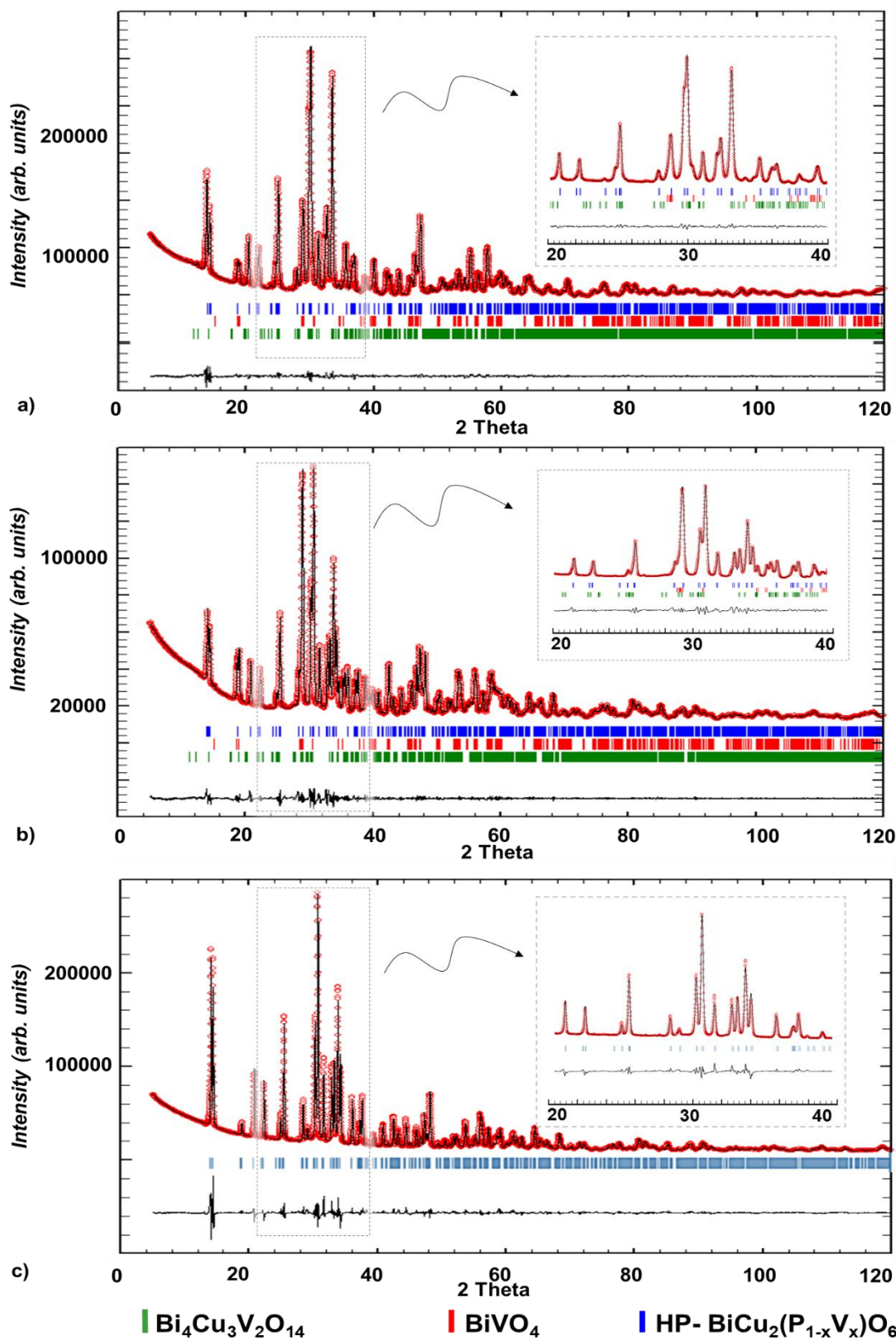
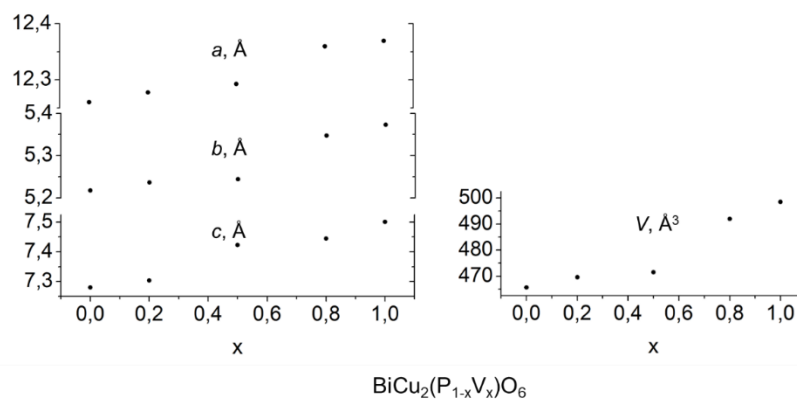


Figure 32. The Rietveld refinement fit High-Pressure form of BiCu<sub>2</sub>(P<sub>0.8</sub>V<sub>0.2</sub>)O<sub>6</sub> (a), BiCu<sub>2</sub>(P<sub>0.5</sub>V<sub>0.5</sub>)O<sub>6</sub> (b) and BiCu<sub>2</sub>(P<sub>0.2</sub>V<sub>0.8</sub>)O<sub>6</sub> (c). The colored ticks correspond to Bragg position of phases. Diff. curve is shown in black line.

The detailed crystallographic data and refinement parameters are given in Table 5. Atom parameters are given in Supplementary information in Table 10. The refined unit cell parameters of listed samples are well corresponding with the trend that has been proposed based on the values of the extreme members of  $\text{BiCu}_2(\text{P}_{1-x}\text{V}_x)\text{O}_6$  family, where  $x = 1$  and  $0$ . The plot of the unit cell parameters dependence on composition is shown on Figure 33.



**Figure 33. Dependence of refined unit cell parameters on  $\text{BiCu}_2(\text{P}_{1-x}\text{V}_x)\text{O}_6$  composition.**

As it was declared in [36], the BCPO transformation from AP to HP phase occurs without formation of any impurities. Whereas, at the end of HP refinement of pure vanadium phase, the quantity of major HP-BCVO phase is only about 80% of the total sample volume. The pure HP-BCVO sample contains  $\text{BiVO}_4$  in amount about 13-14% of weight, while the rest coincide with  $\text{Bi}_4\text{Cu}_3\text{V}_2\text{O}_{14}$  compound. In case of  $\text{BiCu}_2(\text{P}_{0.5}\text{V}_{0.5})\text{O}_6$  composition we observe a slight deviation of the unit cell parameters from general linear trend. This can be explained by the presence of increased amount of impurities or wrong P/V ratio. An additional EDS measurement or repeating of experiment could help to explain this deviation.

Also, the investigation of the crystal structures refined in this part confirmed the similitudes between all crystal structure. As usual, the main modifications come from a rotation of the vanadates along the solid solution.

**Table 5. Crystallographic data and refinement parameters for BiCu<sub>2</sub>(P<sub>1-x</sub>V<sub>x</sub>)O<sub>6</sub> (x = 1, 0.8, 0.5 and 0.2) compounds.**

Phase composition	x = 1	x = 0.8	x = 0.5	x = 0.2	x = 0 [ref 36]
Space group			<i>Pnma</i>		
Z			1		
a (Å)	12.369 (3)	12.360(1)	12.293(1)	12.277 (2)	12.260(1)
b (Å)	5.373 (1)	5.346(1)	5.244(1)	5.236 (1)	5.217(0)
c (Å)	7.501 (1)	7.446(1)	7.314(1)	7.303 (1)	7.279(0)
V (Å <sup>3</sup> )	498.52(2)	492.13(1)	471.51(2)	469.55(1)	465.68(0)
Density (g/cm <sup>3</sup> )	6.436	6.623	6.913	6.730	13.208
Radiation			CuKα <sub>1,2</sub>		
2θ range (deg)			5–120		
Number of points	5609		11501		
Bragg R-factor	0.033	0.007	0.046	0.041	
R <sub>F</sub>	0.021	0.010	0.084	0.062	
R <sub>P</sub>	0.018	0.011	0.022	0.029	
R <sub>wP</sub>	0.026	0.016	0.033	0.045	

The deep investigation of these systems allowed to obtain the purest HP-polymorph of each member of the solid solution. The rationalization was used to limit the number of synthesis done in the press, keeping in mind that each trial is quite expensive. The purest samples were further used for magnetic measurements.

#### - Magnetic Measurements

The magnetic susceptibilities and inverse susceptibilities versus temperature were collected at H= 0.05T and 0.1T for HP-BCVO and at H= 0.1T for HP-BCP<sub>0.8</sub>V<sub>0.2</sub>O and HP-BCP<sub>0.2</sub>V<sub>0.8</sub> (Figure 17); the magnetization versus field (at various temperatures) data have been collected on a polycrystalline sample between 1.8 K and 400 K until H = 3T, using a PPMS Dynacool (Quantum Design) system. Zero field cooled and Field Cooled routines have been employed for  $\chi(T)$ .

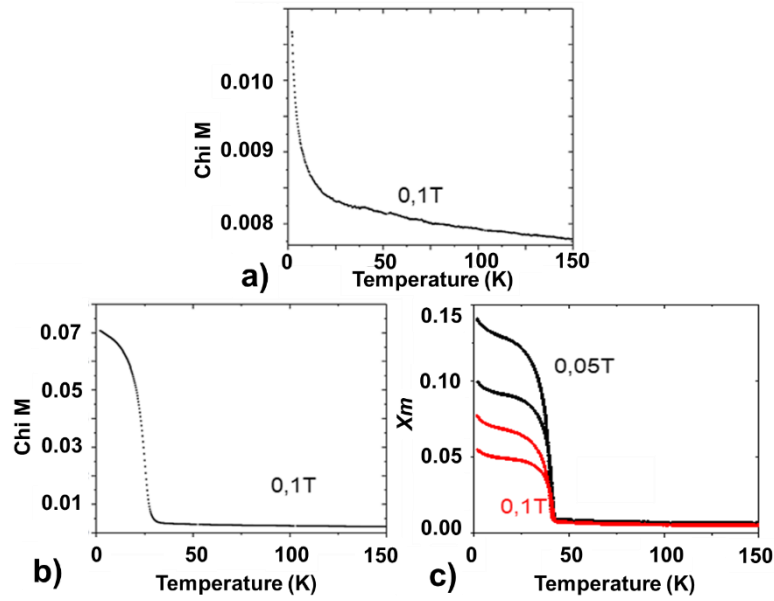


**Figure 34. Magnetic measurement (a)  $\text{BiCu}_2\text{P}_{0.8}\text{V}_{0.2}\text{O}_6$  –HP, (b)  $\text{BiCu}_2\text{P}_{0.2}\text{V}_{0.8}\text{O}_6$  –HP, (c)  $\text{BiCu}_2\text{VO}_6$  –HP.**

First of all, let's precise that among the impurities observed,  $\text{BiVO}_4$  is nonmagnetic and  $\text{Bi}_4\text{Cu}_3\text{V}_2\text{O}_{14}$  is AFM with a TN temperature at 6K [62] and a magnetic susceptibility showing a broad maximum at 20.5K. No related signals are observed on the magnetic susceptibility plots registered on our samples so we conclude that the signals measured totally come from our new phases.

Observing all these data, it is noteworthy that, as soon as a small amount of vanadium is introduced, the typical spin gap behavior of the phosphate disappeared for the benefit of a paramagnetic one.

At higher amount of vanadium, HP-BCP<sub>0.2</sub>V<sub>0.8</sub>O and HP-BCVO show similar behaviors. Concerning the pure vanadate sample: first of all, there is a strong diamagnetic component on the ZFC branch below an intrinsic FM transition observed around  $T_C=43\text{K}$ . This may indicate negative field easily trapped in the sample. The weak ferromagnetism is leading to  $0.08 \mu\text{B}/\text{FU}$ , which indicates a main AFM topology as expected with possible uncompensated sub lattices. However, the magnetization plots (see Figure 35) are clearly not symmetrical which may indicate exchange bias between the main/AFM region and FM domains. Below 40K, a net ferromagnetic component is observed on  $M(H)$ , generally due to spin canting associated to a slight deviation of the moment towards the ideal collinear AFM ordering.

The same global behavior is observed for HP-BCP<sub>0.2</sub>V<sub>0.8</sub>O but with a lower T<sub>c</sub> value around 25K. The magnetization versus field plots performed at various temperatures (see Figure 35) shows again a FM behavior between 25 and 50K.

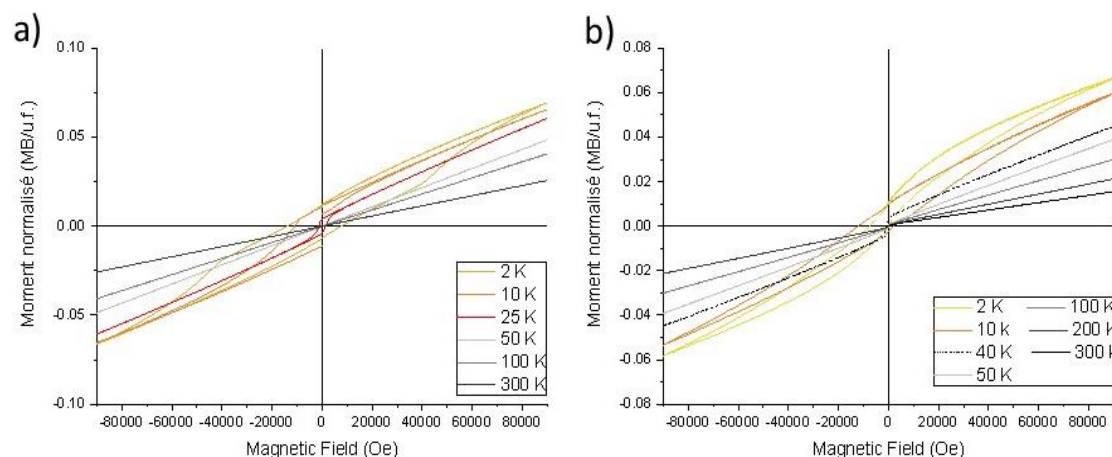


**Figure 35. Magnetization plots for HP-BCP<sub>0.2</sub>V<sub>0.8</sub>O (a) and HP-BCVO (b).**

In a further study, DFT calculation were performed in collaboration with Dr. A. Tsirlin of the University of Augsburg in order to calculate the  $J$ - $J$  coupling as it was done for the AP and the HP-BiCu<sub>2</sub>PO<sub>6</sub>. The list of the  $J$  values is given in Table 6 and compared with the values of the AP and HP-BiCu<sub>2</sub>PO<sub>6</sub>. The denomination of  $J_N$  exactly corresponds to those of the phosphate (see Figure 36) so that we can easily compare the values.

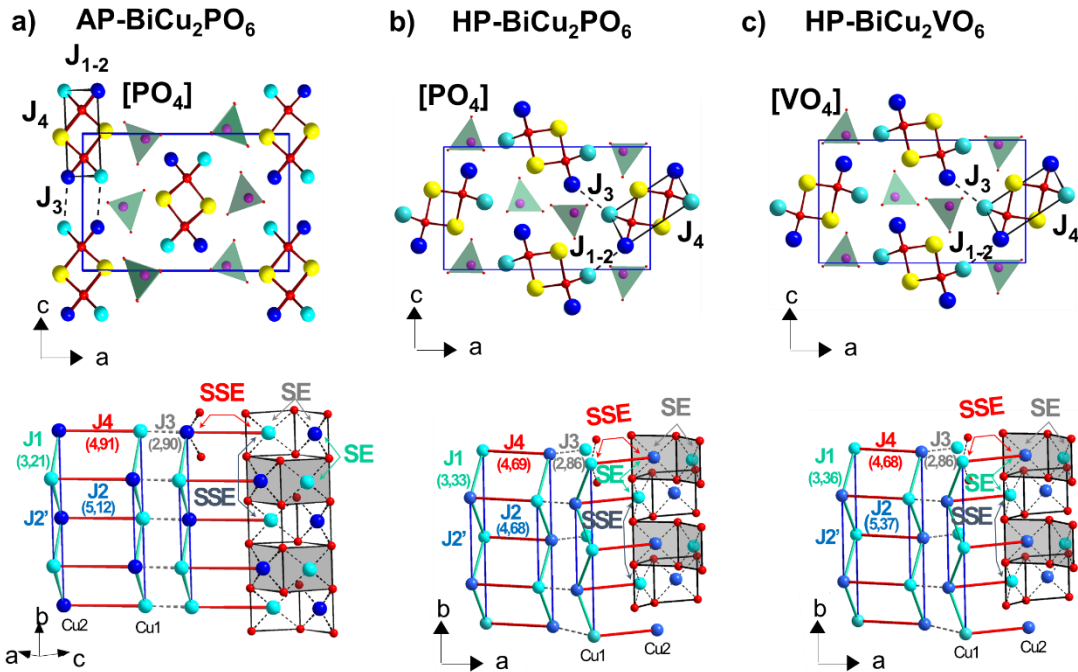


Figure 36. Projections along the b axis of the AP-BCPO (a), HP-BCPO (b) and HP-BCVO crystal structures with evidence of polycationic ribbons surrounded by [PO<sub>4</sub>]/[VO<sub>4</sub>] groups and below there are views of the magnetic ladders with main distances and J labels.

Table 6. List of the J values of the AP and HP-BiCu<sub>2</sub>PO<sub>6</sub> compounds compared with HP- BiCu<sub>2</sub>VO<sub>6</sub>.

	AP-P	HP-P	HP-V		AP-P	HP-P	HP-V
$J_1$	114	181	152	Cu-Cu (Å)	3.21	3.32	3.36
				Cu-O-Cu (°)	112.2	119.6	119.9
$J_2$	68	95	2	Cu-Cu (Å)	5.17	5.22	5.37
$J_2'$	117	108	37	Cu-Cu (Å)	5.17	5.22	5.37
$J_3$	30	-30	-84	Cu-Cu (Å)	2.90	2.86	2.86
				Cu-O-Cu (°)	92.0	92.1	94.6
$J_4$	103	84	83	Cu-Cu (Å)	4.91	4.66	4.68
				O-O (Å)	2.75	2.75	2.78
				Cu-O-O (°)	126.0	127.1	109.64

Here the substitution of P<sup>5+</sup> by V<sup>5+</sup>, less electronegative (Pauling electronegativity values: P<sup>5+</sup>: 2.2 and V<sup>5+</sup>: 1.6) induced drastic changes. The  $J_2$  and  $J_2'$  coupling is much weaker. The oxygen atom that induce the magnetic paths play differently, changing the geometry so the couplings. There are the Next Nearest Neighbors exchanges along the ladder legs. The lowering of  $J_2$  removes the frustration in the leg and with the neighbors.  $J_3$  is that time significantly increased with a ferromagnetic behavior so that the chains see each other and are able to order around 40K, the value at which M(H) show a ferromagnetic component.

### II.1.5. Conclusion

In this part the HP-HT polymorphs of all members of the  $\text{BiCu}_2\text{P}_{1-x}\text{V}_x\text{O}_6$  solid solution were synthesized after the rationalized investigation of HP-HT diagrams. Although HP- $\text{BiCu}_2\text{PO}_6$  was obtained as a pure phase, it is impossible concerning all other members in from of the high stability of  $\text{BiVO}_4$  and  $\text{Bi}_4\text{Cu}_3\text{V}_2\text{O}_{14}$ , two impurities observed in different amounts depending on the rate of vanadium and the pressure and temperature. The magnetic properties were nevertheless investigated without impact of the impurities. The results show that the spin gap behavior observed for the full phosphorous sample is immediately lost as soon as a small amount of vanadium is introduced in the crystal structure. In the middle of the solid solution, the samples are paramagnetic whereas they show a complex behavior for rich amount of vanadium. As already discussed for  $\text{BiCu}_2\text{PO}_6$ , the reversibility of HP- $\text{BiCu}_2\text{VO}_6$  is proved and the AP-phase is appeared after heating at  $700^\circ\text{C}$ .

Another system including  $\text{BiMPO}_5$  structures, is promising concerning the properties and, as a consequence, was used for further studies detailed in the next part.

## II.2. Investigation of the HP- BiNiPO<sub>5</sub> polymorph

### II.2.1. State of the Art

#### *a. On the interest in BiMXO<sub>5</sub> compounds*

The crystal structures belong to the BiMXO<sub>5</sub> family show 1D oxo-centered [O<sub>2</sub>Bi<sub>2</sub>M<sub>2</sub>]<sup>6+</sup> chains built on (OBi<sub>2</sub>M<sub>2</sub>) tetrahedra sharing edges with M<sup>2+</sup> cations sitting mainly in *trans* position. Only BiCaVO<sub>5</sub> [8] and BiCdVO<sub>5</sub> have Ca<sup>2+</sup> and Cd<sup>2+</sup> in *cis* position. [12] Around them, the [XO<sub>4</sub>] groups are independent.

Depending on the size of the [XO<sub>4</sub>] entities ([PO<sub>4</sub>] < [AsO<sub>4</sub>] < [VO<sub>4</sub>]), the symmetry of the unit cell varies. In general, due to steric effects, the system is usually monoclinic (S.G. P2<sub>1</sub>/n) (except for BiCaVO<sub>5</sub> that is orthorhombic (S.G. Pbc<sub>a</sub>)) and becomes triclinic (S.G. P-1) in case of bigger cations (Pb<sup>2+</sup> or As<sup>5+</sup> for example). The unit cell parameters of a list of BiMXO<sub>5</sub> phases are given in Table 7. It is accompanied by references and studied properties. Current research is dedicated to investigation of BiNiPO<sub>5</sub> compound.

**Table 7. Crystalline characteristics of BiMXO<sub>5</sub> phases**

Compound	Space Group	a (Å), α (°)	b (Å), β (°)	c (Å), γ (°)	Z	Ref.	Studied properties
BiCaVO <sub>5</sub>	<i>Pbca</i>	11.2022(25) 90	5.4283(15) 90	15.5605(19) 90	8	[8], [9]	dielectric and optical properties
BiMgVO <sub>5</sub>	<i>P2<sub>1</sub>/n</i>	7.542(6) 90	11.615(5) 107.38(5)	5.305(3) 90	4	[10]	optical properties
BiCdVO <sub>5</sub>	<i>Pc2<sub>1</sub>n</i>	5.505(2) 90	11.699(4) 90	14.276(4) 90	8	[12]	optical properties
α-BiPbVO <sub>5</sub>	<i>P-1</i>	5.6088(3) 108.957(2)	7.1109(3) 111.889(2)	7.2978(3) 94.833(2)	2	[11]	thermal behavior
β-BiPbVO <sub>5</sub>	<i>C2/m</i>	13.61(1) 90	5.64(1) 113.75(1)	7.18(1) 90	4	[11]	thermal behavior
BiMnVO <sub>5</sub>	<i>P-1</i>	6.912(4) 108.55(2)	6.991(2) 95.98(4)	5.354(1) 109.73(4)	2	[13], [14]	magnetic properties
BiNiAsO <sub>5</sub>	<i>P-1</i>	6.7127(8) 107.625(2)	6.8293(8) 95.409(2)	5.2345(6) 111.158(2)	2	[16]	
BiCoAsO <sub>5</sub>	<i>P-1</i>	5.2380(3) 111.631(2)	6.8286(4) 108.376(2)	7.6150(4) 108.388(2)	2	[17]	high- temperature behavior and magnetic properties
BiMnAsO <sub>5</sub>	<i>P-1</i>	6.868(1) 109.47(2)	6.905(2) 95.91(2)	5.360(1) 109.32(2)	2	[13]	
BiPbPO <sub>5</sub>	<i>P-1</i>	7.1082(5) 111.788(5)	7.2802(6) 95.207(5)	5.6203(4) 108.717(5)	2	[15]	
BiNiPO <sub>5</sub>	<i>P2<sub>1</sub>/n</i>	7.1664(8) 90	11.206(1) 107.28(1)	5.1732(6) 90	4	[18], [26] [21], [19]	magnetic properties, lone pair localisation and infrared characterisation.
BiCoPO <sub>5</sub>	<i>P2<sub>1</sub>/n</i>	7.2470(1) 90	11.2851(2) 107.843(1)	5.2260(1) 90	4	[20], [26] [19]	
BiMnPO <sub>5</sub>	<i>P2<sub>1</sub>/n</i>	7.4339(3) 90	11.356(4) 109.19(2)	5.3577(2) 90	4	[21]	

## II.2.2. Ambient-pressure BiNiPO<sub>5</sub> phase (AP-BNPO)

The ambient-pressure BiNiPO<sub>5</sub> phase (AP-BNPO) crystallizes in the P2<sub>1</sub>/n space group. Its crystal structure is built on infinite, [O<sub>2</sub>Bi<sub>2</sub>Ni<sub>2</sub>]<sup>6+</sup> oxo-centered chains surrounded by isolated phosphates (Figure 37(a)). The [O<sub>2</sub>Bi<sub>2</sub>Ni<sub>2</sub>]<sup>6+</sup> oxo-centered chain is shown in another projection on Figure 37(b). The one-dimensional oxo-centered chains have Ni and Bi in *trans* configurations.

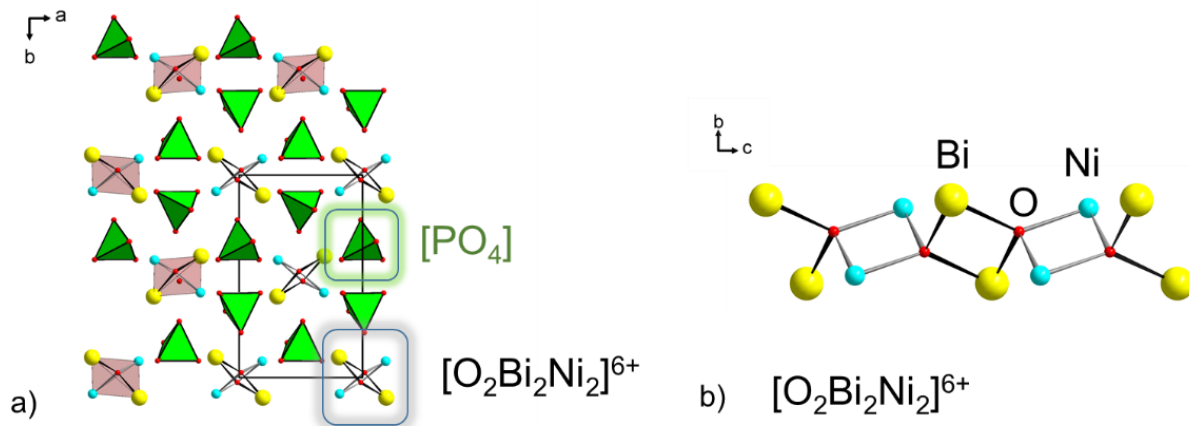


Figure 37. General projection of crystal structure of AP-BiNiPO<sub>5</sub> along the c-axis (a). The infinite [O<sub>2</sub>Bi<sub>2</sub>Ni<sub>2</sub>]<sup>6+</sup> oxo-centered chain along a-axis (b).

Ambient-pressure BiNiPO<sub>5</sub> phase (AP-BNPO) is also known for its amazing magnetic behavior. The magnetic structure, refined from neutron data, highlights ferromagnetic interactions inside the Ni<sub>2</sub>O<sub>10</sub> dimers that are antiferromagnetically coupled together. Most of the interactions arise from Ni–O–O–Ni SSE (super–super-exchange) pathways. [22] Ni cations share an O–O edge leading to dominant ferromagnetic Ni–O–Ni superexchanges (Ni–O–Ni = 99.9°) well predicted by Kanamori-Goodenough rules. [23]

The HP-HT synthesis route was used to isolate a HP polymorph of BNPO and investigate the consequences on the magnetic couplings.

## II.2.3. The new HP-polymorph

### a. Synthesis of the raw BiNiPO<sub>5</sub>

The synthesis procedure of the AP compound totally corresponds to the description given in ref [21]. Polycrystalline samples of BiNiPO<sub>5</sub> have been prepared by a standard solid-state reaction method. Stoichiometric amounts of Bi<sub>2</sub>O<sub>3</sub> (previously decarbonated at 600°C during 12 hours),

NiO and  $(\text{NH}_4)_2\text{HPO}_4$  were seriously mixed in agate mortar and heated in alumina crucible up to  $950^\circ\text{C}$ . The resulted powder was checked by X-ray diffraction to confirm the purity of the sample.

***b. HP-HT synthesis***

The Belt-type apparatus of the Neel Institute was used to provide HP-HT experiment at 5GPa and  $600^\circ\text{C}$ . Polycrystalline sample of AP- compound was well grinded in agate mortar and loaded in  $5 \times 2 \text{ mm}^2$  platinum capsule.

After removing the capsule from the press, it was carefully removed from surrounding material to avoid sample contamination. Subsequent opening of the capsule revealed that the sample is a dense homogeneous grey mass. The recovered sample was well grained in agate mortar. The photo of yellow powder of AP-  $\text{BiNiPO}_5$  [18] compound is given on Figure 38(a), whereas Figure (b) demonstrates light-grey color of resulted sample after HP-HT experiment.

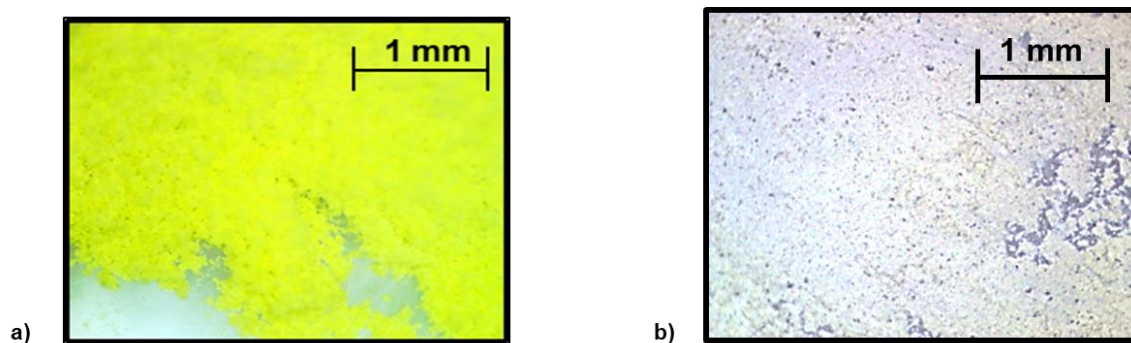


**Figure 38. Photos of sample of AP-BNPO (a) and recovered after HP-HT experiment (b).**

X-Ray diffraction experiment was provided at room temperature to obtain high-quality powder diffraction data in the range of  $2\theta = 5 - 120^\circ$ , with 0.02 step. D8 Advance Bruker AXS diffractometer in Bragg Brentano geometry equipped with a 1D LynxEye detector was used. On this step two powder patterns of initial and modified samples were roughly compared. Both diffraction patterns were normalized for maximum intensities. Selected range of  $2\theta = 10 - 70^\circ$  is shown on Figure 39 to demonstrate the difference of powder diffraction powders between AP-  $\text{BiNiPO}_5$  [18] compound (a) and modified sample. According to PDF database, pattern (b) well corresponds to  $\text{BiNiAsO}_5$  (PDF card № 54-0700) compound.

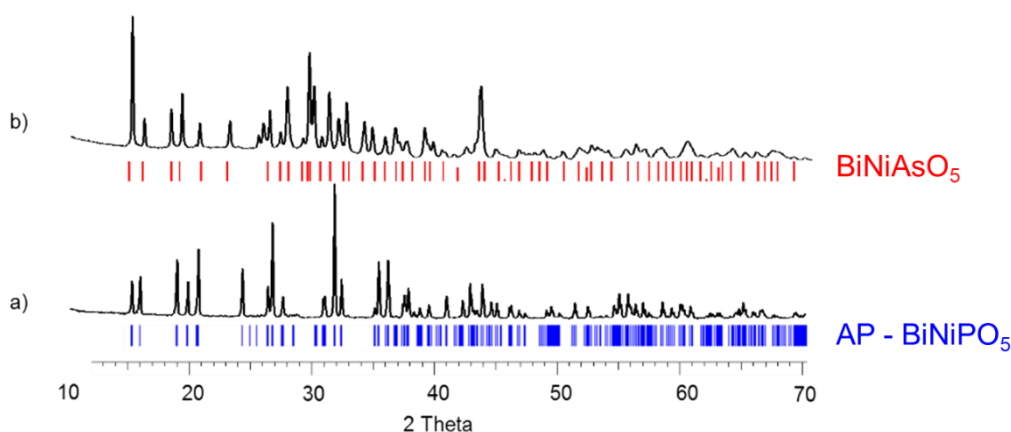


**Figure 39. Comparison of pure powder of AP-  $\text{BiNiPO}_5$  compound (a) and it's HP-HT modification (b).**

The preliminary X-Rays diffraction study reveals total dissimilitude between started AP- $\text{BiNiPO}_5$  and the resulted after HP-HT experiment. Obviously, it transforms into  $\text{BiNiAsO}_5$  – like crystal structure, that is sufficiently different.  $\text{BiNiAsO}_5$  crystallizes in triclinic  $P-1$  space group with unit cell parameters  $a = 6.7127(8)$  (Å),  $b = 6.8293(8)$  (Å),  $c = 5.2345(6)$  (Å),  $\alpha = 107.625(2)^\circ$ ,  $\beta = 95.409(2)^\circ$ ,  $\gamma = 111.158(2)^\circ$ . This model was used for the Rietveld refinement.

### *c. Rietveld refinement of new high pressure $\text{BiNiPO}_5$ phase*

Crystal structure of HP  $\text{BiNiPO}_5$  phase was refined from powder diffraction data. Its XRD pattern is different from the one of the AP-BNPO but is reminiscent of the  $\text{BiNiAsO}_5$  phase. The space group of the HP-HT phase is  $P-1$  as  $\text{BiNiAsO}_5$  (BNAO). [18] The Rietveld refinement was performed starting from the BNAO model. It was indexed in the triclinic unit cell  $a = 7.4209(2)$ ,  $b = 6.5611(2)$ ,  $c = 5.1638(2)$  Å,  $\alpha = 83.814(3)$ ,  $\beta = 110.724(3)$  and  $\gamma = 123.410(2)$ . The isomorphism between HP-BNPO and BNAO structures was validated. The unit cell volume is smaller than the one of the AP phase as expected in case of a HP polymorph ( $V_{\text{AP}} = 396.96 \text{ \AA}^3$  v.s.  $2 * V_{\text{HP}} = 380 \text{ \AA}^3$ ). The Rietveld refinement was finalized using M-O distance restrictions using the more accurate model further optimized by DFT ionic relaxation fixing the experimental lattice parameters.

The Rietveld Refinement performed in Crystallographic Computing System JANA2006 is given on Figure 40. Structure refinement data for new high-pressure modification of  $\text{BiNiPO}_5$  is given in Table 11, atomic parameters – in Table 12, anisotropic atomic displacement

parameters – in Table 13 and selected interatomic distances - in Table 14. List of bond valence sums is given in Table 15.

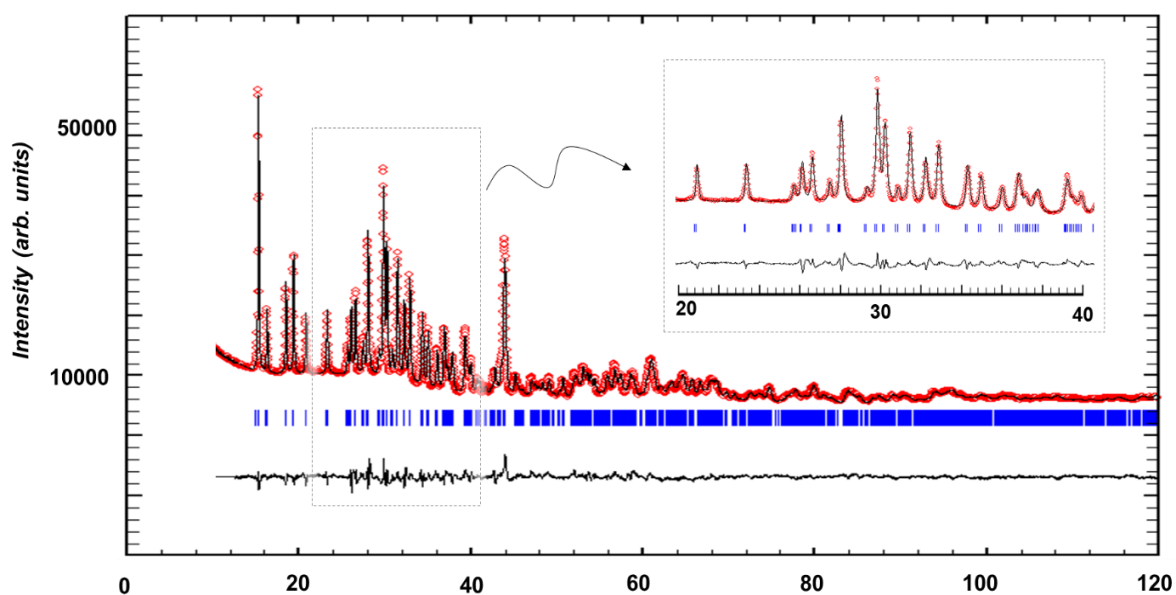


**Figure 40. Rietveld Refinement of high-pressure polymorph of  $\text{BiNiPO}_5$**

The Rietveld refinement performed starting from the crystal structure of BNAO gives satisfactorily reliability factors but the P-O distances and O-P-O angles were slightly out of range. A more accurate model was further optimized using DFT calculations and fixing the experimental unit cell parameters. To get the final refined structure, the Rietveld refinement was repeated with the relaxed structure and leads to final agreement factors  $R_p = 0.0282$ ,  $wR_p = 0.0387$  keeping all oxygen atoms fixed. A pseudo-Voigt function was used for describing the diffraction peak shapes. Asymmetry correction by Howard (Bode's rule) method was applied. 7 terms of Legendre polynomials combined with the manual background. Preference orientation with respect to the axis (1 0 0) according to March & Dollase was applied.

## II.2.4. Crystal structures comparison between HP-BiNiPO<sub>5</sub> and AP- BiNiPO<sub>5</sub>

The crystal structure of new HP-HT polymorph of BiNiPO<sub>5</sub> is shown on Figure 41 (a) with details on the 1D [OBiNi]<sup>3+</sup> oxo-centered *trans*-chains surrounded by isolated phosphates. It demonstrates maintenance of [PO<sub>4</sub>] tetrahedra and oxo-centered chains as basic structural units. These units are reorganized compared to ambient-pressure form. Compared to the AP- sample (b), there are no drastic changes in bond lengths distribution in crystal structure of new high-pressure polymorph. For example, the average O – Ni bond length in AP phase is 2.075(5) Å, whereas in HP– 2.082(8) Å. In the crystal structure, the Bi-Bi distances intra and inter ribbons are surprisingly identical, lowering the effect of oxygen bonding. Thus, typical Bi-Bi distances in the [BiMO]<sup>3+</sup> units are mediated through strong  $\sigma_{\text{Bi-O}}$  bonds ( $d_{\text{Bi-Bi}} \approx 3.43$  Å). This internal distance is usually longer through LP-LP interaction. the analysis of the molecular orbital in the dimers is relevant. It leads to a bonding  $\sigma$  and  $\sigma^*$  antibonding levels, both two electrons occupied. It follows the creation of non-bonding Bi-Bi interactions, well pictured in the electron localization function (ELF) map shown on Figure 41.

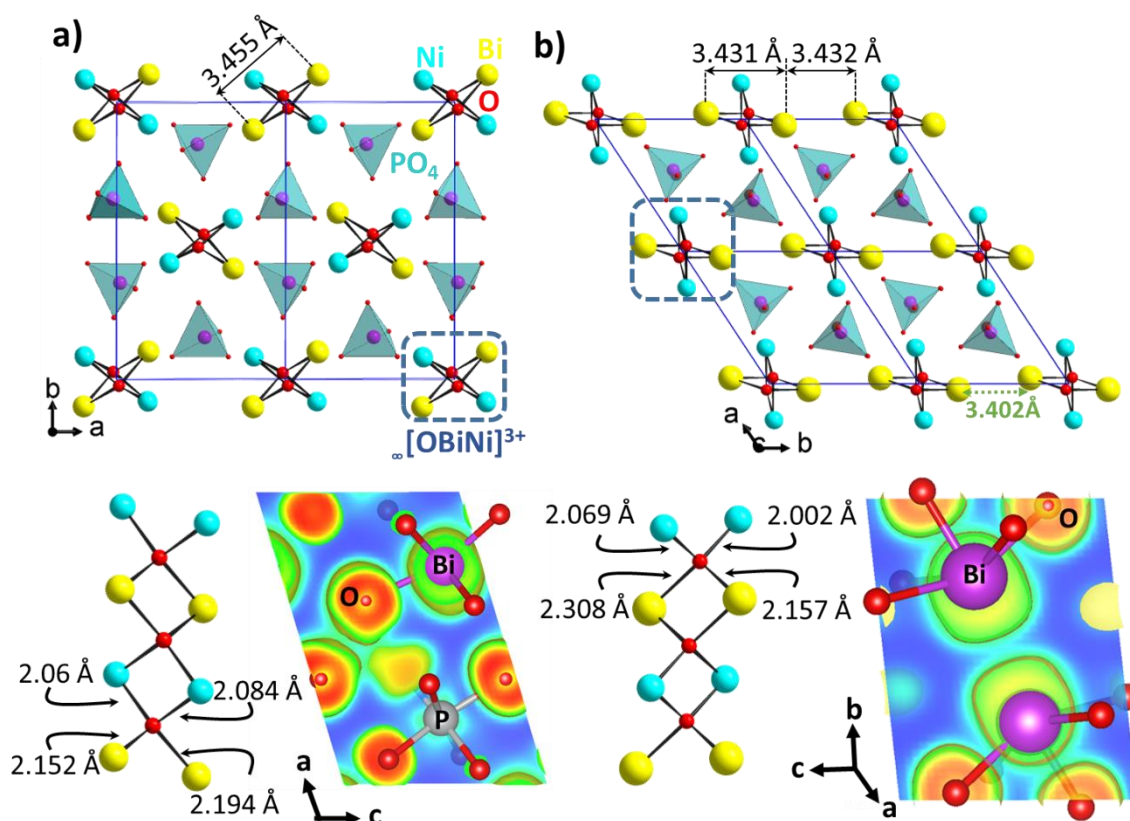


Figure 41. Projection along the c-axis of the (a) AP-BNPO, and (b) HP-BNPO. In both cases, electron localization function (ELF) of bismuth is shown as well as main distances in the ribbons.

### a. Lone Pair activity

The role played by anionic ligands in the structural distortion and shape of lone-pairs was intensively discussed [28] and finds a major origin from the primary antibonding Bi 6s–O 2p interactions, while the Bi 6p orbitals play a secondary role. To better understand the role of the Lone Pair, extended Hückel calculations were performed for single  $\text{BiO}_3(\text{PO}_4)$  and dimeric  $\text{Bi}_2\text{O}_6(\text{PO}_4)_2$  units, chosen in order to take into account direct Bi-O and O-P interactions. [29] This scheme occurs on the HOMO level calculated for monomeric units shown Figure 42.

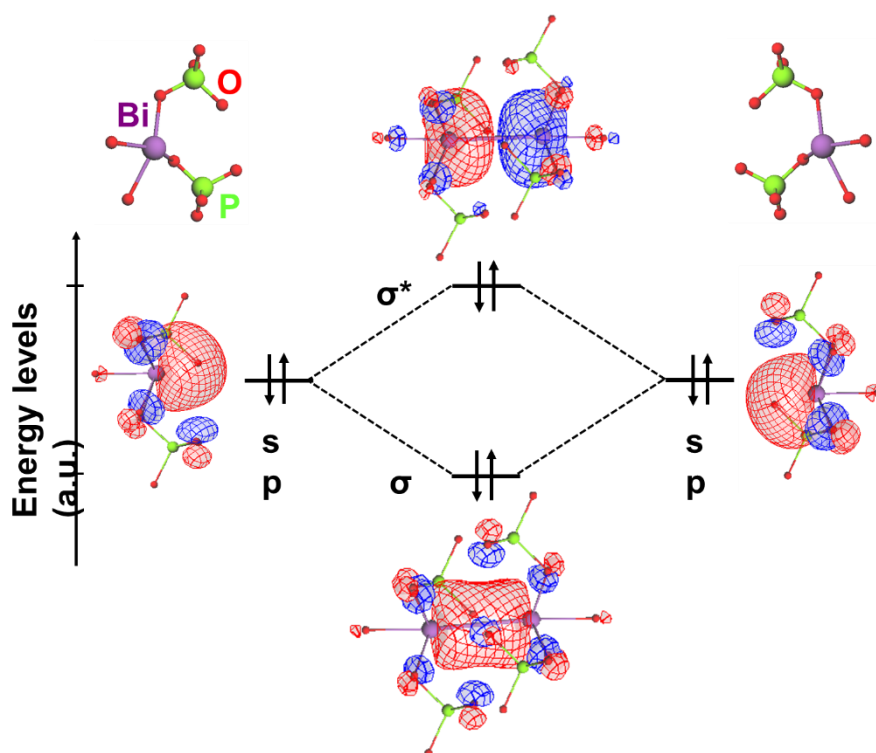


Figure 42. EHTB molecular orbitals for  $\text{BiO}_3(\text{PO}_4)$  and  $\text{Bi}_2\text{O}_6(\text{PO}_4)_2$  with creation of  $\sigma$  and  $\sigma^*$  levels.

In the case of the AP phase, the electronic anisotropy around  $\text{Bi}^{3+}$  is less pronounced. We performed density functional theory (DFT) band structure calculations using the full-potential local-orbital scheme (FPLO9.00-33). [30] The local density approximation was applied (LDA + U,  $U = 7$  eV) with the exchange-correlation potential by Perdew and Wang. [31] The Vienna *ab initio* simulation package (VASP) was used [32] with the basis set of projected augmented waves. [33] The typical k mesh included 4631 (AP,  $P2_1/n$ ) and 1124 (HP,  $P-1$ ) points in the symmetry-irreducible part of the first Brillouin zone for the crystallographic unit cell using the spin polarized ferromagnetic configuration. The main features of the LDA+U density of states

(DOS) are typical for bismuth transition metal phosphates [34] and conserve the same topology for both the AP and HP-polymorphs.

The top of the broad valence band (VB) are a mixture of Ni, Bi and O states with small contribution of the P states. These bands lie between  $\sim -7$  eV and  $E_F$  and account essentially for the bonding within the 1D-chains and with their surrounding oxygen ligands. Only the lowest part of VB shows an appreciable contribution of  $P_{3p}$  orbitals within the strongly covalent P-O bonds. The magnetic Ni 3d orbitals lie between -2eV and unoccupied Ni d states, O2p and Bi6p and 6s states form the bottom of the conduction band (CB). The compounds presented have very similar bandgap calculated dictated by the similar  $[O\text{BiNi}]^{3+}$  trans-chains. The strongest Bi---Bi interaction and lone pair activity is pictured by the sharp Bi *s* and *p* states contribution at  $E_F$  in the HP-form, see the insets on Figure 43 (a) and (b).

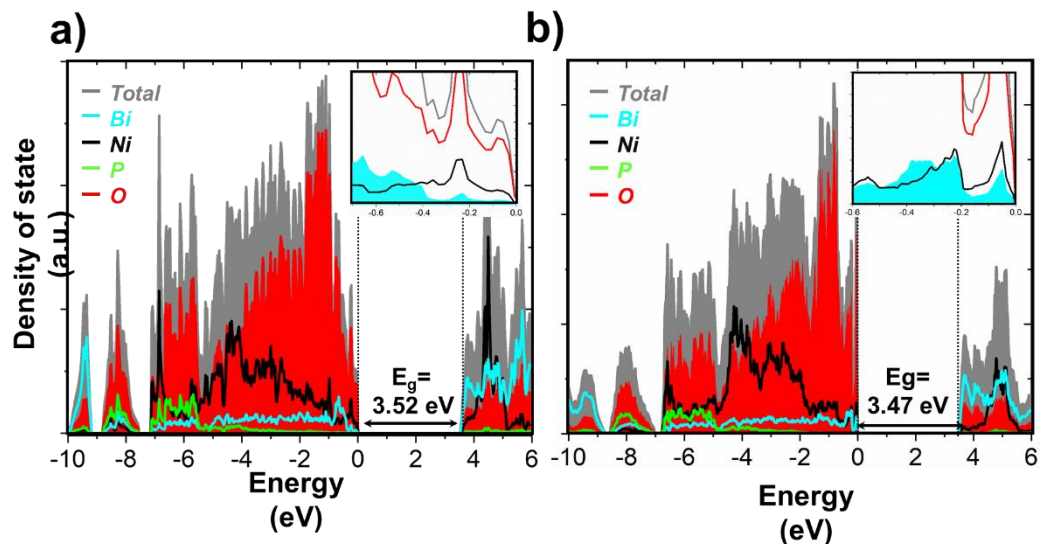


Figure 43. Total and atomic resolved projected DOS calculated for a) the AP-BNPO and b) the HP-BNPO. The Fermi level is set to 0.

### *b. High-temperature X-ray Diffraction*

In order to investigate HT behavior, HTXRD experiments were provided on both HP and AP- $\text{BiNiPO}_5$  phases. The X-ray diffraction characterization of the sample was done using a Rigaku SMARTLAB multipurpose diffractometer (9 kW rotating anode) in Bragg–Brentano reflection beam mode (with a PSD 1D detector DTEX) delivering  $\text{CuK}\alpha$  radiation ( $\lambda = 1.5418 \text{ \AA}$ ). High-temperature XRD measurements were done on an Anton Paar DHS1100 hot plate stage between room temperature and  $950^\circ\text{C}$ , heating rate  $5^\circ\text{C}/\text{min}$ . Omega-2theta scans were performed

between  $10^\circ$  and  $90^\circ$  with a scan speed of  $10^\circ/\text{min}$ . The experiments were provided with a step of  $25\text{-}50^\circ\text{C}$ .

- HTXRD of ambient-pressure  $\text{BiNiPO}_5$  phase

The evolution of powder diffraction patterns with increasing of temperature is shown on Figure 44 for AP-  $\text{BiNiPO}_5$  phase. On this 2D picture the stability of AP phase under the influence of temperature is shown. In order to prove this, the initial (at room temperature) and the final (at  $850^\circ\text{C}$ ) powder diffraction patterns are shown in a selected  $15^\circ$  to  $21^\circ$   $2\theta$  range in 1D view. The (hkl) indexes of Bragg peaks are given in italics.

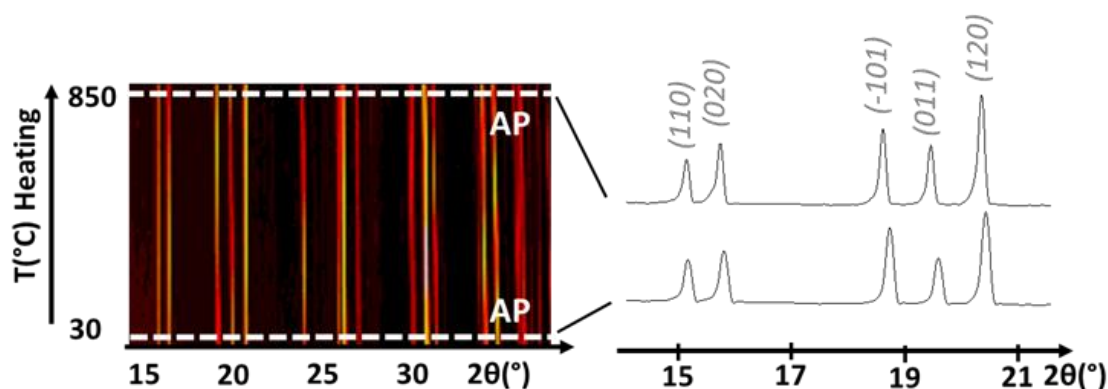
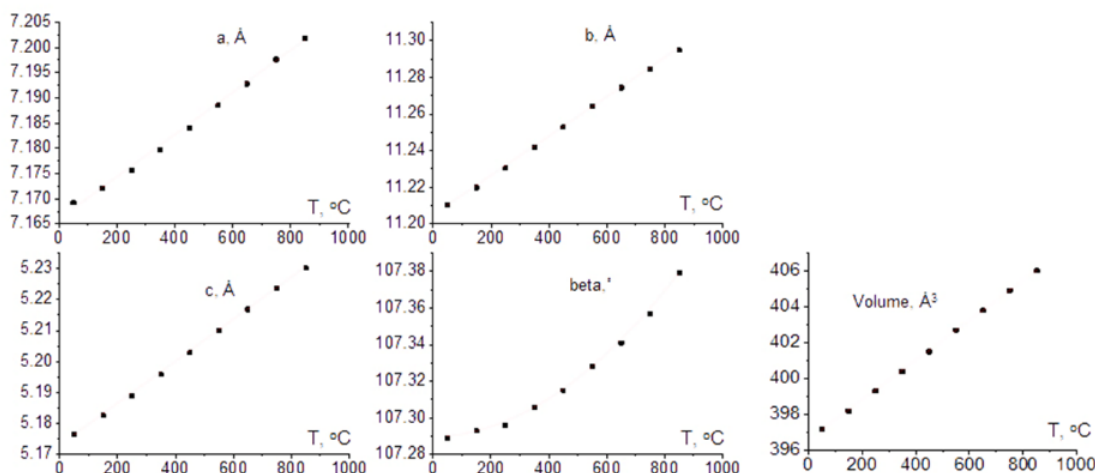


Figure 44. The evolution of powder diffraction patterns for ambient-pressure  $\text{BiNiPO}_5$  phase.

LeBail Pattern matching was used to determine unit cell parameters from room temperature to  $850^\circ\text{C}$  with a  $100^\circ\text{C}$  step. The evolution of unit cell parameters is shown on graphics on Figure 45 Changing parameters occurs uniformly without shocks and deflections. This indicates the absence of any phase transitions.



**Figure 45. The evolution of unit cell parameters of ambient-pressure BiNiPO<sub>5</sub> phase.**

- HTXRD of high-pressure BiNiPO<sub>5</sub> phase.

The evolution of powder diffraction patterns of HP-HT BiNiPO<sub>5</sub> phase is shown on Figure 46 in 2D mode. During heating, the peaks of AP- BiNiPO<sub>5</sub> started to appear abruptly at around 700°C. This transformation is shown in highlighted by dotted lines area. Selected 15° to 21° 2θ range is given in 1D view to show the evidence of transformation from HP to AP phase. The HP-form starts to transform back into the AP-form above ~700°C in air, but remains significant up to 950°C. This transformation can be described as a first order transition. The black powder pattern on Figure 46 corresponds to HP phase at room temperature, where peaks are indexed in bold. Red color powder pattern corresponds to powder pattern obtained at 950°C that characterizes the transition zone, where HP and AP phases coexist. As in the previous powder pattern, peaks corresponding to HP are indexed in **bold**, whereas AP are given in *italics*.

For technical reasons, it is not possible to reach higher temperatures in this experiment and determine the temperature of complete transformation. The effect of a constant temperature impact is shown on upper blue figure, that corresponds to powder pattern of sample heated at 950°C for 2 hours. The reduction of peaks of HP phase can be clearly observed. Undoubtedly, the complete transition from one phase to another occurs at slightly higher temperature or longer time of heating.

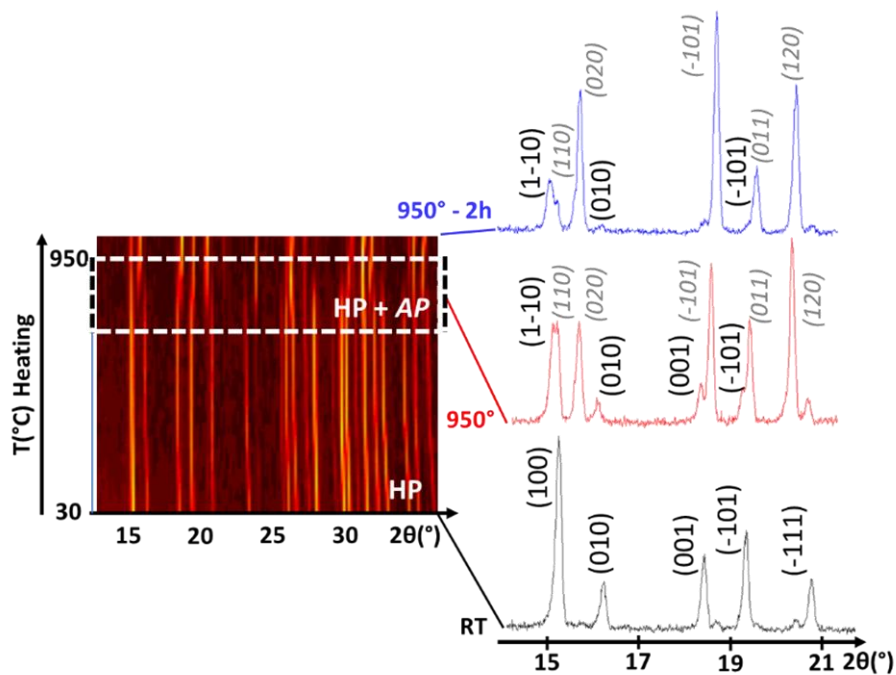


Figure 46. The evolution of powder diffraction patterns for triclinic high-pressure  $\text{BiNiPO}_5$  phase.

Determination of unit cell parameters was provided with a  $100^\circ\text{C}$  step from ambient temperature to  $800^\circ\text{C}$  using LeBail Pattern matching in Jana2006 software. The evolution of unit cell parameters of HP-  $\text{BiNiPO}_5$  phase is shown on Figure 47. As in the case with heating of ambient-pressure  $\text{BiNiPO}_5$  phase, the unit cell parameters change smoothly and gradually. We can observe a general trend of values increasing along a, b and c axes, with the  $\alpha$  angle reiterating the tendency. At the same time  $\beta$  and  $\gamma$  angles demonstrate a decreasing of values.

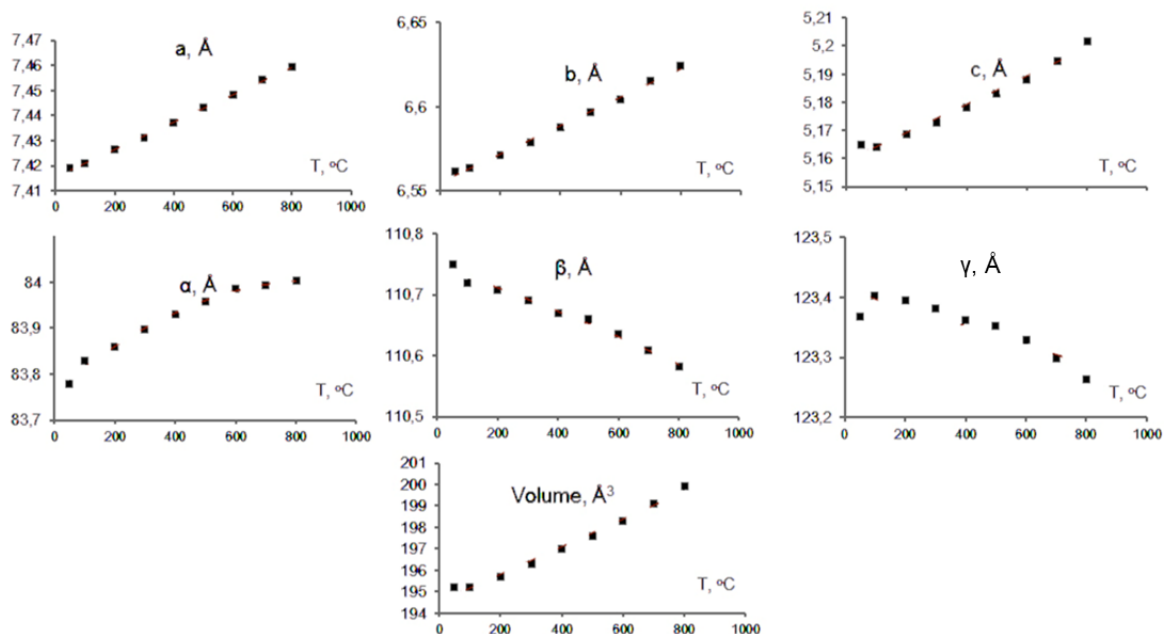


Figure 47. The evolution of unit cell lattice parameters for triclinic high -pressure  $\text{BiNiPO}_5$  phase.

For the last 950°C diffraction pattern, the estimated amount of each phases were calculated by Rietveld refinement. The relative amount in mass of the main ambient-pressure  $\text{BiNiPO}_5$  phase is about 85%, the rest corresponds to the high-pressure modification. Plotting the refined volume per formula unit as a function of temperature (Figure 48) gives two distinct thermal expansion coefficients of  $3.6 \cdot 10^{-5}$  and  $2.9 \cdot 10^{-5} \text{ } ^\circ\text{C}^{-1}$  respectively. However, the  $V(T)$  plot of the HP form shows an inflexion around 700°C, temperature at which the sample demixed into two phases of similar volume corresponding respectively to the AP and HP phases.

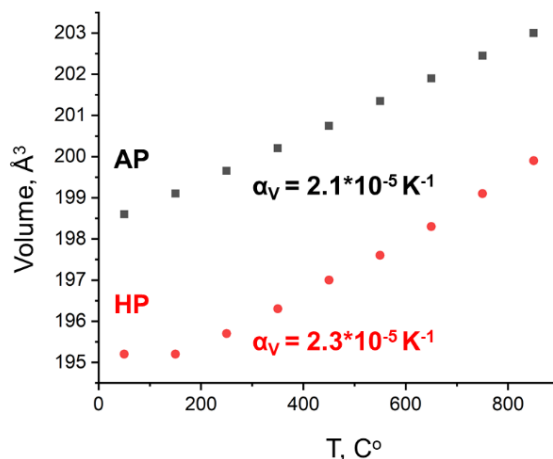


Figure 48. Plot of the volume per formula unit depending on temperature for the two forms.

### c. AP- and HP BiNiPO<sub>5</sub> magnetic properties

Magnetic measurements were performed on a Physical Properties Measurement System (PPMS) Dynacool (9T) system from Quantum Design. Zero field cooling (ZFC) and field cooling (FC) procedures between  $2 < T < 300$  K were measured.

The magnetic properties of AP-BiNiPO<sub>5</sub> were largely studied in [22, 27]. From the magnetic point of view, the cation-centered type of crystal structure description is more useful. An easy observation of that was described in case of BiCuPO<sub>6</sub> compound, where Cu<sup>2+</sup> ( $S = 1/2$ ) ladders is formed between two adjacent [BiCu<sub>2</sub>O<sub>2</sub>]<sup>3+</sup> polycations,  $n = 2$  tetrahedra wide. [40]

In AP-BiNiPO<sub>5</sub> it evidenced nearly collinear magnetic structure built on Ni<sub>2</sub>O<sub>6</sub> dimers with ferromagnetic coupling inside and antiferromagnetic coupling between dimers. Same Ni<sub>2</sub>O<sub>6</sub> dimers can be observed in crystal structure of new HP- BiNiPO<sub>5</sub> polymorph. A comparison of the Ni<sub>2</sub>O<sub>6</sub> dimers orientation between two structures is shown on Figure 49. Where the AP-phase is on (a) figure and HP- one – on (b). On this figure the number of neighbor dimers of central Ni<sub>2</sub>O<sub>10</sub> dimer (in green) are shown. For AP phase the number of neighbor dimers is 14, whereas there are 12 of them in case of HP BiNiPO<sub>5</sub>.

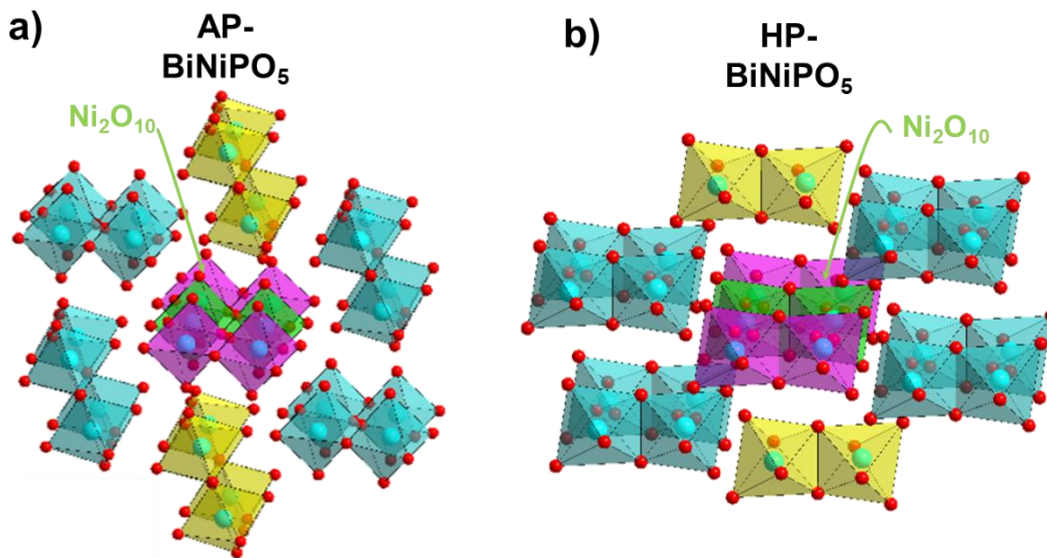


**Figure 49.** Respective number of dimers neighbor of Ni<sub>2</sub>O<sub>10</sub> dimer at the center of the figure (in green) for (a) AP (14), and (b) HP (12) BiNiPO<sub>5</sub>.

The negative value of  $\theta_{CW}$  is coherent with strong AFM couplings. Even if approximate, the AF interactions were quantified using  $\theta_{CW} = \sum_i z_i S(S+1) J_i/3K_b$ , considering that  $S= 2$  for  $Ni_2O_6$  dimers and  $Z$  corresponding to the number of neighbors. Looking carefully at the crystal structure, each dimer is surrounded by 12 other ones. Although they were 14 in case of AP-BiNiPO<sub>5</sub>. This lead to  $J_i/3K_b = -1$  K coherent with weak “average” AFM coupling between dimers through a process occurring probably occurring through Super-Super Exchanges Ni-O-(P)-O-Ni as it was already the case for the AP phase (with  $J_i/3K_b = -0.5$  K).

The role of  $Ni_2O_6$  dimers of the chains which are internally ferromagnetic coupled, while antiferromagnetic super-super exchanges inter-dimer couplings order the spins below  $T_N = 17.5$  K. The magnetic susceptibility plot and inverse susceptibility as a function of temperature are shown on Figure 50, where measurements for AP-BiNiPO<sub>5</sub> are given in black and white colors (a) figure, [22] and for HP-BiNiPO<sub>5</sub> – on (b). It shows a paramagnetic regime above  $T_N = 16.7$  K, characterized by a Curie Weiss law  $\chi = C/(T-\theta_{CW})$  with  $\theta_{CW} = -28.0$  K and  $\mu_{eff} = 3.29 \mu_B/Ni^{2+}$  which denotes a significant but rather common orbital contribution. Here again from Goodenough Kanamori rules the exchanges inside the dimers are expected FM. The mean field approach allows estimation of the mean inter-chain exchanges, using  $\theta_{CW} = \sum_i z_i S(S+1) J_i/3K_b$ , where  $S= 2$  for FM  $Ni_2O_6$  dimers and  $Z = 12$  is the number of connected neighbors by SSEs. It leads to  $J_{inter}/K_b = -1.16$  K. Compared to AP-BNPO ( $\theta_{CW} = -11.5$  K,  $Z=14$ ) the  $J_{inter}/K_b$  value of  $-0.41K$  is well scaled by Ni-Ni interatomic distances in the compact HP-BNPO (4.7 to 5.6 Å along the SSE paths against 5.2 to 5.7 Å for AP-BNPO). Comparison of main magnetic factors for BiNiPO<sub>5</sub> AP and HP are given in Table 8.

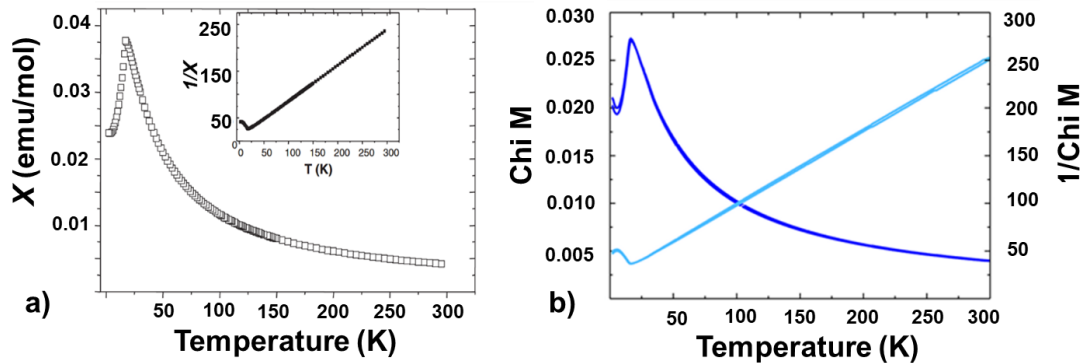


Figure 50. Plot of magnetic susceptibility versus T for AP-BiNiPO<sub>5</sub> (a). Magnetic susceptibility (dark blue) and inverse susceptibility (light blue) of HP-BiNiPO<sub>5</sub> as a function of temperature (b).

**Table 8. Comparison of main magnetic factors for BiNiPO<sub>5</sub> AP and HP.**

BiNiPO <sub>5</sub>	S	$\mu_{\text{eff}}$ ( $\mu\text{B}$ )	$\theta_{\text{CW}}$ (K)	Num. of neighbors	$\text{J}/\text{K}_{\text{bav}}$ (K)	$T_{\text{N}}$
AP	1	3.22	-11.5	14	-0.51	17.5
HP	1	3.29	-28	12	-1	16.3

### II.2.5. Conclusion

Similarly with HP-BCPO, [11] HP-BNPO adopt the AP-form of the arsenate BNAO. The substitution of phosphates by arsenates in the AP-forms induced a chemical pressure at the origin of the reorganization of the polycationic units. In the process of stabilization of the HP-BNPO, the physical pressure applied during the synthesis acts in a similar way. This opens a wide range of possibilities in the prediction and stabilization of new materials, not only in the field of bismuth oxyphosphate but in many other chemical systems.

Another possibility of investigation is to work in a medium range of pressure, using autoclaves and liquid media. This was done in the last part of this chapter.

## II.3. Oxo-centered architectures obtained by Supercritical Steam

Recently,  $\text{Bi}_3(\text{PO}_4)\text{O}_3$  [63] announced as “*the simplest bismuth(III) oxophosphate never synthesized*” was prepared under supercritical hydrothermal pressure, around 50 MPa at 700K. Being aware of the size effects of  $[\text{PO}_4]$  for  $[\text{AsO}_4]$  or  $[\text{VO}_4]$  substitution, mainly combining steric effect in tetrahedral voids, the replacement of phosphate by bigger tetrahedral groups may give rise to innovative architectures and properties. In  $\text{Bi}_6\text{ZnO}_7(\text{XO}_4)_2$  ( $\text{X} = \text{P}, \text{As}$ ) [64] the modification induced by P/As substitution kills the inversion symmetry (centrosymmetric/CS- $\text{PO}_4$ : CS vs. NCS- $\text{AsO}_4$ ) which is of great interest for nonlinear optical applications. Combining the HP-water method and chemical substitution is the leitmotif of this chapter.

### II.3.1. Synthesis

A series of hydrothermal experiments was provided on Bi-based oxo-centered compounds with various components. Several initial compositions were tried before the first results were obtained. It was proposed to use potassium as a mineralizer because it was mentioned in related publication. [65] Starting materials were prepared from  $(\text{BiO})_2\text{CO}_3$ ,  $\text{NaVO}_3$  and  $\text{K}_2\text{CO}_3$  with stoichiometric ratio of 3:1:1 respectively for first experiment. At the same time  $(\text{BiO})_2\text{CO}_3$  and  $\text{KH}_2\text{AsO}_4$  precursors were taken with a 3:1 ratio for second experiment.

1 mg of the reactant mixture was sealed in a gold capsule that was half-filled of water. A gold capsule was placed under counter supercritical water pressure during 3 days in a Novaswiss autoclave. First experiment provided at  $450^\circ\text{C}$  -150 bars, whereas  $700^\circ\text{C}$  - 200 bars were reached during the experiment on arsenate-containing mixture. The furnace was then cut off and the autoclave left open at room temperature (RT) after cooling. The products were extracted from the tubes and washed several times with distilled water, filtered and finally dried at RT. Samples contain colorless polycrystalline material and needle-shaped single crystals corresponding to the novel phases (Figure 51).

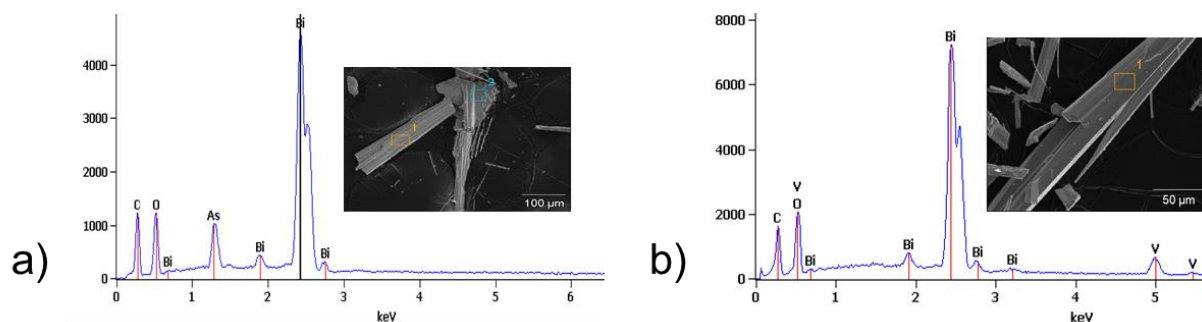


**Figure 51.** The crystal shape and chemical analysis of the crystals from : (a)  $(\text{BiO})_2\text{CO}_3$ ,  $\text{NaVO}_3$  and  $\text{K}_2\text{CO}_3$  and (b)  $(\text{BiO})_2\text{CO}_3$  and  $\text{KH}_2\text{AsO}_4$  chemical systems.

An EDX study confirmed the presence of Bi and V for the crystals from  $(\text{BiO})_2\text{CO}_3$ ,  $\text{NaVO}_3$  and  $\text{K}_2\text{CO}_3$  chemical system. In second chemical system, the presence of Bi and As were confirmed.

### II.3.2. Crystal structures of the new compounds obtained by Supercritical Steam

Suitable crystals from both samples were selected and isolated for XRD-crystal structure determination. Crystal structure of **(1)** was refined in  $P-1$  space group with unit cell parameters  $a= 5.682(1)\text{\AA}$ ,  $b= 8.479(2)\text{\AA}$ ,  $c= 14.243(3)\text{\AA}$ ,  $\alpha= 81.39(1)^\circ$ ,  $\beta= 86.91(1)^\circ$  and  $\gamma= 88.53(1)^\circ$  ( $R_{\text{obs}}= 0.045$ ,  $R_{\text{all}}= 0.051$ ,  $\text{GOF}= 2.38$ ). **(2)** was refined in  $P2_1/n$  space group with unit-cell parameters  $a= 11.7264(14)\text{\AA}$ ,  $b= 5.4063(7)\text{\AA}$ ,  $c= 24.213(3)\text{\AA}$ ,  $\beta= 98.66(1)^\circ$  ( $R_{\text{obs}}= 0.039$ ,  $R_{\text{all}}= 0.088$ ,  $\text{GOF}= 1.09$ ). The experimental data collection and refinement results are listed in Table 16.

These new compounds are new pertinent examples of well- adapted antiphase description. [69] Oxo-centered  $[\text{OBi}_4]$  tetrahedra are associated to  $[\text{OBi}_3]$  triangles and/or  $[\text{OBi}_5]$  units leading to polycationic bi-dimensional (2D) units.

#### *a. The new $\text{Bi}_3(\text{VO}_4)\text{O}_3$*

In the  $\text{Bi}_3(\text{VO}_4)\text{O}_3$  there are six independent oxygen are involved in  $[\text{OBi}_4]$  tetrahedra ( $Td$ ), namely O1, O2, O3, O5, O6 and O9. As in the homologous systems, the  $[\text{OBi}_4]$  tetrahedra are strongly distorted with Bi-O distances varying from  $2.128(11)\text{\AA}$  for Bi1-O1 to  $2.733(11)\text{\AA}$  for Bi5-O6. They share edges to build a 4- $Td$ -wide ribbon, decorated on both side by  $[\text{OBi}_5]$  square pyramids ( $SP$ ) centered on O5, sharing their square-face with the ribbons. Figure 52 (a) demonstrates the 4- $Td$ -wide ribbons along the  $a$  axis. The corrugated layers are built on association of anion-centered groups:  $[\text{OBi}_4]$  (in yellow) forming the 4-tetrahedra wide ribbons, decorated on both side by the  $[\text{OBi}_5]$  square-based pyramids (in grey), connected to others ribbons by  $[\text{OBi}_3]$  triangles (in green). These polycationic ribbons are connected together through two edge connected  $[\text{OBi}_3]$  triangles ( $Tr$ ) centered on O3, forming  $[\text{Bi}_3\text{O}_3]^{3+}$  corrugated layers parallel to (010) (Figure 52(b)).

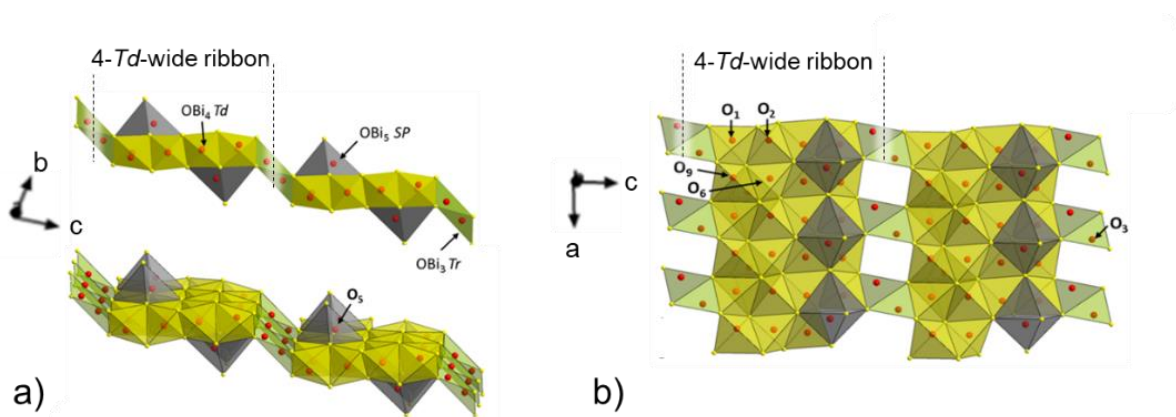


Figure 52. Projection of (a) 4-*Td*-wide ribbons along the *a* axis; corrugated layers (b) along the *b* axis.

These layers sandwiches slabs of isolated  $[\text{VO}_4]$  tetrahedra (Figure 53(a)), according to the refined formula of  $\text{Bi}_3(\text{VO}_4)\text{O}_3$ . It involves very complex oxo-centered layers compared to the  $[\text{BiO}]^+$  fluorite ones. Due to the steric effect of  $[\text{VO}_4]$  groups, this new phase is different from the referenced  $\text{Bi}_3(\text{PO}_4)\text{O}_3$  (Figure 53(b)). In this  $\text{Bi}_3(\text{PO}_4)\text{O}_3$  compound the structure shows also corrugated layers but built on double-*Td*-wide ribbons connected through association of two  $[\text{OBi}_3] \text{Tr}$ .

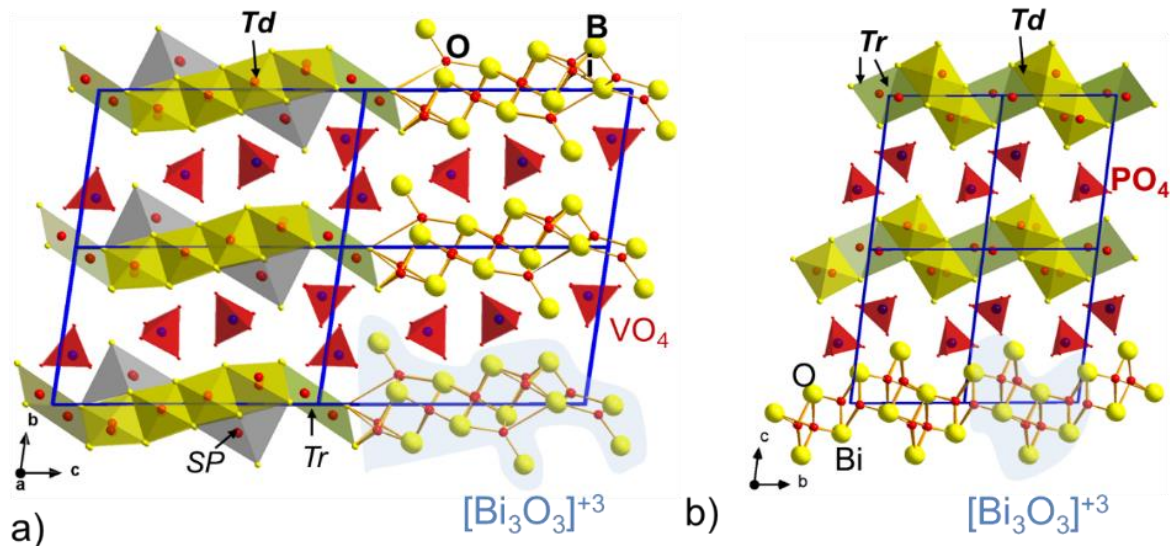


Figure 53. Projection of a)  $\text{Bi}_3(\text{VO}_4)\text{O}_3$  (1) and b)  $\text{Bi}_3(\text{PO}_4)\text{O}_3$  along the *a* axis. The anion-centered units are drawn in yellow for  $\text{OBi}_4 \text{ Td}$ , green for  $\text{OBi}_3 \text{ Tr}$  and grey for  $\text{OBi}_5 \text{ SP}$ . The  $\text{XO}_4$  tetrahedra ( $\text{X} = \text{P}$  and  $\text{V}$ ) are shown in red.

In order to determine the phase composition of samples obtained by Supercritical Steam, the resulted precipitations were removed by filtration from the solution. The precipitate was washed several times with distilled water. Room temperature X-Rays powder diffraction is shown on Figure 54 revealed the presence of major  $\text{Bi}_3(\text{VO}_4)\text{O}_3$  compound, assorted with  $\text{Bi}_2\text{O}_3$  [85] and  $\text{Bi}_{14}\text{V}_4\text{O}_{30}$  [86] impurities.

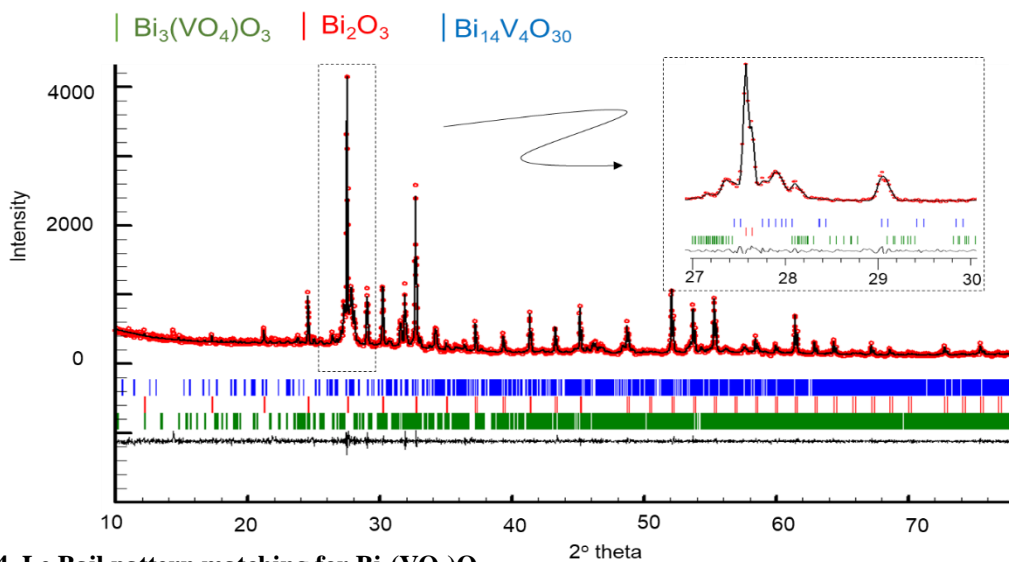


Figure 54. Le Bail pattern matching for  $\text{Bi}_3(\text{VO}_4)\text{O}_3$ .

***b. The new  $\text{Bi}_{3.5}\text{O}_4(\text{AsO}_4)\text{H}_{0.5}$***

The  $\text{Bi}_{3.5}\text{O}_4(\text{AsO}_4)\text{H}_{0.5}$  demonstrated the same kind of quadruple ribbons as in  $\text{Bi}_3(\text{VO}_4)\text{O}_3$  ones. It is built on the edge sharing of four  $[\text{OBi}_4]$  tetrahedrons  $Td$  centered on O1, O4, O8 and O10, respectively. There are additional  $[\text{OBi}_5]$   $SP$  units (centered on O3 atom) decorating the ribbons in their middle. The main difference with  $\text{Bi}_3(\text{VO}_4)\text{O}_3$  lie from the layers, the way how ribbons are connected. As is presented on Figure 55, where the ribbons are presented along the  $b$  axis and connected through triangles  $[\text{OBi}_3]$   $Tr$  (centered on O5, O15 and O16). In  $\text{Bi}_{3.5}\text{O}_4(\text{AsO}_4)\text{H}_{0.5}$  they are connected by corner instead of edge as in  $\text{Bi}_3(\text{VO}_4)\text{O}_3$ .

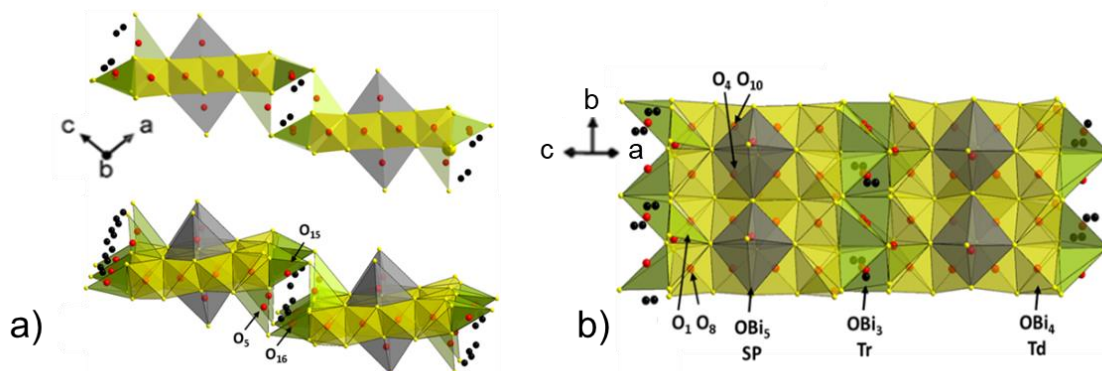


Figure 55. Presentation along three different orientations of  $[\text{Bi}_{3.5}\text{O}_{3.5}]^{10.5+}(\text{OH})_{0.5}^{1-}$  units in  $\text{Bi}_{3.5}(\text{AsO}_4)\text{O}_{3.5}(\text{OH})_{0.5}$ . The corrugated layers are built on association of anion-centered groups:  $\text{OBi}_3$  in green,  $\text{OBi}_4$  in yellow and  $\text{OBi}_5$  in grey.

The associations of triangles  $[\text{OBi}_3]$  *Tr* form four member rings units hosting a local Bi-disorder. A half-occupied  $\text{Bi6a/Bi6b}$  and  $\text{Bi7a/Bi7b}$  pairs are shown on Figure 56(b) forming in-layer channels along *b* direction. However, on the Fourier map some residual electronic density still present close to the O15 atom suggesting the presence of hydroxyl groups pointing to the vacant space of these channels. Finally, as in the structure of  $\text{Bi}_3(\text{VO}_4)\text{O}_3$  can be describe by corrugated layers sandwiching isolated  $[\text{AsO}_4]$  tetrahedra and after structural refinement, the final formula is  $(\text{Bi}_{3.5}\text{O}_{3.5})(\text{AsO}_4)(\text{OH})_{0.5}$  and the corresponding crystal structure shown Figure 56 (a).

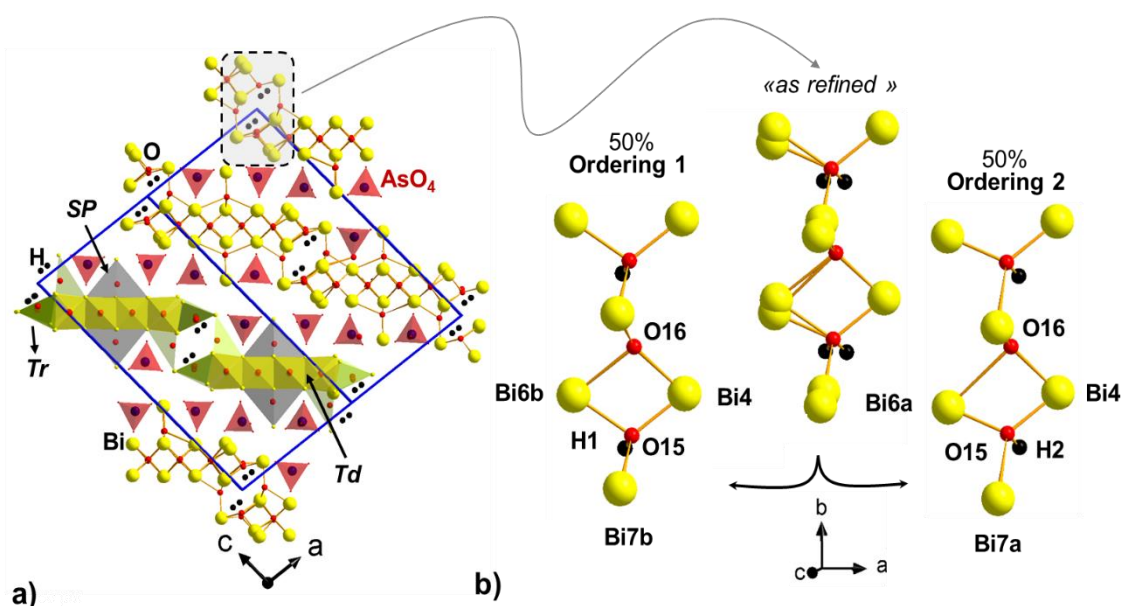


Figure 56. a) General overview of the new  $\text{Bi}_{3.5}\text{O}_4(\text{AsO}_4)\text{H}_{0.5}$  along the *b* axis. The anion-centered units are drawn in yellow for  $\text{OBi}_4$  *Td*, green for  $\text{OBi}_3$  *Tr* and grey for  $\text{OBi}_5$  *SP* whereas  $\text{AsO}_4$  groups are shown in red. b) Possible ordering between two consecutive ribbons.

The bond valence sum calculations (Table 19) is in accordance with the hydroxyl groups assignment and their presence is confirmed by infra-red spectroscopy (Figure 57). The wide and intense peaks observed in the 300-900 $\text{cm}^{-1}$  region can be attributed to: a) the classical stretching vibration modes of arsenate groups  $\text{AsO}_4$ , as in, [83] and b) to Bi-O-Bi vibrations, as in  $\delta\text{-Bi}_2\text{O}_3$  or  $\text{Bi}(\text{OH})_3$ . [83] However the broad and weak bands around 1300 $\text{cm}^{-1}$  can be attributed to O-H vibration of Bi-OH, as seen in  $\text{Bi}(\text{OH})_3$ . The broadness of this latter can plausibly be due to the hydroxides local disorder and the weak interactions of H with other atoms of the lattice. Indeed, two 50% occupied OH bonds exist on O15. This disorder is linked to the local disorder on Bi6 and Bi7 mentioned above and allows local ordering. It significantly modifies Bi-O distances i.e.  $\text{Bi7a/b-O16} = 2.395(14)/2.045(13)\text{\AA}$  and  $\text{Bi6a/b-O15} = 2.091(12)/2.236(12)\text{\AA}$  depending on the proton presence or not.

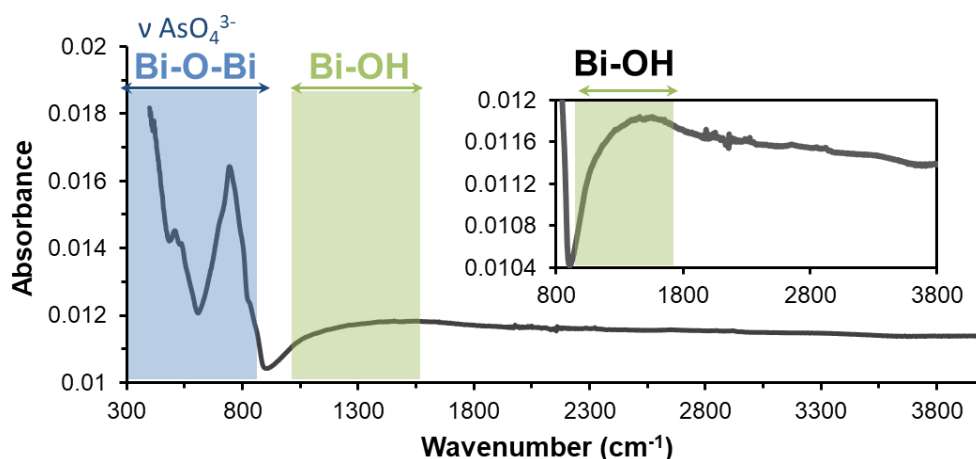


Figure 57. Infra-Red spectrum of crushed crystals of  $\text{Bi}_{3.5}\text{O}_4(\text{AsO}_4)\text{H}_{0.5}$ . The right inset shows the weak bands due to Bi-OH vibration.

The powder sample of  $\text{Bi}_{3.5}\text{O}_4(\text{AsO}_4)\text{H}_{0.5}$  is pure, as shown on Figure 58.

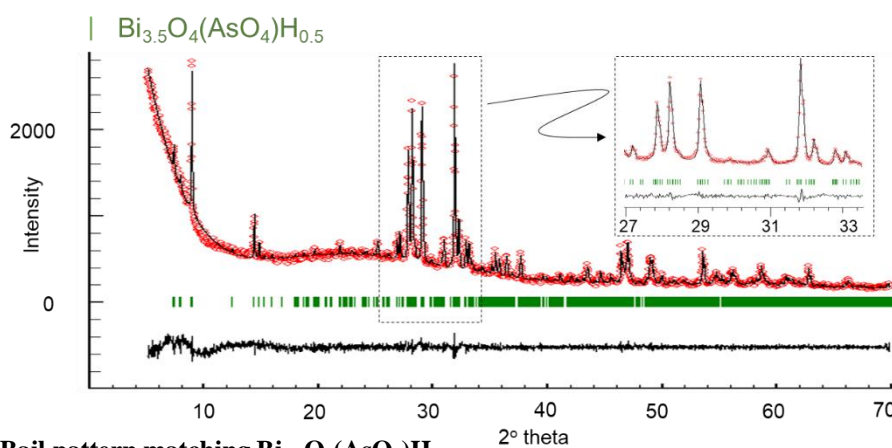
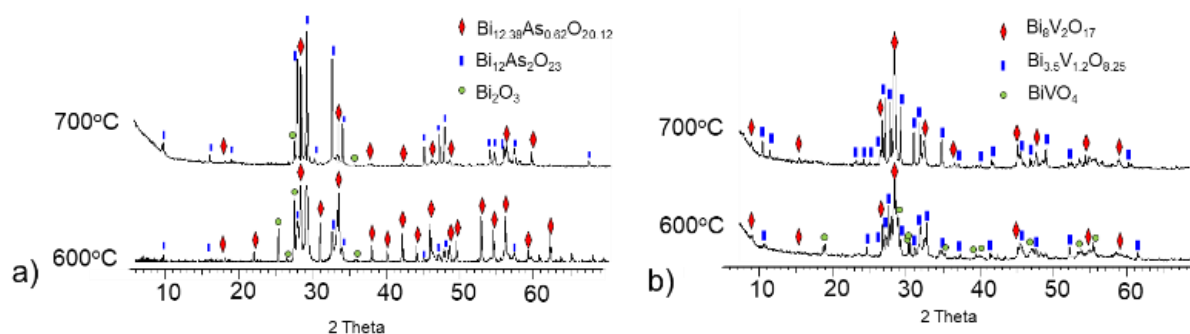


Figure 58. Le Bail pattern matching  $\text{Bi}_{3.5}\text{O}_4(\text{AsO}_4)\text{H}_{0.5}$ .

### c. Solid-state synthesis of the new phases

In order to investigate the possibility to reproduce new compounds by solid-state reaction, a series of experiments was provided. In the first case, the  $\text{Bi}_2\text{O}_3$  and  $\text{As}_2\text{O}_5$  precursors were taken in stoichiometric amount to a new  $(\text{Bi}_{3.5}\text{O}_{3.5})(\text{AsO}_4)(\text{OH})_{0.5}$  compound. Another mixture stoichiometric to another new  $\text{Bi}_3(\text{VO}_4)\text{O}_3$  composition. It was prepared from  $\text{Bi}_2\text{O}_3$  and  $\text{V}_2\text{O}_5$  precursors. The initial mixtures were well grained in agate mortar. The resulted powders were heated at 600 and 700°C, as it shown on Figure 59.



**Figure 59. Powder diffraction patterns in series of solid-state reactions trying to reproduce (a)  $(\text{Bi}_{3.5}\text{O}_{3.5})(\text{AsO}_4)(\text{OH})_{0.5}$  and (b)  $\text{Bi}_3(\text{VO}_4)\text{O}_3$  compounds.**

To date, it was not possible to synthesize the pure phases using solid-state synthesis from mixtures of  $\text{Bi}_2\text{O}_3$ ,  $\text{V}_2\text{O}_5$  and  $\text{As}_2\text{O}_5$ , even after testing the effect of temperature. In both cases, the resulted powder patters correspond to a number of oxides.

### II.3.3. Structural complexity

$\text{Bi}_3\text{O}_3(\text{PO}_4)$  was analyzed on the basis of its structural complexity [63] using Shannon information content per atom ( $I_G$ ) and per unit cell ( $I_{G,\text{total}}$ ). [70] It was described laconically as the simplest term in the oxo (hydroxo)-phosphate series. Indeed  $I_{G,\text{total}}$  value varies from 76.104 to 2592.966 bits/unit cell for  $\text{Bi}_3\text{O}_3(\text{PO}_4)$ , with 2D corrugated layers, to  $\text{Bi}_{14}\text{O}_{15}(\text{PO}_4)_4$  with 2D-thick blocks respectively. It denotes a versatile crystal-chemistry of oxo-centered polyhedra while associated with small phosphate groups ( $r_{\text{P}^{5+}}=0.17\text{\AA}$ ). One could also plausibly suggest the effect of steam pressure for  $\text{Bi}_3(\text{PO}_4)\text{O}_3$  leading to a more symmetrical edifice. A similar analysis on series of oxo (hydroxo)- vanadates and arsenates concerned here is summarized in Table 9.

**Table 9. Complexity of each Bi/V/O +H and Bi/As/O +H members of existing phases Containing Oxo-Centered Tetrahedrons.**

Compound/ Mineral	S.G. Z	a (Å), α (°)	b (Å), β (°)	c(Å), γ (°)	V [Å <sup>3</sup> ]	v (atoms)	IG (bits/ atoms)	IG,total (bits/unit cell)
<b>Vanadate compounds</b>								
Bi <sub>4</sub> O <sub>4</sub> (VO <sub>3.5</sub> )[71]	C2/m 6	5.6120(2)	15.2829(4) 89.756(1)	16.60139(50)	1423.85	11	2.187	24.054
Bi <sub>6</sub> O <sub>6</sub> (VO <sub>3.33</sub> ) <sub>3</sub> [72]	Pnma 4	5.4721(1)	17.2542(3)	14.9174(2)	1408.45	100	3.844	384.386
Bi <sub>4</sub> O <sub>4</sub> (VO <sub>3.5</sub> )[73]	I4/mmm 1	3.99172(5)	3.99172(5)	15.4309(3)	245.87	11	2.187	24.054
Bi <sub>4</sub> O <sub>4</sub> (VO <sub>3.5</sub> )[74]	Amam 4	11.2331(3)	5.6491(2)	15.3469(3)	973.87	36	2.837	102.117
Bi <sub>46</sub> O <sub>57</sub> (VO <sub>4</sub> ) <sub>8</sub> [75]	C2/m 2	20.02938(5)	11.59621(3) 111.3366(2)	21.12860(6)	4571.07	150	5.562	834.323
Bi <sub>14</sub> O <sub>14</sub> (VO <sub>4</sub> ) <sub>4</sub> [76]	C2/c 8	9.9345(3)	11.5464(2) 110.8813(9)	27.9515(4)	6011.09	184	5.524	1016.355
Bi <sub>23</sub> O <sub>28</sub> (VO <sub>4</sub> ) <sub>4</sub> [77]	Immm	12.1371(4)	11.6935(4)	16.0191(6)	2273.51	84	4.083	342.955
Bi <sub>2</sub> O(OH)(VO <sub>4</sub> ) <sub>4</sub> [78]	P2 <sub>1</sub> /c 4	6.971(1)	7.535(1)	10.881(1)	546.57	36	3.17	114.117
Bi <sub>3</sub> O <sub>3</sub> (VO <sub>4</sub> ) [(1) this work]	P-1 2	5.6823(12) 81.39(1)	8.4789(19) 86.91(1)	14.2428(26) 88.5287(1)	677.39	44	4.46	196.22
<b>Arsenate compounds</b>								
Bi <sub>24</sub> O <sub>33.2</sub> (AsO <sub>4</sub> ) <sub>1.7</sub> [79]	I23 1	10.2094(5)	10.2094	10.2094	1064.14	33	1.952	64.426
Bi <sub>3</sub> O(OH)(AsO <sub>4</sub> ) <sub>2</sub> [80]	P-1 2	9.993(3) 87.82(2)	7.404(3) 115.01(2)	6.937(3) 111.07(2)	430.07	30	3.907	117.207
Bi <sub>2</sub> O(OH)(AsO <sub>4</sub> ) <sub>4</sub> [81]	P2 <sub>1</sub> /c 4	7.000(2)	107.08(2)	10.831(2)	538.48	36	3.17	114.117
Bi <sub>3.5</sub> O <sub>3.5</sub> (OH) <sub>0.5</sub> (AsO <sub>4</sub> ) [(2) this work]	P2 <sub>1</sub> /n	11.7264(14)	5.4063(7) 98.66(1)	24.2131(30)	1517.51	104	4.7	488.85

The structural complexity per atom ( $I_G$ ) and per unit cell ( $I_{G,\text{total}}$ ) were also calculated for both new structures. The structural information amounts of Bi<sub>3</sub>(VO<sub>4</sub>)O<sub>3</sub> and Bi<sub>3.5</sub>O<sub>4</sub>(AsO<sub>4</sub>)H<sub>0.5</sub> are respectively equal to 196.22 and 488.85 bits per/unit cell.

The comparison with other vanadate and arsenate phases clearly reveals for bigger XO<sub>4</sub> groups ( $r_{\text{As}^{5+}\text{-V}^{5+}} = 0.33\text{-}0.35 \text{ \AA}$ ), a more homogeneous distribution of complexities ( $I_{G,\text{total}}$  varying from 24.054 to 1016.355 for vanadates and from 64.426 to 488.85 for arsenates). One must note that the bigger [XO<sub>4</sub>] unit is, the less is the complexity, which pictures well a less variable matching between the [XO<sub>4</sub>] groups and the [BiO<sub>x</sub>] oxo-centered framework. The most complex phase is a vanadate: Bi<sub>14</sub>V<sub>4</sub>O<sub>30</sub> (1016.35 bits per unit cell). [77] In comparison, the number of phases referenced in the literature with bismuth and arsenic is very limited: only three to date and two of them hosting hydroxides.

Clearly Bi<sub>3.5</sub>O<sub>4</sub>(AsO<sub>4</sub>)H<sub>0.5</sub> is the most complex (hydro)oxo-arsenate of bismuth, it is mainly due to the structural disorder and  $I_{G,\text{total}}$  drops to 513.53 bits/unit cell considering local ordering only. Bi<sub>3</sub>(VO<sub>4</sub>)O<sub>3</sub> stands in the lowest range in terms of complexities within its chemical series. Dealing within absence of O/OH tandem, similarly to the Bi<sub>3</sub>(PO<sub>4</sub>)O<sub>3</sub> case, the high-pressure conditions may be responsible for its relatively simple (i.e. symmetrical) structure. It is of course far below

the complexity calculated for some silicate minerals such as the recently solved Ilmajokite ( $\text{Na}_{11.24}\text{K}_{1.10}\text{Ba}_{0.90}\text{Ce}_2\text{Ti}_{12}\text{Si}_{37.52}\text{O}_{94}(\text{OH})_{30.38}(\text{H}_2\text{O})_{29.06}$  [82] with a multilevel hierarchical framework based ( $I_{G,\text{total}} = 1990.129$  bits per cell) in which natural conditions brewed a diversity of cationic species. Taking into account that our experimental conditions using super-critical water steam vapor may simulate some mineralogical conditions, it emphasizes the broad perspectives offered by working in more rich more diversified chemical systems.

### II.3.4. Conclusion

Considering the title compounds and the phosphate equivalent of  $\text{Bi}_3(\text{VO}_4)\text{O}_3$ , the  $[\text{XO}_4]$  size effect drastically impact the crystal structure substituting  $\text{P}^{5+}$  by  $\text{V}^{5+}$  or  $\text{As}^{5+}$ . We observe a true preference of the oxo-centered framework for fluorine-type 2D slabs separated by  $[\text{XO}_4]$  entities, which topology and complexity are versatile. [72] In these rich chemical systems, the supercritical water-pressure parameter is barely used for the moment, while it is shown here to open wide possibilities. It seems very promising to further stabilize stable or metastable compounds into more complex Bi-based chemical systems. Especially, the possibility to isolate new bismuth vanadate is promising considering the broad impact of  $\text{BiVO}_4$  in the current development of new photocatalytic materials.

## II.4. Conclusion and perspectives

This chapter is a springboard towards the stabilization of new materials.

Working with high pressure - until 10GPa - open the door of further polytypes. We are especially interested in the possible modification of the arsenate-based compounds under pressure. Undoubtedly, this would require really high pressure but the recent arrival of a multi-anvil press at the University of Lille will allow to press up to 26GPa and heat until 2000°C. Thinking more largely, it should be possible to predict the formation of polymorph of structures based on  $[XO_4]$  groups into a crystallographic form corresponding to smaller  $[XO_4]$  anionic groups as done twice in our work. The chemical pressure insures by a big  $[XO_4]$  entity can be substituted by a smaller  $[XO_4]$  group if applying physical pressure. This is particularly interesting and could help to raise current technological bolts for synthesis process, not only in the field of oxo-centered materials but also in wider systems.

Concerning the use of hydrothermal pressure, our first trial was conclusive and act as a proof of stability of the oxo-centered units in these particular conditions. A next step will be the introduction of transition metals in order to introduce several properties. Particularly, the fact to work in liquid media is promising to easily modify the valence of the metal.

## II.5. Supplementary information

**Table 10. Atom parameters for  $\text{BiCu}_2(\text{P}_{1-x}\text{V}_x)\text{O}_6$  ( $x = 1, 0.8, 0.5$  and  $0.2$ ) compounds**

<i>Atom</i>	<i>Occ.</i>	<i>x/a</i>	<i>y/b</i>	<i>z/c</i>	<i>U<sub>iso</sub></i>
<b>HP-BiCu<sub>2</sub>VO<sub>6</sub></b>					
<b>Bi1</b>	1	0.55656(1)	0.25	0.13970(2)	0.069(3)
<b>Cu1</b>	1	0.30550(3)	0.25	0.04143(6)	0.069(3)
<b>Cu2</b>	1	0.37168(2)	0.75	0.29244(5)	0.069(3)
<b>V</b>	1	0.36815(4)	0.25	0.53271(7)	0.998(1)
<b>O1</b>	1	0.40322(8)	0.99104(2)	0.12661(2)	0.998(1)
<b>O2</b>	1	0.30739(9)	0.99158(2)	0.44613(2)	0.998(1)
<b>O3</b>	1	0.37977(1)	0.25000(0)	0.75152(2)	0.998(1)
<b>O4</b>	1	0.48128(1)	0.25000(0)	0.44324(2)	0.998(1)
<b>HP-BiCu<sub>2</sub>(V<sub>0.8</sub>P<sub>0.2</sub>)O<sub>6</sub></b>					
<b>Bi1</b>	1	0.557405(2)	0.25	0.14155(3)	0.0048(1)
<b>Cu1</b>	1	0.30323(7)	0.25	0.04424(1)	0.0112(3)
<b>Cu2</b>	1	0.37134(5)	0.75	0.29798(9)	0.0012(2)
<b>V</b>	0.8	0.37095(8)	0.25	0.53067(1)	0.0013(2)
<b>P</b>	0.2	0.37095(8)	0.25	0.53067(1)	0.0013(2)
<b>O1</b>	1	0.39927(1)	0.9813(3)	0.1441(3)	0.0057(6)
<b>O2</b>	1	0.30561(2)	0.0031(4)	0.4414(3)	0.0001(6)
<b>O3</b>	1	0.3697(3)	0.25	0.7285(4)	0.0075(12)
<b>O4</b>	1	0.4672(3)	0.25	0.4347(3)	0.0035(11)
<b>HP-BiCu<sub>2</sub>(V<sub>0.5</sub>P<sub>0.5</sub>)O<sub>6</sub></b>					
<b>Bi1</b>	1	0.55773(6)	0.25	0.14845(1)	0.0114(2)
<b>Cu1</b>	1	0.3036(2)	0.25	0.0531(3)	0.0192(9)
<b>Cu2</b>	1	0.3765(2)	0.75	0.3080(3)	0.0056(6)
<b>V</b>	0.5	0.3630(2)	0.25	0.5397(3)	0.0353(7)
<b>P</b>	0.5	0.3630(2)	0.25	0.5397(3)	0.0353(7)
<b>O1</b>	1	0.3737(4)	0.008(1)	0.1123(8)	0.009(2)
<b>O2</b>	1	0.3145(6)	0.978(1)	0.4767(1)	0.015(2)
<b>O3</b>	1	0.3978(6)	0.25	0.8041(12)	0.007(3)
<b>O4</b>	1	0.4787(8)	0.25	0.4361(14)	0.058(5)
<b>HP-BiCu<sub>2</sub>(V<sub>0.2</sub>P<sub>0.8</sub>)O<sub>6</sub></b>					
<b>Bi1</b>	1	0.55625(6)	0.25	0.15002(1)	0.0218(3)
<b>Cu1</b>	1	0.3046(2)	0.25	0.0481(3)	0.0275(1)
<b>Cu2</b>	1	0.3781(1)	0.75	0.3016(4)	0.0228(8)
<b>P1</b>	0.8	0.3653(4)	0.25	0.5414(8)	0.035(3)
<b>V1</b>	0.2	0.3653(4)	0.25	0.5414(8)	0.035(3)
<b>O1</b>	1	0.4093(4)	0.9907(1)	0.1110(1)	0.010(2)
<b>O2</b>	1	0.3171(5)	0.0134(1)	0.4721(1)	0.004(2)
<b>O3</b>	1	0.3825(7)	0.25	0.7625(1)	0.008(3)
<b>O4</b>	1	0.4773(9)	0.25	0.4658(2)	0.071(5)

**Table 11. Data collection and structure refinement form powder for HP- BiNiPO<sub>5</sub>.**

<b>Crystal data</b>	
Formula	HP-BiNiPO <sub>5</sub>
Formula weight (g)	378.6
Temperature (K)	293
Cell setting	triclinic
Space group	P -1
a (Å)	7.421(1)
b (Å)	6.561(1)
c (Å)	5.163(8)
$\alpha$ °	83.813(3)
$\beta$ °	110.723(5)

$\gamma$ °	123.410(6)
V (Å <sup>3</sup> )	195.072(4)
Z	1
<b>Data collection</b>	
Diffractometer	Bruker D8 Advance A25
Radiation; $\lambda$	CuK $\alpha$ ; 1.5418
Absorption coefficient, $\mu$ (mm <sup>-1</sup> )	47.8
F(000)	332
2 $\theta$ step (deg)	0.02
Data range 2 $\theta$ (°);	5 – 119.68 ( 5 – 12.49 excluded region)
No. of measured points	5615
<b>Refinement</b>	
Profile function	Pseudo-Voigt
Weight scheme	sigma
R <sub>p</sub>	2.82
R <sub>wP</sub>	3.87
Goodness of fit	3.63

**Table 12. Atomic parameters of HP- BiNiPO<sub>5</sub>.**

Atom	X	Y	Z	U <sub>eq</sub>
<b>Bi1</b>	0.9542(3)	0.2291(3)	0.3991(3)	0.0014(2)
<b>Ni1</b>	0.7272(8)	0.8622(8)	0.8282(10)	0.017(2)
<b>P1</b>	0.6076(15)	0.2808(15)	0.8371(17)	0.0135
<b>O1</b>	0.9545	0.9503	0.217	0.035(9)
<b>O2</b>	0.7837	0.2243	0.8934	0.021(3)
<b>O3</b>	0.725	0.5408	0.7403	0.021(3)
<b>O4</b>	0.5703	0.3042	0.1102	0.021(3)
<b>O5</b>	0.6174	0.8607	0.4055	0.021(3)

**Table 13. Anisotropic atomic displacement parameters of HP- BiNiPO<sub>5</sub>.**

Atom	U <sup>11</sup>	U <sup>22</sup>	U <sup>33</sup>	U <sup>12</sup>	U <sup>13</sup>	U <sup>23</sup>
<b>Bi1</b>	0.0006(9)	0.0015(9)	0.0068(9)	0.0000(8)	0.0073(9)	0.0081(8)
<b>Ni1</b>	0.025(6)	0.044(6)	0.029(5)	0.034(5)	0.029(4)	0.037(4)

**Table 14. Selected interatomic distances of HP- BiNiPO<sub>5</sub>.**

Atom 1	Atom 2	d, Å
<b>Bi1</b>	O1	2.147(2)
	O1	2.2802(17)
	O5	2.3407(15)
	O3	2.342(2)
	O2	2.4612(14)
	O4	2.994(2)
	O1	3.2110(7)
	O5	3.4622(5)
<b>Ni1</b>	O4	1.984(6)
	O1	1.997(4)
	O5	2.041(5)
	O1	2.068(6)

Atom 1	Atom 2	d, Å
P1	O3	2.195(7)
	O2	2.216(6)
	O2	1.473(13)
	O5	1.511(7)
	O3	1.1.551(8)
	O4	1.568(11)

Table 15. List of bond valence sums for HP- BiNiPO<sub>5</sub>

Atom	Sum
Bi1	3.066(7)
Ni1	2.021(12)
O1	2.226(10)
P1	4.96(7)
O2	2.07(5)
O3	1.91(3)
O4	1.65(3)
O5	2.20(3)

(R, b) parameters for Bi - O (2.09; 0.37), Ni - O (1.654; 0.37) and P - O (1.604; 0.37).

Table 16. Crystal parameters, data collection and structure refinement details for the crystal of new compound

Crystal data		
Formula	Bi <sub>3.5</sub> O <sub>4</sub> (AsO <sub>4</sub> )H <sub>0.5</sub>	Bi <sub>3</sub> (VO <sub>4</sub> )O <sub>3</sub>
Formula weight (g)	1869.7	1579.7
Temperature (K)	293	293
Cell setting	Monoclinic	Triclinic
Space group	P 2 <sub>1</sub> /n (No. 14)	P-1 (No. 2)
a (Å)	11.7264 (14)	5.682 (1)
b (Å)	5.4063 (7)	8.479 (2)
c (Å)	24.213(3)	14.243 (3)
α (°)	90	81.39 (1)
β (°)	98.659 (7)	86.91 (1)
γ (°)	90	88.53 (1)
V (Å <sup>3</sup> )	1517.5 (3)	677.389 ( )
Z	4	2
Crystal size (mm)	0.1 × 0.15 × 0.8	0.5 × 0.5 × 0.1
Crystal form	Columnar	Needle shaped
Data collection		
Diffractometer	SMART APEX DUO	SMART APEX DUO
Radiation; λ	MoKα; 0.71073	MoKα; 0.71073Å
Absorption coefficient. μ (mm <sup>-1</sup> )	85.286	79.025
F (000)	3104	1312
Data range θ (°); h, k, l	1.7 - 30.78; -16 < h < 16, -4 < k < 7, -34 < l < 34	1.4 - 33.52; -7 < h < 8, -12 < k < 13, -18 < l < 20
No. of measured reflections	16876	11559
Total reflections (N <sub>2</sub> )/unique (N <sub>1</sub> )	4707 / 2691	4232 / 3168
Criterion for observed reflections	I > 3σ(I)	I > 3σ(I)
R <sub>int</sub> (%)	5.45	4.06
Refinement		
Refinement on	Full-matrix last squares on F	Full-matrix last squares on F
Weight scheme	1/(σ <sup>2</sup>  F  + 0.0001 F <sup>2</sup> )	1/(σ <sup>2</sup>  F  + 0.0001 F <sup>2</sup> )
R <sub>gt</sub> , R <sub>all</sub> (%)	3.89, 8.83	4.52, 5.05
wR <sub>gt</sub> , wR <sub>ref</sub> (%)	3.63, 4.34	5.59, 5.68

GOF <sub>gt.</sub> GOF <sub>ref</sub>	1.09, 0.97	2.38. 2.55
Max. /min. residual e density. (eÅ <sup>-3</sup> )	3.36 / -2.85	7.25 / -2.68

**Table 17. Fractional atomic coordinates, and atomic equivalent atomic displacement parameters of Bi<sub>3.5</sub>O<sub>4</sub>(AsO<sub>4</sub>)H<sub>0.5</sub>**

Site	x	y	z	U <sub>eq</sub>
Bi1	0.66919(5)	0.32032(9)	0.20548(2)	0.01212(16)
Bi2	0.47964(5)	0.74643(9)	0.10374(2)	0.01154(15)
Bi3	0.82726(5)	0.78275(9)	0.14015(2)	0.01429(16)
Bi4	0.75155(5)	0.72550(9)	-0.03179(2)	0.01644(17)
Bi5	0.51157(5)	0.77542(9)	0.27593(3)	0.01728(17)
Bi6a	0.9594(3)	0.3482(3)	0.06514(13)	0.0123(5)
Bi6b	0.9671(3)	0.2686(4)	0.06853(14)	0.0215(6)
Bi7a	0.35186(12)	0.3298(2)	0.33735(6)	0.0148(4)
Bi7b	0.35775(11)	0.2621(2)	0.36240(7)	0.0167(4)
As1	0.64851(12)	0.2367(2)	0.05615(6)	0.0105(4)
As2	0.34132(12)	1.2740(2)	0.18591(6)	0.0123(4)
O1	0.9854(8)	0.5390(15)	0.1435(4)	0.011(2)
O2	0.6313(9)	-0.0735(16)	0.0538(4)	0.015(2)
O3	0.6011(9)	0.7085(16)	0.1729(4)	0.016(2)
O4	0.8274(8)	0.5234(15)	0.2144(4)	0.0108(20)
O5	0.8753(12)	0.745(2)	0.0406(6)	0.045(3)
O6	0.6883(9)	0.3289(17)	-0.0045(4)	0.019(2)
O7	0.7607(9)	0.2977(17)	0.1085(4)	0.020(2)
O8	0.5111(8)	0.5403(15)	0.3521(4)	0.0096(19)
O9	0.4350(10)	1.3371(19)	0.2435(5)	0.030(3)
O10	0.6649(9)	0.5315(16)	0.2822(4)	0.016(2)
O11	0.5278(10)	0.3679(18)	0.0722(5)	0.024(3)
O12	0.2050(13)	1.262(2)	0.1985(6)	0.052(4)
O13	0.3728(11)	0.996(2)	0.1624(6)	0.039(3)
O14	0.3482(9)	1.4892(18)	0.1350(4)	0.022(2)
O15	0.3785(10)	0.0016(18)	0.4392(5)	0.026(3)
O16	0.3624(14)	0.489(2)	0.4303(6)	0.053(6)
H1	0.421711	0.09302	0.471994	0.0356

**Table 18. Anisotropic atomic displacement parameters for Bi<sub>3.5</sub>O<sub>4</sub>(AsO<sub>4</sub>)H<sub>0.5</sub>**

Site	U <sub>11</sub>	U <sub>22</sub>	U <sub>33</sub>	U <sub>12</sub>	U <sub>13</sub>	U <sub>23</sub>
Bi1	0.0108(3)	0.0162(2)	0.0095(3)	-0.00218(19)	0.0023(2)	-0.0027(2)
Bi2	0.0102(3)	0.0124(2)	0.0116(3)	0.00087(19)	0.0004(2)	-0.0004(2)
Bi3	0.0154(3)	0.0152(2)	0.0116(3)	0.0058(2)	-0.0002(2)	-0.0010(2)
Bi4	0.0187(3)	0.0159(2)	0.0160(3)	0.0020(2)	0.0066(2)	0.0004(2)
Bi5	0.0122(3)	0.0162(2)	0.0213(3)	0.0036(2)	-0.0041(2)	-0.0038(2)
Bi6a	0.0120(8)	0.0134(8)	0.0119(9)	0.0014(7)	0.0030(6)	-0.0016(8)
Bi6b	0.0152(8)	0.0362(13)	0.0139(8)	0.0034(11)	0.0043(6)	0.0075(12)
Bi7a	0.0109(6)	0.0138(6)	0.0202(8)	-0.0027(4)	0.0041(6)	-0.0033(5)
Bi7b	0.0116(6)	0.0122(5)	0.0265(9)	0.0008(5)	0.0034(6)	0.0023(5)
As1	0.0113(7)	0.0103(5)	0.0102(7)	-0.0007(5)	0.0028(6)	-0.0013(5)

**Table 19. Bond valance calculations for  $\text{Bi}_{3.5}\text{O}_4(\text{AsO}_4)\text{H}_{0.5}$** 

Site	Bi1	Bi2	Bi3	Bi4	Bi5	Bi6a	Bi6b	Bi7a	Bi7b	As1	As2	$\Sigma \rightarrow$
O1			0.14		0.42	0.87		0.54	0.37			2.34
O2		0.34								1.23		1.57
O3	0.51	1.15	0.11		0.12							1.89
O4	1.20		0.60		0.57							2.36
O5			0.28	0.97		0.43						1.68
O6		0.11		0.44						1.25		1.81
O7	0.18		0.97							1.15		2.30
O8			0.51		0.66		0.62	0.81	0.81			3.41
O9					0.24						1.28	1.52
O10	1.12		0.56		0.71							2.39
O11		0.59								1.26		1.86
O12					0.19						1.29	1.48
O13		0.39									1.30	1.69
O14		0.59		0.13							1.18	1.89
O15				0.90		1.00	0.67					2.57
O16				0.57			0.33	0.33	0.44			1.67
H1						0.99						0.99
H2				0.29		0.13	0.16		0.12			0.71
$\Sigma \downarrow$	3.00	3.16	3.18	3.01	2.92	2.30	1.62	1.68	1.61	4.90	5.06	

**Table 20. Main bond distances for  $\text{Bi}_{3.5}\text{O}_4(\text{AsO}_4)\text{H}_{0.5}$** 

Bond		Bond length, Å
As1	O2	1.689(9)
	O11	1.680(12)
	O7	1.717(10)
	O6	1.683(11)
As2	O13	1.670(12)
	O12	1.673(15)
	O9	1.675(11)
	O14	1.706(10)
Bi1	O4	2.139(9)
	O10	2.187(10)
	O10	2.477(10)
	O3	2.340(9)
Bi2	O3	2.038(9)
	O14	2.287(11)
	O13	2.436(14)
	O11	2.285(10)
	O2	2.494(11)
Bi3	O1	2.266(9)
	O10	2.302(10)
	O8	2.337(9)
	O4	2.280(9)
Bi4	O5	2.103(13)
	O6	2.394(10)
	H2	2.17(19)
	O16	2.298(15)
Bi5	O15	2.129(12)
	O10	2.217(10)
	O4	2.299(9)
	O8	2.241(9)
	O1	2.412(9)
Bi6a	H1	2.209(3)
	Bi6b	0.445(3)

	<b>O1</b>	2.14(1)
	<b>O5</b>	2.397(13)
	<b>O15</b>	2.091(12)
	<b>H2</b>	2.38(12)
	<b>H1</b>	2.254(3)
<b>Bi6b</b>	<b>H1</b>	2.436(3)
	<b>H1</b>	2.475(3)
	<b>O15</b>	2.236(12)
	<b>O8</b>	2.265(9)
	<b>O1</b>	2.315(9)
<b>Bi7a</b>	<b>O1</b>	2.463(9)
	<b>O8</b>	2.170(9)
	<b>O16</b>	2.395(14)
	<b>Bi7b</b>	0.703(2)
<b>Bi7b</b>	<b>O1</b>	2.222(9)
	<b>O8</b>	2.386(9)
	<b>O15</b>	2.316(11)
	<b>O16</b>	2.045(13)

**Table 21. Fractional atomic coordinates, and atomic equivalent atomic displacement parameters  $\text{Bi}_3(\text{VO}_4)\text{O}_3$**

Site	x	y	z	$U_{\text{eq}}$
<b>Bi1</b>	0.78954(11)	0.73389(8)	0.15828(5)	0.00993(18)
<b>Bi2</b>	0.30373(11)	0.75705(8)	0.36989(5)	0.01118(18)
<b>Bi3</b>	0.75663(11)	0.86019(8)	0.54476(5)	0.0117(2)
<b>Bi4</b>	0.25441(11)	1.39022(8)	0.19022(5)	0.01124(18)
<b>Bi5</b>	0.82351(11)	1.07519(8)	0.28717(5)	0.0126(2)
<b>Bi6</b>	0.31333(11)	0.99072(8)	0.10645(5)	0.0108(2)
<b>V1</b>	0.2396(5)	0.6858(4)	-0.04677(19)	0.0083(8)
<b>V2</b>	0.7447(5)	0.4620(4)	0.3684(2)	0.0116(9)
<b>O1</b>	0.9875(19)	0.8804(15)	0.2327(8)	0.013(3)
<b>O2</b>	0.9862(18)	0.9657(14)	0.4161(8)	0.010(2)
<b>O3</b>	0.6740(19)	0.9309(14)	0.0582(8)	0.013(3)
<b>O4</b>	0.008(2)	0.7461(15)	-0.1170(9)	0.018(3)
<b>O5</b>	1.1783(19)	1.1842(15)	0.2860(8)	0.014(3)
<b>O6</b>	0.4777(19)	0.9505(15)	0.4157(8)	0.013(3)
<b>O7</b>	0.514(2)	1.2388(15)	0.1182(9)	0.016(3)
<b>O8</b>	0.203(2)	0.7491(15)	0.0660(9)	0.016(3)
<b>O9</b>	0.493(2)	0.8340(16)	0.2348(9)	0.018(3)
<b>O10</b>	0.808(2)	0.2950(18)	0.4463(10)	0.030(4)
<b>O11</b>	0.643(2)	0.6231(16)	0.4210(9)	0.020(3)
<b>O12</b>	0.536(3)	1.421(2)	0.2952(11)	0.042(4)
<b>O13</b>	0.258(2)	0.4949(16)	-0.0351(9)	0.021(3)
<b>O14</b>	0.992(2)	0.5183(17)	0.2998(10)	0.026(3)

**Table 22. Anisotropic atomic displacement parameters for  $\text{Bi}_3(\text{VO}_4)\text{O}_3$**

Site	$U_{11}$	$U_{22}$	$U_{33}$	$U_{12}$	$U_{13}$	$U_{23}$
<b>Bi1</b>	0.0137(3)	0.0082(3)	0.0081(3)	-0.0011(2)	-0.0003(2)	-0.0018(2)
<b>Bi2</b>	0.0142(3)	0.0103(3)	0.0092(3)	-0.0025(3)	0.0020(2)	-0.0025(3)
<b>Bi3</b>	0.0128(3)	0.0091(4)	0.0128(3)	-0.0013(3)	0.0036(3)	-0.0018(3)
<b>Bi4</b>	0.0131(3)	0.0086(3)	0.0115(3)	-0.0003(2)	0.0017(3)	-0.0006(3)
<b>Bi5</b>	0.0157(3)	0.0129(4)	0.0092(3)	0.0047(3)	-0.0012(3)	-0.0019(3)
<b>Bi6</b>	0.0112(3)	0.0119(4)	0.0094(3)	-0.0004(2)	0.0010(2)	-0.0020(3)
<b>V1</b>	0.0095(13)	0.0133(16)	0.0028(13)	-0.0005(11)	0.0010(11)	-0.0035(11)
<b>V2</b>	0.0131(14)	0.0080(16)	0.0127(16)	0.0007(12)	0.0019(12)	0.0011(12)

**Table 23. Bond valance calculations for Bi<sub>3</sub>(VO<sub>4</sub>)O<sub>3</sub>**

Site	Bi1	Bi2	Bi3	Bi4	Bi5	Bi6	V1	V2	Σ→
O1	0.91	0.15			0.96	0.25			2.27
O2		0.24	0.65+0.61		0.81				2.30
O3	0.87					0.75+0.51			2.13
O4				0.58	0.15		1.27		1.99
O5			0.40	1.01	0.67				2.08
O6		0.88	0.79+0.32		0.18				2.16
O7				0.67		0.38	1.13		2.17
O8	0.24					0.54	1.09		1.87
O9	0.78	0.80				0.48			2.07
O10		0.23	0.16					1.28	1.67
O11		0.56						1.22	1.77
O12				0.57				1.34	1.92
O13							1.71		1.71
O14	0.15			0.38				1.31	1.84
Σ↓	2.94	2.86	2.92	3.20	2.76	2.91	5.19	5.16	

**Table 24. Main bond distances for Bi<sub>3</sub>(VO<sub>4</sub>)O<sub>3</sub>**

Bond		Bond length, Å
<b>Bi1</b>	O1	2.1270
	O3	2.1413
	O9	2.1812
	O8	2.6251
<b>Bi2</b>	O6	2.1372
	O9	2.1716
	O11	2.3079
	O2	2.6234
	O10	2.6319
<b>Bi3</b>	O6	2.1788
	O2	2.2508
	O2	2.2749
	O5	2.4294
	O6	2.5109
<b>Bi4</b>	O5	2.0877
	O7	2.2383
	O4	2.2934
	O12	2.2947
	O14	2.4510
<b>Bi5</b>	O1	2.1043
	O2	2.1706
	O5	2.2372
<b>Bi6</b>	O3	2.1972
	O8	2.3192
	O3	2.3373
	O9	2.3586
	O7	2.4516
	O1	2.6021
<b>V1</b>	O13	1.6051
	O4	1.7155
	O7	1.7592
	O8	1.7699
<b>V2</b>	O12	1.6941
	O14	1.7035
	O10	1.7106
	O11	1.7290

## II.6. References

1. Abraham, F., Debreuille-Gresse, M. F., Mairesse, G., & Nowogrocki, G. (1988). *Phase transitions and ionic conductivity in  $\text{Bi}_4\text{V}_2\text{O}_{11}$  an oxide with a layered structure*. *Solid State Ionics*, 28-30, 529–532. doi: 10.1016/S0167-2738(88)80096-1;
2. Abraham, F., Boivin, J., Mairesse, G., & Nowogrocki, G. (1990). *The BIMEVOX series: A new family of high performances oxide ion conductors*. *Solid State Ionics*, 40-41, 934–937. doi:10.1016/0167-2738(90)90157-M;
3. Colmont, M., Huvé, M., & Mentré, O. (2006).  *$\text{Bi}^{3+}/\text{M}^{2+}$  Oxyphosphate: A Continuous Series of Polycationic Species from the 1D Single Chain to the 2D Planes. Part 2: Crystal Structure of Three Original Structural Types Showing a Combination of New Ribbonlike Polycations*. *Inorganic Chemistry*, 45(17), 6612–6621. doi: 10.1021/ic060343j;
4. Kennedy, I., Hunter, B. A. (1996). *Structural and Surface Properties of  $\text{Bi}_3(\text{MSb}_2)\text{O}_{11}$  ( $M = \text{Al}, \text{Ga}$ )*. *Journal of Solid State Chemistry*, 127(2), 178–185. doi:10.1006/jssc.1996.0374;
5. Huvé, M., Colmont, M., & Mentré, O. (2004). *HREM: a Useful Tool to Formulate New Members of the Wide  $\text{Bi}^{3+}/\text{M}^{2+}$  Oxide Phosphate Series*. *Chemistry of Materials*, 16(13), 2628–2638. doi: 10.1021/cm040152j;
6. Petříček, V., & Dušek, M. (2017). *Nuclear structures: Twinning and modulation in crystals*. *EPJ Web of Conferences*, 155, 00003. doi:10.1051/epjconf/201715500003;
7. Bryce, D. L. (2017). *NMR crystallography: structure and properties of materials from solid-state nuclear magnetic resonance observables*. *IUCrJ*, 4(4), 350–359. doi: 10.1107/S2052252517006042;
8. Boje, J., & Muller-Buschbaum, H. (1993). *Synthese und Kristallstruktur von  $\text{CaBiVO}_5$* . *Zeitschrift Fur Anorganische Und Allgemeine Chemie*, 619(3), 521–524. doi:10.1002/zaac.19936190315;
9. Kai, C., Li, C., Xiang, H., Tang, Y., Sun, Y., & Fang, L. (2018). *Phase formation and microwave dielectric properties of  $\text{BiMVO}_5$  ( $M = \text{Ca}, \text{Mg}$ ) ceramics potential for low temperature co-fired ceramics application*. *Journal of the American Ceramic Society*. doi:10.1111/jace.15943;
10. Benmokhtar, S., El Jazouli, A., Chaminade, J. P., Gravereau, P., Guillen, F., & de Waal, D. (2004). *Synthesis, crystal structure and optical properties of  $\text{BiMgVO}_5$* . *Journal of Solid State Chemistry*, 177(11), 4175–4182. doi:10.1016/j.jssc.2004.06.030;
11. Labidi, O., Roussel, P., Porcher, F., Drache, M., Vannier, R.-N., & Wignacourt, J.-P. (2008). *Polymorphism in  $\text{PbBiOXO}_4$  compounds ( $X = \text{V}, \text{P}, \text{As}$ ). Part I: Crystal structures of  $\alpha$ - and  $\beta$ - $\text{PbBiOVO}_4$* . *Journal of Solid State Chemistry*, 181(9), 2260–2267. doi:10.1016/j.jssc.2008.05.026;
12. Radosavljevic, I., Howard, J. A., Sleight, A. W. (2000). *Synthesis and structure of two new bismuth cadmium vanadates,  $\text{BiCdVO}_5$  and  $\text{BiCd}_2\text{VO}_6$ , and structures of  $\text{BiCa}_2\text{AsO}_6$  and  $\text{BiMg}_2\text{PO}_6$* . *International Journal of Inorganic Materials*, 2(6), 543–550. doi:10.1016/s1466-6049(00)00080-5;
13. Xun, X., Yokochi, A., Sleight, A. W. (2002). *Synthesis and Structure of  $\text{BiMnVO}_5$  and  $\text{BiMnAsO}_5$* . *Journal of Solid State Chemistry*, 168(1), 224–228. doi:10.1006/jssc.2002.9714;
14. Chowki, S., Kumar, R., Mohapatra, N., & Mahajan, A. V. (2016). *Long-range antiferromagnetic order and possible field induced spin-flop transition in  $\text{BiMnVO}_5$* . *Journal of Physics: Condensed Matter*, 28(48), 486002. doi:10.1088/0953-8984/28/48/486002;

15. Brixner, L. H., & Foris, C. M. (1974). *BiPbVO<sub>5</sub> — A new bismuth lead vanadate*. *Materials Research Bulletin*, 9(3), 273–276. doi:10.1016/0025-5408(74)90076-2;
16. Roberts, A. C., Burns, P. C., Gault, R. A., Criddle, A. J., Feinglos, M. N., & Stirling, J. A. R. (2001). *Paganoite, NiBi<sup>3+</sup>As<sup>5+</sup>O<sub>5</sub>, a new mineral from Johanngeorgenstadt, Saxony, Germany: description and crystal structure*. *European Journal of Mineralogy*, 13(1), 167–175. doi:10.1127/0935-1221/01/0013-0167;
17. Aliev, A., Kozin, M. S., Colmont, M., Siidra, O. I., Krivovichev, S. V., & Mentré, O. (2015). *Synthesis, crystal structure, high-temperature behavior and magnetic properties of CoBiO(AsO<sub>4</sub>), a Co analogue of paganoite*. *Physics and Chemistry of Minerals*, 42(8), 663–670. doi:10.1007/s00269-015-0752-y;
18. Abraham, F., & Ketatni, M. (1995). *Crystal structure of a new bismuth nickel oxophosphate: BiNiOPO<sub>4</sub>*. *European Journal of Solid State and Inorganic Chemistry* 32, 429;
19. Ketatni, M., Abraham, F., & Mentré, O. (1999). *Channel structure in the new BiCoPO<sub>5</sub>. Comparison with BiNiPO<sub>5</sub>. Crystal structure, lone pair localization and infrared characterisation*. *Solid State Sciences*, 1(6), 449–460. doi:10.1016/s1293-2558(00)80097-7;
20. Nadir, S., Swinnea, J. S., & Steinfink, H. (1999). *Crystal Structure and Physical Properties of BiCoPO<sub>5</sub>*. *Journal of Solid State Chemistry*, 148(2), 295–301. doi:10.1006/jssc.1999.8450
21. Xun, X., Uma, S., & Sleight, A. W. (2002). *Synthesis and structure of BiMnPO<sub>5</sub>*. *Journal of Alloys and Compounds*, 338(1-2), 51–53. doi:10.1016/s0925-8388(02)00213-x ;
22. Mentré, O., Bouree, F., Rodriguez-Carvajal, J., El Jazouli, A., El Khayati, N., & Ketatni, E. M. (2008). *Magnetic structure and analysis of the exchange interactions in BiMO(PO<sub>4</sub>) (M = Co, Ni)*. *Journal of Physics: Condensed Matter*, 20(41), 415211. DOI: 10.1088/0953-8984/20/41/415211;
23. Goodenough, J. B. (1976). *Magnetism and the chemical bond*. Huntington, N.Y.: R. E. Krieger Pub. Co. ISSN 0539-2004;
24. . Petříček, V., Dušek, M., & Palatinus, L. (2014). *Crystallographic Computing System JANA2006: General features*. *Zeitschrift Für Kristallographie - Crystalline Materials*, 229(5). doi:10.1515/zkri-2014-1737;
25. Brese, N. E., & O’Keeffe, M. (1991). *Bond-valence parameters for solids*. *Acta Crystallographica Section B Structural Science*, 47(2), 192–197. doi:10.1107/s0108768190011041;
26. Langreiter, T., & Kahlenberg, V. (2015). *TEV—A Program for the Determination of the Thermal Expansion Tensor from Diffraction Data*. *Crystals*, 5(1), 143–153. doi:10.3390/cryst5010143;
27. Mathews, E., Ranjith, K. M., Baenitz, M., & Nath, R. (2013). *Field induced magnetic transition in low-dimensional magnets Bi(Ni,Co)PO<sub>5</sub>*. *Solid State Communications*, 154, 56–59. doi:10.1016/j.ssc.2012.10.033;
28. Yang, J., & Dolg, M. (2007). *Computational investigation of the Bi lone-pairs in monoclinic bismuth triborate BiB<sub>3</sub>O<sub>6</sub>*. *Physical Chemistry Chemical Physics*, 9(17), 2094. doi:10.1039/b615210d ;
29. Wang, S., Mitzi, D. B., Landrum, G. A., Genin, H., & Hoffmann, R. (1997). *Synthesis and Solid State Chemistry of CH<sub>3</sub>BiI<sub>2</sub>: A Structure with an Extended One-Dimensional Organometallic Framework*. *Journal of the American Chemical Society*, 119(4), 724–732. doi:10.1021/ja961753h .

30. Koepernik, K., & Eschrig, H. (1999). *Full-potential nonorthogonal local-orbital minimum-basis band-structure scheme*. Physical Review B, 59(3), 1743–1757. doi:10.1103/physrevb.59.1743;
31. Perdew, J. P., & Wang, Y. (1992). *Accurate and simple analytic representation of the electron-gas correlation energy*. Physical Review B, 45(23), 13244–13249. doi:10.1103/physrevb.45.13244;
32. Kresse, G.; et Furthmüller, J. (2012). *Ab-initio Simulation Package (VASP)*, Institut für Materialphysik: Vienna;
33. Mortensen, J. J., Hansen, L. B., & Jacobsen, K. W. (2005). *Real-space grid implementation of the projector augmented wave method*. Physical Review B, 71(3). doi:10.1103/physrevb.71.035109;
34. Olchowka, J., Mentré, O., Kabbour, H., Colmont, M., Adlung, M., Suta, M., & Wickleder, C. (2017). *Bonding Scheme and Optical Properties in BiM<sub>2</sub>O<sub>2</sub>(PO<sub>4</sub>) (M=Cd, Mg, Zn); Experimental and Theoretical Analysis*. Chemistry - A European Journal, 23(62), 15694–15703. doi:10.1002/chem.201702373;
35. Abraham, F.; Ketatni, E. M.; Mairesse, G.; Mernari, B. (1994). *Crystal structure of a new bismuth copper oxyphosphate: BiCu<sub>2</sub>PO<sub>6</sub>*. Eur. J.Solid State Inorg. Chem., 31, 313–323;
36. Colmont, M., Darie, C., Tsirlin, A. A., Jesche, A., Colin, C., & Mentré, O. (2018). *Compressibility of BiCu<sub>2</sub>PO<sub>6</sub>: Polymorphism against S = 1/2 Magnetic Spin Ladders*. Inorganic Chemistry, 57(10), 6038–6044. doi:10.1021/acs.inorgchem.8b00445 ;
37. Mentré, O., Janod, E., Rabu, P., Hennion, M., Leclercq-Hugeux, F., Kang, J., ... Petit, S. (2009). *Incommensurate spin correlation driven by frustration in BiCu<sub>2</sub>PO<sub>6</sub>*. Physical Review B, 80(18). doi:10.1103/physrevb.80.180413;
38. Tsirlin, A. A., Rousochatzakis, I., Kasinathan, D., Janson, O., Nath, R., Weickert, F., ... Rosner, H. (2010). *Bridging frustrated-spin-chain and spin-ladder physics: Quasi-one-dimensional magnetism of BiCu<sub>2</sub>PO<sub>6</sub>*. Physical Review B, 82(14). doi:10.1103/physrevb.82.144426;
39. Ono, S. (2018). *High-pressure phase transition of bismuth*. High Pressure Research, 1–8. doi:10.1080/08957959.2018.1541456;
40. Mentré, O., Ketatni, E. M., Colmont, M., Huvé, M., Abraham, F., & Petricek, V. (2006). *Structural Features of the Modulated BiCu<sub>2</sub>(P<sub>1-x</sub>V<sub>x</sub>)O<sub>6</sub> Solid Solution; 4-D Treatment of x= 0.87 Compound and Magnetic Spin-Gap to Gapless Transition in New Cu<sup>2+</sup> Two-Leg Ladder Systems*. Journal of the American Chemical Society, 128(33), 10857–10867. doi:10.1021/ja0631091 ;
41. Radosavljevic, I., Evans, J. S. O., & Sleight, A. W. (2010). *ChemInform Abstract: Synthesis and Structure of Bismuth Copper Arsenate, BiCu<sub>2</sub>AsO<sub>6</sub>*. ChemInform, 30(21), no–no. doi:10.1002/chin.199921027;
42. Sleight, A. W., Chen, H. -y., Ferretti, A., & Cox, D. E. (1979). *Crystal growth and structure of BiVO<sub>4</sub>*. Materials Research Bulletin, 14(12), 1571–1581. doi:10.1016/0025-5408(72)90227-9;
43. Martin, K., McCarthy, G. (1991). North Dakota State Univ., Fargo, ND, USA. ICDD Grant-in-Aid;
44. Deacon, G. B., Gatehouse, B. M., & Ward, G. N. (1994). *Cu<sub>3</sub>Bi<sub>4</sub>V<sub>2</sub>O<sub>14</sub>, a new compound*. Acta Crystallographica Section C Crystal Structure Communications, 50(8), 1178–1180. doi:10.1107/s010827019400466x;
45. Ketatni, E. M., Mernari, B., Abraham, F., & Mentre, O. (2000). *Crystal Structure of BiZn<sub>2</sub>PO<sub>6</sub>. Filiation between Related Compounds*. Journal of Solid State Chemistry, 153(1), 48–54. doi:10.1006/jssc.2000.8738;

46. Radosavljevic, I., & Sleight, A. W. (2000). *Variable Temperature X-Ray Diffraction Study of Bismuth Magnesium Vanadate, BiMg<sub>2</sub>VO<sub>6</sub>*. *Journal of Solid State Chemistry*, 149(1), 143–148. doi:10.1006/jssc.1999.8512 ;
47. PAC (1994) 66, 577. *Definitions of terms relating to phase transitions of the solid state*, IUPAC Recommendations, 581;
48. Radosavljevic, I., Howard, J. A., Sleight, A. W. (2000). *Synthesis and structure of two new bismuth cadmium vanadates, BiCdVO<sub>5</sub> and BiCd<sub>2</sub>VO<sub>6</sub>, and structures of BiCa<sub>2</sub>AsO<sub>6</sub> and BiMg<sub>2</sub>PO<sub>6</sub>*. *International Journal of Inorganic Materials*, 2(6), 543–550. doi:10.1016/s1466-6049(00)00080-5;
49. Barros, A., Deloncle, R., Deschamp, J., Boutinaud, P., Chadeyron, G., Mahiou, R., ... Brik, M. G. (2014). *Optical properties and electronic band structure of BiMg<sub>2</sub>PO<sub>6</sub>, BiMg<sub>2</sub>VO<sub>6</sub>, BiMg<sub>2</sub>VO<sub>6</sub>:Pr<sup>3+</sup> and BiMg<sub>2</sub>VO<sub>6</sub>:Eu<sup>3+</sup>*. *Optical Materials*, 36(10), 1724–1729. doi:10.1016/j.optmat.2014.02.006 ;
50. Huang, J., Gu, Q., & Sleight, A. W. (1993). *Synthesis and Characterization of Bismuth Magnesium Phosphate and Arsenate: BiMg<sub>2</sub>PO<sub>6</sub> and BiMg<sub>2</sub>AsO<sub>6</sub>*. *Journal of Solid State Chemistry*, 105(2), 599–606. doi:10.1006/jssc.1993.1254;
51. Radosavljevic, I., Evans, J. S. O., & Sleight, A. W. (1998). *Synthesis and Structure of Bismuth Copper Vanadate, BiCu<sub>2</sub>VO<sub>6</sub>*. *Journal of Solid State Chemistry*, 141(1), 149–154. doi:10.1006/jssc.1998.7931;
52. Huang, J., & Sleight, A. W. (1992). *Synthesis, crystal structure, and optical properties of a new bismuth magnesium vanadate: BiMg<sub>2</sub>VO<sub>6</sub>*. *Journal of Solid State Chemistry*, 100(1), 170–178. doi:10.1016/0022-4596(92)90168-u;
53. Radosavljević Evans, I., Howard, J. A. K., & Sleight, A. W. (2005). *Synthesis and crystal structure of BiCd<sub>2</sub>AsO<sub>6</sub>*. *Solid State Sciences*, 7(3), 299–302. doi:10.1016/j.solidstatesciences.2004.10.040 ;
54. Radosavljevic, I., Evans, J. S. O., & Sleight, A. W. (1998). *Synthesis and Structure of BiCa<sub>2</sub>VO<sub>6</sub>*. *Journal of Solid State Chemistry*, 137(1), 143–147. doi:10.1006/jssc.1997.7741 ;
55. Mizrahi, A., Wignacourt, J.-P., & Steinfink, H. (1997). *Pb<sub>2</sub>BiO<sub>2</sub>PO<sub>4</sub>, a New Oxophosphate*. *Journal of Solid State Chemistry*, 133(2), 516–521. doi:10.1006/jssc.1997.7520;
56. Labidi, O., Wignacourt, J. P., Roussel, P., Drache, M., Conflant, P., & Steinfink, H. (2004). *A reinvestigation of the crystal structure of α-Pb<sub>2</sub>BiVO<sub>6</sub>*. *Solid State Sciences*, 6(8), 783–790. doi:10.1016/j.solidstatesciences.2004.03.024;
57. Xun, X., Uma, S., Yokochi, A., & Sleight, A. W. (2002). *Synthesis and Structure of New BiMn<sub>2</sub>MO<sub>6</sub> Compounds Where M=P, As, or V*. *Journal of Solid State Chemistry*, 167(1), 245–248. doi:10.1006/jssc.2002.9654;
58. Olchowka, J. Thèse: *Structural versus optical properties in selected Bismuth based oxo-salts and compounds*, Lille University, 2015;
59. Nath, R., Ranjith, K. M., Roy, B., Johnston, D. C., Furukawa, Y., & Tsirlin, A. A. (2014). *Magnetic transitions in the spin-5/2 frustrated magnet BiMn<sub>2</sub>PO<sub>6</sub> and strong lattice softening in BiMn<sub>2</sub>PO<sub>6</sub> and BiZn<sub>2</sub>PO<sub>6</sub> below 200 K*. *Physical Review B*, 90(2). doi:10.1103/physrevb.90.024431;
60. Evans, I. R., Howard, J. A. K., Evans, J. S. O., & Withers, R. L. (2001). *Ab initio structure determination of BiPb<sub>2</sub>VO<sub>6</sub> from powder diffraction data*. *Chemical Communications*, (19), 1984–1985. doi:10.1039/b105242j;
61. Rodríguez-Carvajal, J. (2001). *Recent Developments of the Program FULLPROF*, in *Commission on Powder Diffraction (IUCr). Newsletter*, 26, 12-19;

62. Sakurai, H., Yoshimura, K., Kosuge, K., Tsujii, N., Abe, H., Kitazawa, H., ... Hilscher, G. (2002). *Antiferromagnetic Order in  $\text{Bi}_4\text{Cu}_3\text{V}_2\text{O}_{14}$  with Novel Spin Chain*. Journal of the Physical Society of Japan, 71(4), 1161–1165. doi:10.1143/jpsj.71.1161;
63. Aksenov, S. M., Yamnova, N. A., Borovikova, E. Y., Volkov, A. S., Ksenofontov, D. A., Dimitrova, O. V., ... Burns, P. C. (2018).  *$\text{Bi}_3(\text{PO}_4)\text{O}_3$ , the Simplest Bismuth(III) Oxophosphate: Synthesis, IR Spectroscopy, Crystal Structure, and Structural Complexity*. Inorganic Chemistry, 57(12), 6799–6802. doi:10.1021/acs.inorgchem.8b01195;
64. Olchowka, J., Colmont, M., Aliev, A., Tran, T. T., Halasyamani, P. S., Hagemann, H., & Mentré, O. (2017). *Original oxo-centered bismuth oxo-arsenates; critical effect of  $\text{PO}_4$  for  $\text{AsO}_4$  substitution*. Cryst.Eng.Comm., 19(6), 936–945. doi:10.1039/c6ce02466a;
65. Feger, C. R., Schimek, G. L., & Kolis, J. W. (1999). *Hydrothermal Synthesis and Characterization of  $\text{M}_2\text{Te}_3\text{O}_8$  ( $\text{M}=\text{Mn}, \text{Co}, \text{Ni}, \text{Cu}, \text{Zn}$ ): A Series of Compounds with the Spiroffite Structure*. Journal of Solid State Chemistry, 143(2), 246–253. doi:10.1006/jssc.1998.8101;
66. SAINT: Area-Detector Integration Software. Madison: Siemens Industrial Automation, Inc., (1996);
67. Sheldrick G. M. (2004). SADABS, version2, University of Göttingen, Germany;
68. Palatinus, L., & Chapuis, G. (2007). *SUPERFLIP—a computer program for the solution of crystal structures by charge flipping in arbitrary dimensions*. Journal of Applied Crystallography, 40(4), 786–790. doi:10.1107/s0021889807029238;
69. Krivovichev, S. V., Mentré, O., Siidra, O. I., Colmont, M., & Filatov, S. K. (2013). *Anion-Centered Tetrahedra in Inorganic Compounds*. Chemical Reviews, 113(8), 6459–6535. doi:10.1021/cr3004696;
70. Krivovichev, S. V. (2013). *Which Inorganic Structures are the Most Complex?* Angewandte Chemie International Edition, 53(3), 654–661. doi:10.1002/anie.201304374;
71. Joubert, O., Jouanneaux, A., & Ganne, M. (1994). *Crystal structure of low-temperature form of bismuth vanadium oxide determined by rietveld refinement of X-ray and neutron diffraction data ( $\alpha$  -  $\text{Bi}_4\text{V}_2\text{O}_{11}$ )*. Materials Research Bulletin, 29(2), 175–184. doi:10.1016/0025-5408(94)90138-4;
72. Olchowka, J., Colmont, M., Aliev, A., Tran, T. T., Halasyamani, P. S., Hagemann, H., & Mentré, O. (2017). *Original oxo-centered bismuth oxo-arsenates; critical effect of  $\text{PO}_4$  for  $\text{AsO}_4$  substitution*. CrystEngComm, 19(6), 936–945. doi:10.1039/c6ce02466a;
73. Mairesse, G., Roussel, P., Vannier, R. N., Anne, M., Pirovano, C., & Nowogrocki, G. (2003). *Crystal structure determination of  $\alpha$ ,  $\beta$  and  $\gamma$ - $\text{Bi}_4\text{V}_2\text{O}_{11}$  polymorphs. Part I:  $\gamma$  and  $\beta$ - $\text{Bi}_4\text{V}_2\text{O}_{11}$* . Solid State Sciences, 5(6), 851–859. doi:10.1016/s1293-2558(03)00015-3;
74. Vannier, R. (2003).  *$\text{Bi}_4\text{V}_2\text{O}_{11}$  polymorph crystal structures related to their electrical properties*. Solid State Ionics, 157(1-4), 147–153. doi:10.1016/s0167-2738(02)00202-3;
75. Kuang, X., Payne, J. L., Farrell, J. D., Johnson, M. R., & Evans, I. R. (2012). *Polymorphism and Oxide Ion Migration Pathways in Fluorite-Type Bismuth Vanadate,  $\text{Bi}_4\text{V}_8\text{O}_{89}$* . Chemistry of Materials, 24(11), 2162–2167. doi:10.1021/cm3008107;
76. Labidi, O., Drache, M., Roussel, P., & Wignacourt, J.-P. (2007). *Crystal structures and conductivity properties of  $\text{MBi}_6\text{V}_2\text{O}_{15}$  family type compounds ( $\text{M}=\text{Pb}, \text{Sr}, \text{Ca}, \text{Cd}, \text{Na}_{0.5}\text{Bi}_{0.5}$ )*. Solid State Sciences, 9(10), 964–972. doi:10.1016/j.solidstatesciences.2007.07.004;

77. Labidi, O., Drache, M., Roussel, P., & Wignacourt, J.-P. (2008). *(M<sub>2</sub>Bi)<sub>46</sub>V<sub>8</sub>O<sub>y</sub>-family type (M=Pb, Sr, Ca, Cd, Na<sub>0.5</sub>Bi<sub>0.5</sub>): Syntheses, crystal structures and conductivity properties*. *Solid State Sciences*, 10(8), 1074–1082. doi:10.1016/j.solidstatesciences.2007.11.014;
78. Krause, W., Bernhardt, H.-J., Blaß, G., Effenberger, H., Graf, H.-W., (1997) *Hechtsbergite, Bi<sub>2</sub>O(OH)(VO<sub>4</sub>), a new mineral from the Black Forest, Germany, Neues Jahrb. Für Mineral. - Monatshefte*, 1997(6), 271- 287. DOI: 10.1127/njmm/1997/1997/271;
79. Horowitz, H., Jacobson, A., Newsam, J., Lewandowski, J., & Leonowicz, M. (1989). *Solution synthesis and characterization of sillenite phases, Bi<sub>24</sub>M<sub>2</sub>O<sub>40</sub> (M=Si, Ge, V, As, P)*. *Solid State Ionics*, 32-33, 678–690. doi:10.1016/0167-2738(89)90344-5;
80. Bedliby, D., Mereiter, K. (1982). *Preisingerite, Bi<sub>3</sub>(OH)(AsO<sub>4</sub>)<sub>2</sub>, a new species from San Juan Province, Argentina: its description and crystal structure*. *American Mineralogist*, 833- 840;
81. Mereiter, K., Preisinger, A. (1986). *Kristallstrukturdaten der Wismutminerale Atelestite, Mixite und Pucherite*. *Sitzungsberichte - Oesterreichische Akademie der Wissenschaften, Mathematisch-Naturwissenschaftliche Klasse, 2b: Chemie*, 79- 81;
82. Zolotarev, A. A., Krivovichev, S.V., Camara, F. Bindi, L., Zhitova, E.S., Hawthorne, F., Sokolova, E. (2020) *Extraordinary structural complexity of ilmajokite: a multilevel hierarchical framework structure of natural origin*, *IUCrJ*, 7(1), 121- 128 doi: 10.1107/S2052252519016622;
83. (a) Ondrus, P., Skala, R., Viti, C., Veselovsky, F., Novak, F., Jansa, J. (1999) *Parascorodite, FeAsO<sub>4</sub> · 2H<sub>2</sub>O; a new mineral from Kank near Kutna Hora, Czech Republic*. *Am. Mineral.*, 84(9), 1439- 1444; (b) Hobosyan, M. A., Yolchinyan, S. A., Martirosyan, K. S. (2016) *A novel nano-energetic system based on bismuth hydroxide*. *RSC Adv.*, 6(71), 66564- 66570;
84. Saison, T., Chemin, N., Chanéac, C., Durupthy, O., Mariey, L., Maugé, F., ... Jolivet, J.-P. (2015). *New Insights Into BiVO<sub>4</sub> Properties as Visible Light Photocatalyst*. *The Journal of Physical Chemistry C*, 119(23), 12967–12977. doi:10.1021/acs.jpcc.5b01468;
85. Cornei, N., Tancret, N., Abraham, F., Mentré, O. (2006). *New ε-Bi<sub>2</sub>O<sub>3</sub> Metastable Polymorph*. *Inorganic Chemistry*, 45(13), 4886–4888. doi:10.1021/ic0605221;
86. Đorđević, T., & Karanović, L. (2014). *A new anion-deficient fluorite-related superstructure of Bi<sub>28</sub>V<sub>8</sub>O<sub>62</sub>*. *Journal of Solid State Chemistry*, 220, 259–269. doi:10.1016/j.jssc.2014.09.010;



---

III. *High-pressure exploration in the lanthanide-  
based oxo-centered systems*

---

At UCCS, the MISSP team is known for its skills in the development of innovative inorganic compounds for applications mainly oriented towards energetic issues. More precisely, its goal is to obtain new materials with magnetic, electronic or optical properties for various applications. In that sense, a big part of the research is devoted to the study of Bi-based oxo-centered materials as largely discussed in the previous chapter. Few years ago, a new orientation was taken through the full substitution of  $\text{Bi}^{3+}$  by  $\text{Ln}^{3+}$ . According to the chemical nature of cations, the  $\text{Ln}^{3+}$  form, in most of the cases, regular  $[\text{OLn}_4]$  tetrahedral that may be isolated (i.e.  $[\text{OCe}_4]$  tetrahedra in  $\text{Ce}[\text{Ce}_4\text{O}]\text{Pb}_3$  [1]), connected together to form chains (i.e.  $[\text{Tb}_3\text{O}_2]\text{Cl}(\text{SeO}_3)_2$  [2]) or layers (i.e.  $[\text{Nd}_7\text{O}_5]\text{Cl}_3(\text{SeO}_3)_4$  [3]) or 3D frameworks (i.e.  $\text{Li}[\text{Ln}_6\text{O}_5](\text{BO}_3)_3$   $\text{Ln} = \text{Pr, Nd, Sm, Eu, Gd, Tb, Dy, Y, Ho, Er, Tm}$  [4]). Other possible triangle configuration of oxo-centered unit are observed in several materials, in  $[\text{Ln}_3\text{O}](\text{GeO}_4)(\text{PO}_4)$  ( $\text{Ln} = \text{Nd-Sm}$ ) series [5] for example. There are also examples of oxo/hydroxo cluster involving tetrahedral as  $[\text{OEr}_4]$  in  $[\text{Er}_{13}\text{O}_7](\text{OH})(\text{GeO}_4)_6$ . [6] These few examples give an overview of the dimensionality that can be obtained with  $[\text{OLn}_4]$  units. The change of supporting cation is not so obvious. It implies:

(1) an adaptation of the synthesis conditions. Although  $\text{Bi}_2\text{O}_3$  has a melting at  $817^\circ\text{C}$ , most of the  $\text{Ln}_2\text{O}_3$  ( $\text{Ln} = \text{La, Yb, Nd, Gd} \dots$ ) have their melting point above  $2000^\circ\text{C}$  which of course needs some adaptation to the classical solid-state route synthesis, first to obtain a good reactivity and second to be able to grow crystals. In previous study, crystal growth synthesis was used, leading to the new  $\text{Pb}_4\text{La}_2\text{O}_7$  [7] that will be used as a starting point of the last part of this thesis. To increase the reactivity, the pressure is also an interesting parameter to play with in order to obtain new structures.

(2) a modification of the characterization techniques. In some cases, due to the impossibility to grow single crystals with a suitable size, and in front of the difficulties to solve the structure in case of a big unit cell parameters and in the presence of heavy elements, some other routes are required as electron crystallography or microdiffraction.

One of the remarkable examples from the first trials performed at UCCS is the recent research on “Pure and  $\text{RE}^{3+}$ -Doped  $\text{La}_7\text{O}_6(\text{VO}_4)_3$  ( $\text{RE} = \text{Eu, Sm}$ ) compounds”. [8] A complex 3D framework was deduced from precession electron diffraction data tomography and kinematical refinement and further used for the final Rietveld refinement. After  $\text{Eu}^{3+}$  and  $\text{Sm}^{3+}$  doping, the matrix shows an emission that is bright and orange under UV excitation.

Another series of experiments were provided in Lille University and lead to the successful synthesis and crystal structure determination of  $\text{KLa}_5\text{O}_5(\text{VO}_4)_2$  (labeled as ‘an interesting material showing blue emission under UV excitation’). [9] Once more, it was solved and refined using PEDT and both kinematical and dynamical refinement in a process of comparison of the two methods. Analogous phases were obtained by substitution of potassium by several alkali (Rb, Na or Li).

The two stories developed in this chapter are in continuity with the two new structures developed so far at UCCS.

### III.1. High-pressure exploration in the Li – Ln – V – O system

In order to continue preliminary investigations done at UCCS and with the ulterior motif of finding new Ln-based oxo-centered materials, new trials were performed. The most useful way of synthesis is classically solid-state reaction at a wide range of temperature conditions. It allowed the successful synthesis and crystal structure determination of  $\text{KLa}_5\text{O}_5(\text{VO}_4)_2$  – an interesting material showing a blue emission under UV excitation [9] recently obtained in the lab and solved using the precession electron diffraction method. Analogous phases were further obtained by substitution of potassium by several alkali such as Rb, Na or Li.

Our aim is to use pressure and temperature as independent thermodynamic parameters influencing the products. Thus, the synthesis conditions or the material itself can be deeply modified by application of pressure because it will efficiently modify the atomic distances as well as the electronic shell. Starting from the known  $\text{LiLa}_5\text{O}_5(\text{VO}_4)_2$ , two new metastable phases will be evidenced. Also pressure and temperature will act as crucial parameters in the synthesis of the pure  $\text{LiNd}_5\text{O}_5(\text{VO}_4)_2$ .

In this chapter we investigate the role of HP-HT conditions in obtaining innovative rare-earth based oxo-centered materials in the Li-Ln-V-O system after selecting pertinent samples through and using *in situ* high-pressure Raman study. From the chemical point of view, this system is particularly interesting because only few structures are referenced to date:  $\text{LiLa}_5\text{O}_5(\text{VO}_4)_2$  [9],  $\text{LiLa}_2\text{VO}_6$ , a double perovskite [67] and  $\text{LaVO}_4$  doped with several amounts of Li ion. [68] This kind of materials may generate high efficient luminescent properties either by doping with emitters [68,69] or by self-activation of vanadates. [70,71]

### III.1.1. Evidence of phase transition by in situ high-pressure Raman spectroscopy

Raman spectroscopy is a useful characterization technique for detecting subtle changes of the local symmetry in solids. In order to rationalize our investigations, *in-situ* high-pressure Raman spectroscopy was used to follow possible structural changes or phase transitions. It was chosen to explore the pressure-induced phase transformation due to its sensitivity to structural transitions. The spectral changes (appearance or disappearance) of Raman modes with pressure gives information about structural modifications of materials and might help to get new structures as done by Grzechnik et al. [78]

The diamond anvil cell preparation for high-pressure experiment provided under mentorship of Professor Sébastien MERKEL from UMET - University of Lille. The Screw Driven Plate Diamond Anvil Cell was chosen to provide a Raman spectroscopy experiment due to flat design that offers a horizontal aperture of more than 80° on 3 sectors offering a near-panoramic view. In the Almax Plate DAC two kinematically-mounted steel plates are elastically deflected with the use of a driving gearbox. The diamonds were perfectly aligned against each other and prepared for further experiments during stage in Madrid University under supervision of Javier Sánchez-Benítez. The operating pressure was specified between ambient conditions and pressures below 30 GPa. Soft solids, liquids, and gases (often as supercritical fluids) are used as practical pressure transmitting media. In case of our experiment silicon oil was chosen as a pressure transmitting medium. Silicone fluid behaves equally well as a pressure medium as the 4:1 methanol:ethanol mixture at low and intermediate pressures below 30 GPa. [81] Different materials of gaskets can be used depending on required experimental conditions: from cheap stainless steel to expensive rhenium and others. In case of our experiment, stainless steel is enough to reach pressures below 30 GPa. In this steel gasket was pre-indented manually to reach about 30 µm thick and 100 µm diameter hole was drilled in the center using Betsa Electric Discharge Machine.

Raman spectrum was registered for  $\text{LiLa}_5\text{O}_5(\text{VO}_4)_2$  (synthesized following the protocol detailed in ref [9], at ambient pressure in the Raman frequency shift of 100-1500  $\text{cm}^{-1}$ . Here we focused on the region 100-1000  $\text{cm}^{-1}$  to avoid the signal of the diamond (Figure 60).

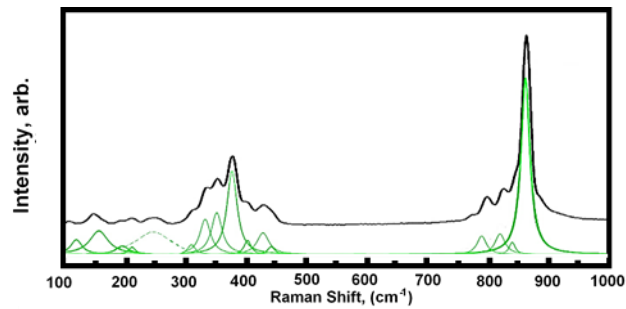


**Figure 60.** Room temperature – Ambient-pressure Raman spectrum of LiLa<sub>5</sub>O<sub>5</sub>(VO<sub>4</sub>)<sub>2</sub> experimental data (in black line) are fitted with Lorentzian profiles (green lines).

The number of Raman active modes were deduced using the Bilbao Crystallographic server. [72] 36Ag + 27Bg modes are expected and only 16 of them are measurable in our range of study, after Lorentzian deconvolution. The difference is supposed to be related to overlapping of Raman bands or to too small Raman scattering cross section. The spectra is rather complicated but at least the specific Raman modes of vanadates are evidenced: up to 300cm<sup>-1</sup>, rotational and translational modes; in the range 300-500 cm<sup>-1</sup>, bending vibrations (O-V-O) and then above 700 cm<sup>-1</sup> the stretching modes (V-O) [72-75]. Also La/Li-O vibration modes are expected below 300 cm<sup>-1</sup>. [76]

Figure 61(a) shows the evolution of Raman spectra under pressure. Figure 61(b) shows the Lorentzian deconvoluted spectra at 1, 10 and 15 GPa on the spectral range 600-1000 cm<sup>-1</sup>. The pressure evolution of Raman frequencies deduced from the deconvolution of each independent spectrum is shown in Figure 61(c). First of all, an increase of the Raman frequencies for the 16 visible modes is observed upon higher pressure as expected as a consequence of bonds hardening and therefore the compression of the unit cell. [77]

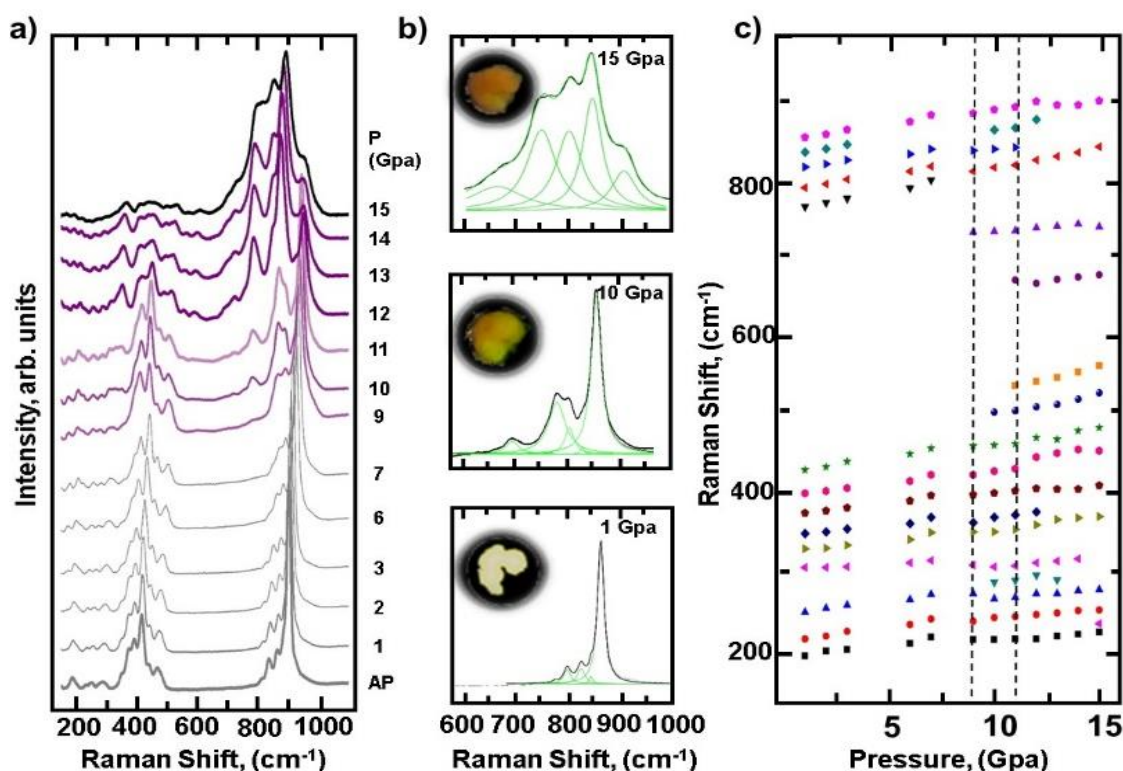


**Figure 61.** a) Evolution of Raman spectra from ambient pressure to 15 GPa (DAC) at room temperature, b) deconvolution of three spectra measured at 1, 10 and 15 GPa using Lorentzian profiles, insets show color changes with pressure and c) Pressure evolution of the identified Raman modes, dashed lines indicate average pressure of phase transitions.

Secondly, changes occur around 9-10 GPa and 11-12 GPa. At 9-10 GPa new bands appear at 290, 510 and 745  $\text{cm}^{-1}$  whereas the one at 811  $\text{cm}^{-1}$  disappeared. Around 11-12 GPa, three modes disappear at 290, 380 and 854  $\text{cm}^{-1}$ . These modifications can be explained by the structural changes occurring in the material. Another evidence of these possible phase transitions arises from color changes observed upon pressure using an optical microscope. The sample, initially white became successively yellow-green at 9 GPa and orange at 11 GPa (see Figure 61). *In situ* XRD will be needed in order to completely understand these spectral changes and directly correlate them with the structure but it was impossible in our working conditions.’ As a consequence, we used a combination of pressure and temperature in order to confirm structural changes *ex situ*. It is well known that temperature can help to reduce the pressure necessary to tackle the phase transition. For example, concerning the case of  $\text{Mn}_3\text{TeO}_6\text{-I}$ , a structural transition was evidenced around 18 GPa doing an *in situ* Raman spectroscopy in a diamond anvil cell without the use of high temperature. [79] At the same time, the new  $\text{Mn}_3\text{TeO}_6\text{-II}$  was isolated after modification of  $\text{Mn}_3\text{TeO}_6\text{-I}$  at 1173 K and 8 GPa, reducing the

transformation pressure in 10 GPa by adding high temperature. [80] Following this idea, the achievement of the new structural types of  $\text{LiLa}_5\text{O}_5(\text{VO}_4)_2$  was pursued using a Piston Cylinder Press able to work up to 3 GPa and 2000 K.

### III.1.2. Synthesis using High-Pressure High-Temperature experiments

Several compositions were tried. The initial precursors  $\text{Li}_2\text{CO}_3$ ,  $\text{V}_2\text{O}_5$  and  $\text{La}(\text{OH})_3$  or  $\text{Nd}_2\text{O}_3$  have been taken in different stoichiometric amounts as listed in Table 25. In order to remove residual water or carbonate molecules, the precursors have been preheated at 600°C overnight.

Powders of each compounds were hard-packed in 5x2 mm<sup>2</sup> Platinum capsule and sealed. Reactions were done in a Piston Cylinder press equipped with a 1/2 inch cell. Series of experiments were performed at different pressure-temperature conditions listed in Table 25. Throughout the experiment, the temperature was monitored with a W3Re–W25Re (Type D) thermocouple, the junction of which was placed near the sample. After the experiment, temperature was quenched and pressure was slowly released. The results are solid pellets made of a majority of powder assorted with tightly pressed small transparent crystals that were systematically studied.

**Table 25. Table of High-Pressure High-Temperature experiment conditions.**

Stoichiometry			Target conditions		Result after powder X-Ray analysis
Li	La	V	P (GPa)	T (°C)/ duration (h)	
1	5	2	2	700/3hr	unreacted mixture
1	5	2	2	900/2hr	HP- $\text{LiLa}_5\text{O}_5(\text{VO}_4)_2$ , $\text{La}(\text{OH})_3$ , $\text{LaVO}_4$
1	5	2	2.5	900/night	HP- $\text{LiLa}_5\text{O}_5(\text{VO}_4)_2$ , $\text{La}(\text{OH})_3$ , $\text{LaVO}_4$
1	5	2	2	1000/2hr	HP- $\text{LiLa}_5\text{O}_5(\text{VO}_4)_2$ , $\text{La}(\text{OH})_3$ , $\text{LaVO}_4$
1	5	2	2	1050/3hr	HP- $\text{LiLa}_5\text{O}_5(\text{VO}_4)_2$
1	5	2	2	1100/3hr	HP- $\text{LiLa}_5\text{O}_5(\text{VO}_4)_2$
1	5	4	2	900/2hr	AP- $\text{LiLa}_5\text{O}_5(\text{VO}_4)_2$ , $\text{LaVO}_4$
1	2	1	2	750/3hr	HP- $\text{LiLa}_2\text{O}_2\text{VO}_4$ , $\text{La}(\text{OH})_3$ , $\text{LaVO}_4$ , $\text{Li}_{0.52}\text{La}_2\text{O}_{2.52}(\text{CO}_3)_{0.74}$
1	2	1	2	850/3hr	HP- $\text{LiLa}_2\text{O}_2\text{VO}_4$ , $\text{La}(\text{OH})_3$ , $\text{LaVO}_4$ , $\text{Li}_{0.52}\text{La}_2\text{O}_{2.52}(\text{CO}_3)_{0.74}$
Li	Nd	V	P (GPa)	T (°C)	Result after powder X-Ray analysis
1	5	2	2	1100/3hr	HP- $\text{LiNd}_5\text{O}_5(\text{VO}_4)_2$

A first series of trials were started from stoichiometric ratio of Li:La:V corresponding to 1:5:2. Working at 2 GPa and 700 °C, the sample did not react. By increasing the temperature to 900°C a mixture of the ambient-pressure form of  $\text{LiLa}_5\text{O}_5(\text{VO}_4)_2$  and an unknown new compound was observed. The purification of the sample was tested through two different ways: increasing pressure or temperature. The increase of pressure up to 2.5 GPa while keeping the same temperature led to obtain the targeted phase assorted with lanthanum hydroxide, which origin may come from absorbed water when loading the high-pressure cell. However, a pure sample of new HP form of  $\text{LiLa}_5\text{O}_5(\text{VO}_4)_2$  (**1**) achieved in the  $1000^\circ\text{C} < T < 1100^\circ\text{C}$  temperature range, as it shown on Figure 62.

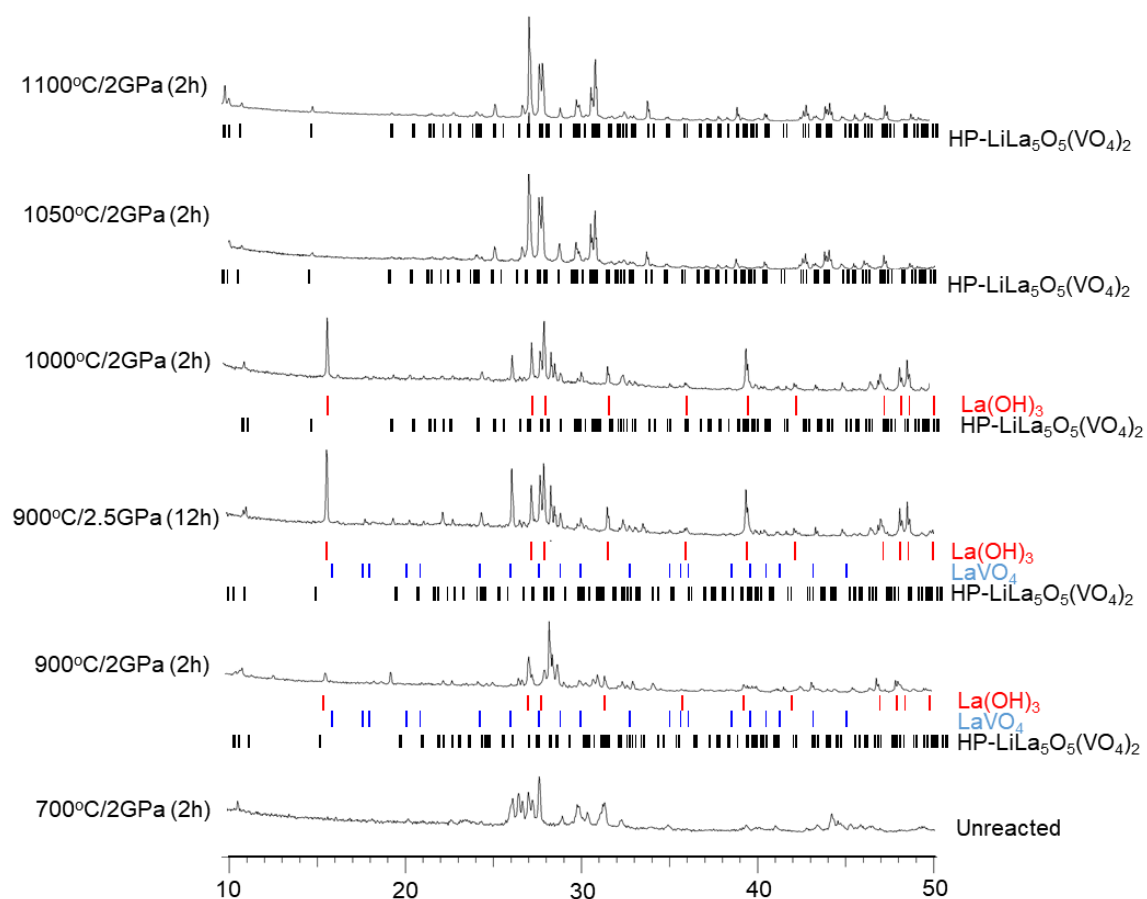


**Figure 62.** X-Rays powder diffraction patterns at different pressure-temperature conditions in series of trials were stoichiometric ratio of Li:La:V corresponding to 1:5:2.

Further changes of the ratio/composition were performed in order to check if it leads to the stabilization of another metastable phase.

Second series includes experiments on changed stoichiometric ratio of Li:La:V corresponding to 1:2:1. Grey non-homogenous tight mass became a result of both HP-HT experiments (see Table 25) and performed at 750°C and 850°C and a pressure of 2 GPa. The XRDP of the two experiments are shown on Figure 63. Tiny transparent colorless crystals of HP-LiLa<sub>2</sub>O<sub>2</sub>VO<sub>4</sub> phase (2) were found. They were associated with impurities of La(OH)<sub>3</sub>, LaVO<sub>4</sub> and Li<sub>0.52</sub>La<sub>2</sub>O<sub>2.52</sub>(CO<sub>3</sub>)<sub>0.74</sub>.

At this point, we were able to isolate two new phases: HP-LiLa<sub>5</sub>O<sub>5</sub>(VO<sub>4</sub>)<sub>2</sub> and HP-LiLa<sub>2</sub>O<sub>2</sub>VO<sub>4</sub>.

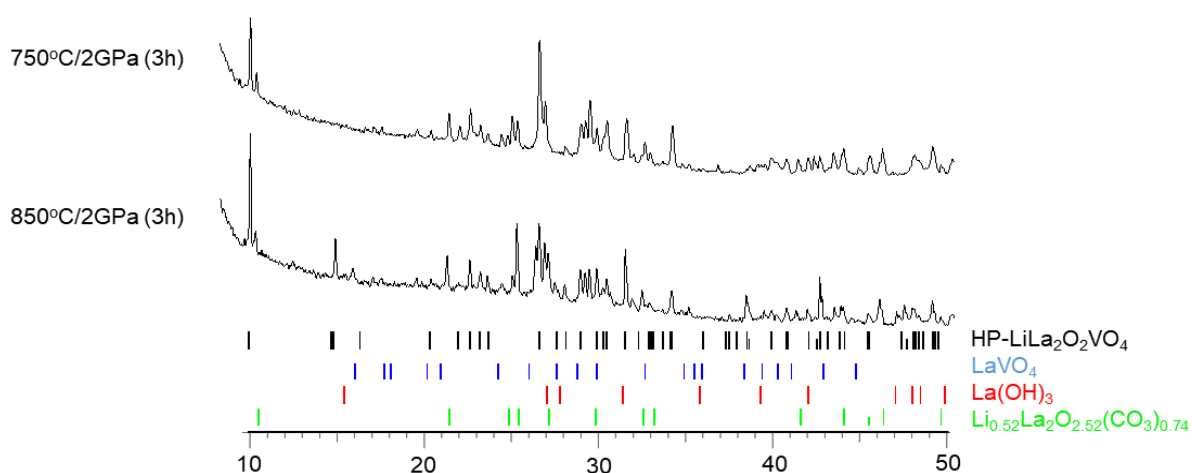


**Figure 63.** X-Rays powder diffraction patterns at different pressure-temperature conditions in second series of trials with stoichiometric ratio of Li:La:V corresponding to 1:2:1.

In a third step and in order to modify the magnetic or optical properties (*e.g.* as possible matrix hosting emitters for applications in WLEDs or lasers) [93] we tried to obtain the pure equivalent LiNd<sub>5</sub>O<sub>5</sub>(VO<sub>4</sub>)<sub>2</sub> compound. The previous experiments performed using common synthesis conditions (without pressure) systematically failed. Nevertheless, in literature, some works on the thermodynamic stability of Rare Earth based materials under extreme conditions are established. [60] For example, investigation of contraction or pressure versus ionic radii employed in the synthesis of cuprates gave informative results [94] concerning the possibility to substitute La by Nd in LiNd<sub>5</sub>O<sub>5</sub>(VO<sub>4</sub>)<sub>2</sub> and encourage us to apply pressure during the process.

The stoichiometry was exactly the same with the first series of experiments: Li:Nd:V ratio corresponding to 1:5:2. On the next Figure 64 the resulted powder of  $\text{LiNd}_5\text{O}_5(\text{VO}_4)_2$  (**3**) after HT-HP experiment is compared with initial compound synthesized at  $1100^\circ\text{C}$ . Powder patterns of both samples are similar to each other, except for one peak of  $\text{Li}_3\text{V}_6\text{O}_{13}$  impurity [95] in initial compound. Obviously in case of La to Nd substitution no phase transition can be detected applying the HP-HT conditions.

All the three phases evidenced in this part will be structurally characterized in the next part.

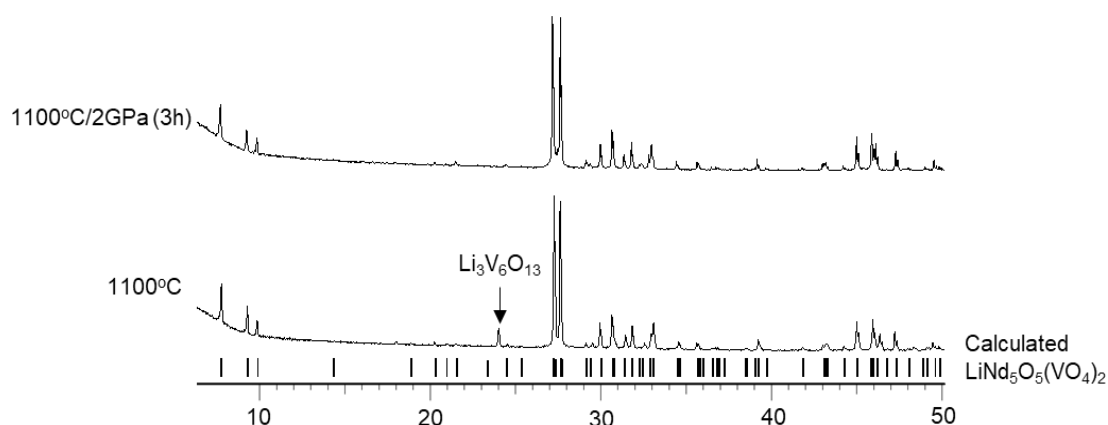


**Figure 64.** X-Rays powder diffraction patterns of initial  $\text{LiNd}_5\text{O}_5(\text{VO}_4)_2$  compound and HP-HT modified.

### III.1.3. Investigation of the new compounds

Tiny single crystals corresponding to each new compound were isolated from the samples before crushing:  $\text{LiLa}_5\text{O}_5(\text{VO}_4)_2$  (**1**),  $\text{LiLa}_2\text{O}_2\text{VO}_4$  (**2**) and  $\text{LiNd}_5\text{O}_5(\text{VO}_4)_2$  (**3**).

#### *a. The new HP form of $\text{LiLa}_5\text{O}_5(\text{VO}_4)_2$*

##### *- Single crystal XRD*

Tiny unshaped and colorless crystals of obtained  $\text{LiLa}_5\text{O}_5(\text{VO}_4)_2$  (**1**) were isolated and studied at ambient pressure using single crystal X-ray diffraction under conditions given in supplementary information (SI) in Table 27. It crystallized undoubtedly in a triclinic unit cell with lattice parameters of  $a = 5.8265(7) \text{ \AA}$ ,  $b = 12.3046(1) \text{ \AA}$ ,  $c = 18.737(2) \text{ \AA}$ ,  $\alpha = 102.125(7)^\circ$ ,  $\beta = 98.768(7)^\circ$ ,  $\gamma = 103.498(7)^\circ$  and  $P-1$  space group. The structure was solved using the charge flipping method [32] and refined using JANA 2006. [33] There are 10 symmetrically independent lanthanum and 4 independent vanadium positions whose atomic and anisotropic

thermal parameters were refined. 26 oxygen positions were added with isotropic thermal parameters. A careful analysis of the Fourier difference maps evidenced residual electronic density in the empty spaces around the  $[\text{VO}_4]$  units. It was assigned to two lithium positions. Due to its light contribution close to heavier atoms, atomic positions and thermal parameters were fixed. At the end of the refinement, residual factors led to merging factor  $R_{\text{int}} = 7.62\%$  for 9444 refined parameters and 6539 reflections with  $I > 3\sigma(I)$ . The atomic positions, displacement parameters are listed in SI Table 28, and Table 29. The main interesting distances are gathered in Table 30 and bond valence calculation in Table 31. Structural data for HP- $\text{LiLa}_5\text{O}_5(\text{VO}_4)_2$  phase were deposited with the number CSD-2005677. The crystal structure of HP form of  $\text{LiLa}_5\text{O}_5(\text{VO}_4)_2$  is shown in Figure 65.

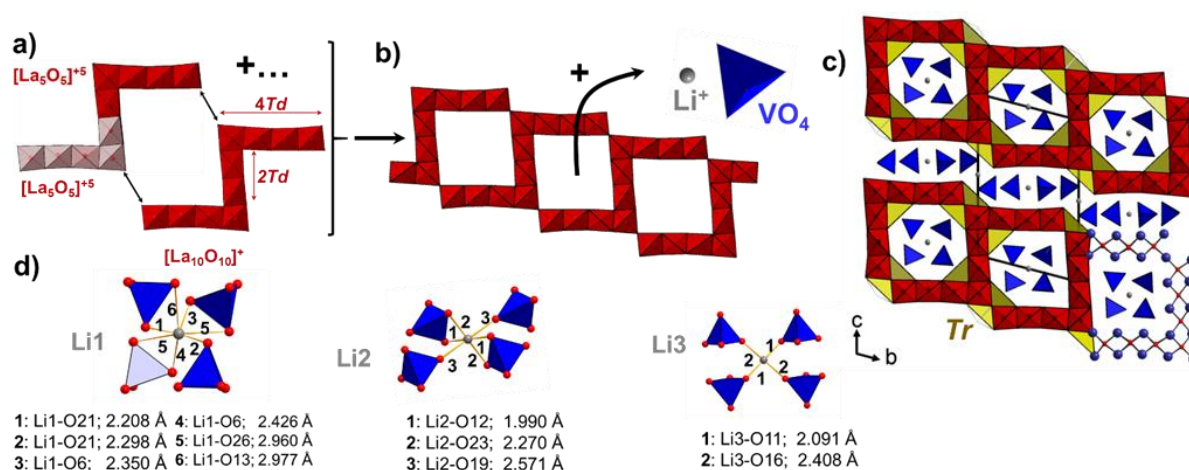


**Figure 65.** (a) Two  $[\text{La}_5\text{O}_5]^{5+}$  units are connected together by edge sharing to build  $[\text{La}_{10}\text{O}_{10}]^{10+}$  entity (b) sharing two corners with another  $[\text{La}_{10}\text{O}_{10}]^{10+}$  unit leading to (c) 2D opened layers hosting  $\text{VO}_4$  and  $\text{Li}^+$  cations to build the HP form of  $\text{LiLa}_5\text{O}_5(\text{VO}_4)_2$ . The oxo-centered tetrahedra ( $Td$ ) are marked by red and triangles ( $Tr$ ) by yellow. (d) Geometrical environment of the Li sites in the structure of HP form of  $\text{LiLa}_5\text{O}_5(\text{VO}_4)_2$ .

The description of the structure is performed using the antiphase approach as it was the case for the AP (ambient-pressure) polymorph. [9] The O-La bonds building regular  $[\text{OLa}_4]$  tetrahedra ( $Td$ ) varied from 2.29(1) to 2.51(1) Å, in good agreement with what it is classically observed for similar structures. [83] Five  $Td$  share common edges and form  $[\text{La}_5\text{O}_5]^{5+}$  units of four  $4Td$  width and  $2Td$  height (Figure 65(a)). Two of these units are connected together by edge sharing of  $Td$  in the height, leading to another  $[\text{La}_{10}\text{O}_{10}]^{10+}$  entity (Figure 65(b)). These entities are sharing corners to build 2D corrugated layers with 1D tunnels of  $3Td$  width and height (Figure 65(c)). These tunnels are hosting four isolated vanadate. The layers are stacked together,

separated by sheets of isolated vanadate (Figure 65(c)). The association of  $[\text{VO}_4]$  marked out square channels and open spaces in layers and tunnels occupied by  $\text{Li}^+$  cations respectively coordinated by four and six oxygen. Li-O bond distances are in the same order of magnitude as what it is commonly observed in related oxo-centered phases ranging from 2.20(1) to 2.57(1) Å. There are two (for Li2) and one (for Li1)  $\text{Li}^+$  cations per tunnel, along a period of about 5.8 Å (Figure 65(d)).

The filling of square channels shows strong similarities with the AP phase (Figure 66(a)). In AP and HP crystal structures, one oxygen per  $[\text{VO}_4]$  group is involved in  $\text{OLA}_3$  triangular units (*Tr*) which strengthen the polycationic backbone. A possible transformation process from the AP phase can be envisaged by the collapse of one of the step or height that completes the square channels in the HP form as presented in Figure 66 (b).

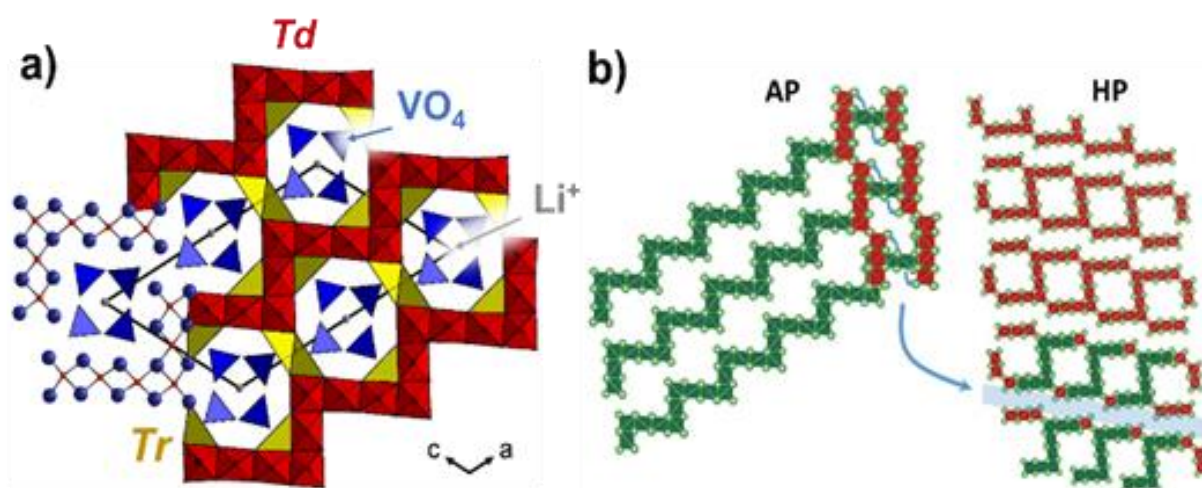


**Figure 66.** (a) crystal structure of AP- $\text{LiLa}_5\text{O}_5(\text{VO}_4)_2$  and (b) relationship between the AP and the HP form of  $\text{LiLa}_5\text{O}_5(\text{VO}_4)_2$ .

The purity of the sample was checked with Topas-Academic [82] and doing a Rietveld refinement. Due to the small amount of sample impacting the quality of XRPD data and the complexity of the crystal structure the number of parameters refined was limited. The unit cell parameters of HP- $\text{LiLa}_5\text{O}_5(\text{VO}_4)_2$  were refined to  $a = 5.8295(2)$  Å,  $b = 12.3033(4)$  Å,  $c = 18.7438(5)$  Å,  $\alpha = 102.115(1)^\circ$ ,  $\beta = 98.707(2)^\circ$  and  $\gamma = 103.451(2)^\circ$  that is in good agreement with the single crystal structure refinement. As it can be observed on Figure 67, the powder sample consists in the only HP- $\text{LiLa}_5\text{O}_5(\text{VO}_4)_2$  phase.

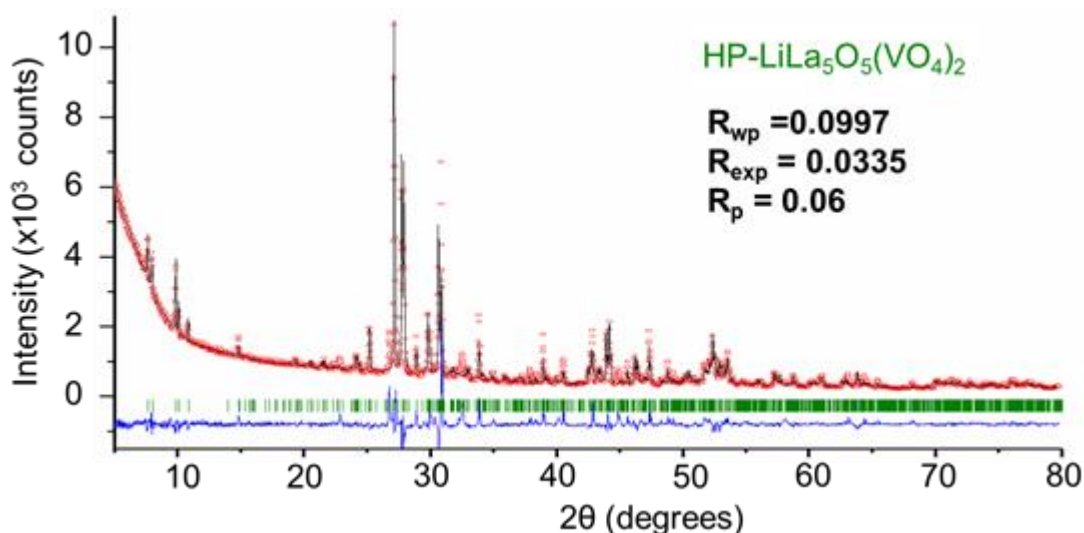


Figure 67. X-Ray powder data is shown as dark curve and Rietveld refinement for HP-LiLa<sub>5</sub>O<sub>5</sub>(VO<sub>4</sub>)<sub>2</sub> is red. Difference curve is shown in blue color.

To confirm the existence of new crystal structure and to identify possible local phenomena, a HAADF study was provided.

- High-angle annular dark-field imaging (HAADF)

The HAADF image allowed a real view of the crystal structure and confirmed the observed stacking by showing the perfect arrangement of the square tunnels and the layers. Generally speaking, in the HAADF-STEM images, the contrast is proportional to the square of the atomic number ( $Z$ ), which allows to consider these images as a projection of the structure with the heavy atoms brighter. The high-angle annular dark field (HAADF) image has been obtained on a TEM FEI TITAN Themis. The powder was crushed and dropped in the form of alcohol suspension on carbon supported copper grids followed by evaporation under ambient condition.

The [100] HAADF image for  $\beta$ -LiLa<sub>5</sub>O<sub>5</sub>(VO<sub>4</sub>)<sub>2</sub> is shown in Figure 68(a). As observed from the crystal structure, the image confirmed the stacking by showing the perfect arrangement of the square tunnels and the layers. The white and the grey dots correspond to lanthanum and vanadium respectively, Li atoms are not visible. In some areas pointed out by red arrows in Figure 68(a) and (c), some defects are evidenced. They are due to the substitution of vanadium by lanthanum inside the square tunnels so that it is possible to expect a substitution of [VO<sub>4</sub>] groups by [OLa<sub>4</sub>] Td. A hypothetical representation of the structure of the defect is drawn on Figure 68(c).

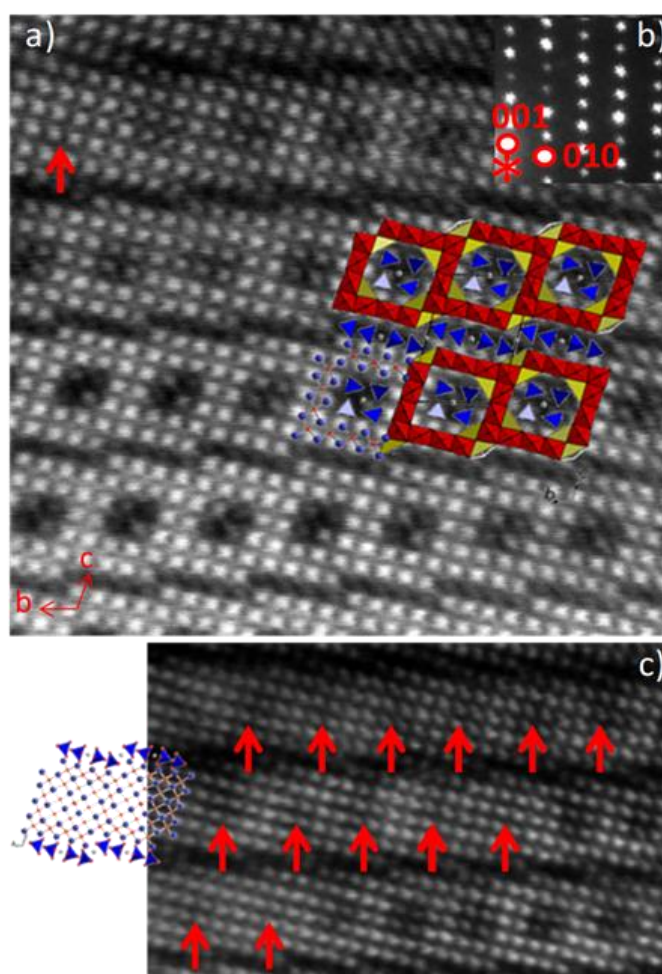


**Figure 68.** (a) [100] HAADF image and superimposition of the projected structure of the new  $\text{LiLa}_5\text{O}_5(\text{VO}_4)_2$ . It clearly evidenced the  $[\text{La}_5\text{O}_5]^{5+}$  layers (white dots corresponding to La atoms) and the darker part corresponding to the related  $[\text{Li}_{0.5}(\text{VO}_4)]^{1.5-}$  tunnels and  $[\text{Li}_{0.5}(\text{VO}_4)]^{1.5-}$  interlayer. (b) shows the corresponding indexed electron diffraction pattern (EDP) and (c) red arrows highlight areas where the square tunnels disappeared due to the local substitution of V by La atoms. The corresponding projected model is presented.

At a local scale, this intergrowth is the proof of the possibility to obtain 2D layers build on association of  $[\text{OLa}_4]$  tetrahedra sharing edges which has, to the best of our knowledge, never been observed at atomic scale. This open the doors to a wide range of structural possibilities implying the combined use of pressure and temperature and the rational use of a negative balancing counterpart able to fit in the interlayer space. The presence of square channels was already observed in an oxo-centered Bi-based phase:  $[\text{Bi}_{12}\text{O}_{15}]\text{Li}_2(\text{SO}_4)_4$  [84] (structure shown in Figure 69) which is an example of a 3D porous network built on  $[\text{OBi}_4]$  entities and hosting 1D channels with sulfates and  $\text{Li}^+$  cations.

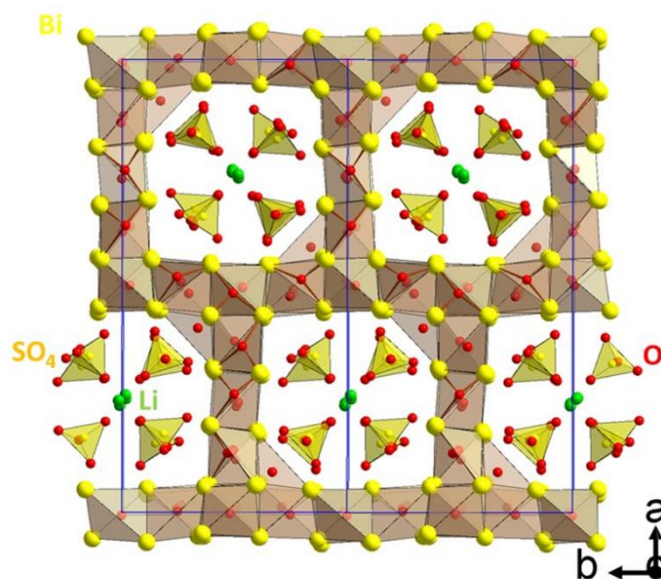


**Figure 69. Reminder of the crystal structure of  $[\text{Bi}_{12}\text{O}_{15}]\text{Li}_2(\text{SO}_4)_4$ [84]. The multi-dimensional framework is evidenced (3D porous cationic framework with 1D channels hosting sulfates and  $\text{Li}^+$  cations).**

There are also similar triangular  $[\text{OBi}_3]$  units holding the polycationic backbone. To date in the literature, the multi-dimensional behavior based on the association of oxo-centered units is scarce and only based on Bi-phases. Three examples have been reported so far, showing layers of triangular pores with various sizes of sections separated by sheets of chlorine. [85] To the best of our knowledge, this multi-dimensionality behavior is observed for the first time in Ln-based compounds. Here the application of pressure may compress the units leading to the formation of unusual entities.

### *b. $\text{LiNd}_5\text{O}_5(\text{VO}_4)_2$ characterization*

#### *- Single crystal XRD*

The single crystal structure of  $\text{LiNd}_5\text{O}_5(\text{VO}_4)_2$  (**3**) was solved in the monoclinic space group  $C2/m$  with cell parameters of  $a = 19.4507(2) \text{ \AA}$ ,  $b = 5.7848(5) \text{ \AA}$ ,  $c = 12.2593(1) \text{ \AA}$  and  $\beta = 117.847(5)^\circ$  with  $Z = 2$  (Table 32).  $\text{LiNd}_5\text{O}_5(\text{VO}_4)_2$  is isostructural to the known AP- $\text{LiLa}_5\text{O}_5(\text{VO}_4)_2$  which projection is shown in Figure 66(a). The refinement satisfactory converged with residual factors refined to  $R_F = 0.0380$  and  $wR_F = 0.0814$ . All main information are gathered in SI in Table 33, Table 34, Table 35 and Table 36. Structural data for phase (**3**) were deposited with the number CSD-2005696. The unit cell volume of  $\text{LiNd}_5\text{O}_5(\text{VO}_4)_2$  (**3**) is

smaller than the La analogue, in accordance with the lanthanide contraction as going through the series. In literature, some examples, mainly focused on perovskites, agreed wholeheartedly with the possibility to successfully replace La by smaller lanthanides. [97]

The purity of the  $\text{LiNd}_5\text{O}_5(\text{VO}_4)_2$  powder sample was confirmed also by X-Ray diffraction on Figure 70. The unit cell parameters are reproducible with single crystal data:  $a = 19.4670(4) \text{ \AA}$ ,  $b = 5.7881(1) \text{ \AA}$ ,  $c = 12.2749(3) \text{ \AA}$  and  $\beta = 117.864(1)^\circ$ . In absence of impurities, the magnetic properties were investigated.

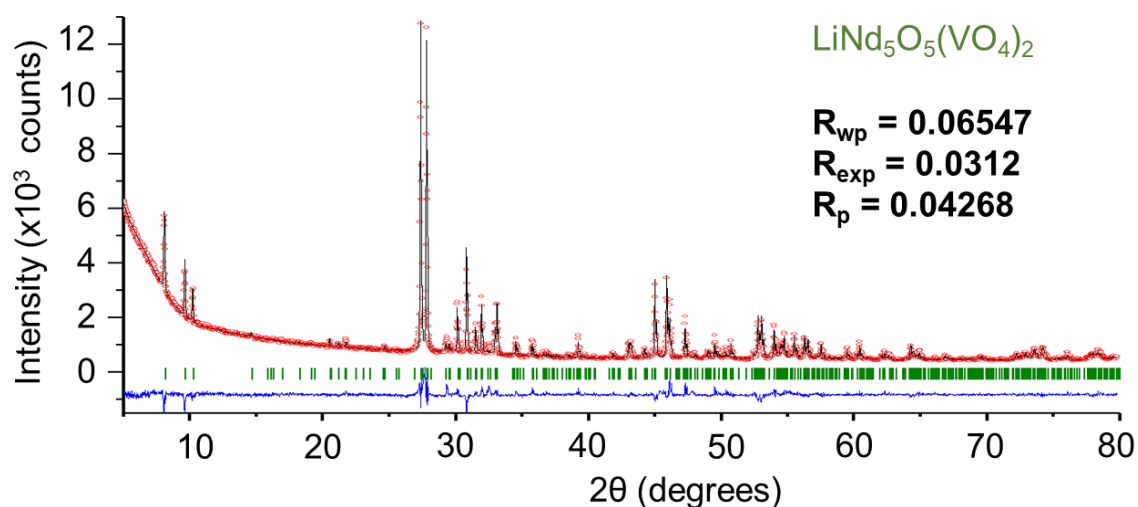


Figure 70. X-Ray powder data is shown as dark curve and Rietveld refinement for  $\text{HP-LiLa}_5\text{O}_5(\text{VO}_4)_2$  is red. Difference curve is shown in blue color.

- Magnetic measurements

Substitution of La for Nd opens up for further magnetic studies so the magnetic susceptibility for  $\text{LiNd}_5\text{O}_5(\text{VO}_4)_2$  was measured.

Magnetic measurements were performed on a Physical Properties Measurement System (PPMS) Dynacool (9T) system from Quantum Design. Zero field cooling (ZFC) and field cooling (FC) procedures between  $2 < T < 300 \text{ K}$  under a 0.1 T magnetic field were measured.

However, no transition was detected down to 2 K probably due to the relative large distance between the  $\text{Nd}^{3+}$  cations (from 3.6 to  $4 \text{ \AA}$ ). The direct and inverse magnetic susceptibility are shown for  $\text{LiNd}_5\text{O}_5(\text{VO}_4)_2$  on Figure 71. Curie-Weiss law fit gives  $C = 8.24$  and  $\theta = -34 \text{ K}$  implying AFM interactions and an experimental value of  $\mu_{\text{eff}} = 3.6 \mu_{\text{B}}$ , in accordance with the theoretical value of  $\mu_{\text{theo}} = 3.62 \mu_{\text{B}}$  for  $\text{Nd}^{3+}$ .

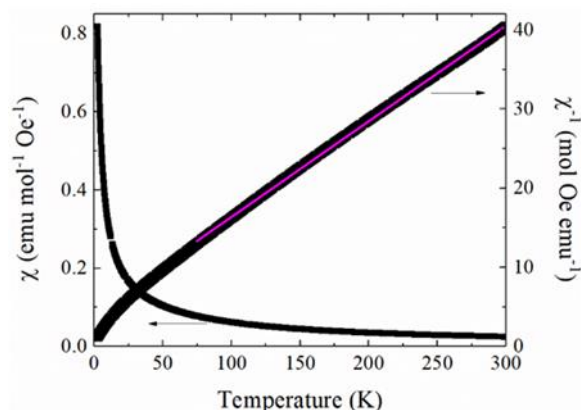


**Figure 71.** Direct and inverse magnetic susceptibility for  $\text{LiNd}_5\text{O}_5(\text{VO}_4)_2$ . The purple line shows a Curie-Weiss law fit.

To finish with, a crystal was selected from a sample of composition Li:La:V in ratio: 1:2:1 and study by single crystal X-Ray Diffraction.

*c. The new  $\text{LiLa}_2\text{O}_2\text{VO}_4$*

- Single crystal XRD

Again, the crystal structure was solved on a single crystal. New HP- $\text{LiLa}_2\text{O}_2\text{VO}_4$  also crystallized in  $P-1$  space group with  $a = 5.8144(7) \text{ \AA}$ ,  $b = 5.8167(7) \text{ \AA}$ ,  $c = 8.527(1) \text{ \AA}$ ,  $\alpha = 98.184(7)^\circ$ ,  $\beta = 100.662(7)^\circ$  and  $\gamma = 92.579(7)^\circ$  unit cell parameters. Crystal parameters, data collection and structure refinement details for the crystal of  $\beta\text{-LiLa}_2\text{O}_2\text{VO}_4$  are given in SI Table 37. The procedure of solving and refining the structure exactly coincides with the one previously described for HP form of  $\text{LiLa}_5\text{O}_5(\text{VO}_4)_2$ .

There are 2 symmetrically independent sites of lanthanum atoms in this crystal structure. Both lithium and vanadium atoms have just one unique symmetrically independent position. There is a total of six oxygen positions. All atoms were well localized and refined with isotropic thermal parameters. Atomic data parameters are shown in SI Table 38, anisotropic atomic displacement and main interesting distances added to SI Table 39 and

Table 40, respectively. Bond valence calculations for cations and anions are in good agreement with the expected values are given in SI table 41. It confirms the possibility to describe the structure in terms of oxo-centered tetrahedra. Structural data were deposited with the number CSD-2005672.

At the end of the refinement, residual factors led to  $R_{\text{int}} = 2.07\%$  (817 refined parameters and 667 reflections with  $I > 3\sigma(I)$ ).  $[\text{OLa}_4]$   $Td$  are formed around O(2) and O(3) atoms, with the O – La distances in a range of 2.345(5) to 2.466(3) Å. Oxo-centered  $Td$  shared common edges, forming  $[\text{La}_2\text{O}_2]^{2+}$  infinite 2D layers. Between them, vanadium forms regular  $[\text{VO}_4]$  tetrahedra. Only O(1) atom is not shared with another tetrahedron. 2D infinite layers are formed by two  $[\text{LiO}_4]$  tetrahedra sharing an edge and all their oxygen being corner-shared with  $[\text{VO}_4]$  tetrahedra (see Figure 72(a)). Li-O bond lengths are very regular varying from 1.959(6) to 1.974(9) Å (see Figure 72(b)).

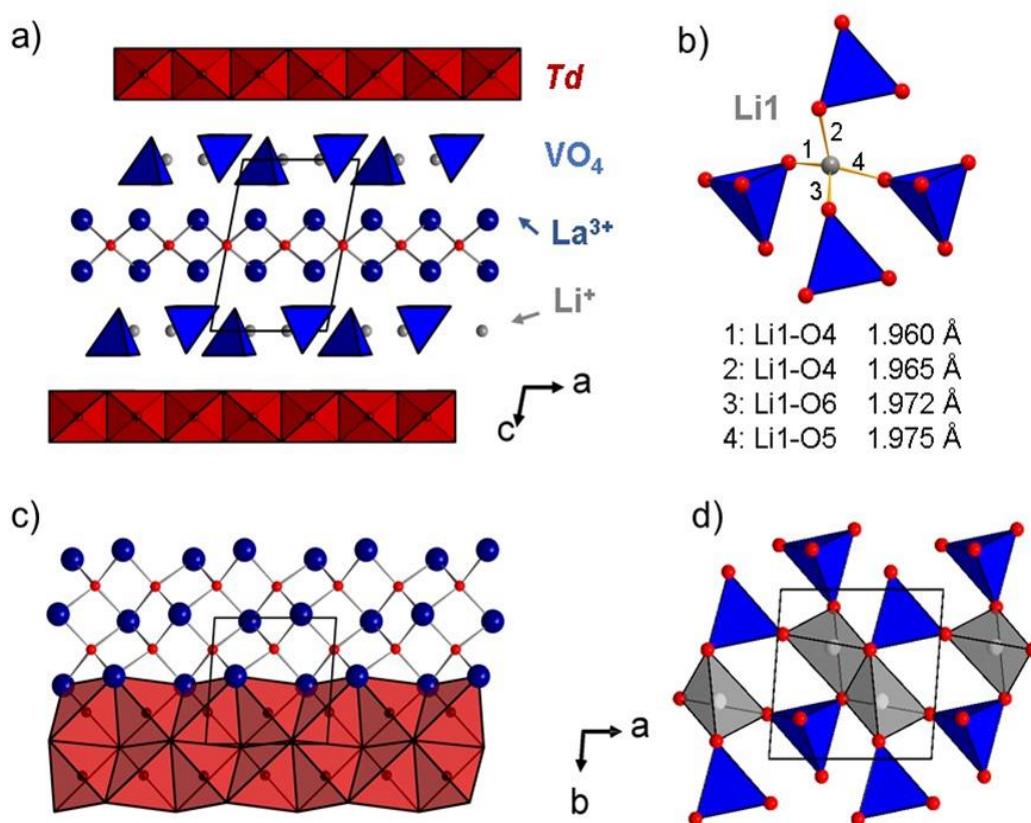


**Figure 72.** (a) General projections of the  $\text{LiLa}_2\text{O}_2\text{VO}_4$  crystal structure and (b) Li atom tetrahedrally coordinated. Types of alternated layers: (c)  $[\text{La}_2\text{O}_2]^{2+}$  and (d)  $[\text{LiVO}_4]^{2-}$ .

Different arrangements of  $[\text{LiO}_4]$  and  $[\text{VO}_4]$  polyhedrons exist and result in networks of variable dimensionality, for instance, 1D infinite chains in  $\text{LiMnVO}_4$ . [86] There,  $[\text{LiO}_4]$  and  $[\text{VO}_4]$  are edge-sharing and these two-component units form corner-sharing 1D chains.  $\text{Rb}_2\text{LiVO}_4$  shows 2D layers based on edge- and corner-sharing  $[\text{LiO}_4]$  and  $[\text{VO}_4]$  tetrahedra. [87] 3D framework with tunnels are formed with corner-sharing  $[\text{LiO}_4]$  and  $[\text{VO}_4]$  as observed

in  $\text{Ba}_3\text{Li}_2\text{V}_2\text{O}_7\text{C}_{14}$ . [88] To the best of our knowledge,  $\text{LiLa}_2\text{O}_2\text{VO}_4$  sub-anionic layer appears to be innovative.

As depicted on Figure 72 (c) and (d), the crystal structure of new  $\beta$ -  $\text{LiLa}_2\text{O}_2\text{VO}_4$  is based on  $[\text{La}_2\text{O}_2]^{2+}$  and  $[\text{LiVO}_4]^{2-}$  different types of layers.  $[\text{La}_2\text{O}_2]^{2+}$  layers can be found in  $\text{La}_2\text{O}_2(\text{XO}_4)$ , ( $\text{X} = \text{S}, \text{Mo}$  or  $\text{Cr}$ ). [89] Also these anti-fluorite-type  $[\text{Ln}_2\text{O}_2]^{2+}$  layers can be observed in d-metal pnictide oxides. [90] The number of crystal structures found with these layers remain limited compared with those found with the equivalent  $[\text{Bi}_2\text{O}_2]^{2+}$ , mainly concerning Aurivillius phases. This is probably due to the bismuth capacity to fit into a more distorted tetrahedron related to its lone pair.

The X-ray powder diffraction analysis of a  $\text{LiLa}_2\text{O}_2\text{VO}_4$  shows that the sample mainly corresponds to the new HP- $\text{LiLa}_2\text{O}_2\text{VO}_4$  phase, with some impurities as  $\text{LaVO}_4$  [91] and  $\text{Li}_{0.52}\text{La}_2\text{O}_{2.52}(\text{CO}_3)_{0.74}$ . [92] Resulted plot is shown on Figure 73. The refined unit-cell parameters are  $a = 5.7565(3) \text{ \AA}$ ,  $b = 5.8036(3) \text{ \AA}$ ,  $c = 8.4846(3) \text{ \AA}$ ,  $\alpha = 98.304(4)^\circ$ ,  $\beta = 100.560(4)^\circ$  and  $\gamma = 93.383(4)^\circ$ .

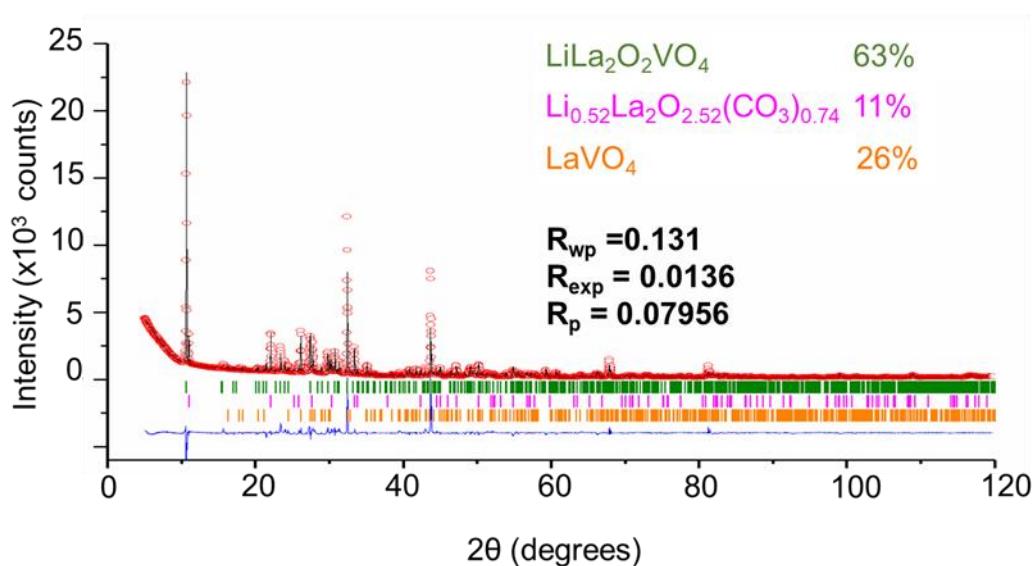


Figure 73. Rietveld refinement pattern of new HP- $\text{LiLa}_2\text{O}_2\text{VO}_4$  phase and several impurities, that are shown in orange, green and pink colors.

### III.1.4. Conclusion

The interests in using high pressure for stabilizing new inorganic materials are various and were largely detailed in. [96] This research gives three different examples of these interests:

- In the case of  $\text{LiLa}_5\text{O}_5(\text{VO}_4)_2$  the new high-pressure polymorph appears thanks to the so called '*densification effect*'. This process enables the stabilization of a phase/polymorph that would never be obtained without pressure and is strongly linked to the compression of the entailed chemical bonds. In our example, calculating the volume variation over the number of chemical units per unit cell between the HP phase and the AP phase for  $\text{LiLa}_5\text{O}_5(\text{VO}_3)_2$ , result in a foreseen negative value equal to  $-31\text{\AA}^3$  that totally confirmed the phenomena.
- Concerning  $\text{LiNd}_5\text{O}_5(\text{VO}_4)_2$ , the reason of the efficiency of using high pressure is linked to the possibility to compress the atoms themselves through a modification of their electronic configuration and atomic orbitals. This enables to connect atoms that would never react together. Some examples exist in literature, mainly focused on perovskites in which La was successfully replaced by Pr or Nd. [98,97]
- The case of  $\text{LiLa}_2\text{O}_2(\text{VO}_4)$  is slightly different. To date, using AP conditions, this stoichiometry was never tackled. In here, high pressure is stabilizing metastable phases over more thermodynamically stable ones. This implies that the thermodynamic factors modified by the use of high pressure are crucial, increasing the reactivity of precursors through a reduction of the inter-atomic bond length. [97]

In situ DAC-Raman spectroscopy was used to identify a potential system for high-pressure synthesis, Li-Ln-V-O. Three new phases have been obtained via HP-HT combined conditions. All of them can be described on oxo-centered tetrahedral units.  $\beta\text{-LiLa}_5\text{O}_5(\text{VO}_3)_2$  shows a straight relation to its ambient-pressure polymorph through a collapse of one of its building units through the application of pressure. The multi-dimensional behavior was also observed through HAADF microscopy. A new  $\text{LiLa}_2\text{O}_2(\text{VO}_4)$  phase has been obtained with novel 2D layers. New  $\text{LiNd}_5\text{O}_4(\text{VO}_4)_2$  has been also obtained and demonstrates that the incorporation of smaller rare earth cations is promoted by high pressure. More extreme conditions may allow access the  $\beta$  polymorph for  $\text{Ln} = \text{Nd}$ . This work demonstrates the possibility to easily modify the original polymorphs, to access unknown and to incorporate other cations into oxo-centered based compounds through HP-HT treatments and opens up a wide range for investigation.

In the next part, another system will be presented with the isolation of the new and complex  $Gd_8V_2O_{17}$  and its reduced form.

## III.2. Ln-V-O system investigation

### III.2.1. Context

#### *a. From $La_7V_3O_{18}$*

This investigation follows the discovery of polytypes  $\alpha$  and  $\beta$  of the new oxyvanadate  $La_7O_6(VO_4)_3$ . [8] The  $\alpha$ -form shows a complex structure solved using precession electron diffraction and X-ray diffraction data. The monoclinic unit cell ( $a= 13.0148(3)$  Å,  $b= 19.1566(5)$  Å,  $c= 7.0764(17)$  Å, and  $\beta= 99.87(1)^\circ$ , (S.G.  $P2_1$ ) turns into a different one ( $a= 13.0713(4)$  Å,  $b= 18.1835(6)$  Å,  $c= 7.1382(2)$  Å, and  $\beta= 97.31(1)^\circ$ , S.G.  $P2_1/n$ ) at  $525^\circ\text{C}$ . Both polytypes are built on  $[La_7O_6]^{9+}$  polycationic units building a 3D cationic network showing rectangular channels hosting isolated  $[VO_4]$  tetrahedra. The difference between the two polymorphs is mainly related to a rotation of vanadates while the polycationic network remain almost unchanged. This new structure acted as a phosphor able to host emitters. It was successfully doped with different amounts of  $Sm^{3+}$  and  $Eu^{3+}$ . The photoluminescence, photoluminescence spectra and decay times were measured and analyzed. Under UV excitation, the emission light becomes bright and reddish orange which is mainly related to the V-O band. A summary of these points is presented on Figure 74.

During this study, several other experiments were provided in order to substitute lanthanum by other lanthanide, expecting other properties. It is well known that lanthanides may substitute themselves quite easily nevertheless with some exception. [10] Particularly, gadolinium gave interesting results. The ionic radii of  $La^{3+}$  and  $Gd^{3+}$  in coordination VIII are respectively 1.16 and 1.05 Å which plays in favor of a possible substitution. Although  $La^{3+}$  has no particular output in terms of properties, using gadolinium may open the door of further physical properties, for example magnetocaloric properties. [12] Also Gadolinium Oxide in particular shape and size can be used as Multimodal Contrast Agents for Optical and Magnetic Resonance Imaging. [11]

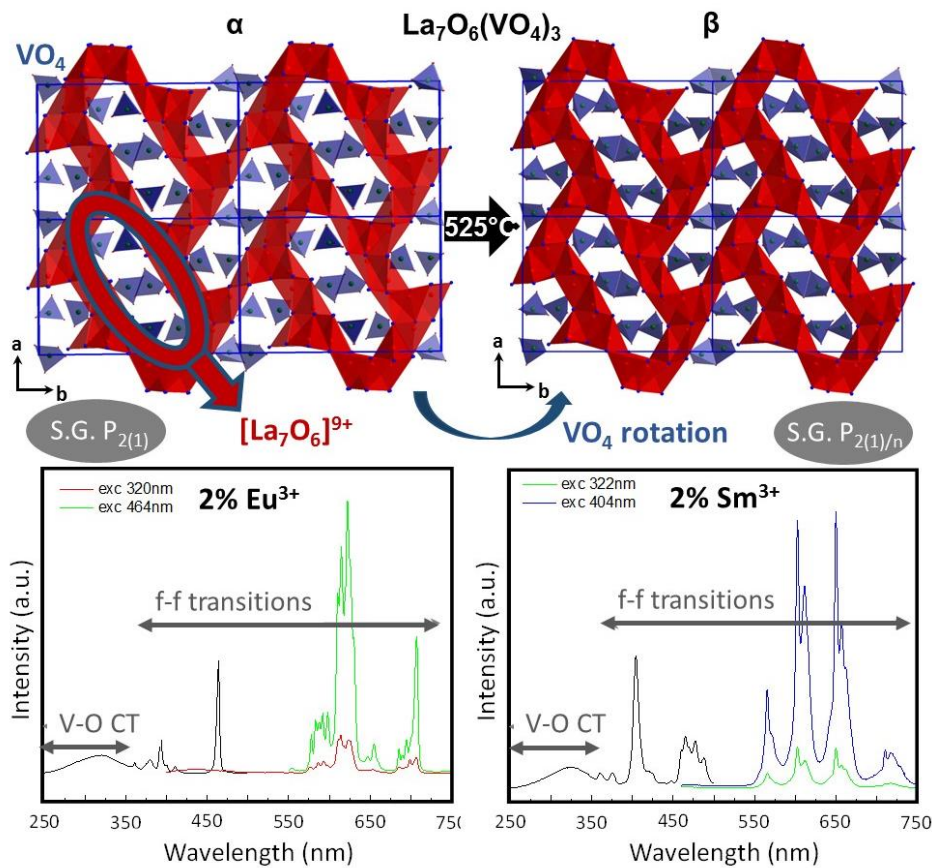


**Figure 74.** General overview on crystal structure organization of  $\alpha$ - $\text{La}_7\text{O}_6(\text{VO}_4)_3$  and  $\beta$ - $\text{La}_7\text{O}_6(\text{VO}_4)_3$ . The  $[\text{La}_7\text{O}_6]^{9+}$  polycationic backbone are shown in red, isolated  $\text{VO}_4$  tetrahedra in blue. RT combined excitation–emission spectrum of 2%  $\text{Eu}^{3+}$  compared to 2%  $\text{Sm}$ -doped  $\text{La}_7\text{O}_6(\text{VO}_4)_3$ .

### *b. Bibliography of $\text{Ln}_8\text{V}_2\text{O}_{17}$ phases*

The initial sample with  $\text{La}_7\text{O}_6(\text{VO}_4)_3$  composition was synthesized under conditions detailed in ref [8].  $\text{Gd}_2\text{O}_3$  precursor has been preheated at  $900^\circ\text{C}$  and grinded in an agate mortar with  $\text{V}_2\text{O}_5$ . The purpose was to prepare homogeneous powder with stoichiometric composition of  $\text{Gd}/\text{V}/\text{O}$  respective to 7:3:18 ratio. Ethanol was added to initial mixture of precursors to provide better homogenization. Initial powder was overgrinded and gradually heated at  $500^\circ$  and  $1100^\circ\text{C}$  during 12h. Platinum crucible was used in this experiment series in order to avoid adverse interactions with any component of other crucibles.

The X-Ray analysis of the resulted sample revealed a mixture of two phases:  $\text{GdVO}_4$  [13] and  $\text{Gd}_8\text{V}_2\text{O}_{17}$  referenced by the PDF2 standard card No. 22-0297 in the International Centre for Diffraction Data (ICDD) database. This card is intriguing. It is of low precision and almost empty. A bibliography investigation on the  $\text{Ln}_8\text{V}_2\text{O}_{17}$  phases showed recent studies on lanthanides with atomic number between 64 and 70 namely  $\text{Gd}$ ,  $\text{Tb}$ ,  $\text{Dy}$ ,  $\text{Ho}$ ,  $\text{Er}$ ,  $\text{Tm}$  and  $\text{Yb}$

and also Y. This implies that the ionic radii of the cation have a key role in formation of phases with general formula of  $\text{Ln}_8\text{V}_2\text{O}_{17}$ . According to the published data of existing compounds, it was supposed that for successful formations of this phases ionic radii has to be under 1.053 Å.

Many investigations were performed on these Ln-V-O systems. The thermodynamic properties and phase equilibria were studied long time ago on all cations. [14-23] The luminescence properties of self-activation [24] or emission through  $\text{Eu}^{3+}$  doping [25] were studied for the  $\text{Gd}_8\text{V}_2\text{O}_{17}$  phase. Also, the electrical transport properties were studied on  $\text{Yb}_{8-x}\text{Y}_x\text{V}_2\text{O}_{17}$  ( $x = 0, 2, 8$ ) compounds. [26] Nevertheless, no crystal structure exists for no-one of existing phases. As a consequence, no structure-properties correlation was established. However, unit cell parameters are mentioned even if they are controversial. In order to have an overall perspective of the bibliographic information, a Table 26 of reported compounds in Ln-V-O systems was created.

**Table 26. Table of reported compounds in Ln-V-O systems.**

<b>Ln</b> <i>Ionic radii</i> (Å)	<b>Crystal system</b>	<b>Unit cell parameters</b>	<b>Studied properties</b>	<b>References</b>
<b>Gd</b> 1.053	Triclinic		Optical, luminescence	[27, 28]
<b>Dy</b> 1.027	Monoclinic	$a= 10.69\text{Å}; b= 8.81\text{Å}, c=15.75\text{Å}; \beta= 99.1^\circ; V=1460\text{Å}^3$	Thermodynamic	[20]
	Tetragonal	$a= 9.32\text{Å}; c= 17.34\text{Å}, =1506\text{Å}^3$		
<b>Y</b> 1.019	Monoclinic	$a= 8.56\text{Å}; b= 8.16\text{Å}, c= 10\text{Å}; \beta= 89.26^\circ; V= 698\text{Å}^3$	Electronic transport, thermodynamic	[30]
	Triclinic	$a= 9\text{Å}; b= 9.32\text{Å}, c= 9.86\text{Å}; \alpha= 77.61^\circ; \beta= 116.82^\circ; \gamma= 116.29^\circ; V= 662\text{Å}^3$		
<b>Ho</b> 1.015	Monoclinic	$a= 10.69\text{Å}; b= 8.43\text{Å}, c= 15.22\text{Å}; \beta= 98.4^\circ; V= 1360\text{Å}^3$	Thermodynamic	[20]
<b>Er</b> 1.004	Monoclinic	$a= 10.45\text{Å}; b= 8.42\text{Å}, c= 16.05\text{Å}; \beta= 98.08^\circ; V= 1397\text{Å}^3$	Thermodynamic	[21]
<b>Tm</b> 0.994	Monoclinic	$a= 10.42\text{Å}; b= 8.30\text{Å}, c= 16.07\text{Å}; \beta= 98.1^\circ; V= 1377\text{Å}^3$	Thermodynamic	[22]
	Monoclinic	$a= 10.39\text{Å}; b= 8.24\text{Å}, c= 15.89\text{Å}; \beta= 98.47^\circ; V= 1346\text{Å}^3$	Electronic transport, thermodynamic	[27]
<b>Yb</b> 0.985	Triclinic	$a= 8.93\text{Å}; b= 9.25\text{Å}, c= 9.79\text{Å}; \alpha= 77.68^\circ; \beta= 106.36^\circ; \gamma= 116.35^\circ; V= 1397\text{Å}^3$		[31]

In this chapter,  $\text{Gd}_8\text{V}_2\text{O}_{17}$  will be structurally fully investigated and its magnetocaloric properties studied in collaboration with R. Sanchez Punch from the Universidad Complutense of Madrid. Its reduction under several reducing agents was also studied.

### III.2.2. A new 3D framework: $Gd_8V_2O_{17}$

#### *a. Synthesis of the powder*

Aware of the interest in working on these systems, a sample of composition  $Gd_8V_2O_{17}$  was synthesized using the conditions mentioned above. Different temperatures were tested, ranging from 1100°C to 1700°C. A pure sample was obtained for a temperature of 1500°C. The XRDP shows a perfect matching with the PDF card No. 22-0297 corresponding to the targeted phase (see Figure 75).

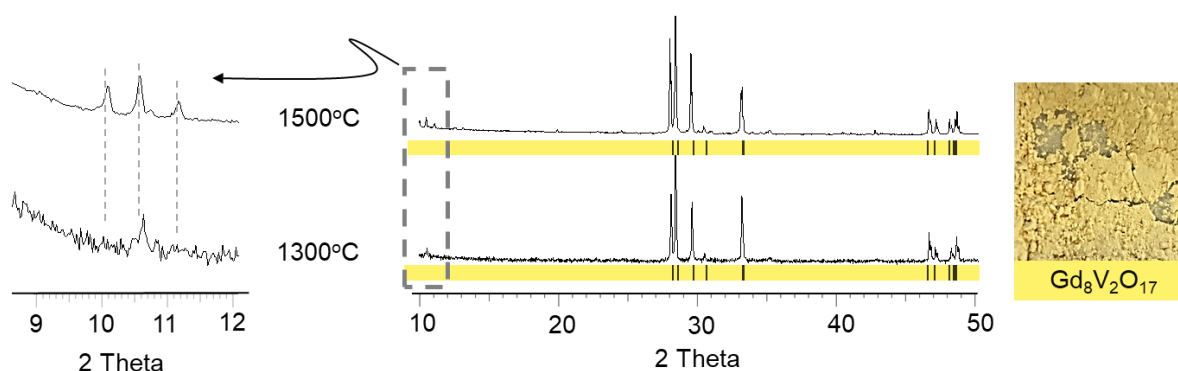


**Figure 75.** The XRDP of the  $Gd_8V_2O_{17}$  compound at different temperatures. Black marks on yellow correspond to Bragg peaks of  $Gd_8V_2O_{17}$  from PDF2 standard card No. 22-0297.

Concerning a possible unit cell, none of those mentioned above was satisfactory at this moment so that it was decided to grow single crystals.

#### *b. Crystal structure of $Gd_8V_2O_{17}$ phase*

To do so, the powder was heated slowly under air, in a platinum crucible, at the rate of 1°C/min before reaching 1500°C, held during 24 hours at 1500 C and then cooled down at a rate of 1°C/min. As a result of synthesis, a yellow indiscrete mass was obtained. An SEM study performed at this stage (1) confirmed the presence of Gd and V on crystals and (2) shows very small crystals of 10-20µm, see Figure 76. A tiny crystal was selected and analyzed.

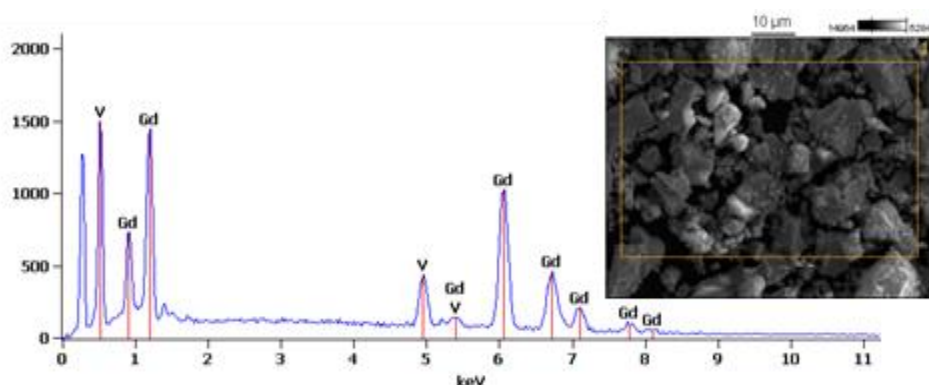


**Figure 76.** SEM image and EDS spectra of  $Gd_8V_2O_{17}$ .

Because of the size of the crystal, each photo was collected during 60s. The integration of the data led to a triclinic unit cell with unit cell parameters equal to  $a = 9.791(4) \text{ \AA}$ ,  $b = 15.974(6) \text{ \AA}$ ,  $c = 17.791(7) \text{ \AA}$ ,  $\alpha = 66.30(2)^\circ$ ,  $\beta = 82.51(2)^\circ$ ,  $\gamma = 88.722(19)^\circ$ ,  $V = 2525.(3) \text{ \AA}^3$ . The space group is  $P-1$ . The crystal structure was further solved using the charge flipping method [32] and refined using JANA2006. [33]

A total of 26 symmetrically independent gadolinium and 7 vanadium (one in  $1e$  and the others in  $2i$ ) were found and their atomic parameters and anisotropic thermal parameters refined. 58 oxygen are localized. They belong to oxo-centered  $[OGd_4]$  tetrahedra. Some oxygen atoms of the environment of vanadium were found but in absence of some of them not evidenced even after careful analysis of the Fourier difference map, it was decided to introduce rigid body blocks. The tetrahedra of the 6 vanadium in  $2i$  crystallographic sites were found. The problem persists concerning the one in  $1e$ . So at this stage of the refinement, the general formula is  $Gd_{52}O_{58}(VO_4)_{13}$  which is not neutral (total charge of -1). The temporary crystal structure is presented on Figure 77. The structure can be described like a classical  $Gd_2O_3$  type structure in which some Gd atoms are locally replaced by V ones. The vanadium atoms are surrounded by four O atoms forming  $[VO_4]$  tetrahedra apart from the one in  $1e$  being involved in a problematic  $[VO_4]$  square plane configuration.

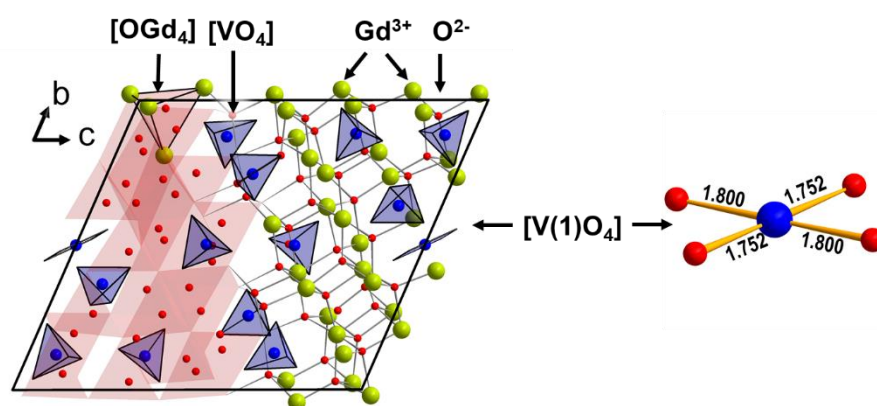


Figure 77. General presentation of  $Gd_8V_2O_{17}$  unit cell, where the vanadium atoms are given in blue, gadolinium – in green, and oxygen – in red.

A careful analysis of the precession images (see Figure 78) calculated for the  $0kl$ ,  $h0l$  and  $hk0$  layers from single crystal XRD data, shows additional tiny spots along  $c$ -axis, suggesting a doubling of  $c$ . Nevertheless, due to the very small intensity and number of additional spots, a new integration in the double unit cell did not converged satisfactorily. As a consequence, it was decided to ask for synchrotron beam time at SOLEIL using the BAG (Block Allocation Group) of the RECIPROCS network. The proposal was accepted and the collect performed by Pierre FERTEY (local contact).

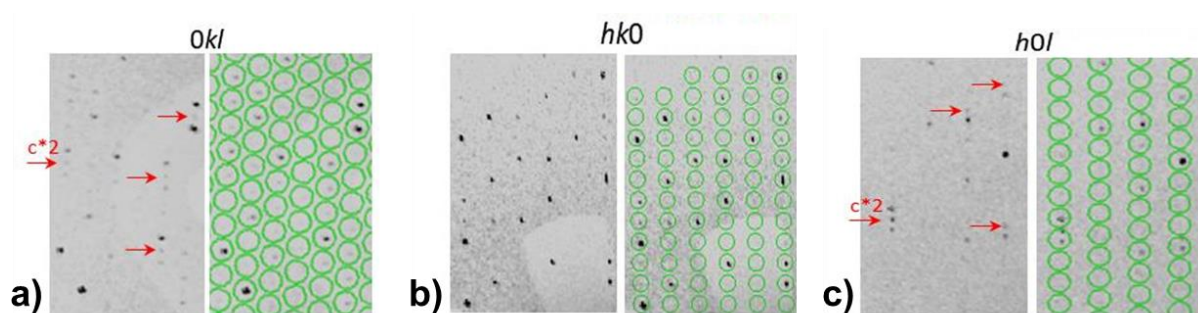
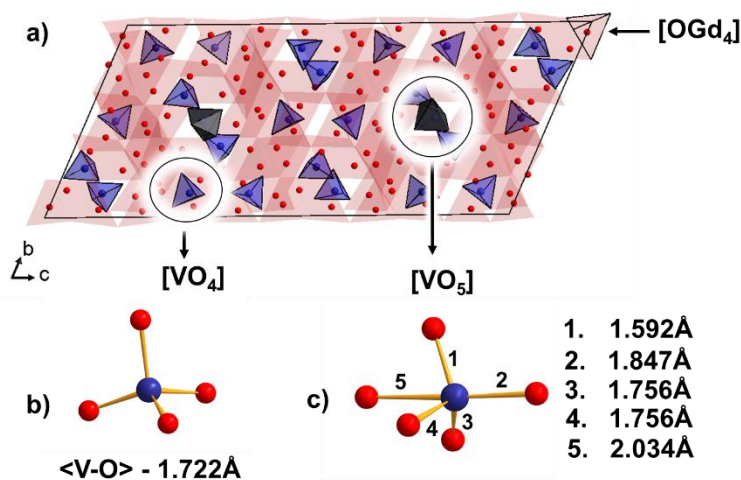


Figure 78. Precession images for  $Gd_8V_2O_{17}$ , where red arrows are indicating the satellite reflections.

A crystal of  $13\mu\text{m}$  width was analyzed using a beam energy of 24 keV (corresponding to a wavelength of  $\lambda = 0.51313 \text{ \AA}$ ). The diffraction intensities were measured on a Xcalibur Atlas 4-circle diffractometer equipped with a CCD plate and further extracted from the set of frames using the program CrysAlisPro. In agreement with what was expected before, the triclinic lattice parameters  $a = 9.7899(2)$ ,  $b = 15.9626(3)$ ,  $c = 35.681(5) \text{ \AA}$ ,  $\alpha = 66.2521(16)^\circ$ ,  $\beta = 82.4549(16)^\circ$ ,

$\gamma = 88.4644(16)^\circ$  was found. This unit cell corresponds exactly to the previous one with the  $c$  parameter multiplied by two. Absorption corrections based on spherical harmonic models were performed during the integration. The crystal structure refinement was satisfactorily performed in the centrosymmetric space group  $P-1$ . The detailed information about the refinement is given in SI in Table 42. As already obtained before, there are 52 symmetrically-independent positions of gadolinium atoms and 13 of vanadium in crystal structure. Gadolinium atoms are surrounded by four oxygen atoms each and forming oxo-centered regular tetrahedron  $[\text{OGd}_4]$ . The O – Gd bond lengths vary from 2.191 Å to 2.499 Å. On Figure 79 (a) the oxo-centered tetrahedrons are shown in transparent red color, forming infinite 3D framework similar to  $\text{Gd}_2\text{O}_3$ . It differs by presence of space forming by vanadium polyhedrons. The coordination of vanadium polyhedrons is of particular interest.

There are two possible coordination environments of vanadium in crystal structure of this compound. The majority of vanadium atoms are surrounding by four oxygen atoms forming regular tetrahedral coordination, shown on Figure 79 (b). The V – O bond length distribution within tetrahedral  $[\text{VO}_4]$  coordination varies from maximum 1.813 Å to minimum 1.651 Å, whereas the average value is 1.722 Å. The only vanadium atom has a dissimilar coordination environment, shown on Figure 79(c). Five oxygen atoms surrounding V(7) atom forming  $[\text{V}(7)\text{O}_5]$  trigonal bipyramid, where the minimum bond length is 1.592 Å and the maximum is 2.034 Å. At this step of the refinement and because some oxygen atoms are still missing in the environment of vanadium, it is not possible to confirm the 5+ valence of vanadium, even if practically, there are reasons why it could have changed during the synthesis (starting source of vanadium is  $\text{V}_2\text{O}_5$  heated at high temperature under air).



**Figure 79.** General overview on crystal structure of  $Gd_8V_2O_{17}$  based on  $[OGd_4]$  tetrahedrons, that are shown in red,  $[VO_4]$  in blue and  $[V(7)O_5]$  in grey colors (a). Example of coordination environment of regular  $[VO_4]$  tetrahedron (b). Bond lengths distribution within  $[V(7)O_5]$  trigonal bipyramid.

The crystal structure description of  $Gd_8V_2O_{17}$  compound is based on terms of oxo-centered approach. There are two types of polyhedrons that are forming the crystal structure:  $[OGd_4]$  tetrahedrons and  $[VO_4]$  /  $[V(7)O_5]$  polyhedrons. The cationic part is complex and will be discussed later, in comparison with  $Gd_8V_2O_{16.92}$ .

### *c. Magnetocaloric properties of $Gd_8V_2O_{17}$ phase*

This study is dedicated to characterization of magnetocaloric effect (MCE) of  $Gd_8V_2O_{17}$  compound. The MCE is a physical phenomenon that occurs in ferromagnetic materials under magnetization/demagnetization cycles which consist of a reversible temperature change. Nowadays magnetocaloric effect is important conditioned upon a big interest of refrigeration processes. This technology is involved in many devices that we use day to day such as refrigerators, air conditioner, food conservation, liquefaction of gases and other applications in medicine and others. The importance of cooling in the world is well illustrated by the fact that in 2015, cooling accounted for 25% of residential and 15% of commercial electricity consumption. [34]

The main cooling technology during last century is based on evaporation-compression cycles of refrigerant gases, also known as elastocaloric effect. [35] This classic refrigeration process has some significant drawbacks, especially in Western countries. Firstly, the ecological problem is that chlorofluorocarbons (CFC's) and hydrofluorocarbons (HFC's) refrigerant gases are using. These CFC's and HFC's gases are the Ozone Depleting Substances, over and above

HFC's are also long-lived potent greenhouse gases. [36] HFC's are regulated under both the 1997 Kyoto Protocol and the 2016 Kigali Amendment to the Montreal Protocol. [37] Another problem is hardness to significantly optimize and improve both efficiency and cooling capacity in rather mature technology, where is difficult to reduce energy consumption in using devices.

Recent efforts are focused on developing of new materials and alloys which have MCE near room temperature in order to reduce expenses and to find a better chemical control over the structure. Gadolinium-based structures are well-known in terms of discovering a new compound with Magnetocaloric effect.

Gadolinium-based inorganic compounds has two fundamental advantages as functional material in cryogenic magnetic coolers - a large magnetic moment [38,39] and good thermal and chemical stability. [40-42] A prototype of a magnetic refrigerator with MCE at room temperature was discovered in 1976. D.P. Brown presented ISABELLE Forced Circulation System: Method of Producing and Distributing Helium Refrigerant for 4.5 K Superconducting Magnets. [44] It based on Ericsson cycle with metallic Gadolinium as magnetocaloric material and a magnetic field created by superconducting magnets. The main problem of this refrigerator system was the use of superconducting magnets. Solution to solve this problem was proposed by Pecharsky and Gschneider in 1997, who discovered Giant Magnetocaloric Effect in  $Gd_5(Si_2Ge_2)$  compound, [45] being a material shifted to first order magnetic phase transitions (FOPTs). This compound demonstrates a second order magnetic transition at 293 K and the large  $\Delta S$  that is 50% higher than metallic Gadolinium. The giant MCE occurs due to the first order transition from a ferromagnetic state with low magnetic moment to a ferromagnetic state of higher magnetic moment at a lower temperature. In second order magnetic phase transitions materials (SOPTs)  $\Delta S$  curves are usually broader.

In collaboration with Regino Sáez Puche from Madrid University, a sample of composition  $Gd_8V_2O_{17}$  was studied. The thermal dependence magnetic susceptibility as well as its inverse are presented Figure 80. The Curie-Weiss law is verified with a Curie constant of  $0.032 \mu_B^{-1}$  ( $\mu_{eff} = 7.84 \mu_B$ ) which is closed to the theoretical value expected for an isolated  $Gd^{3+}$  cation ( $\mu_{Btheo} = 7.88 \mu_B$  with  $S = 7/2$ ).  $\Theta$  was refined to 10.5K. Of course, these results are in strong relation with the crystal structure and the presence of non-connected  $Gd^{3+}$  cations (distance Gd-Gd around 3.5 to 3.8Å).

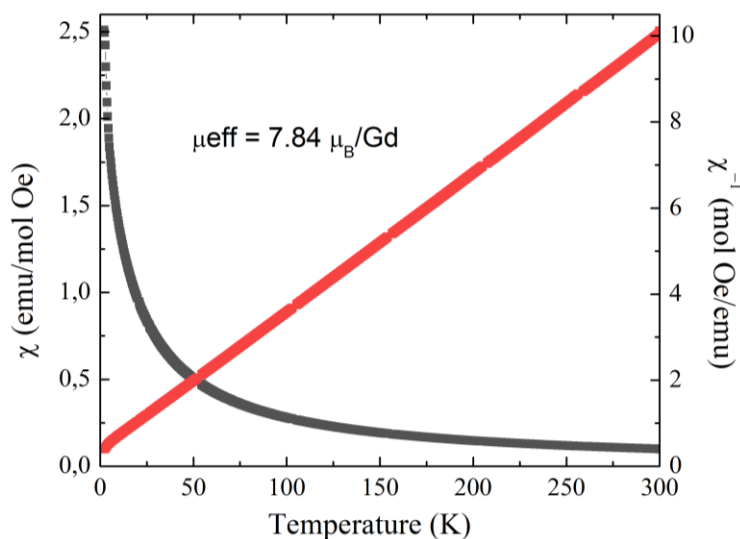


**Figure 80. Direct and inverse magnetic susceptibility for  $Gd_8V_2O_{17}$ .**

The sample is paramagnetic so it was decided to put the sample under reducing agents so that the valence of vanadium could change into 3+ or 4+ which could induce magnetic couplings.

The reduction was carried out under Forming Gas (5%  $H_2$ , 95%  $N_2$ ). The reduction was carried out at 900°C during 12 hours in a tube furnace. After the reaction, the color of the sample changed to green suggesting that something happened, probably a reduction from  $V^{5+}$  to  $V^{3+}$  or  $V^{4+}$ . An XRD study was performed on  $Gd_8V_2O_{17}$  and on the reduced sample to evidence possible structural changes. The results are shown on Figure 81. The XRDP were measured in Madrid. Even if the quality is low, some changes are observed and suggested local structural changes keeping unchanged the global matrix as the main peaks remain mainly unchanged.

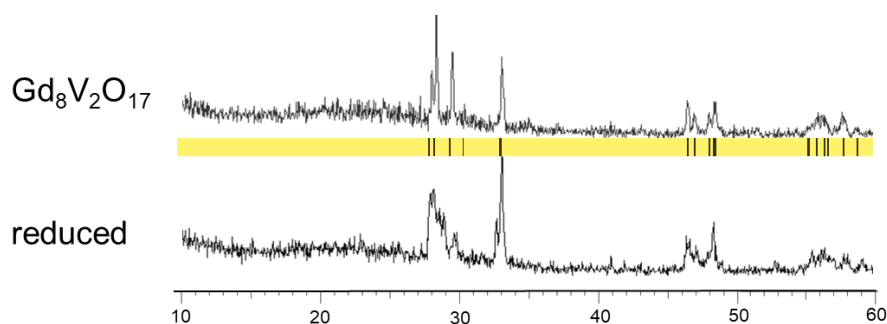


**Figure 81. X-Ray diffraction patterns of initial  $Gd_8V_2O_{17}$  and reduced compound. Black marks on yellow correspond to bragg peaks of  $Gd_8V_2O_{17}$  from PDF2 standard card No. 22-0297.**

The efficiency of the reduction was analyzed through a thermogravimetric analysis (also performed in Madrid) performed under oxygen. On heating, an increase of the mass is related to an uptake of oxygen so an oxidation of the vanadium ( $Gd^{3+}$  cannot change its valence).

The reduced sample was heated from RT to 1000°C with a temperature gradient of 5°C/min. The result, shown on Figure 82 indicates a mass gain that occurs in two stages. In a first stage, between 350 and 450 °C, a slight increase in mass was detected. Second stage occurred between 450 and 600 degrees. The global mass gain turns out to be about 0.71% which coincides with the incorporation of 0.71 oxygen atom in the modified material. That indicates changes in oxidation state of vanadium but it is not possible to conclude if it is  $V^{4+}$ ,  $V^{3+}$  or a mixture of both. In addition, an X-ray diffraction analysis performed after the TGA analysis indicates that sample is back to the  $Gd_8V_2O_{17}$  form. Therefore, it is probably a reversible oxidation-reduction process.

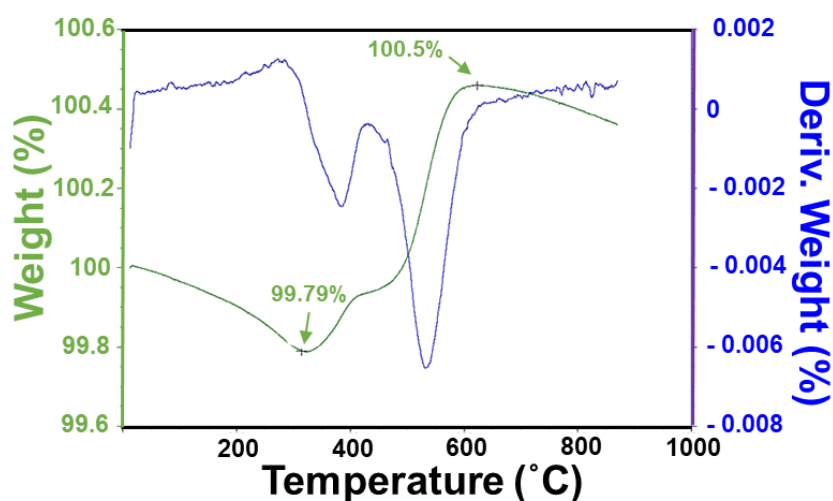


**Figure 82.** Thermogravimetric analysis of reduced phase in an oxygen atmosphere.

After these preliminary results performed during my internship in Madrid and in front of the impossibility to get the sample back, it was decided to study the reduction process directly at UCCS.

### III.2.3. Reduction of $Gd_8V_2O_{17}$

#### *a. Synthesis routes*

For technical reasons detailed reproduction of the reduction experiment made in Madrid was impossible in Lille University. Several similar routes of sample treatment with reducing atmosphere have been provided in order to obtain the same phase.

-Thermogravimetric analysis (TGA) of  $Gd_8V_2O_{17}$  was performed using a TGA TA Instruments SDT2960 under flowing atmosphere of 5%  $H_2$  and 95% Ar, from room temperature to 1100°C (heating rate 5 °C/min) and at ambient-pressure conditions. Here the reduction can occur without risks of nitrogen incorporation. Thermogravimetric analysis (TGA) of  $Gd_8V_2O_{17}$  is shown on Figure 83. The weight loss is about 0.7% corresponding to the loss of 0.7 oxygen in the formula  $Gd_8V_2O_{17}$ . This loss of oxygen is necessary assorted with a reduction of vanadium but, again, it is not possible to conclude about the real valence of vanadium at this step of the study. The resulted powder has a light-grey color. It's powder pattern is shown on Figure 84(a).

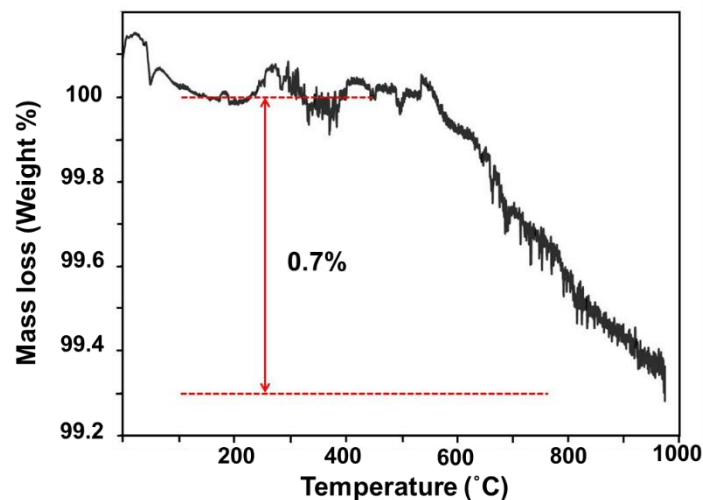
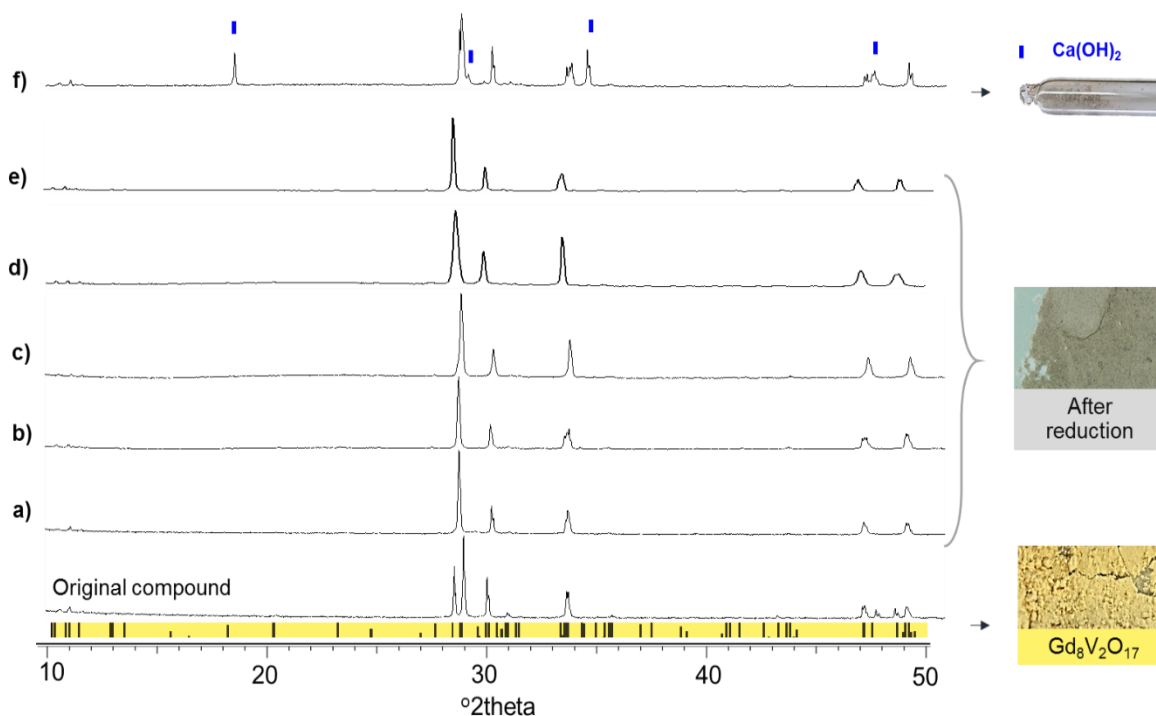


Figure 83. Results of thermogravimetric analysis (TGA) of  $Gd_8V_2O_{17}$ .

The comparison with the XRDP of the raw  $Gd_8V_2O_{17}$  (Figure 84) is a proof that something happened during the reduction.



**Figure 84. Powder pattern diffraction representation of original sample at the bottom of the picture and samples reduced at different conditions: after thermogravimetric analysis under flowing atmosphere of 5% H<sub>2</sub> and 95% Ar (a), after the thermal treatment with ammonia at 600° (b), 700° (c), 750° (d), after reduction under pure H<sub>2</sub> flow at 700° (e) and via the hydride route (f).**

-The thermal treatment with ammonia has been provided in collaboration with Dr. Franck Tessier of the University of Rennes. This corresponds to the original treatment performed in Madrid.

The method is rather common and used in the case of topochemical reduction. [46] The action of ammonia is related to its decomposition at a temperature above 500°C into active nitrogen species and molecular hydrogen following this equation:  $\text{NH}_3 \rightarrow \frac{1}{2} \text{N}_2 + \frac{3}{2} \text{H}_2$ . Whereas hydrogen will react with oxygen atoms of the solid, nitrogen may be incorporated in the resulting oxygen vacancies. Here NH<sub>3</sub> is a powerful and soft reducing agent that may remove a maximum of 1/6<sup>th</sup> of the initial oxygen content. The problem is the possibility to introduce nitrogen in the host lattice during the process.

Four samples were respectively heated during 12-24 hours at 600°, 700°, 750° and 900°. First three samples demonstrate changing of color from yellow to grey, whereas the last one turns to black. The color change gives a first idea about a possible modification of the sample. The XRDP are shown on Figure 84 (b), (c) and (d). They all show the achievement of the same

reduced phase. Concerning the sample treated at 900°, it is totally destroyed into GdVO<sub>3</sub>, V<sub>4</sub>O<sub>7</sub> and G<sub>2</sub>O<sub>3</sub> see Figure 85 (a).

-The reduction via the hydride route were also tried. This method is commonly used to reduce samples (Ln<sub>2</sub>Ti<sub>2</sub>O<sub>7</sub> [47], YMnO<sub>3</sub> [46], SrFeO<sub>2</sub> [48]). This synthesis route is interesting because it may reduce vanadium in our case without introducing nitrogen. A potential negative point is the possibility to get byproducts as Ca(OH)<sub>2</sub> in our case.

The reduction was performed using 0.08g of initial Gd<sub>8</sub>V<sub>2</sub>O<sub>17</sub> and 0.02g of CaH<sub>2</sub> were grinded together. The powder was then flame-sealed in an evacuated silica tube at pressure under 10<sup>-2</sup> bar. The tube was heated at 450 °C over the night. The color changed from yellow to grey. In order to be sure that the reduction was over, it was this time heated at 500 °C during the night. The color did not change so that the tube was opened to recover the sample. It was further washed several times with 0.1 M methanol to remove excess of CaH<sub>2</sub> and CaO and then dried at 100 °C in an oven. The XRDP is shown Figure 84 (f) and shows also the same new phase assorted with remaining impurities of Ca(OH)<sub>2</sub>.

- Another series of experiment was provided using tube furnace under pure H<sub>2</sub> flow. The raw sample was put in alumina boat and evacuated by carbon underlay. One sample was heated at 1000° during 5 hours and cooled down slowly. The resulted powder has an intense black color. According to XRD analysis, the sample is totally decomposed into a mixture of V<sub>4</sub>O<sub>7</sub> (PDF card № 27-0940), GdVO<sub>3</sub> (PDF card № 86-2395) and Gd<sub>2</sub>O<sub>3</sub> (PDF card № 12-1797), see Figure 85 (b). As a consequence, a second sample was heated at lower temperature, 700°C, during the same time. The resulted powder has a grey color similar to samples obtained through the other methods. X-Ray Powder diffraction pattern of this sample is compared to other sample on Figure 84 (e).

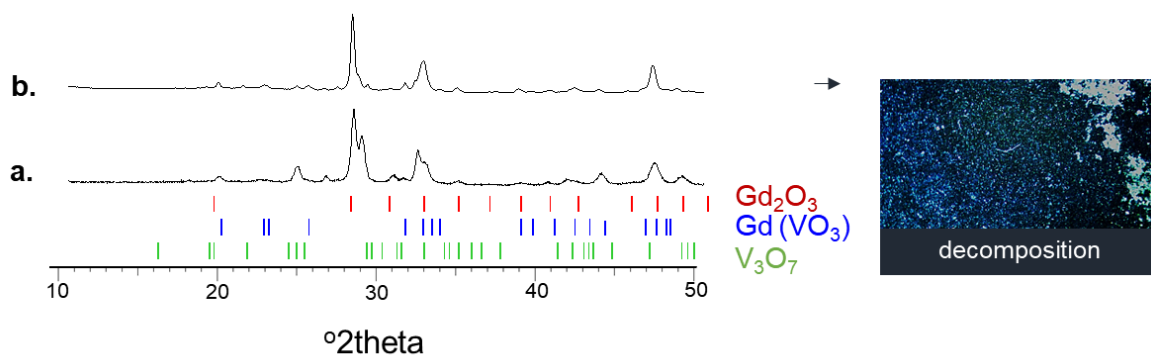


**Figure 85. Powder pattern diffraction representation of samples (a) after treatment under ammonia at 900°C and (b) after heating at 1000°C under H<sub>2</sub> flow.**

Some general preliminary conclusions based on the analysis of XRDP have been drawn:

- (1) all listed experiments lead to the identical patterns,
- (2) diffraction pattern of the new unknown phase is different from the raw Gd<sub>8</sub>V<sub>2</sub>O<sub>17</sub>,
- (3) apparently, the diffraction pattern of new phase seems to be related to the one of Gd<sub>8</sub>V<sub>2</sub>O<sub>17</sub>, with the disappearance of the peak at 28.2 °.
- (4) The synthesis conditions able to produce the targeted phase are highlighted in this part.

The unit cell of the modified sample is probably related to the first one but it is difficult to conclude as it is certainly triclinic with big unit cell parameters. At the moment, the reliable determination of the crystal lattice parameters in the triclinic system is a nontrivial task.

In the same time, a question persists concerning the possibility of presence of nitrogen in the reduced phase for sample obtained from the use of ammonia. As a consequence, a combustion analysis was performed by our colleague F. Tessier gave the results detailed below:

- sample heated at 600°: O wt.% = 16.57 and N wt.% = 0.08;
- sample heated at 700°: O wt.% = 16.47 and N wt.% = 0.36;
- sample heated at 750°: O wt.% = 15.2 and N wt.% = 0.56;
- sample heated at 900°: O wt.% = 13.8 and N wt.% = 0.91.

Are these amounts of nitrogen significant? Our reference to discuss that point is LaVO<sub>2.78</sub>N<sub>0.10</sub>. [29] This phase was also obtained by reaction of LaVO<sub>4</sub> under ammonia at 600°C. In that phase, the oxygen amount is about 20.1wt.% and N wt.% is equal to 0.63. This implies that the amount of nitrogen obtained for samples heated at 700°C and 900°C are important and need to be considered.

### *b. Crystal structure of reduced phase*

To be sure of the absence of Nitrogen in our structure, it was decided to select crystals from the sample prepared under ammonia and heated at 600°C for which the amount of N is almost equal to 0 (N wt.% = 0.08).

A tiny crystal of 7  $\mu\text{m}$  was selected and studied on the beamline CRISTAL at the synchrotron Soleil. The conditions were the same as the one used to collect the initial sample.

First of all, triclinic lattice parameters are  $a = 9.7688(3)$ ,  $b = 15.9639(3)$ ,  $c = 65.8845(2)$ ,  $\alpha = 65.8845(19)$ ,  $\beta = 83.120(2)$  and  $\gamma = 88.128(2)$  were refined using 31374 reflections. This unit cell exactly corresponds to the one of  $\text{Gd}_8\text{V}_2\text{O}_{17}$  divided by 2 along  $c$ , that gives a cell volume of  $2528.69(10) \text{ \AA}^3$ . The detailed data collection parameters and conditions are given in Table 42. The refinement was easy concerning the localization of gadolinium atoms and oxygen atoms involved in the  $[\text{OGd}_4]$  units. At the end, the crystal structure demonstrates the similar cationic ordering compared with  $\text{Gd}_8\text{V}_2\text{O}_{17}$ . A general overview of the crystal structure of the reduced phase is shown on Figure 86 (a). The  $[\text{OGd}_4]$  tetrahedra are shown in red color, whereas  $[\text{VO}_4]$  tetrahedrons are in blue. The coordination environment and average V-O bond length are typical for vanadium polyhedra and are presented on Figure 86 (b). One difference comparing to initial  $\text{Gd}_8\text{V}_2\text{O}_{17}$  structure occurs in the coordination environment of one of the thirteen vanadium atoms, V(1). It is shown in grey color on the Figure 86 (a). First of all, V(1), was localized on the particular site  $(\frac{1}{2} \frac{1}{2} 0)$ . Nevertheless, it was still impossible to find a correct environment. For this reason, assorted with remaining electronic density around this position, it was decided to extract it from this particular position and put it in a general position with an occupancy ratio of  $\frac{1}{2}$ . After that and a careful analysis, two configurations arise: first, a square pyramid and a tetrahedron, both of them with half occupancies. Two possible configurations of V(1) environment are shown on Figure 86 (c).

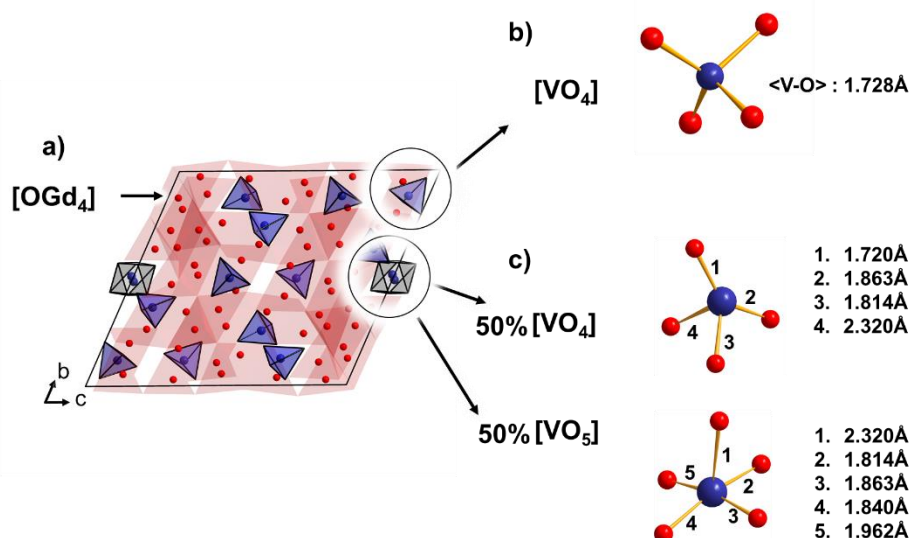


**Figure 86. General overview on crystal structure of  $Gd_8V_2O_{16.92}$  based on  $[OGd_4]$  tetrahedrons, that are shown in red,  $[VO_4]$  in blue and  $[V(1)O_5]$  in grey colors (a). Example of coordination environment of  $[VO_4]$  tetrahedron (b). Bond lengths distribution within the  $[V(1)O_5]$  and  $[V(1)O_4]$ .**

At the end of the refinement, the formula of this compound is  $Gd_{52}V_{13}O_{110}$ , which is neutral if one vanadium is 4+. According to the environment of V(1) and to BVS calculation (BVS:4.11-V(1), 4.85(7) for others in average), this atom tends to be effectively 4+. This formula corresponds to  $Gd_8V_2O_{16.92}$ . To confirm this valence state, and XPS study was performed.

### *c. Confirmation of reduction of vanadium by XPS*

X-ray Photoelectron Spectroscopy method allows to provide a qualitative elemental analysis of all elements presented in the sample, with the exception of hydrogen and helium. It provides access to the binding energies of the main electrons and therefore to the energy level diagram that is specific to each atom and its oxidation state. The area ratio between the various peaks allows for a quantitative determination of the composition of the sample.

X-ray Photoelectron Spectroscopy analysis has been provided in Lille University with Pardis Simon. Two  $Gd_8V_2O_{17}$  and  $Gd_8V_2O_{16.92}$  samples were measured to characterize the oxidation state of vanadium. All the conditions of analysis and treatment of the data are given in appendix.

The XPS spectra of two samples are compared on Figure 87. O1s core level spectra are located in the region 527-538 eV. The O1s spectrum of the samples represents three peaks. The V<sup>5+</sup> oxidation state is shown in both samples by presence of peak at 517 eV corresponding to

vanadium 2p orbital. The deconvolution of  $\text{Gd}_8\text{V}_2\text{O}_{16.92}$  spectra shows the appearance of two peaks at 516 and 514 eV resulting in  $\text{V}2p_{3/2}^{3+/4+}$  and  $\text{V}2p_{3/2}^{1+/2+}$ , respectively. Of course, it is impossible to obtain  $\text{V}^{1+}$  or  $\text{V}^{2+}$  but this small peak is probably due to surficial contributions. Concerning the  $\text{V}2p_{3/2}^{3+/4+}$ , it gives a proof of the reduction of a part of vanadium, even if it is not possible to conclude between  $\text{V}^{3+}$  and  $4+$  thanks to XPS analysis, the previous BVS calculation assorted with these results are sufficient to conclude in the presence of  $\text{V}^{4+}$ .

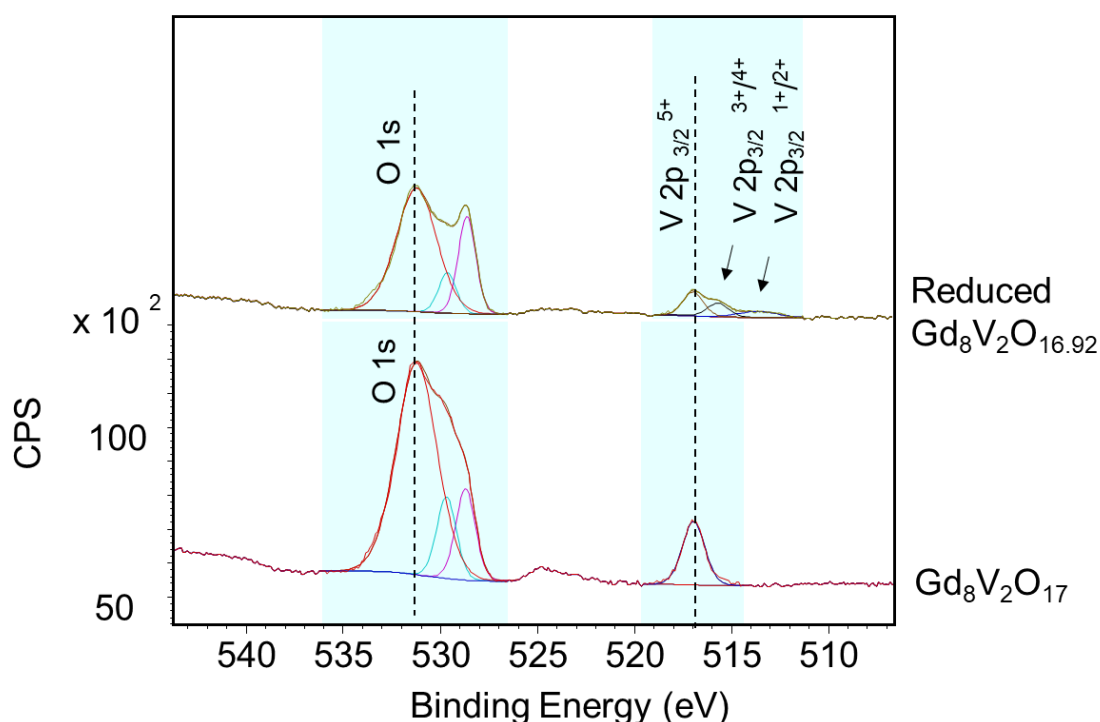


Figure 87. XPS spectra of O 1s and V 2p<sub>3/2</sub> of the two samples.

#### III.2.4. Comparison between the two crystal structures.

Crystal structures of both initial  $\text{Gd}_8\text{V}_2\text{O}_{17}$  and reduced  $\text{Gd}_8\text{V}_2\text{O}_{16.92}$  samples demonstrate similarities in way of their organization. Oxo-centered tetrahedra of  $[\text{OGd}_4]$  share common edges and form infinite 3D framework. This cationic framework gives rise to 1D channels that can be observed on Figure 88(a). These channels are hosting isolated vanadium that are shown together in blue and grey on Figure 88(a). In order to describe distribution of different vanadium polyhedrons within the 3D framework, a formal alternating layers can be found in the unit cell by cross-sectional cutting through the dotted line on Figure 88(a). The general projection of the formal layer is shown on the Figure 88(b). Green color circles correspond to gadolinium atoms,

whereas red circles to oxygen atoms.  $[\text{VO}_4]$  tetrahedrons are given in blue color. The formal layers are made up from shared  $[\text{OGd}_4]$  tetrahedrons and have two possible ways of vanadium to be incorporated in it. Isolated  $[\text{VO}_4]$  tetrahedrons are shown in blue color and associated by four together and form large pore space  $15 \times 12 \text{ \AA}$ . Large pores alternate either with the same-size pores or with a small-size pores of  $9 \times 7 \text{ \AA}$  dimensionalities.

The main difference between two structures is in a small-size pores filler, that is shown on Figure 88 (c). In case of initial  $\text{Gd}_8\text{V}_2\text{O}_{17}$ , the inner space of these pores can be filled by equal to each other  $[\text{V}(7)\text{O}_5]$  trigonal bipyramids. In crystal structure of reduced phase, these small pores are filled out in equal proportion by  $[\text{VO}_4]$  tetrahedrons or  $[\text{V}(1)\text{O}_5]$  square pyramids. They are differently directed due to presence of half occupied oxygen position.

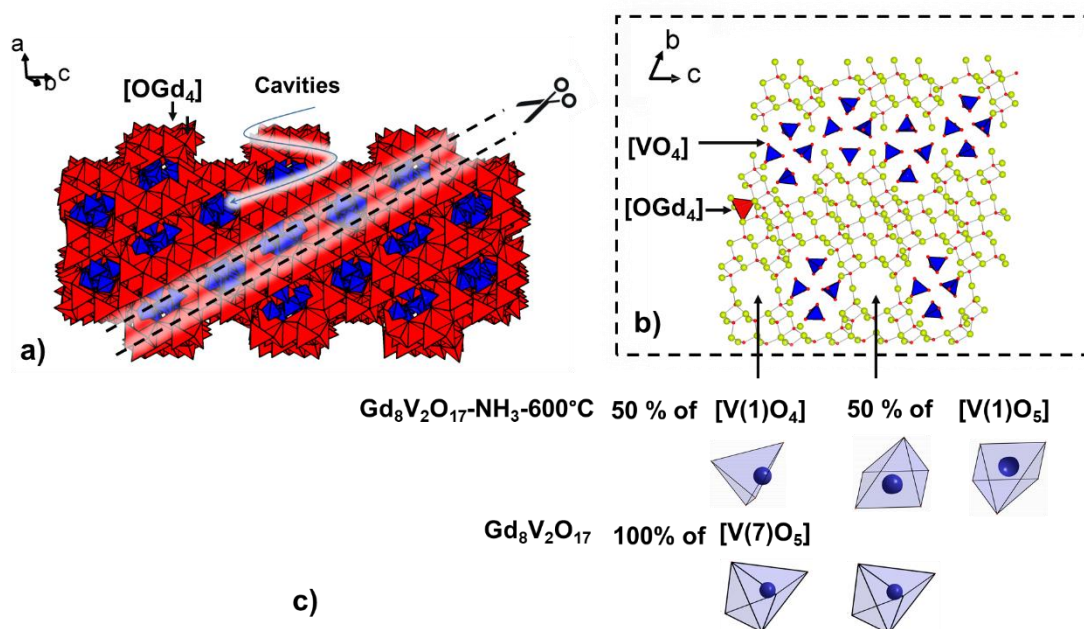


**Figure 88. (a) The general projection of  $\text{Gd}_8\text{V}_2\text{O}_{17}$  crystal structure, where  $[\text{OGd}_4]$  tetrahedrons forming infinite framework are shown in red and the cavities are filled out by blue  $[\text{VO}_4]$  /  $[\text{VO}_5]$  polyhedrons. (b) Cross section along selected direction that shows the different  $[\text{VO}_4]$  /  $[\text{VO}_5]$  association. Distribution of vanadium polyhedra in small pores (c).**

The coordination environment and distances between some atoms are different within infinite 3D frameworks in both structures. In order to prove that statement, the Figure 89 was drawn. Distance variations between two vanadium atoms were chose as the most representable. The equal symmetrically independent positions of vanadium atoms were found in both structures, thus the V11 atom in crystal structure of initial  $\text{Gd}_8\text{V}_2\text{O}_{17}$  compound corresponds to V6 position in reduced sample. Following the same logic, the V12 atom corresponds to the V7 atom.

First comparison was made for V11-V11 versus V6-V6 and V12-V12 and V7-V7 distances. As can be noticed from the picture in case of first pair of atoms, the distance has increased from 4.77 to 4.97 Å. At the same time, the comparison of distances in second pair of vanadium atoms revealed a decreasing from 7.20 to 7.15 Å.

Another comparing was made on selected structural units (vanadium tetrahedrons) using different parameters:

- number of linked Gd atoms,
- minimum and maximum O-Gd bond lengths
- average O-Gd bond lengths.

The results are summarized and shown on Figure 89 (c, d, e and f).

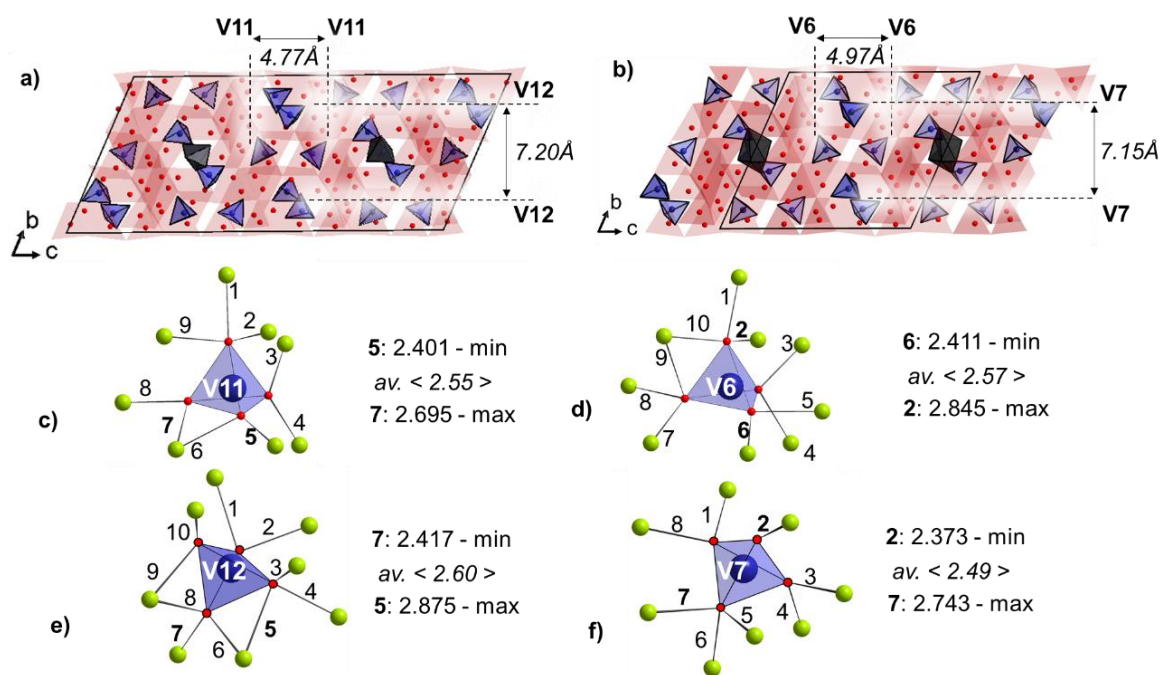


**Figure 89.** General representation of unit cell parameters of initial  $Gd_8V_2O_{17}$  compound (a) and reduced one (b). Different parameters of vanadium tetrahedrons and their coordination environments are compared on figures (c), (d), (e) and (f).

*a. Magnetic properties of  $Gd_8V_2O_{16.92}$*

- First measurements done in Madrid

The study of the magnetic properties on the reduced compound has been carried out in Madrid, on samples synthesized in Madrid. Measurements of magnetic susceptibilities and magnetization were studied in wide temperature ranges between 2 and 300K.

The representation of the magnetic susceptibility against the temperature is given on Figure 90. and shows a Curie-Weiss behavior in a wide temperature range. Calculated value for the Curie Constant is  $C = 25.9 \text{ emu K / mol}$  which leads to magnetic moment  $15.3 \mu_B$  be very close to the theoretical value, which is  $15.8 \mu_B$  corresponding to  $4 Gd^{3+}$  for  $1 V^{4+}$ . The Weiss constant acquires a value of  $-9.58 \text{ K}$  which leads to a followed Curie-Weiss law:  $\chi = \frac{25.9}{T-9.58}$ .

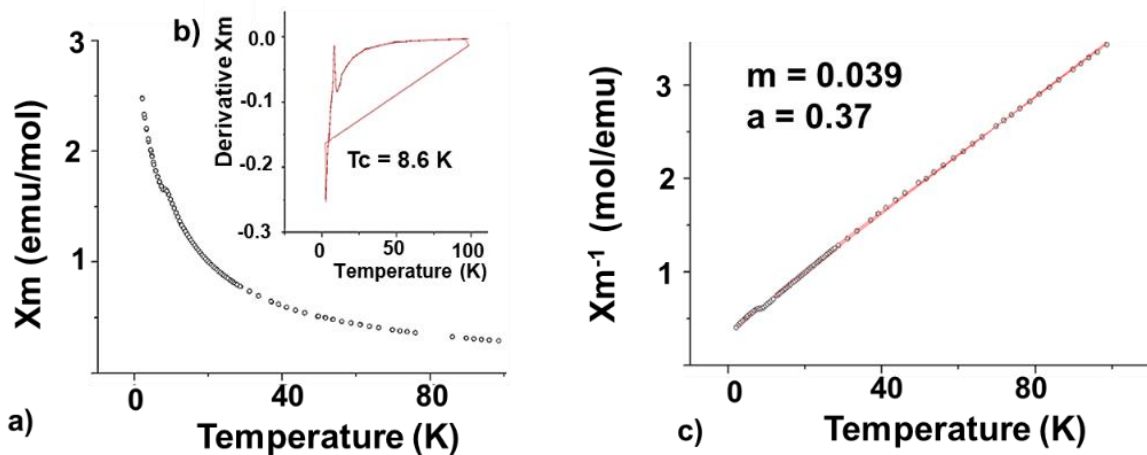


**Figure 90.** (a) Representation of the magnetic susceptibility against the temperature; (b) Derivative of the magnetic susceptibility against the temperature; (c) Inversed value of magnetic susceptibility against temperature.

The negative value of the Weiss constant indicates the existence of anti-ferromagnetic interactions. The estimated value of the Néel temperature from the derivative of the magnetic susceptibility as a function of temperature, Figure 90 (c), resulted to be 8.6K. This value coincides with the anomaly detected in the representation of  $\chi$  vs T around 8 K and even if it could open the door to further magnetocaloric measurements it has still no real sense and remain intriguing. So before further magnetocaloric measurement, the same measurements were performed at UCCS, on samples synthesized and characterized in our lab.

- Magnetic measurements on Gd<sub>8</sub>V<sub>2</sub>O<sub>16.92</sub>

A sample of Gd<sub>8</sub>V<sub>2</sub>O<sub>16.92</sub> synthesized at 600°C under ammonia was measured. The magnetic susceptibility and inverse magnetic susceptibility are shown Figure 91. An experimental value of  $\mu_{\text{eff}} = 7.73 \mu_{\text{B}}/\text{Gd}$  was found, in accordance with the theoretical value. A Curie-Weiss law fit led to  $C = 0.033 \mu_{\text{B}}^{-1}$  and  $\theta = 10.86 \text{K}$ .

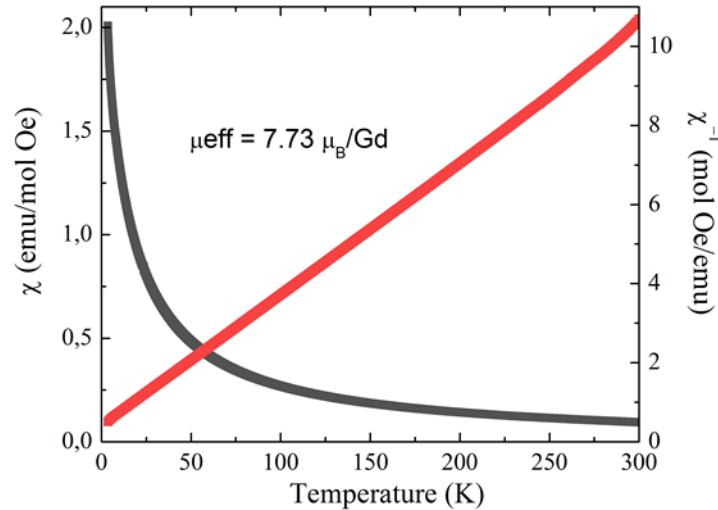


**Figure 91. Direct and inverse magnetic susceptibility for Gd<sub>8</sub>V<sub>2</sub>O<sub>16.92</sub>**

However, no transition was detected down to 0 K (Figure 91) contrary to what was observed by our colleagues. Again, it was not possible to get the sample back so to compare... But, let's remind that, according to the different trials done by ourselves, the sample heated at 900° under ammonia was destroyed into GdVO<sub>3</sub>, V<sub>3</sub>O<sub>7</sub> and Gd<sub>2</sub>O<sub>3</sub>. After some bibliographic study, GdVO<sub>3</sub> gives the same kind of transition on the magnetic susceptibility curve. [99] This implies that the results obtained by our colleagues don't correspond to the real reduced sample. In absence of magnetic transition, there was no point to continue the magnetocaloric study and the investigation stopped here.

To continue the characterization, UV-visible diffuse reflectance spectroscopy was performed to experimentally determine the band gap.

### ***b. Optical Measurements***

UV-visible diffuse reflectance analysis of polycrystalline powder of  $\text{Gd}_8\text{V}_2\text{O}_{17}$ ,  $\text{Gd}_8\text{V}_2\text{O}_{16.92}$  – was measured. A Kubelka-Mink transformation [50] was performed to the measured diffuse-reflectance ( $R$ ) spectra using the function:

$$F(R) = (1-R)^2/(2R).$$

Following this step, a Tauc plot [49] was applied to obtain a value of the optical band gap  $E_g$ , using the relation:

$$[F(R)hv]^{1/n} = k(hv - E_g), \quad hv: \text{the photon energy}$$

$k$ : an independent constant

$E_g$ : the optical band-gap

$n$ : equal to  $\frac{1}{2}$  in case of a direct-allowed transition

or equal to 2 in cases of indirect-allowed transition.

In our case, after several trials, we assumed a direct-allowed transition after plotting both cases. The result is shown on figure 13. The band gap value is deduced from the drawing of a tangent line at the inflection point giving a value of  $E_g = 3.3$  eV for  $\text{Gd}_8\text{V}_2\text{O}_{17}$  and  $E_g = 2.9$  eV for  $\text{Gd}_8\text{V}_2\text{O}_{16.92}$ . The evolution of the band gap value is in good agreement with the color change observed between the two samples. A resembling investigation was provided for Synchronously Achieving Plasmonic Bi Metal Deposition and I– Doping by Utilizing  $\text{BiOIO}_3$  as the Self-Sacrificing Template for High-Performance Multifunctional Applications. [51] Samples are prepared by a simple in situ  $\text{NaBH}_4$  reduction method.

The remarkable enhancement on the optical absorption of investigated series samples is also verified by the color change. All the samples obtained by other reduction routes were also tested and have a similar band gap.

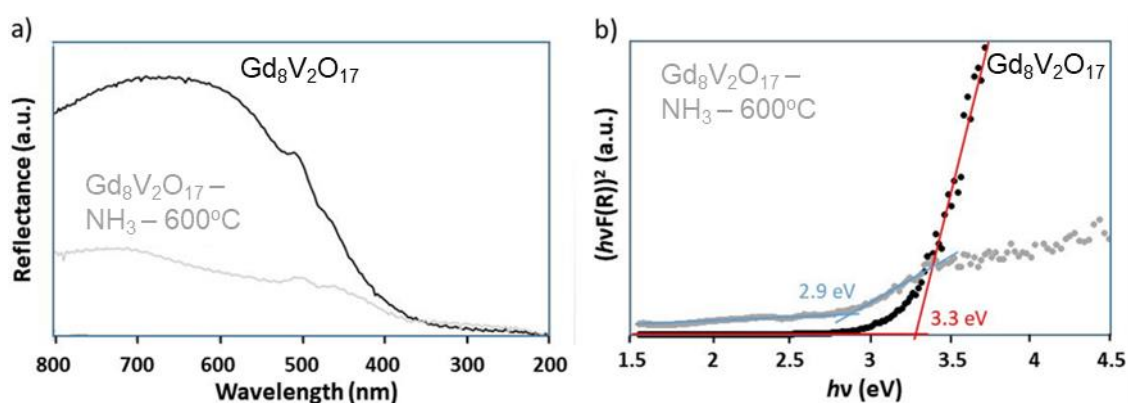


Figure 92. (a) Comparing of UV-visible spectra of initial  $Gd_8V_2O_{17}$  sample - black line and after ammonia treatment at  $600^\circ C$  - grey line. (b) comparing the positions of  $E_g$  values and a tangent lines in red for  $Gd_8V_2O_{17}$  and in blue line for  $Gd_8V_2O_{16.92}$  samples.

### III.2.5. HP-HT investigation of $Gd_8V_2O_{17}$

In addition, in order to investigate possibility of further modification by HP-HT, a series of experiments were provided in Belt type press. The  $Gd_8V_2O_{17}$  compound has been exposed to various High-Temperature High-Pressure conditions. These experiments were provided in Neel Institute (Grenoble). Three experiments were performed at different conditions. The powder patterns of resulted products are compared with  $Gd_8V_2O_{17}$  compound that is shown on Figure 93 (a). First experiment was provided at 5GPa and  $900^\circ C$  (Figure 93(c)). Next experiments was realized at the same temperature of  $900^\circ C$  and decreased pressure - 2GPa (Figure 93(b)). Conversely, the third experiment was provided at 5GPa and  $1100^\circ C$  (Figure 93(c)).

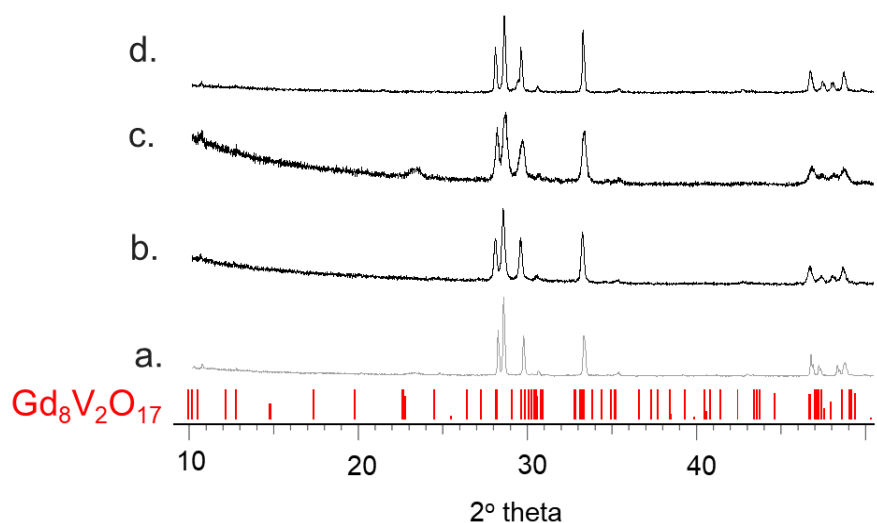


Figure 93. Powder diffraction pattern of initial  $Gd_8V_2O_{17}$  compound (a) at different experimental conditions: 2GPa/ $900^\circ C$  (b), 5GPa/ $1100^\circ C$  (c) and 5GPa/ $900^\circ C$  (d).

The study of the diffraction patterns made it possible to conclude that the crystal structure of this compound does not lead to a phase transition under the applied conditions.

### III.3. Conclusion and perspectives

#### III.3.1. Summary

In this chapter, we were able to fully characterize  $\text{Gd}_8\text{V}_2\text{O}_{17}$ , a phase highlighted in 1969, [28] but whose crystal structure was never solved before. The low symmetry, the size of unit cell parameters and volume, the absence of single crystals of sufficient size to be analyzed on a standard diffractometer were all drags on crystal structure determination.  $\text{Gd}_8\text{V}_2\text{O}_{17}$  was reduced into  $\text{Gd}_8\text{V}_2\text{O}_{16.92}$ , involving a reduction of one of the 13 vanadium atoms from  $\text{V}^{5+}$  to  $\text{V}^{4+}$  assorted with shift of gadolinium atoms and the loss of 0.08 oxygen in the final formula. This was confirmed by XPS and thermal analysis. Our investigation call into the question the first magnetocaloric properties measured and finally related to  $\text{GdVO}_3$  impurity. In absence of magnetic transition of the magnetic susceptibility curves measured at UCCS on the pure reduced sample, there was no point to measure them again.

#### III.3.2. Perspectives

Due to our bibliographic study and after the full characterization of Gd-based phase, other lanthanides were tried: Nd, Y, Yb and Sm. Preliminary synthesis were performed with oxide precursors taken in stoichiometry corresponding to desired  $\text{Ln}_8\text{V}_2\text{O}_{17}$  composition. In the same time, some investigations were performed to highlight the referenced  $\text{Ln}_{10}\text{V}_2\text{O}_{20}$ . Our preliminary results are encouraging and we isolated the two phases. Single crystals were obtained from slow cooling on samples with samarium, neodymium, yttrium and ytterbium. Nevertheless, again, the single crystals are so tiny that synchrotron beamtime will be required again.

Of course, after full structural characterization, the investigation of the reduction will be performed again, starting another story.

### III.4. Supplementary information

**Table 27. Crystal parameters, data collection and structure refinement details for the crystal of  $\beta$ -LiLa<sub>5</sub>O<sub>5</sub>(VO<sub>4</sub>)<sub>2</sub>**

Crystal data	
Formula	LiLa <sub>5</sub> O <sub>5</sub> (VO <sub>4</sub> ) <sub>2</sub>
Formula weight (g/mol)	1011.3
Temperature (K)	293
Crystal system	triclinic
Space group	<i>P</i> -1
<i>a</i> (Å)	5.8167(15)
<i>b</i> (Å)	12.2954(28)
<i>c</i> (Å)	18.7221(69)
$\alpha$ (°)	102.03(2)
$\beta$ (°)	98.76(2)
$\gamma$ (°)	103.54(2)
<i>V</i> (Å <sup>3</sup> )	1244.37(18)
<i>Z</i>	4
Data collection	
Diffractometer	X8 Bruker
Radiation; $\lambda$ (Å)	AgK $\alpha$ ; 0.56086
Absorption coefficient, $\mu$ (mm <sup>-1</sup> )	9.621
<i>F</i> (000)	1752
Data range $\theta$ (°); <i>h</i> , <i>k</i> , <i>l</i>	1.39 – 25.6; -8 < <i>h</i> < 8, -18 < <i>k</i> < 18, -28 < <i>l</i> < 28
No. of total reflections	9444
Total unique reflections	6539
Criterion for observed reflections	<i>I</i> > 3 $\sigma$ ( <i>I</i> )
<i>R</i> <sub>int</sub> (%)	7.62
Refinement	
Refinement on	Full-matrix least squares on <i>F</i>
Weight scheme	1/( $\sigma^2$   <i>F</i>   + 0.0004 <i>F</i> <sup>2</sup> )
<i>R</i> <sub>gt</sub> , <i>R</i> <sub>all</sub>	7.59, 11.26
w <i>R</i> <sub>gt</sub> , w <i>R</i> <sub>ref</sub>	10.31, 11.25
GOF <sub>gt</sub> , GOF <sub>ref</sub>	2.10, 2.32
Max. /min. residual <i>e</i> density, (eÅ <sup>-3</sup> )	10.84 / -8.89

**Table 28. Atomic parameters  $\beta$ -LiLa<sub>5</sub>O<sub>5</sub>(VO<sub>4</sub>)<sub>2</sub>**

Atom	X	Y	Z	U <sub>eq</sub>
<b>La1</b>	0.75802(17)	0.87839(8)	0.13743(5)	0.0082(3)
<b>La2</b>	0.25481(17)	0.61367(8)	0.38578(5)	0.0069(3)
<b>La3</b>	0.80795(17)	0.10021(9)	0.01963(5)	0.0089(3)
<b>La4</b>	0.86837(19)	0.84533(8)	0.43356(6)	0.0103(3)
<b>La5</b>	0.68837(17)	0.61847(8)	0.25351(5)	0.0077(3)
<b>La6</b>	0.38684(17)	0.09521(8)	0.18105(5)	0.0084(3)
<b>La7</b>	0.96482(18)	0.11704(9)	0.31787(6)	0.0112(3)
<b>La8</b>	0.58736(18)	0.37294(8)	0.34621(6)	0.0102(3)
<b>La9</b>	0.32247(17)	0.86472(8)	0.29150(6)	0.0090(3)
<b>La10</b>	0.0193(2)	0.35818(9)	0.21394(6)	0.0159(3)
<b>V1</b>	0.5072(6)	0.9061(2)	0.56732(16)	0.0136(9)
<b>V2</b>	0.1489(6)	0.6722(3)	0.12267(18)	0.016(010)
<b>V3</b>	0.5510(6)	0.6722(3)	0.92121(19)	0.0184(10)
<b>V4</b>	0.1096(7)	0.3683(3)	0.47882(19)	0.0210(12)
<b>O1</b>	0.432(2)	0.8224(12)	0.4803(8)	0.019(3)
<b>O2</b>	0.529(3)	0.8244(13)	0.6287(8)	0.024(4)
<b>O3</b>	0.034(2)	0.7461(9)	0.3436(6)	0.007(2)
<b>O4</b>	0.609(2)	0.9797(10)	0.2354(7)	0.013(2)
<b>O5</b>	0.969(2)	0.7196(11)	0.1780(7)	0.017(3)
<b>O6</b>	0.574(5)	0.6667(16)	0.0098(10)	0.041(4)

<b>O7</b>	0.891(2)	0.4926(12)	0.2967(8)	0.019(3)
<b>O8</b>	0.222(2)	0.2378(11)	0.2578(7)	0.015(3)
<b>O9</b>	0.539(2)	0.9878(10)	0.0782(7)	0.012(2)
<b>O10</b>	0.028(2)	0.9892(10)	0.0790(7)	0.011(2)
<b>O11</b>	0.809(2)	0.9947(11)	0.5853(7)	0.018(3)
<b>O12</b>	0.231(3)	0.4139(14)	0.4121(9)	0.031(3)
<b>O13</b>	0.140(4)	0.7324(18)	0.0505(11)	0.050(5)
<b>O14</b>	0.434(2)	0.7215(11)	0.1761(7)	0.015(2)
<b>O15</b>	0.823(4)	0.7330(17)	0.9009(11)	0.049(5)
<b>O16</b>	0.328(2)	0.9950(11)	0.5931(8)	0.019(3)
<b>O17</b>	0.357(3)	0.7538(16)	0.8989(11)	0.045(5)
<b>O18</b>	0.748(2)	0.2398(11)	0.2643(7)	0.014(2)
<b>O19</b>	0.828(3)	0.3939(13)	0.4803(8)	0.027(3)
<b>O20</b>	0.047(3)	0.2220(13)	0.4520(9)	0.029(4)
<b>O21</b>	0.064(6)	0.532(3)	0.0927(18)	0.103(10)
<b>O22</b>	0.543(2)	0.7438(10)	0.3384(6)	0.010(2)
<b>O23</b>	0.281(3)	0.3972(13)	0.5662(8)	0.026(3)
<b>O24</b>	0.099(2)	0.9802(10)	0.2380(6)	0.010(2)
<b>O25</b>	0.376(2)	0.4931(11)	0.2891(7)	0.010(2)
<b>O26</b>	0.433(4)	0.536(2)	0.8710(14)	0.073(7)
<b>Li1</b>	0.2651	0.4929	0.9965	0.010(7)
<b>Li2</b>	0.5	0.5	0.5	0.01
<b>Li3</b>	0	0	0.5	0.01

**Table 29. Anisotropic atomic displacement parameters of  $\beta$ -LiLa<sub>5</sub>O<sub>5</sub>(VO<sub>4</sub>)<sub>2</sub>**

Atom	U <sup>11</sup>	U <sup>22</sup>	U <sup>33</sup>	U <sup>12</sup>	U <sup>13</sup>	U <sup>23</sup>
<b>La1</b>	0.0066(4)	0.0083(4)	0.0094(4)	0.0018(3)	0.0014(3)	0.0021(3)
<b>La2</b>	0.0067(4)	0.0060(4)	0.0078(4)	0.0001(3)	0.0024(3)	0.0024(3)
<b>La3</b>	0.0077(4)	0.0132(4)	0.0061(4)	0.0033(3)	0.0025(3)	0.0020(3)
<b>La4</b>	0.0135(4)	0.0078(4)	0.0081(4)	0.0009(3)	0.0018(3)	0.0014(3)
<b>La5</b>	0.0071(4)	0.0058(4)	0.0101(4)	0.0001(3)	0.0032(3)	0.0030(3)
<b>La6</b>	0.0085(4)	0.0079(4)	0.0083(4)	0.0020(3)	0.0011(3)	0.0017(3)
<b>La7</b>	0.0103(4)	0.0123(4)	0.0090(4)	0.0038(3)	0.0004(3)	-0.0014(3)
<b>La8</b>	0.0118(4)	0.0096(4)	0.0102(4)	0.0024(3)	0.0026(3)	0.0050(3)
<b>La9</b>	0.0078(4)	0.0087(4)	0.0118(4)	0.0026(3)	0.0012(3)	0.0057(3)
<b>La10</b>	0.0133(5)	0.0133(5)	0.0168(5)	0.0015(4)	0.0020(4)	-0.0022(4)
<b>V1</b>	0.0267(15)	0.0060(12)	0.0054(11)	0.0045(10)	0.0013(10)	-0.0025(10)
<b>V2</b>	0.0137(15)	0.0184(15)	0.0123(14)	0.0042(12)	0.0003(11)	-0.0036(12)
<b>V3</b>	0.0113(15)	0.0188(16)	0.0190(16)	-0.0009(12)	-0.0003(12)	0.0001(13)
<b>V4</b>	0.0275(16)	0.0258(18)	0.0134(14)	0.0126(15)	0.0036(12)	0.0073(13)

**Table 30. Selected interatomic distances for  $\beta$ -LiLa<sub>5</sub>O<sub>5</sub>(VO<sub>4</sub>)<sub>2</sub>**

Atom1	Atom2	d, Å			
<b>O1</b>	La2	2.6668(14)	<b>O22</b>	La7	2.5089(21)
	La4	2.7680(18)		La4	2.2987(10)
<b>O2</b>	La8	2.5324(22)		La9	2.3721(14)
	La7	2.8548(22)		La5	2.3888(13)
<b>O3</b>	La4	2.3304(13)	<b>O23</b>	La2	2.4361(13)
	La5	2.4035(10)		La2	2.7953(18)
	La9	2.4253(13)		La8	2.8087(17)
<b>O4</b>	La2	2.4642(14)	<b>O24</b>	La4	2.9180(20)
	La1	2.3952(16)		La7	2.3649(13)
	La6	2.4017(17)		La1	2.3968(10)
<b>O5</b>	La7	2.4086(13)		La9	2.4127(14)
	La9	2.4345(16)	<b>O25</b>	La6	2.4398(13)
	La5	2.5885(18)		La5	2.3552(14)
La1	2.6955(19)	La10		2.3573(10)	
<b>O7</b>	La9	2.7071(14)		La2	2.4141(14)
	La5	2.3553(18)	<b>O26</b>	La8	2.4324(16)
	La10	2.3754(17)		La5	2.5770(25)
La8	2.4078(17)	<b>V1</b>		O2	1.6754(23)
<b>O8</b>	La2	2.4415(13)		O1	1.6759(15)
	La10	2.3104(19)		O16	1.7430(19)
	La7	2.4259(18)	<b>V2</b>	O11	1.7592(16)
La8	2.4588(14)	O13		1.6432(37)	
La6	2.4837(18)	O21		1.6764(46)	
<b>O9</b>	La3	2.3690(10)		O5	1.6983(19)
	La3	2.3792(13)	<b>V3</b>	O14	1.7163(15)
	La1	2.3885(14)		O6	1.646(31)
La6	2.5072(13)	O26		1.6890(22)	
<b>O10</b>	La3	2.3795(17)		O15	1.6931(30)
	La3	2.3888(18)	<b>V4</b>	O17	1.6969(30)
	La1	2.3941(17)		O12	1.6595(23)
La6	2.4877(13)	O23		1.6847(18)	
<b>O11</b>	La4	2.5098(18)		O20	1.7138(22)
	La7	2.8455(20)		O19	1.7412(20)
	La9	2.8881(19)		O19	2.7812(20)
<b>O12</b>	La2	2.5989(22)	<b>Li1</b>	O21	2.2083(58)
	La8	2.6410(24)		O21	2.2983(65)
<b>O13</b>	La3	2.6644(39)		O6	2.3504(41)
<b>O14</b>	La5	2.6224(18)		O6	2.4264(34)
	La1	2.6522(16)		O26	2.8163(43)
	La9	2.7408(16)		O26	2.9606(40)
<b>O15</b>	La3	2.5908(22)	<b>Li2</b>	O13	2.9766(36)
	La10	2.6280(30)		O12	1.9904(18)
<b>O16</b>	La4	2.5840(18)			O12
	La9	2.6808(14)		O23	2.2693(20)
	La7	2.8864(18)		O23	2.2701(20)
<b>O17</b>	La3	2.5868(29)		O19	2.5708(20)
	La10	2.6625(24)	<b>Li3</b>	O19	2.5709(20)
	La6	2.8952(30)		O11	2.0905(20)
<b>O18</b>	La10	2.3615(17)			O11
	La7	2.4288(18)		O16	2.4080(17)
	La8	2.4373(17)		O16	2.4086(17)
	La6	2.4743(13)		O20	2.9865(24)
<b>O19</b>	La8	2.6181(19)		O20	2.9871(24)
	La2	2.6228(22)			
<b>O20</b>	La4	2.4411(24)			

**Table 31. BVS calculation for  $\beta$ -LiLa<sub>5</sub>O<sub>5</sub>(VO<sub>4</sub>)<sub>2</sub>**

Atom	La1	La2	La3	La4	La5	La6	La7	La8	La9	La10	V1	V2	V3	V4	Li1	Li2	Li3	$\Sigma a$
O1		0.26		0.04+0.04							1.37							1.70
O2						0.03	0.15+0.04	0.37			1.38							1.98
O3		0.45		0.65	0.54				0.50									2.15
O4	0.55					0.54	0.53		0.49									2.10
O5	0.24				0.32				0.23			1.30						2.09
O6	0.09												1.48		0.17+0.15			1.89
O7		0.48			0.61			0.53		0.58								2.20
O8						0.43	0.50	0.46		0.69								2.08
O9	0.56		0.59+0.57			0.40												2.12
O10	0.55		0.57+0.56			0.42												2.10
O11				0.40+0.06			0.16			0.14	1.11						0.20+0.20	2.27
O12		0.31						0.28						1.43		0.24+0.24		2.49
O13			0.26										1.50		0.04+0.04			1.83
O14	0.27				0.29				0.21				1.24					2.01
O15			0.32			0.05				0.29				1.31				1.97
O16				0.32			0.14			0.25	1.16						0.12+0.12	2.11
O17			0.32			0.14				0.26			1.30					2.02
O18						0.44	0.50	0.49		0.60								2.03
O19		0.29						0.29						1.16		0.10+0.10		1.93
O20				0.48			0.40							1.25			0.05+0.05	2.23
O21										0.04		1.37			0.13+0.11			1.65
O22		0.49		0.72	0.56				0.59									2.35
O23		0.18+0.04		0.13	0.03			0.17						1.35		0.15+0.15		2.21
O24	0.55					0.48	0.60		0.52									2.15
O25		0.52			0.61			0.49		0.61								2.23
O26					0.33								1.33		0.08+0.06			1.80
$\Sigma c$	2.79	3.02	3.19	2.84	3.29	2.93	3.01	3.09	2.92	3.06	5.01	5.41	5.43	5.18	0.77	0.97	0.75	

$\Sigma va$  and  $\Sigma vc$  are the bond valence sums for anions and cations, respectively.

R; b parameters for La-O are 2.179 and 0.359, for V-O are 1.799 and 0.388, for Li-O are 1.062 and 0.642.

**Table 32. Crystal parameters, data collection and structure refinement details for the crystal of  $LiNd_5O_5(VO_4)_2$**

<b>Crystal data</b>	
Formula	$LiNd_5O_5(VO_4)_2$
Formula weight (g/mol)	1038
Temperature (K)	293
Crystal system	monoclinic
Space group	$C2/m$
$a$ (Å)	19.4507(2)
$b$ (Å)	5.7848(5)
$c$ (Å)	12.2593(1)
$\beta$ (°)	117.847(5)°
$V$ (Å <sup>3</sup> )	1219.7(2)
$Z$	4
<b>Data collection</b>	
Diffractometer	X8 Bruker
Radiation; $\lambda$ (Å)	$AgK\alpha$ ; 0.56086
Absorption coefficient, $\mu$ (mm <sup>-1</sup> )	5.649
$F(000)$	1812
Data range $\theta$ (°); $h, k, l$	1.48– 25.38; $-29 < h < 29$ , $-8 < k < 8$ , $-18 < l < 18$
No. of measured reflections	11412
Total reflections ( $N_2$ )/unique ( $N_1$ )	2474 / 1496
Criterion for observed reflections	$I > 3\sigma(I)$
$R_{int}$ (%)	8.15
<b>Refinement</b>	
Refinement on	Full-matrix least squares on $F$
Weight scheme	$1/(\sigma^2 F  + 0.0001 F^2)$
$R_{Ft}$ , $R_{all}$	3.80, 8.14
$wR_{gt}$ , $wR_{ref}$	3.78, 6.31
$GOF_{gt}$ , $GOF_{ref}$	1.19, 1.53
Max. /min. residual $e$ density, ( $e\text{Å}^{-3}$ )	3.80 / -3.99

**Table 33. Atomic parameters for  $LiNd_5O_5(VO_4)_2$**

Atom	X	Y	Z	Ueq
Nd1	0.89074(5)	0	0.44057(9)	0.0057(3)
Nd2	0.76267(5)	0.5	0.25519(9)	0.0067(3)
Nd3	0.19110(5)	0.5	0.41550(9)	0.0070(4)
Nd4	0.83240(5)	0	0.10994(9)	0.0088(4)
Nd5	0.96954(5)	0.5	0.33388(10)	0.0081(3)
V1	0.14892(18)	0.5	0.0552(3)	0.0110(12)
V2	0.05691(17)	0	0.2462(3)	0.0082(11)
O1	1	0.256(2)	0.5	0.007(2)
O2	0.1165(7)	0	0.1824(13)	0.021(3)
O3	0.9655(8)	0	0.1292(14)	0.028(4)
O4	0.0741(5)	0.2359(19)	0.3397(9)	0.018(2)
O5	0.8633(4)	0.7509(84)	0.2669(7)	0.0065(17)
O6	0.9304(10)	0.5	0.0820(18)	0.051(6)
O7	0.2080(5)	0.7343(83)	0.0672(8)	0.0107(18)
O8	0.7840(5)	0.7467(85)	0.4169(8)	0.0087(16)
O9	0.1233(10)	0.5	0.1666(19)	0.054(6)
Li1	1	0.257(16)	0	0.10(2)

**Table 34. Anisotropic atomic displacement parameters for  $LiNd_5O_5(VO_4)_2$** 

Atom	$U^{11}$	$U^{22}$	$U^{33}$	$U^{13}$
<b>Nd1</b>	0.0042(4)	0.0058(5)	0.0066(5)	0.0021(3)
<b>Nd2</b>	0.0061(4)	0.0068(5)	0.0066(4)	0.0025(3)
<b>Nd3</b>	0.0069(4)	0.0047(5)	0.0112(5)	0.0059(4)
<b>Nd4</b>	0.0104(5)	0.0090(5)	0.0057(4)	0.0028(4)
<b>Nd5</b>	0.0064(4)	0.0057(4)	0.0107(4)	0.0028(3)
<b>V1</b>	0.0114(15)	0.0070(16)	0.0164(16)	0.0080(12)
<b>V2</b>	0.0070(13)	0.0091(16)	0.0095(15)	0.0048(11)

**Table 35. Selected interatomic distances ( $\text{\AA}$ ) in  $LiNd_5O_5(VO_4)_2$** 

Atom 1	Atom 2	d, $\text{\AA}$
<b>O1</b>	Nd5	2.3157(71)
	Nd5	2.3163(71)
	Nd1	2.4070(72)
	Nd1	2.4071(72)
<b>O2</b>	Nd2	2.5515(13)
<b>O3</b>	Nd4	2.4877(17)
<b>O4</b>	Nd5	2.5178(11)
	Nd3	2.5301(97)
	Nd1	2.8048(11)
<b>O5</b>	Nd4	2.2489(87)
	Nd5	2.3387(81)
	Nd2	2.3864(88)
	Nd1	2.4147(88)
<b>O6</b>	Nd5	2.8138(22)
<b>O7</b>	Nd4	2.4698(95)
	Nd2	2.5518(92)
	Nd4	2.6046(99)
<b>O8</b>	Nd2	2.3180(96)
	Nd3	2.3199(10)
	Nd3	2.3588(95)
	Nd1	2.4450(97)
<b>O9</b>	Nd3	2.7005(21)
<b>V1</b>	O9	1.6585(27)
	O6	1.6689(16)
	O7	1.7385(10)
	O7	1.7386(10)
<b>V2</b>	O2	1.6748(18)
	O3	1.6834(12)
	O4	1.7118(11)
	O4	1.7120(11)
<b>Li1</b>	O6	2.4671(57)
	O6	2.4676(57)
	O3	2.4821(58)
	O3	2.4826(58)
	O9	2.7060(50)
	O9	2.7062(50)
	O2	2.7588(51)
	O2	2.7590(51)

**Table 36. Bond-valence analysis (v.u.) for the crystal structure of  $\text{LiNd}_5\text{O}_5(\text{VO}_4)_2$** 

	Nd1	Nd2	Nd3	Nd4	Nd5	V1	V2	Li1	$\sum v_a$
<b>O1</b>	0.44 <sup>x2</sup>				0.56 <sup>x2</sup>				2.01
<b>O2</b>		0.30					1.38	0.07 <sup>x2</sup>	1.82
<b>O3</b>				0.35			1.34	0.11 <sup>x2</sup>	1.92
<b>O4</b>	0.15 <sup>x2</sup>		0.32 <sup>x2</sup>		0.33 <sup>x2</sup>		1.25 <sup>x2</sup>		4.09
<b>O5</b>	0.43 <sup>x2</sup>	0.47 <sup>x2</sup>		0.67 <sup>x2</sup>	0.53 <sup>x2</sup>				4.20
<b>O6</b>					0.15	1.40		0.11 <sup>x2</sup>	1.77
<b>O7</b>		0.30 <sup>x2</sup>		0.37 <sup>x2</sup> + 0.26 <sup>x2</sup>		1.17 <sup>x2</sup>			4.19
<b>O8</b>	0.40 <sup>x2</sup>	0.56 <sup>x2</sup>	0.56 <sup>x2</sup> + 0.50 <sup>x2</sup>						4.03
<b>O9</b>			0.20			1.44		0.08 <sup>x2</sup>	1.79
$\sum v_c$	2.85	2.95	2.95	2.96	2.99	5.17	5.23	0.74	

$\sum v_a$  and  $\sum v_c$  are the bond valence sums for anions and cations, respectively.

R; b parameters for Nd-O are 2.103 and 0.371, for V-O are 1.799 and 0.388, for Li-O are 1.062 and 0.642.

**Table 37. Crystal parameters, data collection and structure refinement details for the crystal of  $\beta\text{-LiLa}_2\text{O}_2\text{VO}_4$** **Crystal data**

Formula	$\text{LiLa}_2\text{O}_2\text{VO}_4$
Formula weight (g/mol)	431.7
Temperature (K)	293
Crystal system	triclinic
Space group	$P-1$
$a$ (Å)	5.8144(7)
$b$ (Å)	5.8167(7)
$c$ (Å)	8.527(1)
$\alpha$ (°)	98.184(7)
$\beta$ (°)	100.662(7)
$\gamma$ (°)	92.579(7)
$V$ (Å <sup>3</sup> )	279.7(2)
$Z$	2

**Data collection**

Diffractometer	SMART APEX DUO
Radiation; $\lambda$ (Å)	$\text{MoK}\alpha$ ; 0.71073
Absorption coefficient, $\mu$ (mm <sup>-1</sup> )	16.583
$F(000)$	376
Data range $\theta$ (°); $h, k, l$	2.46 – 23.42; $-6 < h < 6$ , $-6 < k < 6$ , $-9 < l < 9$
No. of measured reflections	2980
Total reflections ( $N_2$ )/unique ( $N_1$ )	917 / 667
Criterion for observed reflections	$I > 3\sigma(I)$
$R_{\text{int}}$ (%)	2.07

**Refinement**

Refinement on	Full-matrix least squares on $F$
Weight scheme	$1/(\sigma^2 F  + 0.0001 F^2)$
$R_{\text{gt}}, R_{\text{all}}$	0.0494, 0.0564
$wR_{\text{gt}}, wR_{\text{ref}}$	0.0646, 0.0651
$\text{GOF}_{\text{gt}}, \text{GOF}_{\text{ref}}$	3.84, 3.47
Max. /min. residual $e$ density, ( $e\text{Å}^{-3}$ )	6.44 / -1.95

**Table 38. Atomic parameters for  $\beta$ -LiLa<sub>2</sub>O<sub>2</sub>VO<sub>4</sub>**

Atom	X	Y	Z	U <sub>eq</sub>
La1	0.79396(16)	0.53683(15)	0.64942(10)	0.0036(4)
La2	0.29049(16)	0.02787(15)	0.6488(1)	0.0036(4)
V1	0.7888(6)	0.1786(6)	0.9378(4)	0.0155(11)
O1	0.827(3)	0.238(3)	0.1319(16)	0.059(7)
O2	0.9974(18)	0.7476(18)	0.4964(12)	0.003(4)
O3	0.5069(18)	0.2472(19)	0.4996(12)	0.005(4)
O4	0.574(2)	0.356(2)	0.8627(15)	0.023(5)
O5	0.030(2)	0.263(2)	0.8566(14)	0.023(5)
O6	0.668(2)	0.896(2)	0.8561(14)	0.024(5)
Li1	0.660(6)	0.660(5)	0.000(4)	0.022(12)

**Table 39. Anisotropic atomic displacement parameters for  $\beta$ -LiLa<sub>2</sub>O<sub>2</sub>VO<sub>4</sub>**

Atom	U <sup>11</sup>	U <sup>22</sup>	U <sup>33</sup>	U <sup>12</sup>	U <sup>13</sup>	U <sup>23</sup>
La1	0.0042(6)	0.0037(6)	0.0029(6)	-0.0006(4)	0.0007(4)	0.0006(4)
La2	0.0039(6)	0.0036(6)	0.0029(6)	-0.0009(4)	0.0001(4)	0.0005(4)
V1	0.0140(18)	0.0142(18)	0.0187(18)	0.0011(14)	0.0023(14)	0.0052(14)
O1	0.092(13)	0.050(11)	0.028(9)	-0.082(10)	0.065(9)	-0.057(8)
O2	0.000(6)	0.005(6)	0.001(6)	0.002(5)	-0.009(5)	0.001(5)
O3	0.004(6)	0.013(7)	-0.004(6)	-0.002(5)	-0.005(5)	0.008(5)
O4	0.023(8)	0.024(8)	0.023(8)	-0.007(6)	0.012(6)	0.005(6)
O5	0.018(7)	0.030(8)	0.021(8)	0.004(6)	0.001(6)	0.009(6)
O6	0.032(9)	0.020(8)	0.019(8)	-0.003(6)	0.006(7)	-0.001(6)
Li1	0.025(19)	0.017(18)	0.03(2)	0.010(15)	0.009(16)	0.004(15)

**Table 40. Selected interatomic distances (Å) for  $\beta$ -LiLa<sub>2</sub>O<sub>2</sub>VO<sub>4</sub>**

Atom 1	Atom2	d, Å
O1	La2	2.7490(17)
	La1	2.7523(15)
O2	La1	2.3455(11)
	La2	2.3619(93)
	La1	2.4306(11)
	La2	2.4351(11)
O3	La1	2.3664(95)
	La2	2.3866(11)
	La2	2.3958(12)
	La1	2.4663(11)
O4	La2	2.7018(11)
	La1	2.7082(14)
O5	La1	2.7645(12)
	La2	2.7917(12)
O6	La1	2.7523(12)
	La2	2.7630(11)
V1	O1	1.6132(14)
	O4	1.7446(12)
	O6	1.7522(11)
	O5	1.7552(13)
Li1	O4	1.9596(40)
	O4	1.9652(30)
	O6	1.9716(36)
	O5	1.9749(33)

**Table 41. Bond-valence analysis (v.u.) for the crystal structure of  $\beta$ -LiLa<sub>2</sub>O<sub>2</sub>VO<sub>4</sub>**

Atom	La1	La2	V1	Li1	$\Sigma v_a$
O1	0.20	0.20	1.61		2.02
O2	0.50+0.63	0.50+0.49			2.22
O3	0.59+0.45	0.56+0.55			2.15
O4	0.23	0.23	1.15	0.25+0.24	2.10
O5	0.20	0.18	1.12	0.24	1.74
O6	0.20	0.20	1.13	0.24	1.77
$\Sigma v_c$	3.00	3.01	5.01	0.98	

$\Sigma v_a$  and  $\Sigma v_c$  are the bond valence sums for anions and cations, respectively. R; b parameters for La-O are 2.179 and 0.359, for V-O are 1.799 and 0.388, for Li-O are 1.062 and 0.642.

**Table 42. Crystal parameters, data collection and structure refinement details for the crystal of Gd<sub>8</sub>V<sub>2</sub>O<sub>17</sub> and reduced sample.**

Crystal data		
Formula	Gd <sub>8</sub> V <sub>2</sub> O <sub>17</sub>	Gd <sub>8</sub> V <sub>2</sub> O <sub>16.92</sub>
Formula weight (g/mol)	21214.2	10599.1
Temperature (K)	293	293
Crystal system	triclinic	triclinic
Space group	<i>P</i> -1	<i>P</i> -1
<i>a</i> (Å)	9.7899(2)	9.7688(3)
<i>b</i> (Å)	15.9626(3)	15.9639(3)
<i>c</i> (Å)	35.6817(5)	17.8972(2)
$\alpha$ (°)	66.2521(16)	65.884(2)
$\beta$ (°)	82.4549(16)	83.120(2)
$\gamma$ (°)	88.4644(16)	88.128(2)
V (Å <sup>3</sup> )	5057.63(17)	2528.7(1)
Z	1	1
Data collection		
Radiation source; $\lambda$ (Å)		synchrotron; 0.51313
Absorption coef., $\mu$ (mm <sup>-1</sup> )	14.592	14.592
F (000)	9022	4507
Data range $\theta$ (°); <i>h</i> , <i>k</i> , <i>l</i>	1.52 – 32.21; -19 < <i>h</i> < 20, -33 < <i>k</i> < 31, -72 < <i>l</i> < 72	1.52 – 32.18; -19 < <i>h</i> < 19, -32 < <i>k</i> < 32, -29 < <i>l</i> < 28
No. of total reflections	69995	9120
Total unique reflections	38400	7642
Criterion for observed reflections		$I > 3\sigma(I)$
Refinement		
Refinement on		Full-matrix least squares on <i>F</i>
Weight scheme		$1/(\sigma^2  F  + 0.0001 F^2)$
R <sub>gt</sub> , R <sub>all</sub>	7.49, 13.91	5.09, 6.74
wR <sub>gt</sub> , wR <sub>ref</sub>	8.13, 10.42	5.96, 6.58
GOF <sub>gt</sub> , GOF <sub>ref</sub>	2.10, 2.32	2.20; 2.18
Max. /min. residual <i>e</i> density, (eÅ <sup>-3</sup> )	74.08 / -40.69	5.94 / -5.65

### III.5. References

1. Macaluso, R. T., Moreno, N. O., Fisk, Z., Thompson, J. D., & Chan, J. Y. (2004). *Structure and Magnetism of  $Ce_5Pb_3O$* . *Chemistry of Materials*, 16(8), 1560–1563. doi:10.1021/cm0352605 ;
2. Lipp, C., & Schleid, T. (2008). *Die Lanthanoid(III)-Chlorid-Oxoselenate(IV)  $MCl[SeO_3]$  ( $M = Sm-Lu$ ) im  $HoCl[TeO_3]$ - oder B-Typ / The Lanthanoid(III) Chloride Oxoselenates(IV)  $MCl[SeO_3]$  ( $M = Sm-Lu$ ) with  $HoCl[TeO_3]$ - or B-Type Structure*. *Zeitschrift Für Naturforschung B*, 63(3), 229–236. doi:10.1515/znb-2008-0301;
3. Zitzer, S., & Schleid, T. (2010). *The New Neodymium(III) Oxide Chloride Oxoselenate(IV)  $Nd_7O_5Cl_3[SeO_3]_4$* . *Zeitschrift Für Anorganische Und Allgemeine Chemie*, 636(7), 1286–1292. 10.1002/zaac.200900575;
4. Chaminade, J.-P., Gravereau, P., Jubera, V., & Fouassier, C. (1999). *A New Family of Lithium Rare-Earth Oxyborates,  $LiLn_6O_5(BO_3)_3$  ( $Ln=Pr-Tm$ ): Crystal Structure of the Gadolinium Phase  $LiGd_6O_5(BO_3)_3$* . *Journal of Solid State Chemistry*, 146(1), 189–196. doi:10.1006/jssc.1999.8331 ;
5. Dzhurinskii, B. F.; Tananaev, I. V.; Tselebrovskaya, E. G.; Prozorovskii, A. I. (1991). *Lanthanoid germanophosphates*. *Izvestiya Akademii Nauk SSSR, Neorganicheskie Materialy*. SSSR, 27, 334;
6. Genkina, E.A.; Maximov, B.A.; Dem'yanets, L.N. (Demyanets, L.N.); Mamin, B.F. (1990). *Synthesis and atomic structure of  $Er_{13}Ge_6O_{31}(OH)$* . *Kristallografiya* 35, 642;
7. Colmont, M., Lemoine, K., Roussel, P., Kabbour, H., Olchowka, J., Henry, N., ... Mentré, O. (2019). *Identification and optical features of the  $Pb_4Ln_2O_7$  series ( $Ln = La, Gd, Sm, Nd$ ), genuine 2D-van der Waals oxides*. *Chemical Communications*. doi:10.1039/c8cc07707j;
8. Gómez Torres, M.A., Gauthier, G.H., Kaczmarek, A.M., Huvé, M., Roussel, P., Dupray, V., Yuan, L., Zadoya, A., Colmont, M. *Inorganic Chemistry*, 2020, 59, 5929-5938; doi: 10.1021/acs.inorgchem.9b03689;
9. Colmont, M., Palatinus, L., Huvé, M., Kabbour, H., Saitzek, S., Djelal, N., & Roussel, P. (2016). *On the Use of Dynamical Diffraction Theory To Refine Crystal Structure from Electron Diffraction Data: Application to  $KLa_5O_5(VO_4)_2$ , a Material with Promising Luminescent Properties*. *Inorganic Chemistry*, 55(5), 2252–2260. doi:10.1021/acs.inorgchem.5b02663;
10. Bünzli, J.-C. G. (2013). *Lanthanides*. *Kirk-Othmer Encyclopedia of Chemical Technology*. doi:10.1002/0471238961.1201142019010215.a0;
11. Das, G. K., Heng, B. C., Ng, S.-C., White, T., Loo, J. S. C., D'Silva, L., ... Tan, T. T. Y. (2010). *Gadolinium Oxide Ultranarrow Nanorods as Multimodal Contrast Agents for Optical and Magnetic Resonance Imaging*, *Langmuir*, 26, 8959–8965;
12. Warburg, E. (1881). *Magnetische Untersuchungen*. *Annalen Der Physik*, 249(5), 141–164. doi:10.1002/andp.18812490510 ;
13. Metcalfe, M. J., & Rosenberg, H. M. (1970). *Heat conduction by magnons in  $GdVO_4$  at low temperatures*. *Physics Letters A*, 33(4), 211–213. doi:10.1016/0375-9601(70)90738-3 ;
14. Kitayama, K., Zoshima, D., & Katsura, T. (1983). *Phase Equilibria in the  $La_2O_3-V_2O_3-V_2O_5$  System at 1200 °C*. *Bulletin of the Chemical Society of Japan*, 56(3), 689–694. doi:10.1246/bcsj.56.689;
15. Kitayama, K., & Katsura, T. (1985). *Phase Equilibria in the  $Ln_2O_3-V_2O_3-V_2O_5$  ( $Ln=Pr, Tb, and Y$ ) Systems at 1200 °C*. *Bulletin of the Chemical Society of Japan*, 58(3), 948–956. doi:10.1246/bcsj.58.948;

16. Kitayama, K., Mizokuchi, C., & Katsura, T. (1983). *Phase Equilibria in the Nd<sub>2</sub>O<sub>3</sub>–V<sub>2</sub>O<sub>3</sub>–V<sub>2</sub>O<sub>5</sub> System at 1200 °C*. Bulletin of the Chemical Society of Japan, 56(3), 695–699. doi:10.1246/bcsj.56.695;
17. Kitayama, K., & Katsura, T. (1977). *Phase Equilibria in Sm<sub>2</sub>O<sub>3</sub>–V<sub>2</sub>O<sub>3</sub>–V<sub>2</sub>O<sub>5</sub> System at 1200 °C*. Bulletin of the Chemical Society of Japan, 50(4), 889–894. doi:10.1246/bcsj.50.889;
18. Kitayama, K., Sou, H., & Katsura, T. (1983). *Phase Equilibria in the Ln<sub>2</sub>O<sub>3</sub>–V<sub>2</sub>O<sub>3</sub>–V<sub>2</sub>O<sub>5</sub>(Ln=Eu and Yb) Systems at 1200°C*. Bulletin of the Chemical Society of Japan, 56(11), 3415–3420. doi:10.1246/bcsj.56.3415;
19. Kitayama, K., & Katsura, T. (1982). *Phase Equilibria in the Gd<sub>2</sub>O<sub>3</sub>–V<sub>2</sub>O<sub>3</sub>–V<sub>2</sub>O<sub>5</sub> System at 1200°C*. Bulletin of the Chemical Society of Japan, 55(6), 1820–1823. doi:10.1246/bcsj.55.1820;
20. Kitayama, K., & Katsura, T. (1984). *Phase Equilibria in the Ln<sub>2</sub>O<sub>3</sub>–V<sub>2</sub>O<sub>3</sub>–V<sub>2</sub>O<sub>5</sub>(Ln=Dy and Ho) Systems at 1200°C*. Bulletin of the Chemical Society of Japan, 57(5), 1222–1226. doi:10.1246/bcsj.57.1222;
21. Kitayama, K., Sugihara, T., & Katsura, T. (1979). *Phase Equilibria in the Er<sub>2</sub>O<sub>3</sub>–V<sub>2</sub>O<sub>3</sub>–V<sub>2</sub>O<sub>5</sub> System at 1200°C*. Bulletin of the Chemical Society of Japan, 52(2), 458–461. doi:10.1246/bcsj.52.458;
22. Kitayama, K., & Katsura, T. (1983). *Phase Equilibria in the Tm<sub>2</sub>O<sub>3</sub>–V<sub>2</sub>O<sub>3</sub>–V<sub>2</sub>O<sub>5</sub> System at 1200°C*. Bulletin of the Chemical Society of Japan, 56(4), 1084–1088. doi:10.1246/bcsj.56.1084;
23. Kitayama, K., & Katsura, T. (1978). *Phase Equilibria in the Lu<sub>2</sub>O<sub>3</sub>–V<sub>2</sub>O<sub>3</sub>–V<sub>2</sub>O<sub>5</sub> System at 1200°C*. Bulletin of the Chemical Society of Japan, 51(5), 1358–1362. doi:10.1246/bcsj.51.1358;
24. Zhang, S., Zhang, P., Huang, Y., & Seo, H. J. (2018). *Self-activated emission and spectral temperature-dependence of Gd<sub>8</sub>V<sub>2</sub>O<sub>17</sub> phosphor*. Journal of Luminescence. doi:10.1016/j.jlumin.2018.11.054 ;
25. Deng, B., Liu, S., Zhou, C., Liu, H., Chen, J., & Yu, R. (2018). *Eu<sup>3+</sup>-Activated Gd<sub>8</sub>V<sub>2</sub>O<sub>17</sub>: Energy Transfer, Luminescence, and Temperature-Dependence Characteristics*. Chemistry - A European Journal, 24(45), 11627–11636. doi:10.1002/chem.201800889;
26. Sawicki, B., Piz, M., Filipek, E., Groń, T., Duda, H. (2017). *Electrical Transport Properties of Yb<sub>8-x</sub>Y<sub>x</sub>V<sub>2</sub>O<sub>17</sub> (x = 0, 2, 8)*. Acta Physica Polonica A., 132, 363-365;
27. Brusset, H., Mahe, R., Laude, P. J. (1973). Bull. Soc. Chim. Fr. 2, 495–499;
28. Brusset, H., Madaule-Aubry, F., Blanck, B., Deboichet, A. (1969). Bull. Soc. Chim. Fr., 1, 15–16;
29. Yoon, S., Maegli, A. E., Karvonen, L., Shkabko, A., Populoh, S., Gałazka, K., ... Weidenkaff, A. (2014). *Synthesis, crystal structure, electric and magnetic properties of LaVO<sub>2.78</sub>N<sub>0.10</sub>*. Zeitschrift für Anorganische und Allgemeine Chemie, 640(5), 797-804. <https://doi.org/10.1002/zaac.201300593>;
30. Levin, E. M. (1967). *Structural Interpretation of Immiscibility in Oxide Systems: IV, Occurrence, Extent, and Temperature of the Monotectic*. Journal of the American Ceramic Society, 50(1), 29–38. doi:10.1111/j.1151-2916.1967.tb14967.x;
31. Piz, M., & Filipek, E. (2017). *Synthesis and homogeneity range of Yb<sub>8-x</sub>Y<sub>x</sub>V<sub>2</sub>O<sub>17</sub> in the Yb<sub>8</sub>V<sub>2</sub>O<sub>17</sub>–Y<sub>8</sub>V<sub>2</sub>O<sub>17</sub> system*. Journal of Thermal Analysis and Calorimetry, 130(1), 277–283. doi:10.1007/s10973-017-6379-0;
32. Petříček, V., Dušek, M., & Palatinus, L. (2014). *Crystallographic Computing System JANA2006: General features*. Zeitschrift Für Kristallographie - Crystalline Materials, 229(5). doi:10.1515/zkri-2014-1737;

33. Palatinus, L., & Chapuis, G. (2007). *SUPERFLIP—a computer program for the solution of crystal structures by charge flipping in arbitrary dimensions*. *Journal of Applied Crystallography*, 40(4), 786–790. doi:10.1107/s0021889807029238;
34. Phan, M.-H., & Yu, S.-C. (2007). *Review of the magnetocaloric effect in manganite materials*. *Journal of Magnetism and Magnetic Materials*, 308(2), 325–340. doi:10.1016/j.jmmm.2006.07.025;
35. Romero Gómez, J., Ferreiro Garcia, R., De Miguel Catoira, A., & Romero Gómez, M. (2013). *Magnetocaloric effect: A review of the thermodynamic cycles in magnetic refrigeration*. *Renewable and Sustainable Energy Reviews*, 17, 74–82. doi:10.1016/j.rser.2012.09.027;
36. IPCC (2005). *Safe guarding the Ozone Layer and the Global Climate System: Issues Related to Hydrofluorocarbons and Per-fluorocarbons*. Cambridge University Press, 185–194;
37. WMO (2018). *Scientific Assessment of Ozone Depletion*, 37;
38. Evangelisti, M., & Brechin, E. K. (2010). *Recipes for enhanced molecular cooling*. *Dalton Transactions*, 39(20), 4672. doi:10.1039/b926030g
39. Evangelisti, M., Roubeau, O., Palacios, E., Camón, A., Hooper, T. N., Brechin, E. K., & Alonso, J. J. (2011). *Cryogenic Magnetocaloric Effect in a Ferromagnetic Molecular Dimer*. *Angewandte Chemie International Edition*, 50(29), 6606–6609. doi:10.1002/anie.201102640;
40. Yang, Y., Zhang, Q.-C., Pan, Y.-Y., Long, L.-S., & Zheng, L.-S. (2015). *Magnetocaloric effect and thermal conductivity of  $Gd(OH)_3$  and  $Gd_2O(OH)_4(H_2O)_2$* . *Chemical Communications*, 51(34), 7317–7320. doi:10.1039/c5cc01254f;
41. Giauque, W. F., & MacDougall, D. P. (1935). *The Production of Temperatures below One Degree Absolute by Adiabatic Demagnetization of Gadolinium Sulfate*. *Journal of the American Chemical Society*, 57(7), 1175–1185. doi:10.1021/ja01310a007;
42. Palacios, E., Evangelisti, M., Sáez-Puche, R., Dos Santos-García, A. J., Fernández-Martínez, F., Cascales, C., ... Rodríguez-Velamazán, J. A. (2018). *Magnetic structures and magnetocaloric effect in  $RVO_4$  ( $R=Gd, Nd$ )*. *Physical Review B*, 97(21). doi:10.1103/physrevb.97.214401;
43. Han, Y., Han, S.-D., Pan, J., Ma, Y.-J., & Wang, G.-M. (2018). *An excellent cryogenic magnetic cooler: magnetic and magnetocaloric study of an inorganic frame material*. *Materials Chemistry Frontiers*. doi:10.1039/c8qm00439k;
44. Brown, D.P. (1976). *ISABELLE Forced Circulation System: Proposed Method of Producing and Distributing Helium Refrigerant for 4.5 K Superconducting Magnets*. United States: N.P.;
45. Pecharsky, V. K., & Gschneidner, Jr., K. A. (1997). *Giant Magnetocaloric Effect in  $Gd_5(Si_2Ge_2)$* . *Physical Review Letters*, 78(23), 4494–4497. doi:10.1103/physrevlett.78.4494;
46. Kabbour, H., Gauthier, G. H., Tessier, F., Huvé, M., Pussacq, T., Roussel, P., ... Mentré, O. (2017). *Topochemical Reduction of  $YMnO_3$  into a Composite Structure*. *Inorganic Chemistry*, 56(14), 8547–8553. doi:10.1021/acs.inorgchem.7b01309;
47. Pussacq, T., Kabbour, H., Colis, S., Vezin, H., Saitzek, S., Gardoll, O., ... Mentré, O. (2017). *Reduction of  $Ln_2Ti_2O_7$  Layered Perovskites: A Survey of the Anionic Lattice, Electronic Features, and Potentials*. *Chemistry of Materials*, 29(3), 1047–1057. doi:10.1021/acs.chemmater.6b03808;
48. Shimakawa, Y., Inoue, S., Haruta, M., Kawai, M., Matsumoto, K., Sakaiguchi, A., ... Kurata, H. (2010). *Topotactic Changes in Thin Films of Brownmillerite  $SrFeO_{2.5}$  Grown*

- on SrTiO<sub>3</sub> Substrates to Infinite-Layer Structure SrFeO<sub>2</sub>. *Crystal Growth & Design*, 10(11), 4713–4715. doi:10.1021/cg101133w;
49. Tauc, J., Grigorovici, R., & Vancu, A. (1966). *Optical Properties and Electronic Structure of Amorphous Germanium*. *Physica Status Solidi (b)*, 15(2), 627–637. doi:10.1002/pssb.19660150224;
  50. Kubelka, P.; Munk, F. (1931). *Ein Beitrag Zur Optik Der Farbanstriche*. *Z. Techn. Phys.*, 12, 593–601;
  51. Yu, S., Huang, H., Dong, F., Li, M., Tian, N., Zhang, T., & Zhang, Y. (2015). *Synchronously Achieving Plasmonic Bi Metal Deposition and I– Doping by Utilizing BiOIO<sub>3</sub> as the Self-Sacrificing Template for High-Performance Multifunctional Applications*. *ACS Applied Materials & Interfaces*, 7(50), 27925–27933. doi:10.1021/acsami.5b09994;
  52. Schipper, W. J., Vroon, Z. A. E. P., Blasse, G., Schleid, T., & Meyer, G. (1991). *Luminescence of Eu<sup>2+</sup>-activated materials with host lattice M<sub>4</sub>OX<sub>6</sub> (M=Sr, Ba; X=Cl, Br)*. *Materials Chemistry and Physics*, 30(1), 43–46. doi:10.1016/0254-0584(91)90152-k;
  53. Lissner, F., & Schleid, T. (1998). *Sulfidchloride (MSCl) der leichten Lanthanide (M=La–Pr)*. *Zeitschrift Für Anorganische Und Allgemeine Chemie*, 624(3), 452–456. doi:10.1002/(sici)1521-3749(199803)624:3<452::aid-zaac452>3.0.co;2-a ;
  54. Grice, J. D.; Maisonneuve, V.; Leblanc, M. *Chem. Rev.* 2007, 107, 114 ;
  55. Gschneidner, K. A.; Bünzli, J.-C. G.; Pecharsky, V. K. *Optical Spectroscopy*; Elsevier North-Holland: Amsterdam, The Netherlands, 2007;
  56. Gschneidner, K. A.; Bünzli, J.-C. G.; Pecharsky, V. K. Preface. (2011) *Handbook on the Physics and Chemistry of Rare Earths*; Elsevier, Vol. 41, pp v–x;
  57. Kaczmarek, A. M.; Van Deun, R. (2013). *Rare earth tungstate and molybdate compounds – from 0D to 3D architectures*. *Chem. Soc. Rev.*, 42 (23), 8835;
  58. Blasse, G.; Grabmaier, B. C. (1994). *Luminescent Materials*; Springer: Berlin;
  59. Yen, W. M., Shionoya, S., Yamamoto, H. (2007) Eds. *Phosphor Handbook*, 2nd ed.; CRC Press: Boca Raton, FL;
  60. Kaczmarek, A. M., Van Hecke, K., Van Deun, R. (2015). *Nano- and micro-sized rare-earth carbonates and their use as precursors and sacrificial templates for the synthesis of new innovative materials*. *Chemical Society Reviews*, 44(8), 2032–2059. doi:10.1039/c4cs00433g;
  61. Bünzli, J.-C. G.; Piguet, C. (2005). *Taking advantage of luminescent lanthanide ions*. *Chem. Soc. Rev.*, 34 (12), 1048;
  62. Cavalli, E.; Angiuli, F.; Belletti, A.; Boutinaud P. (2014). *Luminescence spectroscopy of YVO<sub>4</sub>:Ln<sup>3+</sup>, Bi<sup>3+</sup> (Ln<sup>3+</sup> = Eu<sup>3+</sup>, Sm<sup>3+</sup>, Dy<sup>3+</sup>) phosphors*. *Opt. Mater.*, 36 (10), 1642–1648;
  63. Murakami, M.; Hirose, K.; Kawamura, K.; Sata, N.; Ohishi, Y. (2004). *Post-Perovskite Phase Transition in MgSiO<sub>3</sub>*. *Science.*, 304, 855–858;
  64. Markkula, M.; Arevalo-Lopez, A. M.; Kusmartseva, A.; Rodgers, J. A.; Ritter, C.; Wu, H.; Attfield, J.P. (2011). *Incommensurate spin order in the metallic perovskite MnVO<sub>3</sub>*. *Phys. Rev. B Condens. Matter*. 84, 094450;
  65. Takayama-Muromachi, E. *Chem. Mater.* **1998**, 10, 2686–2698.
  66. Khandy, S. A., Islam, I., Ganai, Zahid Saleem, Gupta, D. C., & Parrey, K. A. (2017). *High-Temperature and High-Pressure Study of Electronic and Thermal Properties of PbTaO<sub>3</sub> and SnAlO<sub>3</sub> Metal Perovskites by Density Functional Theory Calculations*. *Journal of Electronic Materials*, 47(1), 436–442. doi:10.1007/s11664-017-5785-1;

67. Choy, J.-H., Byeon, S.-H., & Demazeau, G. (1988). *Ir, Raman, and X-ray photoelectron spectroscopy investigations of the ordered cubic perovskite La<sub>2</sub>LiVO<sub>6</sub>*. *Journal of Solid State Chemistry*, 76(1), 97–101. doi:10.1016/0022-4596(88)90195-8
68. Park, S. W., Kyoung Yang, H., Won Chung, J., Chen, Y., Kee Moon, B., Chun Choi, B., ... Hwan Kim, J. (2010). *Photoluminescent properties of LaVO<sub>4</sub>:Eu<sup>3+</sup> by structural transformation*. *Physica B: Condensed Matter*, 405(18), 4040–4044. doi:10.1016/j.physb.2010.06.052;
69. Yu, R., Jeong, J. H., & Wang, Y.-F. (2017). *A novel Eu<sup>3+</sup>- and self-activated vanadate phosphor of Ca<sub>4</sub>La(VO<sub>4</sub>)<sub>3</sub>O with oxyvanadate apatite structure*. *Journal of the American Ceramic Society*, 100(12), 5649–5658. doi:10.1111/jace.15102;
70. Kaczmarek, A. M., Ndagsi, D., & Van Deun, R. (2016). *Dopant and excitation wavelength dependent color tunability in Dy<sup>3+</sup>:YVO<sub>4</sub> and Dy<sup>3+</sup>/Eu<sup>3+</sup>:YVO<sub>4</sub> microparticles towards white light emission*. *Dalton Transactions*, 45(41), 16231–16239. doi:10.1039/c6dt02347a;
71. Dang, P., Liu, D., Wei, Y., Li, G., Lian, H., Shang, M., & Lin, J. (2020). *Highly Efficient Cyan-Green Emission in Self-Activated Rb<sub>3</sub>RV<sub>2</sub>O<sub>8</sub> (R = Y, Lu) Vanadate Phosphors for Full-Spectrum White Light-Emitting Diodes (LEDs)*. *Inorganic Chemistry*. doi:10.1021/acs.inorgchem.0c00015;
72. Kroumova, E., Aroyo, M. I., Perez-Mato, J. M., Kirov, A., Capillas, C., Ivantchev, S., & Wondratschek, H. (2003). *Bilbao Crystallographic Server: Useful Databases and Tools for Phase-Transition Studies*. *Phase Transitions*, 76(1-2), 155–170. doi:10.1080/0141159031000076110;
73. Cheng, K., Li, C., Yin, C., Tang, Y., Sun, Y., & Fang, L. (2019). *Effects of Sr<sup>2+</sup> substitution on the crystal structure, Raman spectra, bond valence and microwave dielectric properties of Ba<sub>3-x</sub>Sr<sub>x</sub>(VO<sub>4</sub>)<sub>2</sub> solid solutions*. *Journal of the European Ceramic Society*. doi:10.1016/j.jeurceramsoc.2019.05.030;
74. Azdouz, M., Manoun, B., Azrou, M., Bih, L., El Ammari, L., Benmokhtar, S., & Lazor, P. (2010). *Synthesis, Rietveld refinements and Raman spectroscopy studies of the solid solution Na<sub>1-x</sub>K<sub>x</sub>Pb<sub>4</sub>(VO<sub>4</sub>)<sub>3</sub> (0 ≤ x ≤ 1)*. *Journal of Molecular Structure*, 963(2-3), 258–266. doi:10.1016/j.molstruc.2009.10.047;
75. Azdouz, M., Manoun, B., Essehli, R., Azrou, M., Bih, L., Benmokhtar, S., ... Lazor, P. (2010). *Crystal chemistry, Rietveld refinements and Raman spectroscopy studies of the new solid solution series: Ba<sub>3-x</sub>Sr<sub>x</sub>(VO<sub>4</sub>)<sub>2</sub> (0 ≤ x ≤ 3)*. *Journal of Alloys and Compounds*, 498(1), 42–51. doi:10.1016/j.jallcom.2010.03.066;
76. Cheng, X., Guo, D., Feng, S., Yang, K., Wang, Y., Ren, Y., & Song, Y. (2015). *Structure and stability of monazite- and zircon-type LaVO<sub>4</sub> under hydrostatic pressure*. *Optical Materials*, 49, 32–38. doi:10.1016/j.optmat.2015.08.011;
77. Araújo, B. S., Arévalo-López, A. M., Santos, C. C., Attfield, J. P., Paschoal, C. W. A., & Ayala, A. P. (2020). *Spin-phonon coupling in monoclinic BiCrO<sub>3</sub>*. *Journal of Applied Physics*, 127(11), 114102. doi:10.1063/1.5143347;
78. Grzechnik, A., & McMillan, P. F. (1995). *High temperature and high pressure Raman study of LiVO<sub>3</sub>*. *Journal of Physics and Chemistry of Solids*, 56(2), 159–164. doi:10.1016/0022-3697(94)00145-6;
79. Liu, L., Song, H. X., Li, X., Zhang, D., Mathieu, R., Ivanov, S., ... Lazor, P. (2019). *Pressure-induced polymorphism and piezochromism in Mn<sub>2</sub>FeSbO<sub>6</sub>*. *Applied Physics Letters*, 114(16), 162903. doi:10.1063/1.5090649;
80. Arévalo-López, Á. M., Solana-Madruga, E., Aguilar-Maldonado, C., Ritter, C., Mentré, O., & Attfield, J. P. (2019). *Magnetic frustration in the high-pressure Mn<sub>2</sub>MnTeO<sub>6</sub> (Mn<sub>3</sub>TeO<sub>6</sub>-II) double perovskite*. *Chemical Communications*. 55, 14470. doi:10.1039/c9cc07733b;

81. Shen, Y., Kumar, R. S., Pravica, M., & Nicol, M. F. (2004). *Characteristics of silicone fluid as a pressure transmitting medium in diamond anvil cells*. Review of Scientific Instruments, 75(11), 4450–4454. doi:10.1063/1.1786355
82. Coelho, A. A. (2018). *TOPAS and TOPAS-Academic: an optimization program integrating computer algebra and crystallographic objects written in C++*. Journal of Applied Crystallography, 51(1), 210–218. doi:10.1107/s1600576718000183
83. Colmont, M., Bucataru, G., Borowiec, A., Capron, M., Dumeignil, F., Huvé, M., ... Roussel, P. (2015). *Novel La<sub>3</sub>Fe(MoO<sub>4</sub>)<sub>6</sub> phase: magnetic properties and ethanol reactivity*. Dalton Transactions, 44(32), 14444–14452. doi:10.1039/c5dt01444a;
84. Lü, M., Colmont, M., Huvé, M., De Waele, I., Terryn, C., Aliev, A., & Mentré, O. (2014). *Investigation of New Alkali Bismuth Oxosulfates and Oxophosphates with Original Topologies of Oxo-Centered Units*. Inorganic Chemistry, 53(22), 12058–12065. doi:10.1021/ic501776h;
85. Lü, M., Aliev, A., Olchowka, J., Colmont, M., Huvé, M., Wickleder, C., & Mentré, O. (2013). *Multidimensional Open-Frameworks: Combinations of One-Dimensional Channels and Two-Dimensional Layers in Novel Bi/M Oxo-Chlorides*. Inorganic Chemistry, 53(1), 528–536. doi:10.1021/ic402578m
86. Padhi, A. K., Archibald, W. B., Nanjundaswamy, K. S., & Godenough, J. B. (1997). *Ambient and High-Pressure Structures of LiMnVO<sub>4</sub> and Its Mn<sup>3+</sup>/Mn<sup>2+</sup> Redox Energy*. Journal of Solid State Chemistry, 128(2), 267–272. doi:10.1006/jssc.1996.7217;
87. Hoppe, R., Kissel, J. (1989). *Über Lithovanadate: Zur Kenntnis von Rb<sub>2</sub>[LiVO<sub>4</sub>] und Cs<sub>2</sub>[LiVO<sub>4</sub>]*. Zeitschrift Für Anorganische Und Allgemeine Chemie, 571(1), 113–126. doi:10.1002/zaac.19895710112;
88. Reeswinkel, T., Sparta, K. M., Roth, G. (2008). *Ba<sub>3</sub>Li<sub>2</sub>V<sub>2</sub>O<sub>7</sub>Cl<sub>4</sub>, a new vanadate with a channel structure*. Acta Crystallographica Section C Crystal Structure Communications, 64(4), i38–i40. doi:10.1107/s0108270108002801;
89. Charkin, D. O., Grischenko, R. O., Sadybekov, A. A., Goff, R. J., Lightfoot, P. (2008). *A New Approach to Synthesis of Layered Fluorites Containing Molecular Anions: Synthesis of Ln<sub>2</sub>O<sub>2</sub>CO<sub>3</sub>, K(LnO)CO<sub>3</sub>, and Ln<sub>2</sub>O<sub>2</sub>CrO<sub>4</sub> via Metathesis Reactions*. Inorganic Chemistry, 47(8), 3065–3071. doi:10.1021/ic701558m;
90. Ozawa, T. C., & Kauzlarich, S. M. (2008). *Chemistry of layered d-metal pnictide oxides and their potential as candidates for new superconductors*. Science and Technology of Advanced Materials, 9(3), 033003. doi:10.1088/1468-6996/9/3/033003;
91. Rice, C. E., Robinson, W. R. (1976). *Lanthanum orthovanadate*. Acta Crystallographica Section B Structural Crystallography and Crystal Chemistry, 32(7), 2232–2233. doi:10.1107/s0567740876007450;
92. Attfield, J. P., & Férey, G. (1989). *Structure determinations of La<sub>2</sub>O<sub>2</sub>CO<sub>3</sub>-II and the unusual disordered phase La<sub>2</sub>O<sub>2.52</sub>(CO<sub>3</sub>)<sub>0.74</sub>Li<sub>0.52</sub> using powder diffraction*. Journal of Solid State Chemistry, 82(1), 132–138. doi:10.1016/0022-4596(89)90232-6;
93. Al-Maliky, M. A.; Frentzen, M.; Meister (2019). *Lasers in Medical Science*, 35, 13-30;
94. Bauernfeind, L., Widder, W., & Braun, H. F. (1995). *Ruthenium-based layered cuprates RuSr<sub>2</sub>LnCu<sub>2</sub>O<sub>8</sub> and RuSr<sub>2</sub>(Ln<sub>1+x</sub>Ce<sub>1-x</sub>)Cu<sub>2</sub>O<sub>10</sub> (Ln-Sm, Eu and Gd)*. Physica C: Superconductivity, 254(1-2), 151–158. doi:10.1016/0921-4534(95)00574-9;
95. Bergström, Ö., Gustafsson, T., Thomas, J. O. (1998) *Electrochemically Lithiated Vanadium Oxide, Li<sub>3</sub>V<sub>6</sub>O<sub>13</sub>*. Acta Crystallographica Section C Crystal Structure Communications, 54(9), 1204–1206;
96. Demazeau, G.; Huppertz, H.; Alonso, J. A.; Pöttgen, R.; Moran, E.; Attfield, J. P. (2006) *Materials chemistry under high pressures*. Zeitschrift für naturforschung section b-A journal of chemical sciences. 61b, 1457 – 1470;

97. De, C., Arévalo-López, Á. M., Orlandi, F., Manuel, P., Attfield, J. P., & Sundaresan, A. (2018). *Isovalent Cation Ordering in the Polar Rhombohedral Perovskite Bi<sub>2</sub>FeAlO<sub>6</sub>*. *Angewandte Chemie International Edition*. doi:10.1002/anie.201810122 ;
98. Solana-Madruga, E., Arévalo-López, Á. M., Dos Santos-García, A. J., Urones-Garrote, E., Ávila-Brandé, D., Sáez-Puche, R., & Attfield, J. P. (2016). *Double Double Cation Order in the High-Pressure Perovskites MnRMnSbO<sub>6</sub>*. *Angewandte Chemie International Edition*, 55(32), 9340–9344. doi:10.1002/anie.201603526;
99. Tung, L. D. (2006). *Tunable temperature-induced magnetization jump in a GdVO<sub>3</sub> single crystal*. *Physical Review B*, 73(2). doi:10.1103/physrevb.73.024428;



---

IV. *Crystal chemistry of Pb-based oxo-centered  
compounds*

---

In this chapter, several Pb-based oxo-centered materials will be investigated. In a first part, the family of 2D Van der Waals oxide  $\text{Pb}_4\text{Ln}_2\text{O}_7$  ( $\text{Ln} = \text{Nd}, \text{Sm}$  and  $\text{Gd}$ ) materials is presented. In a second part, the existence of the solid solution  $\text{Bi}_{4.65-x}\text{Pb}_x\text{La}_{1.36}\text{O}_9$  ( $0 < x < 2$ ) is discussed and the ionic conductivity of several terms studied. In the last part, several new crystal structures are presented and structurally described.

#### IV.1. $\text{Pb}_4\text{Ln}_2\text{O}_7$ ( $\text{Ln} = \text{Nd}, \text{Sm}$ and $\text{Gd}$ )

$\text{Pb}_4(\text{Ln})_2\text{O}_7$  series ( $\text{Ln} = \text{La}, \text{Gd}, \text{Sm}$  and  $\text{Nd}$ ) belongs to the restricted group of Van der Waals (VdW) materials. They are built on 2D neutral layers with robust intra-covalent bonds stacked together in the third dimension. The layers are connected through weak covalent / ionic bonds. This unique stacking gives them particular properties and applications in various domains as lubricants, optics, electronics, sensors and energy. Also, they demonstrate an interesting modularity that is an advantage to tune their performances either by modification of the structure of the layer itself or by intercalation of organic/inorganic species between the layers [2]. VdW materials belong to various type of materials: graphene and derivatives [3], transition metal dichalcogenides [4], boron nitrides [5] or phosphorene and group IV-VI compounds [6])... To date, only rare examples of real VdW oxides are reported although the demand of ultrathin layers and possibilities of exfoliation followed by restacking is going exponentially. In classical 2D oxides, the layers are connected together by weak interactions or oxygen bonds with the possibility of element intercalation or oxygen bridges as observed in the cases of  $\text{Mo}/\text{WO}_3$  or  $\text{V}_2\text{O}_5$ . [2, 8] In real 2D VdW compounds, an active lone pair cation act as a templating agent as in the well-known litharge  $\alpha\text{-PbO}$ .

In our group, many new materials were successfully obtained using a predictive approach, including 2D structures build on  $\text{Bi}^{3+}$  or  $\text{Pb}^{2+}$  cations particularly adapted, because its lone pair favors the stacking of monovalent ( $[\text{BiO}]^+$ ), divalent ( $[\text{Bi}_2\text{O}_2]^{2+}$ ) ... or also neutral layers ( $[\text{PbO}]^0$ ). Step by step, the variety of neutral layers increased ( $[\text{PbBi}_2\text{O}_4]^0$ , [9]  $[\text{Bi}_{4.85}\text{La}_{1.85}\text{O}_9]^0$  [20]...) and opened the door to a wide range of possibilities.

Initially, some chemical modifications of  $\text{Bi}_4(\text{Bi}/\text{Ln})_2\text{O}_9$  [11], a 2D VdW compound evidenced in our lab long time ago, were used to obtain a series of new oxygen deficient 2D-VdW compounds with general formula of  $\text{Pb}_4\text{Ln}_2\text{O}_7$  ( $\text{Ln} = \text{La}, \text{Gd}, \text{Sm}, \text{Nd}$ ). The two crystal structures are presented on Figure 94. They have the same specific features, including the specific layers built on  $[\text{O}(\text{Bi}/\text{Pb})_3\text{La}]$ ,  $[\text{O}(\text{Bi}/\text{Pb})\text{La}_3]$  or  $[\text{O}(\text{Bi}/\text{Pb})_4]$  oxo-centered tetrahedra sharing edges. Contrary to the random distribution of Bi/La at the center of layers, a full Pb/La

ordering is observed with  $\text{La}^{3+}$  tacking place exclusively in the middle of layers and  $\text{Pb}^{2+}$  at the external part so that the LP can point towards outside. For the lead structure,  $\text{Pb}^{2+}$  cations are involved in  $[\text{OPb}_3]$  triangles with LP orientation not perpendicular to the ribbons as it is for the Bi-based structure. On the external layer, all  $[\text{OBi}_3]$  triangles are filled by oxygen although there are not for the lead sample, showing a perfect ordering of oxygen vacancies. This help to balance the change of charge induced by the substitution of  $\text{Bi}^{3+}$  by  $\text{Pb}^{2+}$  and drastically change the structure of the layer from flat (for Bi) to sawtooth (for Pb). The oxygen vacancies are promising in terms of ionic conductivity and the results observed for the Bi-based sample may be deeply increased by increasing the oxygen mobility in the external layer.

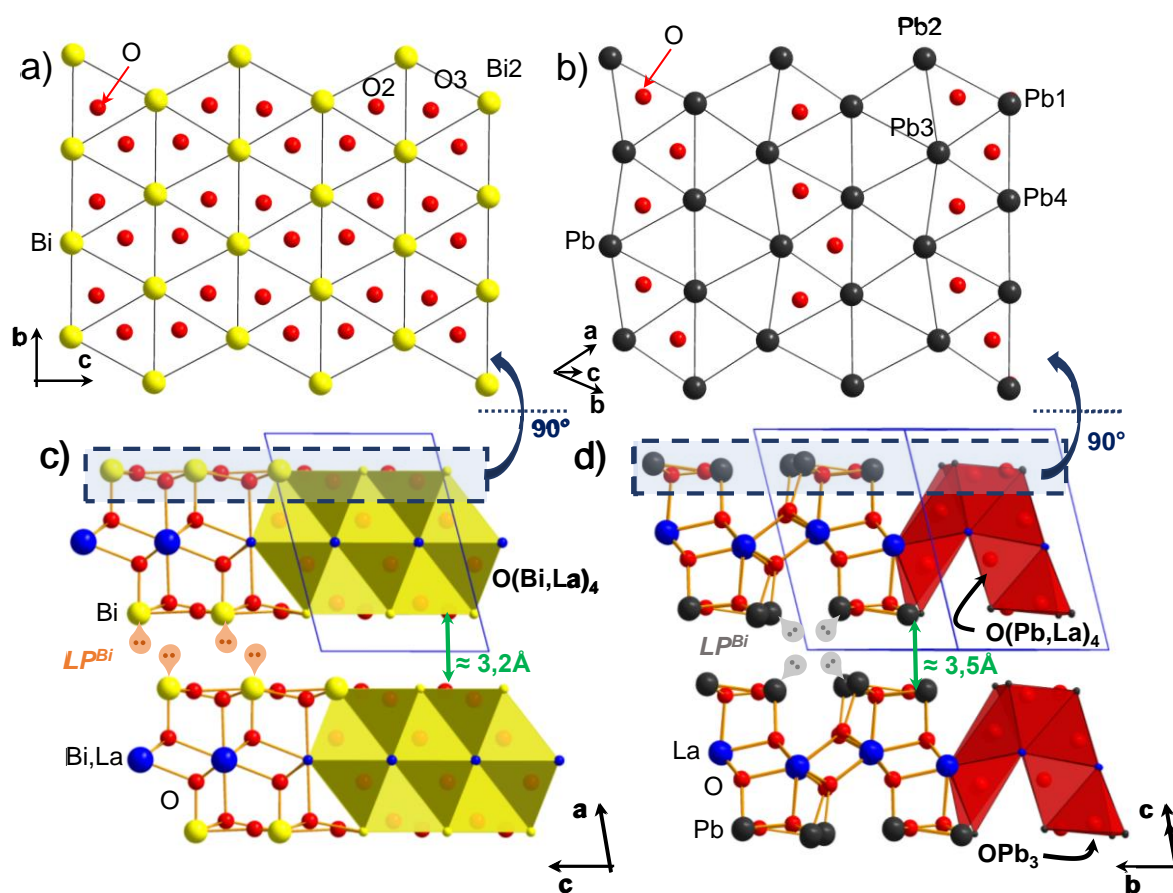


Figure 94. Bismuth/lead oxygen environments in outside part of neutral layers in (a)  $\text{Bi}_4(\text{Bi/La})_2\text{O}_9$  and (b)  $\text{Pb}_4\text{La}_2\text{O}_7$ . The respective crystal structures are shown on (c) and (d).

In the same work,  $\text{Pb}_4\text{Ln}_2\text{O}_7$  (Ln= Gd, Nd and Sm) were also synthesized as powder. The unit cell proposed is the same as the one for  $\text{Bi}_4(\text{Bi/La})_2\text{O}_9$  [11] but remains uncertain. The unit cell parameters of  $\text{Pb}_4\text{La}_2\text{O}_7$  compound are compared to calculated parameters for Gd, Nd and Sm analogues and to  $\text{Bi}_4(\text{Bi/La})_2\text{O}_9$  in Table 43.

**Table 43. Unit cell parameters of  $\text{Pb}_4\text{Ln}_2\text{O}_7$  (Ln= La, Gd, Nd and Sm) series and  $\text{Bi}_4(\text{Bi/La})_2\text{O}_9$**

Compound	S.G.	a(Å) / $\alpha(^{\circ})$	b(Å) $\beta(^{\circ})$	c(Å) $\gamma(^{\circ})$	V(Å <sup>3</sup> )
$\text{Pb}_4\text{La}_2\text{O}_7$	P-1	7.7054(10) 72.574(10)	7.7262(10) 84.285(10)	10.1822(10) 61.737(10)	508.77(12)
$\text{Pb}_4\text{Gd}_2\text{O}_7$	P2/c	6.4148(3) 90	3.8194(2) 91.55(1)	9.6606(4) 90	236.59(2)
$\text{Pb}_4\text{Nd}_2\text{O}_7$	P2/c	6.3243(7) 90	3.8434(4) 91.00(10)	9.6785(10) 90	235.22(6)
$\text{Pb}_4\text{Sm}_2\text{O}_7$	P2/c	6.4558(5) 90	3.8506(2) 91.65(6)	9.6708(7) 90	240.30(4)
$\text{Bi}_4(\text{Bi/La})_2\text{O}_9$	P2/c	9.484(4)	3.982(2) 104.75(3)	7.030(3)	257.07(2)

In front of these results, there are two emerging perspectives:

- 1- The crystal structures of the  $\text{Pb}_4\text{Ln}_2\text{O}_7$  (Ln= Gd, Nd and Sm) compounds must be determined to confirm the purity of the samples before further magnetic or optical measurements keeping in mind that an exfoliation process could be used to prepare optically active ultrathin objects.
- 2- The full substitution of  $\text{Bi}^{3+}$  by  $\text{Pb}^{2+}$  open the door to a possible oxygen mobility and anionic transport.

These two points are the leitmotiv of the first and second part of this chapter.

#### IV.1.1.1. Investigation of samples stability

In literature, [10] the possibility to synthesize the Bi-based compound with Ln= La, Gd and Nd was published. The crystal structure was refined in monoclinic unit cell in the space group P2/c at room temperature and in a rhombohedral unit cell above 450°C. [11]  $\text{Pb}_4\text{La}_2\text{O}_7$  is triclinic (S.G. P-1), so we will investigate the substitution of La by Nd, Sm and Gd.

The synthesis performed was identical with the one mention in ref [12]. The initial  $\text{Nd}_2\text{O}_3$ ,  $\text{Sm}_2\text{O}_3$ ,  $\text{Gd}_2\text{O}_3$  precursors were preheated at 900°C, mixed with PbO and well grinded in agate mortar. The alumina crucibles were used to provide solid-state synthesis in furnace. The initial mixtures were heated at different temperatures to establish the range of stability for each

composition. A series of solid-state synthesis were provided for each composition at temperatures from 800 to 950° degrees with a step of 50°.

*a. Pb<sub>4</sub>Nd<sub>2</sub>O<sub>7</sub>*

As it shown on Figure 95, Pb<sub>4</sub>Nd<sub>2</sub>O<sub>7</sub> demonstrates stability of the main phase across the entire temperature range. This compound was synthesized with different impurities depending on temperatures: Nd<sub>2</sub>O<sub>2</sub>CO<sub>3</sub> (up to 800°C) and PbO. It is almost impossible to conclude about the unit cell from this data. First, there is an important preferential orientation and the number of pics is limited... Using either the monoclinic unit cell of the Bi-based compound or the triclinic unit cell of the Pb-based compound assorted with the impurities doesn't give significant clues to conclude even if, logically and due to the oxygen vacancies, the unit cell would be logically triclinic. Although for the moment, the use of the monoclinic unit cell highlights extra peaks not clearly understood... and the purity of the sample is not confirmed. As a consequence, single crystals were grown in the next step.

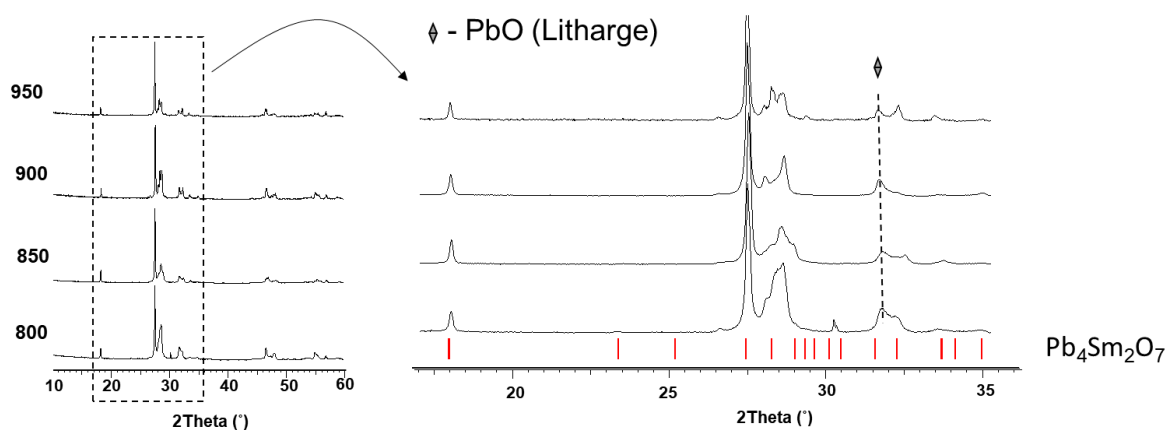


**Figure 95. Evolution of X-Rays powder diffraction patterns of Pb<sub>4</sub>Nd<sub>2</sub>O<sub>7</sub> at different temperatures.**

Slow cooling at 950°C were performed but didn't allow to grow single crystals. In addition, the sample is decomposed when working at higher temperature... Secondly, the flux growth technique was also tried without success... So, it was decided to use HP-HT experiments.

- HP-HT experiments

Sample of Pb<sub>4</sub>Nd<sub>2</sub>O<sub>7</sub> preheated at 900°C (to remove the carbonates, see below), was hardly packed into platinum crucible and pressed at 2.5GPa and 900°C using the Piston-Cylinder of the University of Lille. Resulted light-brown crystals were detected after opening the crucible as shown on Figure 96. Very small tiny crystals are given on maximum zoom. A single crystal was selected to provide data collection.

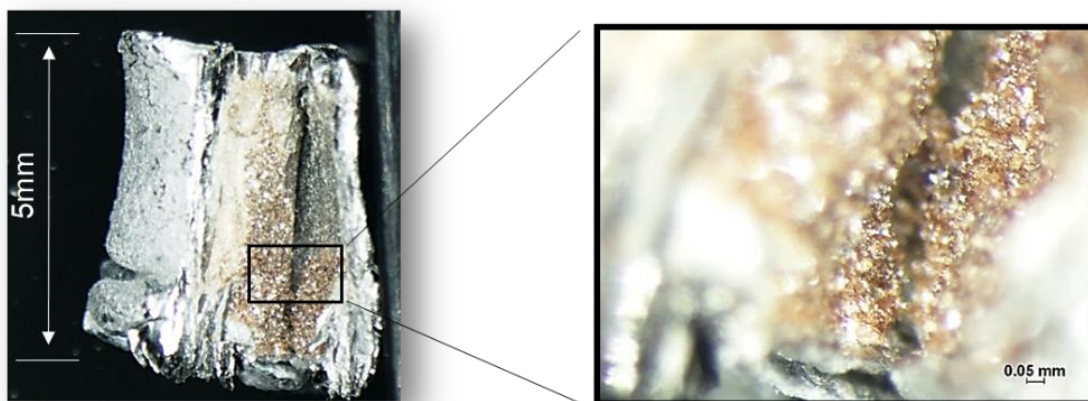


**Figure 96.** Photo of sample after crystal growth using HPHT experiment.

The crystal structure was solved from single crystal XRD data ( $R_{eq} = 3.6\%$ ,  $wR_{ref} = 3.13$ ) in the triclinic  $P-1$  space group ( $a = 7.5913(5) \text{ \AA}$ ,  $b = 7.5989(5) \text{ \AA}$ ,  $c = 10.3380(7) \text{ \AA}$ ,  $\alpha = 69.607(4)^\circ$ ,  $\beta = 80.979(4)^\circ$ ,  $\gamma = 61.518^\circ$ ,  $V = 491.29(6) \text{ \AA}^3$ ). The detailed information about crystal parameters, data collection and structure refinement are given in Table 50. The atomic parameters and interatomic distances are presented in Table 51 and Table 52.

The crystal structure is shown on Figure 97. It is isostructural with  $\text{Pb}_4\text{La}_2\text{O}_7$ , built on identical  $[\text{Pb}_4\text{Nd}_2\text{O}_7]^0$  layers. A comparative table of main features between La- and Nd-based compounds are given in Table 44.

**Table 44.** Main features for  $\text{Pb}_4\text{La}_2\text{O}_7$  and  $\text{Pb}_4\text{Nd}_2\text{O}_7$

	La	Nd
Unit cell parameters	$a = 7.7054(1) \text{ \AA}$ , $\alpha = 72.574(1)^\circ$ $b = 7.7262(1) \text{ \AA}$ , $\beta = 84.285(1)^\circ$ $c = 10.1822(1) \text{ \AA}$ , $\gamma = 61.737(1)^\circ$	$a = 7.5913(1) \text{ \AA}$ , $\alpha = 69.607(1)^\circ$ $b = 7.5989(1) \text{ \AA}$ , $\beta = 80.979(1)^\circ$ $c = 10.3380(1) \text{ \AA}$ , $\gamma = 61.518(1)^\circ$
Volume ( $\text{ \AA}^3$ )	508.77	491.29
Ln ionic radii (VI) ( $\text{ \AA}$ )	1.032	0.98
$\langle \text{Pb-O} \rangle$ ( $\text{ \AA}$ )	2.20 to 2.48	2.15 to 2.44
$\langle \text{Ln-O} \rangle$ ( $\text{ \AA}$ )	2.34 to 2.56	2.31 to 2.51

The substitution of La by Nd induce a strong contraction in the (a,c) plane and the width of the layer is also reduced in agreement with stronger covalent bonds inside the layer. Surprisingly, the *c*- parameter is bigger for the Nd-based compound. Although the width of the layer is bigger for the La- compound, the space of the inter layer is smaller. This is related to Van der Waals forces, naturally weak and holding layers together. The bigger distance between the layers for Nd compound is related to smaller Van der Waal's forces. This would increase the possibility to exfoliate the layers more easily when reducing the ionic radii of the lanthanide.

Again, the oxygen vacancies at the external part of the layer imposed the triclinic unit cell.

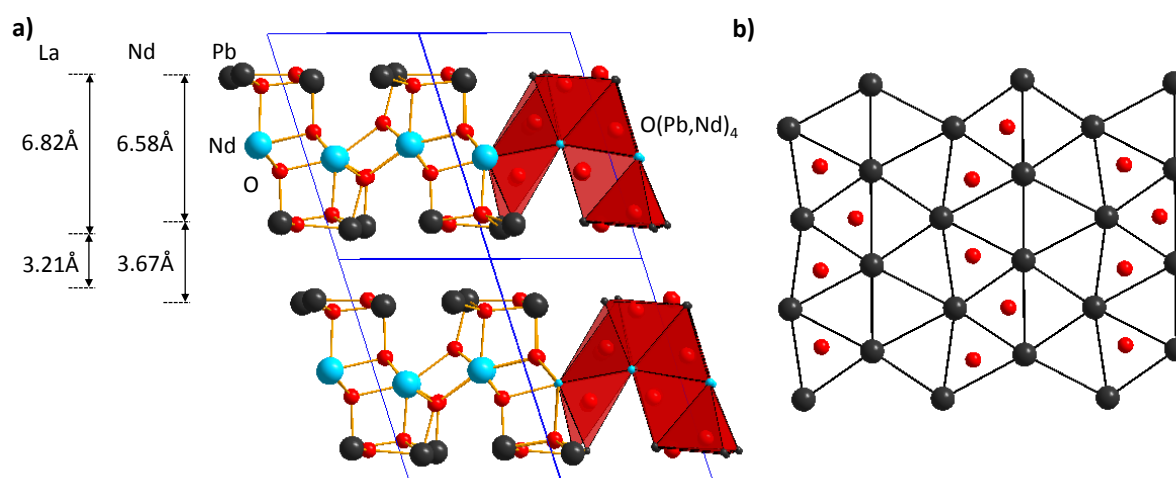


**Figure 97.** (a) Crystal structure of  $Pb_4Nd_2O_7$  showing typical 2D layers. The main distances are presented on the left side and compared with  $Pb_4La_2O_7$ ; (b) External layer with oxygen vacancies.

The powder/crystals from HPHT synthesis were crushed and an XRD study confirm the purity of the sample (see Figure 98). Finally, the combined use of high-pressure and high-temperature is necessary to obtain the pure phase. This was used for further magnetic measurements.

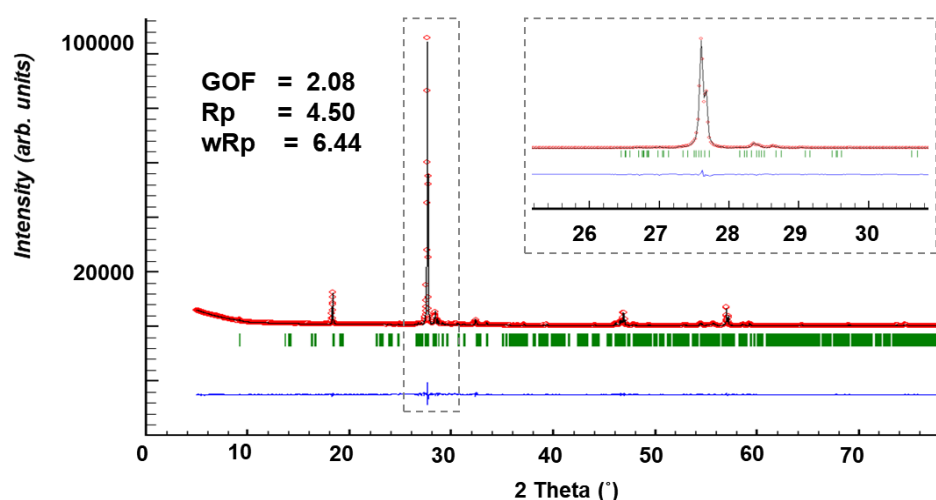


**Figure 98.** Pattern matching of powder  $Pb_4Nd_2O_7$  sample after HPHT experiment with single crystal data. The difference curve is given in blue.

### b. $Pb_4Sm_2O_7$

In case of Sm analogue, the pure phase with the minimum of impurity can be obtained at 850°C. The peak of litharge (PbO) was observed at 850°C and at lower temperature. At 900°C it transforms into another form of PbO – massicot, as is shown on Figure 99. At higher temperatures, the sample reacted with the alumina crucible that lead to the formation of  $Sm(AlO_3)$  [17] and  $Al_{12}O_{32}Pb_8Sm_4$  [18] compounds. The growth of single crystals would require pressure as well but unfortunately the Piston Cylinder was out of order during the last year so that it has not been possible to do it for the moment. Of course, we expect the crystal structure to be triclinic, similarly with La- and Nd- based compounds.

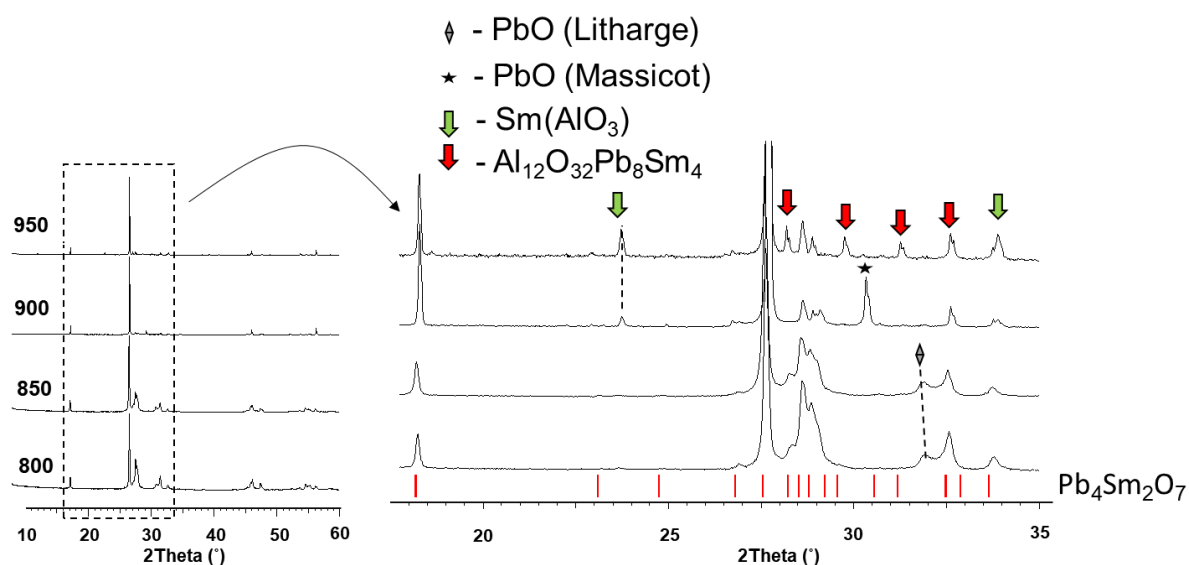


Figure 99. Evolution of X-Rays powder diffraction patterns of  $Pb_4Sm_2O_7$  at different temperatures.

### c. $Pb_4Gd_2O_7$

$Pb_4Gd_2O_7$  compound demonstrates narrower range of stability of the desired phase than its Sm and Nd analogues. As observed on Figure 100, the sample at 800°C is an unreacted mixture of initial oxides. Whereas at 850°C it is already a crystallized phase with a trace of impurity. This compound is stable up to 900°C and start to decompose at higher temperature.

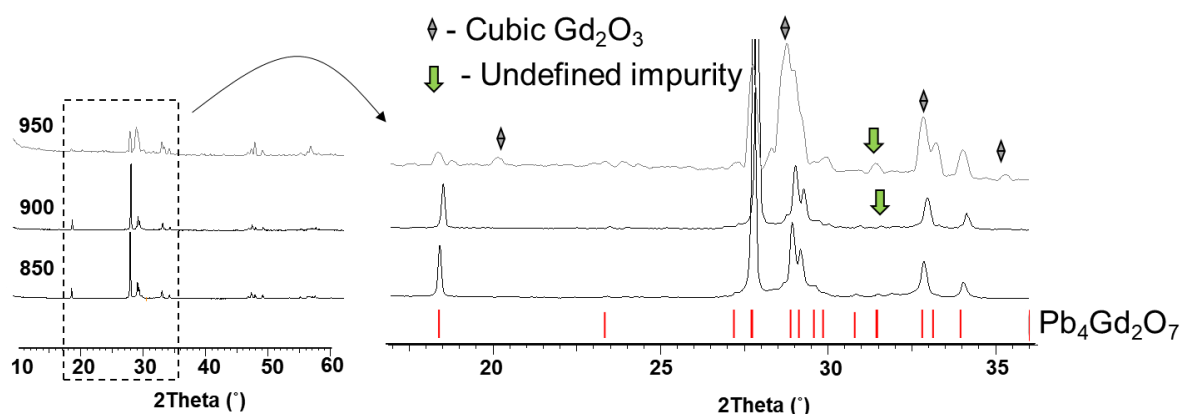


Figure 100. Evolution of X-Rays powder diffraction patterns of  $\text{Pb}_4\text{Gd}_2\text{O}_7$  at different temperature.

The problem of stability of  $\text{Pb}_4\text{La}_2\text{O}_7$  was mentioned in [1]. Throughout the entire time of research of these samples ( $\text{Ln} = \text{Nd}, \text{Gd}$  and  $\text{Sm}$ ), their appearance changed with the passage of time. We noticed that some samples, in particular  $\text{Pb}_4\text{Gd}_2\text{O}_7$  and  $\text{Pb}_4\text{Nd}_2\text{O}_7$ , became less consolidated and changed the tone color. The X-Ray powder diffraction was provided on all three samples synthesized at  $900^\circ\text{C}$ , that were kept for one year on air.  $\text{Pb}_4\text{Sm}_2\text{O}_7$  didn't show any change in powder diffraction pattern, whereas in case of  $\text{Pb}_4\text{Gd}_2\text{O}_7$  and  $\text{Pb}_4\text{Nd}_2\text{O}_7$ , additional peaks were detected. According to PDF database, these additional peaks correspond to Hydrocerussite ( $\text{Pb}_3(\text{CO}_2)_2(\text{OH})_2$ ) [16]. Figure 101 demonstrates the general overview on resulted powder patterns and the most characteristic 2 theta (°) range to demonstrate the presence of  $\text{Pb}_3(\text{CO}_2)_2(\text{OH})_2$  peaks (dashed line) for (a)  $\text{Pb}_4\text{Gd}_2\text{O}_7$  and (b)  $\text{Pb}_4\text{Nd}_2\text{O}_7$ .

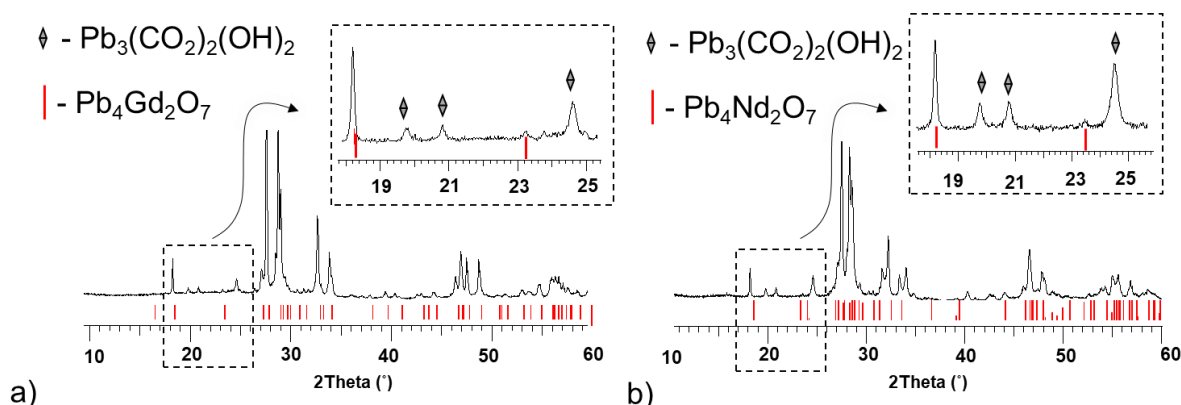
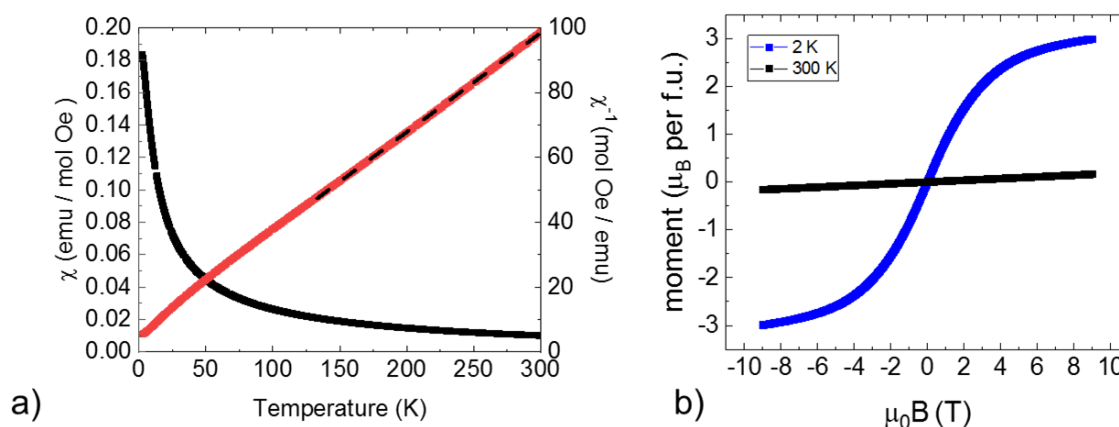


Figure 101. XRD patterns of one-year (a)  $\text{Pb}_4\text{Gd}_2\text{O}_7$  and (b)  $\text{Pb}_4\text{Nd}_2\text{O}_7$  samples, where selected 2 theta (°) range demonstrates the position of  $\text{Pb}_3(\text{CO}_2)_2(\text{OH})_2$  peaks.

In this regard, before further analysis, the samples were preheated at  $900^\circ\text{C}$  in order to get the pure targeted phase.

### IV.1.2. Magnetic measurement

$\text{Nd}^{3+}$  has an electronic configuration in  $6s^2 4f^3$  which could lead to magnetic properties. The  $\text{Nd}^{3+}$ - $\text{Nd}^{3+}$  distances are in values interesting for possible interactions ( $\sim 3.5\text{\AA}$ ), so the magnetic properties were investigated. The temperature variation of the direct and inverse magnetic susceptibility of  $\text{Pb}_4\text{Nd}_2\text{O}_7$  is shown on Figure 102 (a), whereas Magnetic hysteresis loop at different temperatures is given on Figure 102 (b).



**Figure 102.** (a) Temperature variation of the direct and inverse magnetic susceptibility for  $\text{Pb}_4\text{Nd}_2\text{O}_7$ . Curie-Weiss fit as dashed line. (b) Magnetic hysteresis loop at 2 K and 300 K.

ZFC and FC magnetic susceptibilities were measured under an external field of 0.1 T. No clear transition can be observed. Curie-Weiss fit to the inverse susceptibility above 150 K gives  $\mu_{\text{eff}} = 3.6 \mu_{\text{B}}/\text{Nd}^{3+}$ , in good agreement with the theoretical value of  $3.62 \mu_{\text{B}}$ . It shows a Weiss constant  $\theta = -23(1)$  K, which indicates antiferromagnetic interactions. Magnetization versus field at 2 K and 300 K show a paramagnetic behavior.

$\text{Sm}^{3+}$ , as well as  $\text{Eu}^{3+}$ , are special cases between the rare earths. They cannot be fitted with a simple Curie-Weiss law. The reason for this is that their multiplet intervals are not really infinitely large compared to  $kT$  as shown on Figure 103.

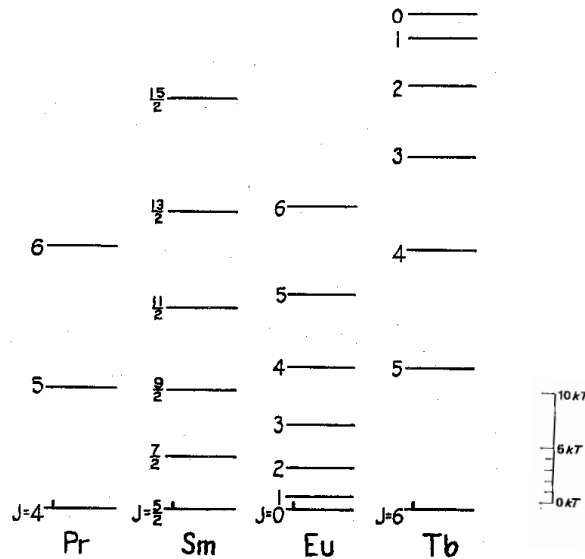


Figure 103. Multiplet spacing of  $\text{Sm}^{3+}$  and  $\text{Eu}^{3+}$ . The scale on the right with thermal energy is for a temperature of 300 K. The case of Pr and Tb are also shown for comparison. [13]

This is clearly shown in the magnetic susceptibility of  $\text{Pb}_4\text{Sm}_2\text{O}_7$  on Figure 104. The temperature variations of the direct and inverse susceptibilities evidence a Van Vleck paramagnetism and the M vs H loops confirm it.

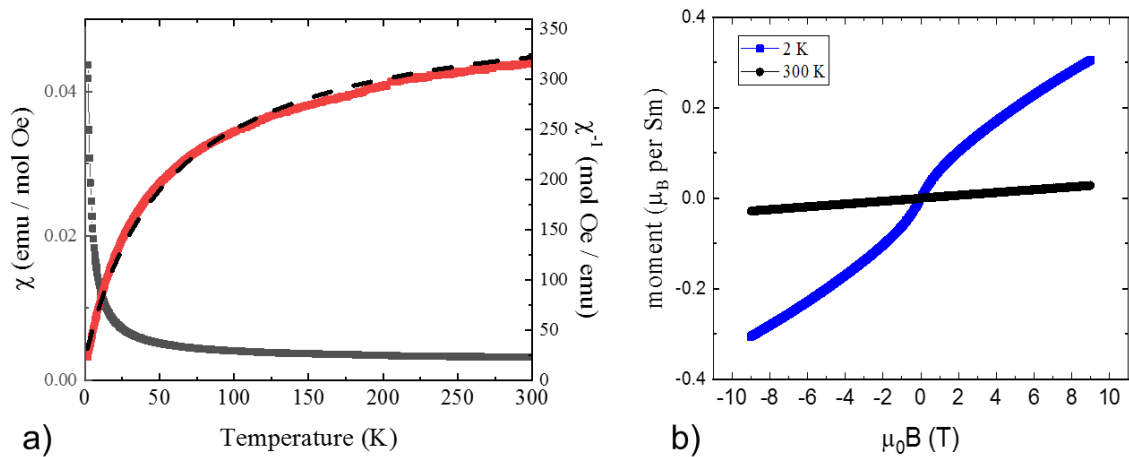


Figure 104. (a) Temperature variation of the direct and inverse magnetic susceptibility for  $\text{Pb}_4\text{Sm}_2\text{O}_7$ . Fit to the Hamaker equation as described in the text. (b) Magnetic hysteresis loop at 2 K and 300 K.

Previous works has shown that  $\chi(T)$  for Sm compounds can often be reasonably well described with the equation [14]:

$$\chi(T) = \frac{N_A}{k_B} \left[ \frac{\mu_{eff}^2}{3(T-\theta_p)} + \frac{\mu_B^2}{\delta} \right]$$

where  $\mu_{eff}$  is the effective magnetic moment,  $\theta_p$  is the Weiss constant,  $\mu_B$  is the Bohr magneton,  $N_A$  is the Avogadro number and  $k_B$  is the Boltzmann constant,  $\delta$  is an energy scale, defined as

$\delta = 7\Delta E/20$  and describes the difference between the first excited angular momentum  $J = 7/2$  and the  $J = 5/2$  ground state.

The fit obtained for the  $\text{Pb}_4\text{Sm}_2\text{O}_7$  data is shown as dashed black curve in Figure 104. The fit resulted in  $\mu_{\text{eff}} = 1.06(1) \mu_{\text{B}}$ ,  $\theta_{\text{p}} = -3.1(1) \text{ K}$  and  $\delta = 142(1) \text{ K}$ . The effective magnetic moment is larger than the  $0.845 \mu_{\text{B}}$  of the free ion for the  $J = 5/2$  Hund's rule ground state of  $\text{Sm}^{3+}$  and with a  $\Delta E = 406 \text{ K}$ . These values are comparable to other Sm compounds, for instance 412 K for  $\text{SmCo}_2\text{Zn}_{20}$ . [15]

### IV.1.3. Diffuse reflectance spectroscopy

The diffuse reflectance spectra of  $\text{Pb}_4\text{Ln}_2\text{O}_7$  ( $\text{Ln} = \text{Nd}, \text{Sm}$  and  $\text{Gd}$ ) materials were registered between 200 and 900 nm (Figure 12). They all show similar behavior with experimental band gap estimated around 3eV which is similar to the experimental value measured for  $\text{Pb}_4\text{La}_2\text{O}_7$ . [1] Concerning the Nd-based sample, the main f-f transitions are observed at higher wavelength. [50]

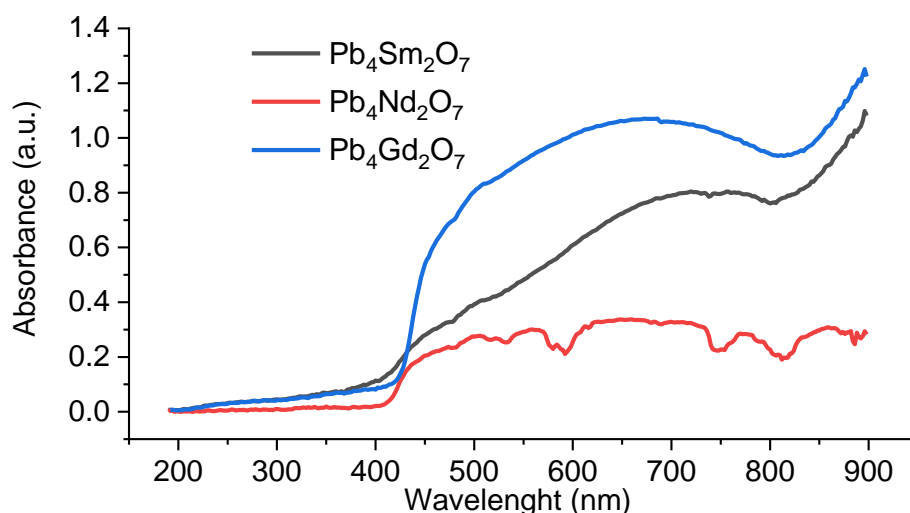


Figure 105. UV-visible Diffuse reflectance spectroscopy (DRS) spectrum for  $\text{Pb}_4\text{Ln}_2\text{O}_7$  ( $\text{Ln} = \text{Nd}, \text{Sm}$  and  $\text{Gd}$ ) series.

#### IV.1.4. IR investigation

A series of IR experiments were provided on  $\text{Pb}_4\text{Ln}_2\text{O}_7$  ( $\text{Ln} = \text{Nd}, \text{Sm}$  and  $\text{Gd}$ ) samples. The resulted plots are given on Figure 106 for three compounds. The band observed around  $450\text{cm}^{-1}$  for  $\text{Pb}_4\text{Nd}_2\text{O}_7$  and  $\text{Pb}_4\text{Gd}_2\text{O}_7$  corresponds to Pb-O stretching [51] and the one around  $555\text{cm}^{-1}$  to Ln-O bands ( $\text{Ln} = \text{Nd}$  and  $\text{Gd}$ ). [52] In the case of  $\text{Pb}_4\text{Sm}_2\text{O}_7$ , the band typical of Pb-O stretching disappeared which is probably structurally related to the higher distance between the layers. Related to that, the Pb-O-Pb band around  $670\text{cm}^{-1}$  is increased for this sample.

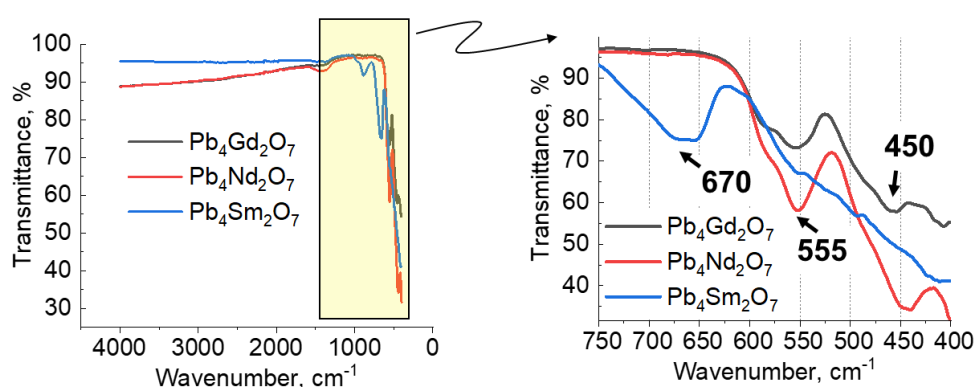
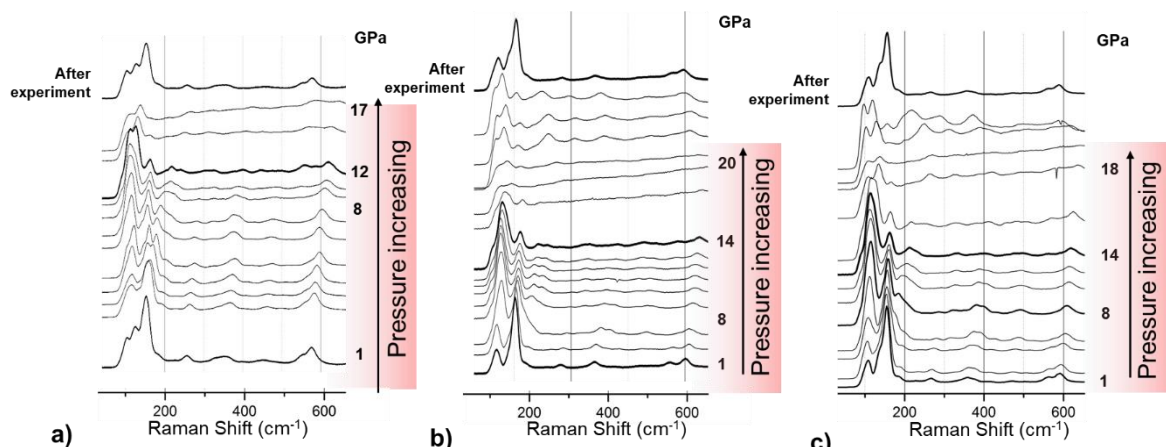


Figure 106. IR spectrum for  $\text{Pb}_4\text{Ln}_2\text{O}_7$  ( $\text{Ln} = \text{Nd}, \text{Sm}$  and  $\text{Gd}$ ) samples.

#### IV.1.5. HP Raman investigation

A series of High-pressure experiment was provided in Madrid University under supervision of Javier Sánchez Benítez. The High-pressure experiments were done in a standard Diamond Anvil Cell (DAC) using silicon oil as pressure transmitting media and controlled by ruby fluorescence. We chose steel gaskets that allowed to reach pressure up to 20 GPa. The pressure dependence of the Raman shift for each compound is given on Figure 107 (a) for  $\text{Pb}_4\text{Nd}_2\text{O}_7$ , (b) for  $\text{Pb}_4\text{Gd}_2\text{O}_7$ , (c) for  $\text{Pb}_4\text{Sm}_2\text{O}_7$ .



**Figure 107. Dependence of the Raman shift on pressure increases for (a) Pb<sub>4</sub>Nd<sub>2</sub>O<sub>7</sub>, (b) Pb<sub>4</sub>Gd<sub>2</sub>O<sub>7</sub>, and Pb<sub>4</sub>Sm<sub>2</sub>O<sub>7</sub> (c).**

As a first approximation, we can observe a significant change in the spectrum with increasing of pressure. Also, we can see a deterioration in quality when approaching about 18-20 GPa, which is related to the limits for the experiment with the selected parameters. Several spectra were recorded with a gradual decrease in pressure. The final spectrum was recorded after 12 hours in the complete absence of pressure in the cell for complete relaxation of the sample. Each sample showed complete reversibility with the original spectrum before the experiment. In order to assess the possibility of any structural transformations during the experiment, the positions of peaks were detected using second order derivative curve. The resulted graphs of peak positions as the pressure increases are shown on Figure 108 (a) for (a) Pb<sub>4</sub>Nd<sub>2</sub>O<sub>7</sub> and (b) Pb<sub>4</sub>Sm<sub>2</sub>O<sub>7</sub> compounds. Pb<sub>4</sub>Gd<sub>2</sub>O<sub>7</sub> showed sufficient similarity with Pb<sub>4</sub>Sm<sub>2</sub>O<sub>7</sub> and is not presented here.

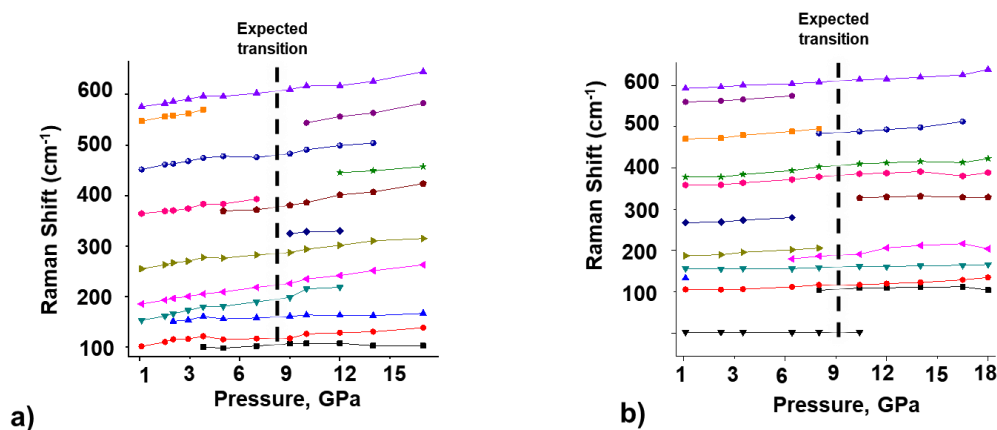


**Figure 108. Graphs of peak positions as the pressure increases for (a) Pb<sub>4</sub>Nd<sub>2</sub>O<sub>7</sub> and (b) Pb<sub>4</sub>Sm<sub>2</sub>O<sub>7</sub>.**

Both graphs show linear evolutionary trends of changing the position of the peaks with pressure. However, a slight shift can be detected around 8-10 GPa accompanied by the appearance of new peaks. Thus, arose the assumption of the expectative transition in crystal structures. This is a preliminary result and further study must be performed to distinguish the phase transition from the possible decomposition.

In order to obtain an expected HP – phase, the high-pressure high-temperature experiments were planned. The subsequent series of experiments using Belt type press was provided with a technical support of Dr. D. José Manuel Gallardo Amores in Madrid University. The pressure of 9 GPa and 900°C were chosen to provide the high-pressure high-temperature experiments on  $\text{Pb}_4\text{Nd}_2\text{O}_7$  and  $\text{Pb}_4\text{Sm}_2\text{O}_7$  compound. In both cases it resulted in changing of sample colors from light-yellow to dark grey. The XRD patterns of resulted samples are given on Figure 109. Both of them corresponds to the number of simple oxides, that tells us about failure to get a new phase.

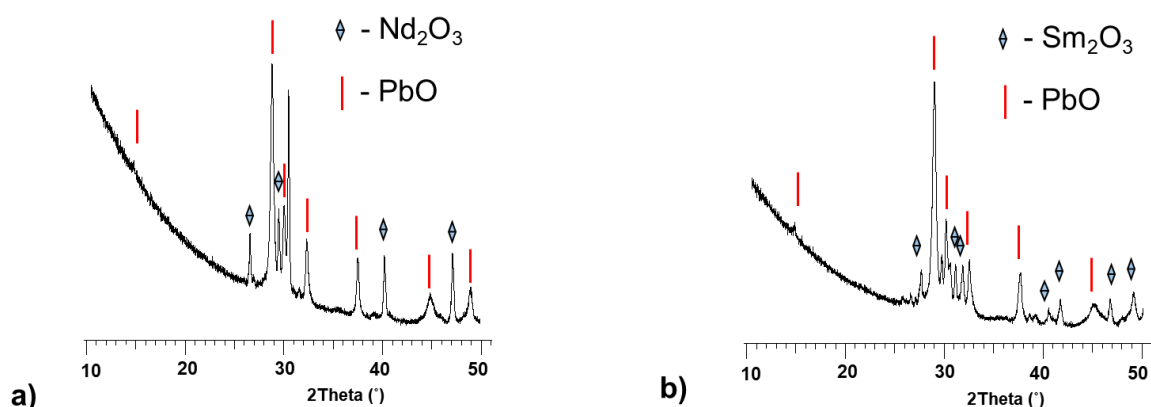


Figure 109. XRD patterns of samples resulted after HP-HT experiments for (a)  $\text{Pb}_4\text{Nd}_2\text{O}_7$  and (b)  $\text{Pb}_4\text{Sm}_2\text{O}_7$ .

#### IV.1.6. Conclusion and perspectives

Based on the above experimental results, it would be interesting to provide a new series of experiments using Belt type press at another pressure-temperature conditions. The repetition of HP experiment using *in situ* x-ray diffraction study would provide an existence of expected transition and insight into its nature. For this reason, several proposals were submitted to use Elettra (Italy) and Diamond (UK) synchrotron lighthouses, but were rejected. The plans remain to provide HP-HT experiments using resistive heaters and a membrane driven diamond anvil cell (DAC).

## IV.2. From $\text{Bi}_{4.65}\text{La}_{1.36}\text{O}_9$ to $\text{Pb}_4\text{La}_2\text{O}_7$

In this part, we investigated the possible existence of a solid solution between  $\text{Bi}_{4.65}\text{La}_{1.36}\text{O}_9$  and  $\text{Pb}_4\text{La}_2\text{O}_7$  ( $\text{Bi}_{4.65-x}\text{Pb}_x\text{La}_{1.36}\text{O}_9$   $0 < x < 2$ ) in order to study the ionic conductivity improvement following increases of number of oxygen vacancies in the external layer of the structure.

As a consequence, a series of experiments were provided to investigate the limits of Bi to Pb substitution between  $\text{Bi}_{4.65}\text{La}_{1.36}\text{O}_9$  and  $\text{Pb}_4\text{La}_2\text{O}_7$  compounds.

### IV.2.1. Bibliography note on $\text{Bi}_{4.65}\text{La}_{1.36}\text{O}_9$

The crystal structure of  $\text{Bi}_{4.65}\text{La}_{1.36}\text{O}_9$  exist under three crystallographic forms:

- a monoclinic distortion of the rhombohedral phase up to  $450^\circ\text{C}$ ,  $\epsilon$  in ref [11],
- HT rhombohedral phase,  $\beta_2$  up to  $680^\circ$  and  $\beta_1$  at higher temperatures.

The differences in the ionic conductivity capacity can be structurally explained as observed on Figure 110. In the HT rhombohedral phase, there is an additional oxygen atom taking place in the Van der Waals gap which increased the oxygen mobility.

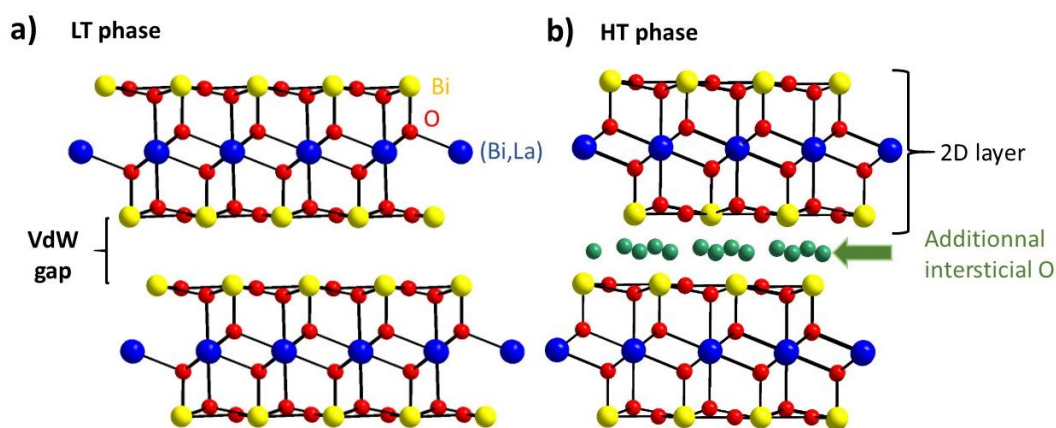


Figure 110. (a) LT and (b) HT forms of  $\text{Bi}_{4.65}\text{La}_{1.36}\text{O}_9$ . In the case of the HT phase, the additional interstitial O increased the ionic conductivity.

The space groups and unit cell parameters of all forms [11] are gathered in Table 45.

**Table 45. Table of unit cell parameters for  $\beta_1$ ,  $\epsilon$  and  $\beta_2$  modifications of  $\text{Bi}_{4.65}\text{La}_{1.36}\text{O}_9$** 

	$\beta_1$	$\epsilon$	$\beta_2$
S.G.	Rhombohedral <i>R-3m</i>	Monoclinic <i>P2/c</i>	Rhombohedral <i>R-3m</i>
Unit cell parameters	$a = 4.025(1) \text{ \AA}$ $c = 27.600(4) \text{ \AA}$	$a = 9.492(2) \text{ \AA}$ $b = 7.951(2) \text{ \AA}$ $c = 7.028(2) \text{ \AA}$ $\beta = 104.74(1)^\circ$	$a = 4.051(1) \text{ \AA}$ $c = 27.785(1) \text{ \AA}$

#### IV.2.2. Investigation of the solid solution

Synthesis. Right before the weighing,  $\text{La}_2\text{O}_3$  and  $\text{Bi}_2\text{O}_3$  precursors were preheated at  $900^\circ\text{C}$  and  $600^\circ\text{C}$  for 12 hours, respectively. Stoichiometric proportions were accurately weighed and intimately ground in an agate mortar. Mixtures of precursors were heated at  $400^\circ\text{C}$  and then pressed in pellets before transfer in alumina crucibles.

In a first step, the stability of  $\text{Bi}_{4.65}\text{La}_{1.36}\text{O}_9$  and  $\text{Pb}_4\text{La}_2\text{O}_7$  compounds were established by heating at different temperatures. A series of experiments was provided for both samples at the temperature range from  $800^\circ$  to  $1000^\circ$  degrees with a step of  $100^\circ$ .

The general overview on evolution of XRDP  $\text{Pb}_4\text{La}_2\text{O}_7$  compound is Figure 111 (a). A calculated pattern of already reported  $\text{Pb}_4\text{La}_2\text{O}_7$  phase is given in blue color as a reference at the bottom on Figure 111. The powder patterns of the samples obtained at  $800$ ,  $900$  and  $1000^\circ\text{C}$  are compared with the  $\text{Pb}_4\text{La}_2\text{O}_7$  phase. In the course of a careful comparison study the powder patterns obtained in this temperature range well correspond to the desired  $\text{Pb}_4\text{La}_2\text{O}_7$  phase. A selected  $2\theta$  range from  $27$  to  $32$  degrees is shown on Figure 111(b). It is the most

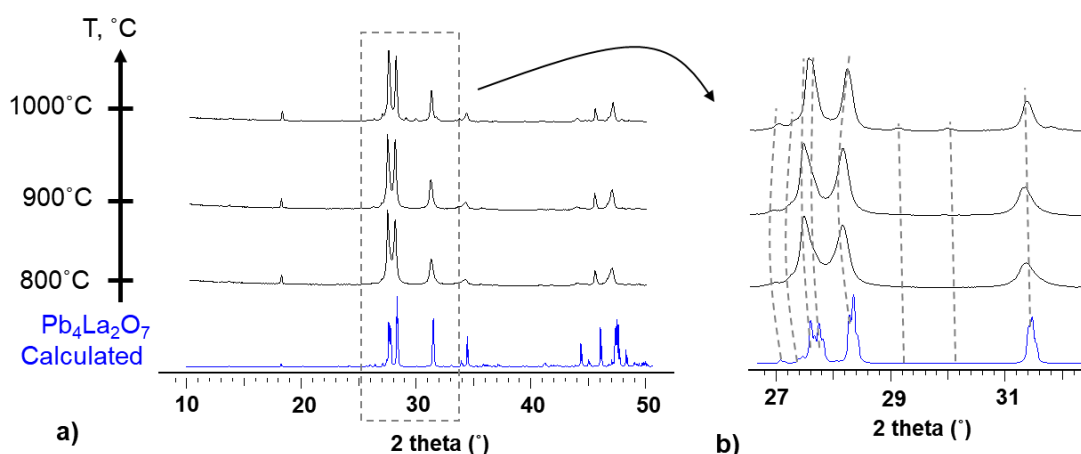


**Figure 111. (a) General overview on evolution of XRDP of  $\text{Pb}_4\text{La}_2\text{O}_7$  at different temperature. (b) Selected  $2\theta$  ( $^\circ$ ) range demonstrates the similarity between XRDP.**

representative to show the similarities between the powder patterns. Selected area is given to show Bragg peaks position.

These powder patterns were treated by pattern matching in Jana 2006. The unit cell parameters depending on the temperatures of synthesis are given in Table 46.

**Table 46. Table of refined unit cell parameters of  $\text{Pb}_4\text{La}_2\text{O}_7$  at different temperatures.**

T, °C	a, Å	b, Å	c, Å	$\alpha$ , °	$\beta$ , °	$\gamma$ , °
Reported [1]	7.7054(10)	7.7262(10)	10.1822(10)	72.574(10)	84.285(10)	61.737(10)
800	7.7005(1)	7.7391(1)	10.1902(1)	72.551(1)	84.181(1)	61.856(1)
900	7.6910(1)	7.7571(1)	10.1253(1)	72.336(1)	84.001(1)	61.409(1)
1000	7.7404(1)	7.8162(2)	10.1796(1)	72.211(1)	83.904(1)	61.318(1)

In case of  $\text{Bi}_{4.65}\text{La}_{1.36}\text{O}_9$ , the same temperature range and step of 100°C degree between the experiments were kept. Powder diffraction patterns of samples heated at 800°C and 900°C correspond to rhombohedral  $\text{Bi}_{4.65}\text{La}_{1.36}\text{O}_9$  phase (PDF card № 48-0346) [19]. At 1000°C and 1100° degrees it shows the maintenance of the main phase and presence of several peaks of  $\text{La}_{10}\text{Al}_4\text{O}_{21}$  impurity (PDF card № 23-0331) due to the reaction with alumina crucible. Selected 2theta range from 27 to 31 degrees is given on Figure 112(b) to show the evolution of the  $\text{Bi}_{4.65}\text{La}_{1.36}\text{O}_9$  rhombohedral phase and peaks of impurity.

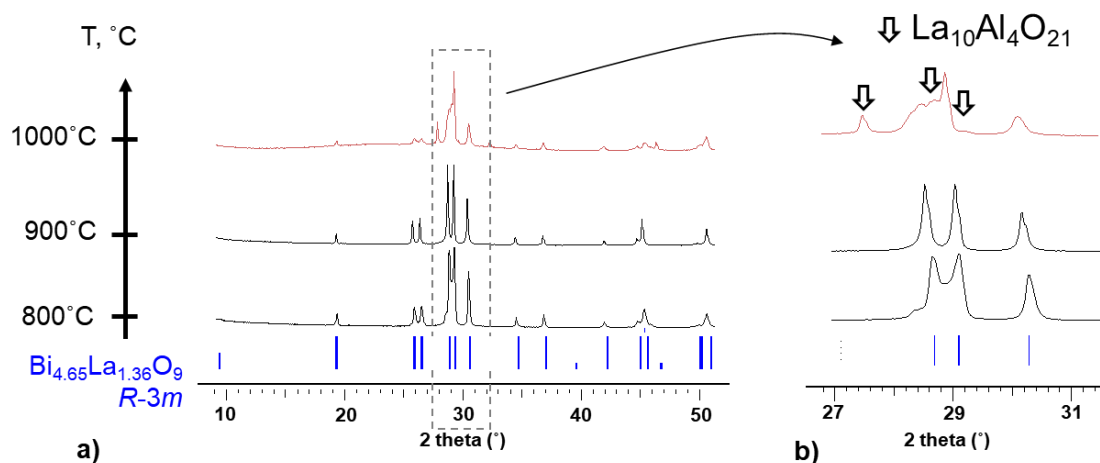


**Figure 112. (a) General overview on evolution of XRDP of  $\text{Bi}_{4.65}\text{La}_{1.36}\text{O}_9$  at different temperature. (b) Selected 2theta (°) range demonstrates the differences between XRDP.**

The unit cell parameters of  $\text{Bi}_{4.65}\text{La}_{1.36}\text{O}_9$  phase were refined at different temperatures and are given in Table 47.

**Table 47. Table of refined unit cell parameters of  $\text{Bi}_{4.65}\text{La}_{1.36}\text{O}_9$  at different temperatures**

T, °C	a, Å	c, Å
Reported [19]	4.021(1)	27.650(1)
800	4.024(5)	27.651(5)
900	4.030(6)	27.543(5)
1000	4.021(9)	27.631(1)

To conclude, the best temperature to synthesize both samples is 900°C so it will be used to investigate the solid solution.

First of all,  $\text{Bi}_{4.65}\text{La}_{1.36}\text{O}_9$  was taken as initial compound and doped by 15%, 30% and 40% of Pb. All this samples were heated at 900°C. A general overview on powder diffraction patterns is presented on Figure 113 (a). A 2theta range of 25 to 31 degrees is given on Figure 113(b) to show the main changes in diffraction patterns. It is obvious that the maintenance of the desired phase occurs only in the case of  $\text{Bi}_{3.95}\text{Pb}_{0.70}\text{La}_{1.36}\text{O}_{8.66}$  compound.

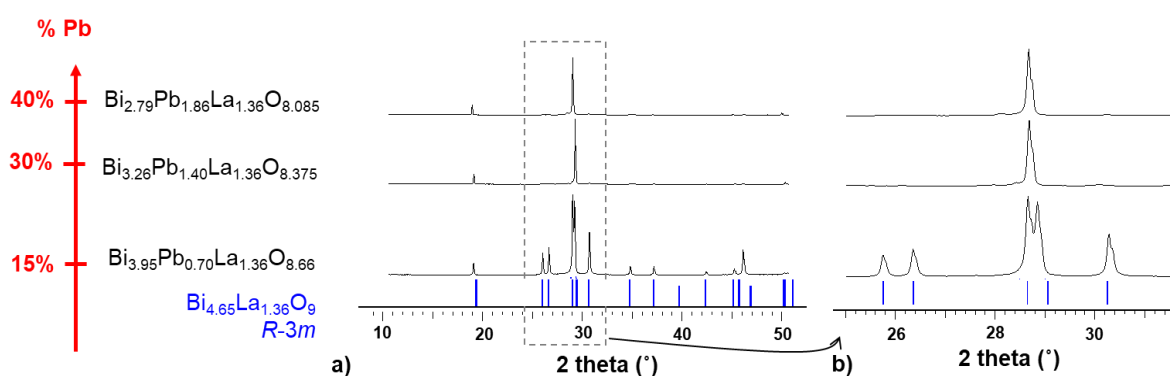


**Figure 113. (a) General overview on evolution of XRDP of  $\text{Bi}_{4.65}\text{La}_{1.36}\text{O}_9$  Pb doped compound. (b) Selected 2theta range to demonstrate the differences between XRDP.**

For substitution rates above 15%, the XRDP are different. The changes can only be discerned at significant Y-axes offset. A zoom of the patterns registered for  $\text{Bi}_{3.26}\text{Pb}_{1.40}\text{La}_{1.36}\text{O}_{8.375}$  and  $\text{Bi}_{2.79}\text{Pb}_{1.86}\text{La}_{1.36}\text{O}_{8.085}$  are shown on Figure 114. The careful analysis of powder patterns in PDF database shows the presence of triclinic  $\text{Pb}_5\text{Bi}_8\text{O}_{17}$  compound (PDF card № 52-1497) coexists with  $\text{Bi}_{4.65}\text{La}_{1.36}\text{O}_9$  phase.

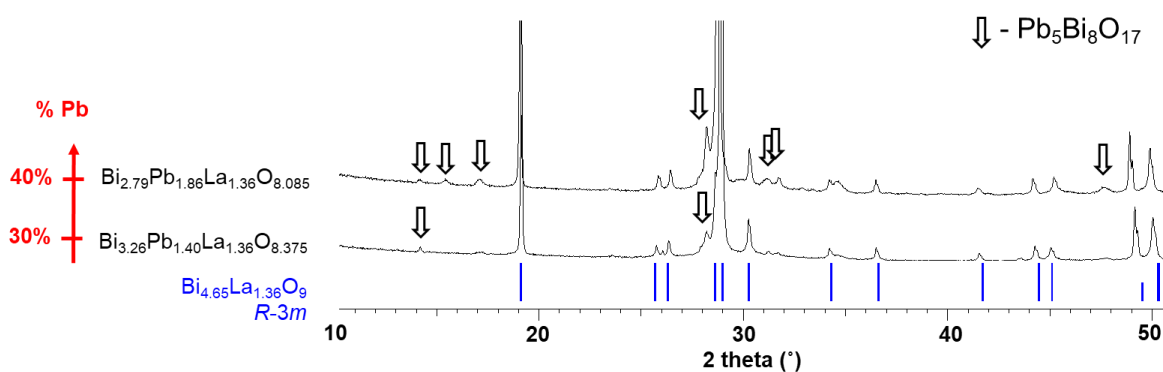


Figure 114. XRDP of  $\text{Bi}_{3.26}\text{Pb}_{1.40}\text{La}_{1.36}\text{O}_{8.375}$  and  $\text{Bi}_{2.79}\text{Pb}_{1.86}\text{La}_{1.36}\text{O}_{8.085}$  in x10 zoom along y-axes, where the Bragg positions of rhombohedral  $\text{Bi}_{4.65}\text{La}_{1.36}\text{O}_9$  phase is given in blue.

This experiment confirmed the limit for solid solutions from  $\text{Bi}_{4.65}\text{La}_{1.36}\text{O}_9$  side. The unit cell parameters of  $\text{Bi}_{3.95}\text{Pb}_{0.70}\text{La}_{1.36}\text{O}_{8.66}$  composition are:  $a = 4.0142(8)$  and  $c = 27.804(2)$  Å. The pattern matching was performed using Jana2006 software and presented on Figure 115.

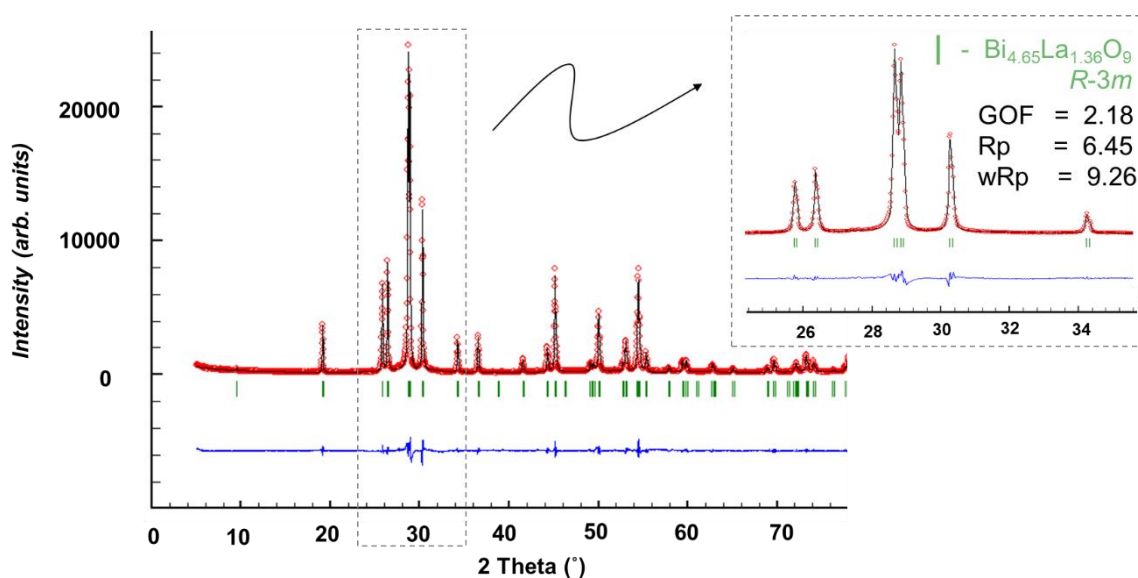


Figure 115. Pattern matching of  $\text{Bi}_{3.95}\text{Pb}_{0.70}\text{La}_{1.36}\text{O}_{8.66}$  composition. The difference curve is given in blue.

### a. $Pb_4La_2O_7$

The previous experiment demonstrated the limit for solid solution at 15% of bismuth by lead substitution. To begin with, we tried to dope  $Pb_4La_2O_7$  by 10% and 20% of Bi. The experiment was performed at 900°C to reproduce the synthesis conditions for initial  $Pb_4La_2O_7$  phase. Comparison of  $Pb_{3.6}Bi_{0.4}La_2O_{7.2}$  and  $Pb_{3.2}Bi_{0.8}La_2O_{7.4}$  XRDP are shown on Figure 116 (a) and led to the conclusion that no solid solution is possible from  $Pb_4La_2O_7$  side. The calculated XRDP of initial  $Pb_4La_2O_7$  is given in blue color on Figure 116. Selected 2theta range from 25 to 33 degree is shown on Figure 116 (b) in enlarged scale to highlight the changes in XRDP with increasing the amount of Bi. The phase analysis using PDF database revealed the appearing of tetragonal  $Bi_2O_3$  (PDF card № 29-0236) with the Bi amount increasing.

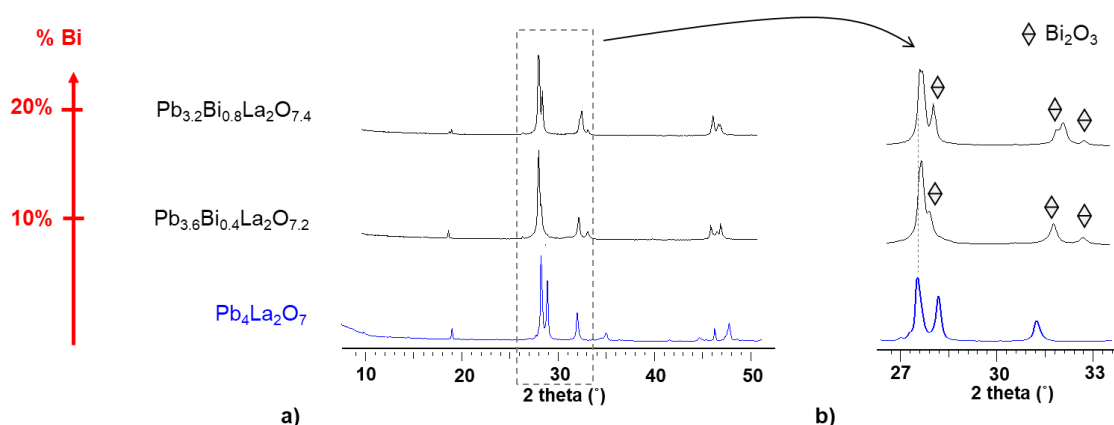


Figure 116. (a) General overview on evolution of XRDP of  $Pb_4La_2O_7$  (in blue) with increasing of the amount of Bi. (b) Selected 2theta (°) range demonstrates the similarity between XRDP.

The possibility to synthesize a large solid solution finally failed. Contrary to what was expected, the amount of oxygen in the external layer is not so flexible and able to adapt to the valence of the cation. Even if a low amount of lead can be inserted in the Bi-based sample, the opposite is not true. As a consequence, it can be mentioned that the number of surrounding oxygens is crucial for respectively  $Bi^{3+}$  and  $Pb^{2+}$ .

So as a consequence, the ionic conductivity measurements were only performed on three samples:  $Bi_{4.65}La_{1.36}O_9$  and  $Pb_4La_2O_7$ , and also on  $Bi_{3.95}Pb_{0.70}La_{1.36}O_{8.66}$ .

### *b. Conductivity measurements*

The powders were obtained following the procedure described in the synthesis part, above. The refined unit cell parameters and reliability parameters of pattern matching for  $\text{Bi}_{3.95}\text{Pb}_{0.70}\text{La}_{1.36}\text{O}_{8.66}$  were given previously and shown on Figure 115. The reliability parameters and general overview on pattern matching for  $\text{Bi}_{4.65}\text{La}_{1.36}\text{O}_9$  are shown on Figure 117.

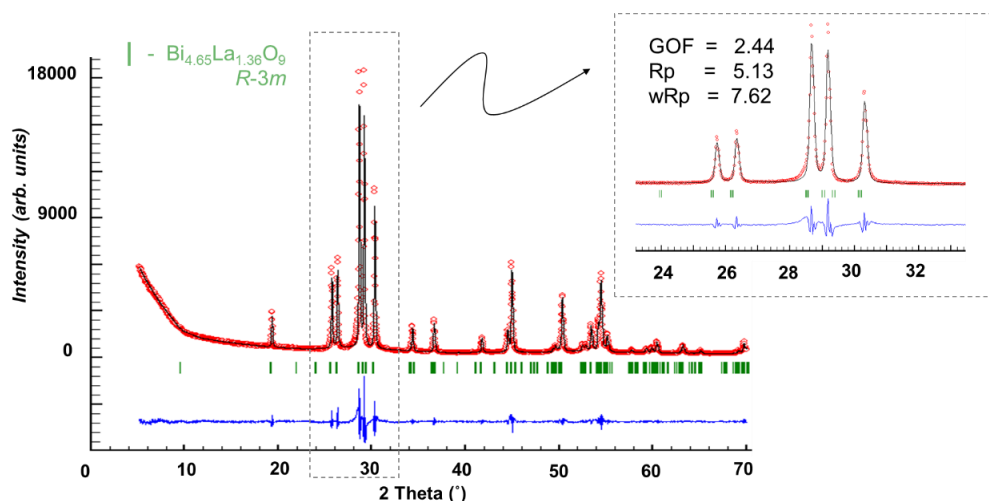


**Figure 117.** The pattern matching of  $\text{Bi}_{4.65}\text{La}_{1.36}\text{O}_9$ , where the difference curve is given in blue.

The pattern matching was also performed for triclinic  $\text{Pb}_4\text{La}_2\text{O}_7$  compound, as is shown on Figure 118. the unit cell parameters were refined to  $a = 7.680(2) \text{ \AA}$ ,  $b = 7.720(1) \text{ \AA}$ ,  $c = 10.184(2) \text{ \AA}$ ,  $\alpha = 72.28(2)^\circ$ ,  $\beta = 83.96(2)^\circ$  and  $\gamma = 61.97(1)^\circ$ .

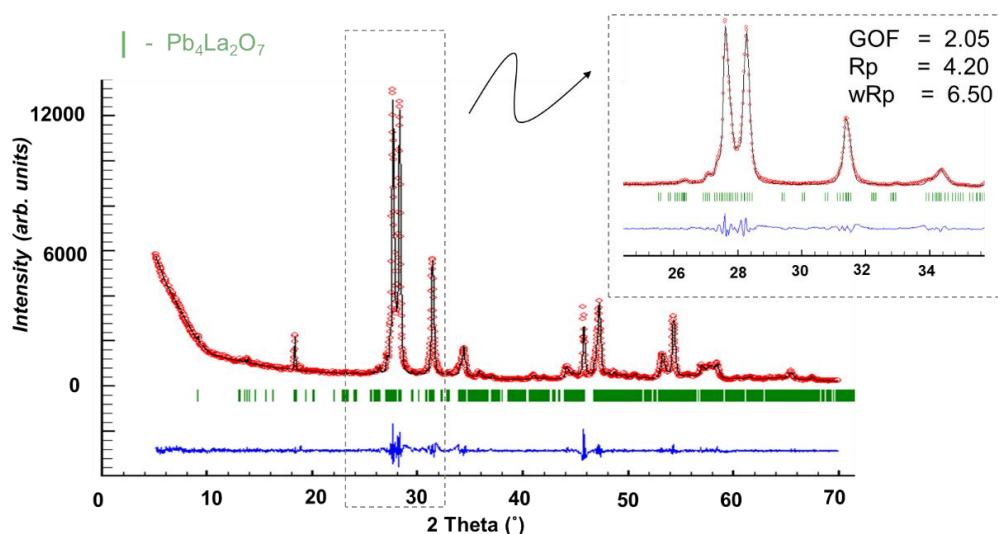


**Figure 118.** The pattern matching of  $\text{Pb}_4\text{La}_2\text{O}_7$ , where the difference curve is given in blue.

As already mentioned above, due to the oxygen vacancies available on external layers of the crystal structure, the ionic conductivities are expected to be higher as soon as  $\text{Bi}^{3+}$  is replaced by  $\text{Pb}^{2+}$  in the crystal structure. Previously, ionic conductivity was already measured on  $\text{Bi}_{4.65}\text{La}_{1.36}\text{O}_9$  by S. Obbade et al. [20] and it showed a relatively good ionic conductivity ( $\sigma_{600} \approx 10^{-3} \text{ S}\cdot\text{cm}^{-1}$ ) comparable with disordered bismuth oxides [23]. To reach our goal, the three samples were prepared and the ionic transport was measured.

For conductivity measurement, pellets (10 mm in diameter and approximately 4 mm in height) were prepared by uniaxial pressing followed by isostatic pressing at 180 MPa. They were then sintered at 800°C for 10 h. A 5 °C/min heating and cooling rate was used. The relative densities of the sintered samples were deduced by measuring the mass and pellet dimensions and were around 75-80%. To achieve better relative densities, it would have been necessary to grind the powder more finely, by attrition for example, but this would have required the preparation of a large quantity of powder.

To measure the ionic conductivity as a function of temperature, a Solartron SI 1260 frequency response analyzers was used in the 0.1 Hz to 1 MHz range, with a 500 mV amplitude signal, between 200°C and 800°C. Measurements were performed with a 20°C step and a 1h holding time to stabilized the temperature before each measurement. A 5 °C/min heating and cooling rate was used. Two heating cycles to 800 C were made in the course of the experiment. During the first cycle, the parts of the equipment are adjusted to each other, thus the resulted Arrhenius plots are performed for the second cycle. The Figure 119 shows the Arrhenius plots of conductivities for all samples.

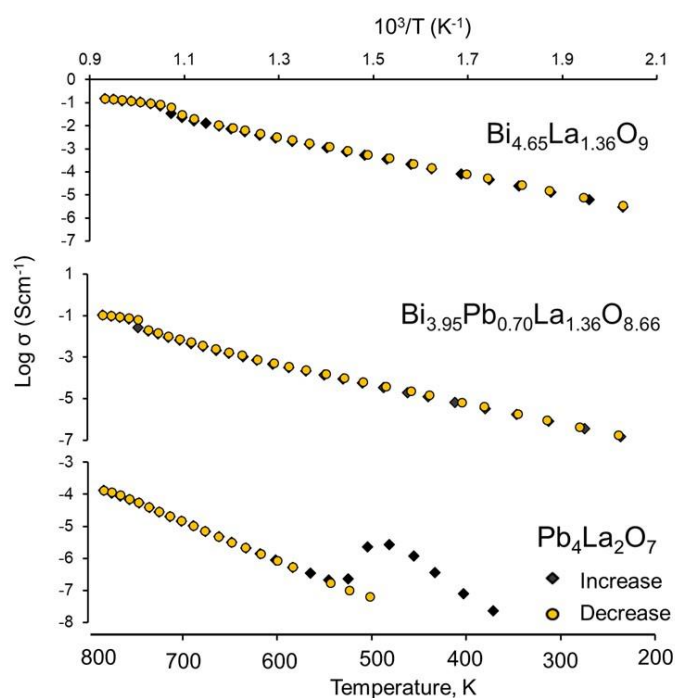


**Figure 119.** Arrhenius plot (heating and cooling) for second thermal cycle of  $\text{Bi}_{4.65}\text{La}_{1.36}\text{O}_9$ ,  $\text{Bi}_{3.95}\text{Pb}_{0.70}\text{La}_{1.36}\text{O}_{8.66}$  and  $\text{Pb}_4\text{La}_2\text{O}_7$ .

First of all, the results obtained for  $\text{Bi}_{4.65}\text{La}_{1.36}\text{O}_9$  used as an etalon are strongly coherent with those mentioned in ref [20]. The electrical characteristics determined at low and high temperatures are gathered in Table 48.

**Table 48.** Electrical characteristics at low and high temperatures.

	$\text{Bi}_{4.65}\text{La}_{1.36}\text{O}_9$	$\text{Bi}_{3.95}\text{Pb}_{0.70}\text{La}_{1.36}\text{O}_{8.66}$	$\text{Pb}_4\text{La}_2\text{O}_7$
EA (eV) at Low Temperature	0.82	0.95	
EA (eV) at High-Temperature	0.51	0.57	1.24

Secondly,  $\text{Pb}_4\text{La}_2\text{O}_7$  shows a linear Arrhenius plot above  $550^\circ\text{C}$ . Below, the behavior is more troubled, closed to the limit of detection of the measurement. The compound is effectively an ionic conductor but in a smaller degree than expected. For that sample, as expected after HTXRD analysis (Figure 120(a)), no real discontinuity is observed (considering errors) up to  $800^\circ\text{C}$  (b).

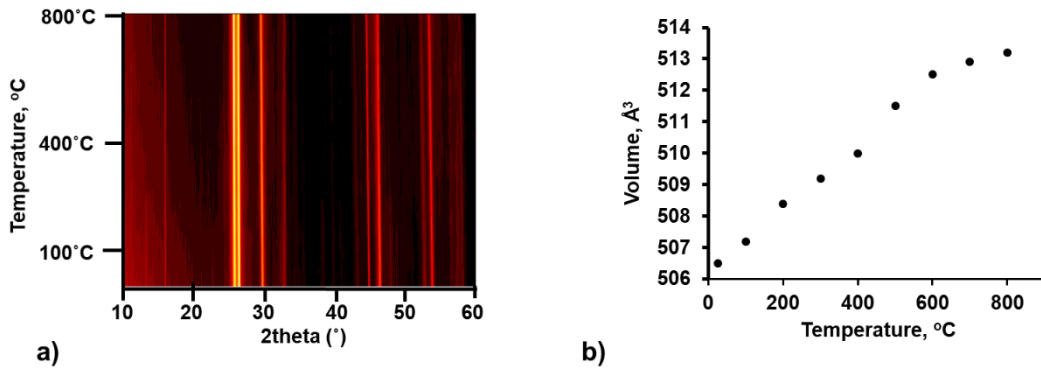


Figure 120. (a) HTXRD of  $\text{Pb}_4\text{La}_2\text{O}_7$  and (b) evolution of volume versus temperature.

Thirdly, in case of  $\text{Bi}_{3.95}\text{Pb}_{0.7}\text{La}_{1.36}\text{O}_{8.66}$ , there is a transition occurring at  $750^{\circ}\text{C}$ . The transition was analyzed by a HTXRD study shown on Figure 121 (a). As already detailed in ref [20], the phase transition is not obvious and arise from the drawing of the unit cell volume depending on temperature as shown on Figure 121 (b). The transitions of  $\text{Bi}_{4.65}\text{La}_{1.36}\text{O}_9$  are also observed. It highlights a step-like modification of the volume at  $750^{\circ}\text{C}$  that correspond to the phase transition between the monoclinic and the rhombohedral phase. It led to a disordered and highly conductive phase. [23]

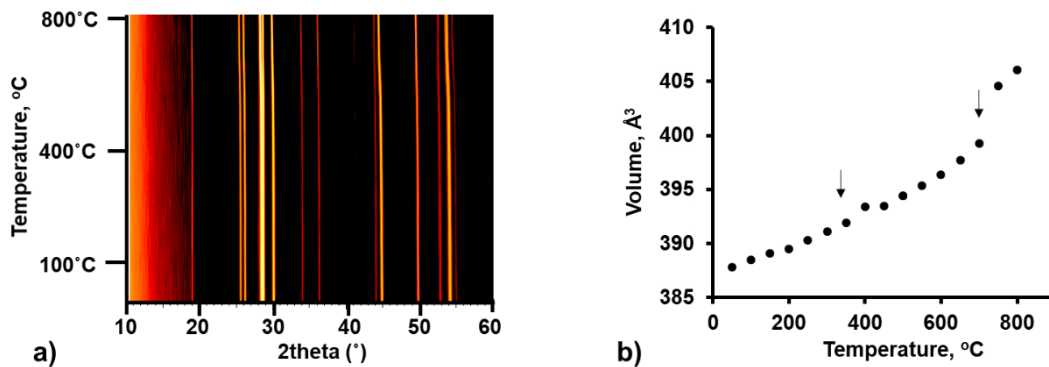


Figure 121. (a) HTXRD of  $\text{Bi}_{3.95}\text{Pb}_{0.7}\text{La}_{1.36}\text{O}_{8.66}$  and (b) evolution of volume versus temperature.

The non-linearity in the different Arrhenius plot domains is amazing and has already been linked to the increase of the distance between the two layers (Van der Waals gap) also related to the displacement of oxygen in the interstitial site. [20]

The introduction of lead increases the temperature of transition which is the opposite of what is expected. Finally, as suggested by the results of  $\text{Pb}_4\text{La}_2\text{O}_7$ , the conductivity is worth than without introduction of  $\text{Pb}^{2+}$  which is questioning...

### IV.2.3. Conclusion

After the different studies of Drache et al. [11, 12], similar systems involving different lanthanides were investigated. The origin of oxygen mobility in the Bi-based phases is still controversial. Two possibilities were discussed: (1) intra-layer with mobility of oxygen located at the extremities of fluorite-like layers and (2) inter-layer pathway with a mobility induced by the additional oxygen position between two layers and partially occupied. The first solution was tested in 2006 by Ahi et al. [21] through neutron scattering and reverse Monte Carlo Simulations and by Mercurio et al. [22] in 1989 whereas the second one was more recently investigated by Jamroz et al. in 2020 [23]. The results presented in this thesis are also favoring the mobility inter-layer which is almost impossible for several reasons:

- In the triclinic unit cell, any evidence of oxygen position in the Van der Waals gap (to date) was observed,
- the distance between the 2D layers is higher than in the case of the Pb-based compound (3.2 v.s. 3.5Å) making more difficult the mobility between the layers,
- the oxygen vacancies are too abundant and it becomes a disadvantage to the oxygen mobility. In addition, the O...O distance is higher in the case of the Pb-based sample which is against the oxygen mobility,
- finally, the lone-pair activity between the two structures is different, reduced in the case of the Pb-based sample as the position and orientation of the lone-pair of Pb(II) is really different. In the case of the Bi-based compound, there are exactly perpendicular to the layer, favoring the motion of oxygen anions as it is the case in the BiMeVOx series of compounds. [24]

### IV.3. Toward new oxo-centered crystal structures in lead containing systems

This part of my work is a collaboration with the University of Saint Petersburg. Dr Oleg Siidra. Our contact is well known in the field of minerals and synthetic lead oxides, most of them being oxo-centered. This project was partially carried out at the St. Petersburg state university during a stage of four months occurring during the closure of the lab for renovations and asbestos removal from August 2019 to January 2020.

The University of Saint Petersburg is internationally recognized for their skills in crystallography and mineralogy. Oleg Siidra and Sergey Krivovichev, the head of the department, were precursors in the use of the oxo-centered theory. In 2013, our group published a review on the subject through their momentum. [25]

The investigation of divalent lead-containing systems is a planetwide tendency. It is due to widespread use of lead-containing compounds and equally common environmental consequences. [36] The coordination geometry of lead was examined in 329 experimentally determined structures and compared with the results of ab initio molecular orbital calculations in the work of Shimoni-Livny, L. et al. (1998) [33]. It was established that the coordination geometry around lead has two distinct structural categories: *holodirected* and *hemidirected*, as shown on Figure 122. In case of *holodirected* coordination geometry, the bonds to ligand atoms (oxygen or fluorine, in our case) are directed throughout the surface of an encompassing globe. In second *hemidirected* type of geometry, the bonds are directed throughout only part of the globe.

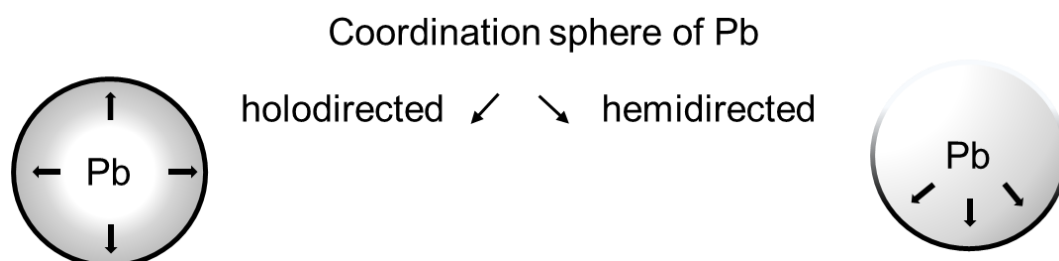


Figure 122. (A) Holodirected and (B) Hemidirected Coordination of lead. [borrowed from ref.[33]

The structures described using oxo-centered cationic blocks can be quite complex. There are also crystal structures involving complex anionic sub-groups as in zeolites. [47] As a consequence, it was proposed to investigate the chemical systems: Pb-Ge-Al-O-X and Pb-Si-Al-O-X during this Russian internship.

For the moment, no oxo-centered crystal structures have been reported in these sophisticated chemical systems. But there are some examples where lead was found in rather simple Pb-Si-O or more complex Pb-Si-Al-O chemical systems. Roymillerite mineral contains all these elements and includes the oxo-centered units. Some oxo-centered compounds in Pb-Ge-O chemical system were observed. At the same time, any compound containing Pb, Ge and Al elements have been detected. It should be noted that one of the first projects in which I took part under supervision of Siidra, O. was dedicated to synthesis and modular structural architectures of mineralogically inspired novel complex Pb oxyhalides [46]. The full list of compounds found in these chemical systems is given in Table 49. So, it appeared to be a promising playground for new phases and establish new topologies.

**Table 49. Compositions have the oxo-centered units in the base of crystal structures in lead containing systems.**

Composition	Space-group Symmetry	Unit cell parameters	Oxo-centered unit	Ref.
Pb <sub>32</sub> (Si <sub>4</sub> O <sub>12</sub> ) <sub>4</sub> O <sub>16</sub>	<i>A2</i> monoclinic	a=19.43(1) Å b=7.64(2) Å c=12.24(1) Å β=99.33(3)°	1D infinite chains	[41]
Pb <sub>11</sub> [SiO <sub>4</sub> ][Si <sub>2</sub> O <sub>7</sub> ]O <sub>6</sub>	<i>P-1</i> triclinic	a=22.502(5) Å b=12.982(2) Å c=7.313(2) Å α=92.52(2)° β=99.17(3)° γ=100.29(2)°	1D infinite chains	[42]
Pb <sub>6</sub> O[(Si <sub>6</sub> Al <sub>2</sub> )O <sub>20</sub> ]	<i>I4/mmm</i> tetragonal	a = 11.7162(10) Å, c = 8.0435(12) Å	Isolated oxo-centered OPb <sub>6</sub> octahedron	[43]
Roymillerite Pb <sub>24</sub> Mg <sub>9</sub> (Si <sub>9</sub> AlO <sub>28</sub> )(SiO <sub>4</sub> )(BO <sub>3</sub> )(CO <sub>3</sub> ) <sub>10</sub> (OH) <sub>14</sub> O <sub>4</sub>	<i>P-1</i> triclinic	a=9.3152(15) Å b=9.3164(15) Å c=26.463(4) Å α=83.295(3)° β=83.308(3)° γ=60.023(2)°	“molybdophyllite” and “plumbonacrite” isolated modules	[44]
Pb <sub>11</sub> [GeO <sub>4</sub> ][Ge <sub>2</sub> O <sub>7</sub> ]O <sub>6</sub>	<i>P-1</i> triclinic	a=22.259(4) Å b=19.910(4) Å c=7.361(1) Å α=97.59(1)° β=95.15(1)° γ=92.35(2)°	1D infinite chains	[45]
Pb <sub>3</sub> [O <sub>10</sub> Pb <sub>20</sub> ](GeO <sub>4</sub> ) <sub>4</sub> Cl <sub>10</sub>	<i>Cmca</i> orthorhombic	a=28.352(19) Å b=11.116(7) Å c=16.513(11) Å	2D infinite layers	[46]

### IV.3.1. A description based on the structure hierarchy hypothesis

In recent years, an extensive work has been provided on the hierarchical classification of many groups of inorganic compounds. Historically, the classification of minerals is the one of relevance and difficult task. Since the first structures of common rockforming minerals were solved, the different classifications were proposed starting from the Bowen “reaction series”. [27] Silicate and aluminosilicate groups are the most common in large-scale Earth processes, and are in the basis of a structure hierarchy. But it also may contain any other tetrahedrally coordinated cation such as  $\text{Ti}^{4+}$ ,  $\text{Fe}^{3+}$ ,  $\text{B}^{3+}$ ,  $\text{P}^{5+}$ ,  $\text{As}^{5+}$ ,  $\text{V}^{5+}$ ,  $\text{Mg}^{2+}$ ,  $\text{Fe}^{2+}$ ,  $\text{Mn}^{2+}$ ,  $\text{Zn}^{2+}$  and possibly  $\text{S}^{6+}$ ,  $\text{Cr}^{6+}$  and  $\text{Li}^+$ .

Another way to describe the structures is based on the Structure Hierarchy Hypothesis which states - “Structures may be ordered hierarchically according to the polymerization of coordination polyhedra of higher bond-valence.” [28] This approach operates with a term of ‘fundamental building block’ (FBB) that used to form: isolated polyhedra; clusters; chains and ribbons; sheets; and frameworks. Hawthorne uses the structure hierarchy to discuss the structures of sheet silicates in terms of n-connected plane nets.

The cation-coordination polyhedra was mainly used to describe many crystal structures before the binary structural representation was proposed. In 1983, Hawthorne [28] introduced the idea of splitting the crystal structure into two components:

- (1) the “structural unit”, and
- (2) the “interstitial complex”.

The first component is represented by the strongly bonded units and the second one – by an assembly of cations, anions and neutral species that weakly link the structural units together [29]. This partitioning is based on the bond valences sums [30], where the value of 0.30 vu is generally a determinant. Thus the bonds weaker than 0.30 vu belong to the interstitial complex. There are some main key aspects of using this hypothesis:

- type of the basic (parent) plane net;
- the direction of constituent tetrahedra (up or down);
- nature of the sheet (planar or folder);
- the multiplicity of the sheet (single or double); and others.

The simplest example to demonstrate the application of this hypothesis to crystal structures is mica. A general projection of trioctahedral mica crystal structure [26] is shown on Figure 123(a). Corner shared  $[\text{Si}/\text{XO}_4]$  tetrahedrons are forming infinite 2D planar sheets (Figure 123(b)). Each tetrahedron is 3-connected, may lie on one side of the sheet (U – up) or the other (D –down). In the particular case, the apical vertices are all in the same direction. The polymerization of  $[\text{XO}_4]$  tetrahedra is commonly described in terms of three-dimensional nets, where the vertices of the net are occupied by tetrahedra, and the edges of the net represent linkages between them, as is shown on Figure 123(c). Each vertex is surrounded by three identical hexagons and is given the symbol  $6^3$ . In the particular case, all six tetrahedra within the ring are pointed in the same direction – up, and have the symbol  $U^6$ .

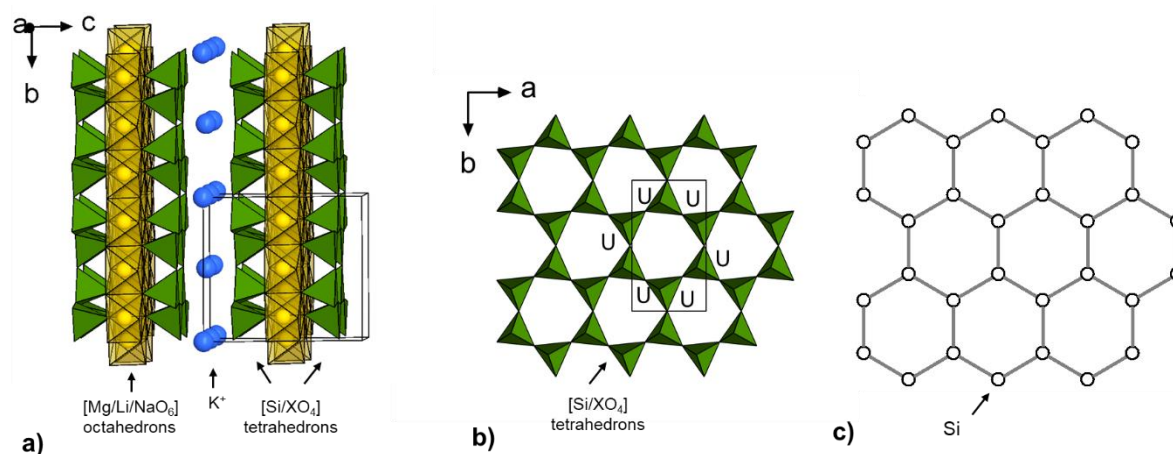


**Figure 123.** (a) General projection of mica[26] crystal structure. (b) The  $[\text{X}_2\text{O}_5]$  sheet in mica. (c)  $6^3$  net representation, where circles correspond to tetrahedra, and lines give an information about tetrahedra connectivity.

In series of experiment with elements that use to form  $[\text{XO}_4]$  tetrahedrons ( $\text{X} = \text{Ge}, \text{Al}$  or  $\text{Si}$ ), a number of new compounds were obtained and explained using the Structure Hierarchy Hypothesis.

### IV.3.2. Pb – Ge – Al – O/F chemical system

#### a. $Pb_{14}Ge_8Al_7O_{31}F_{19}$

Among lots of trials performed, a mixture of  $PbF_2$ ,  $GeO_2$  and  $Al_2O_3$  precursors were taken in 3:1:1 ratio. They were carefully grinded in agate mortar and placed in alumina crucible. The initial mixture was heated to  $600^\circ C$ . As a result, the several tiny shapeless crystals were selected to provide single crystal diffraction and EDS measurement. EDS demonstrated the presence of Pb, F, Ge and Al elements (Figure 124(a)). The image of the selected crystal is given on Figure 124(b).

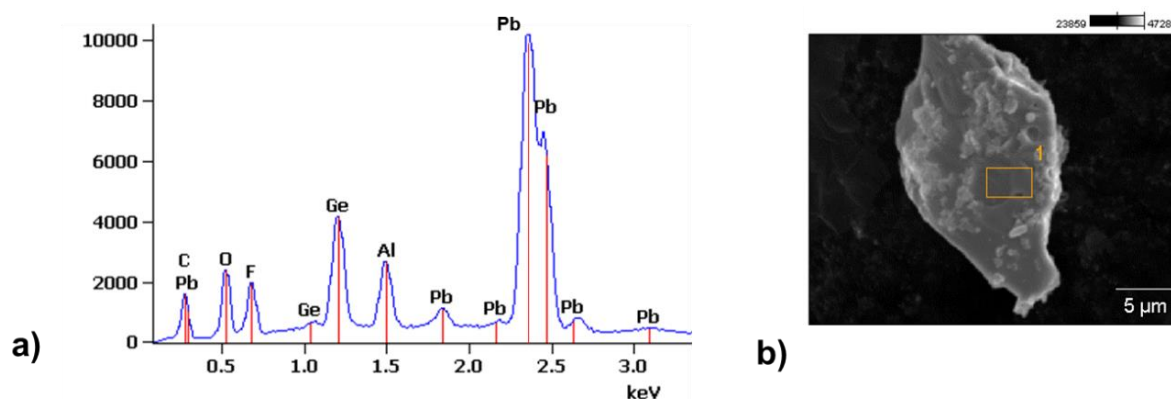


Figure 124. (a) EDS measurement and chemical analysis of mixture heated on  $600^\circ C$ . (b) Image of the crystal.

Single crystal X-Ray diffraction experiment was performed. It was solved and refined using Jana2006 software.[48] It crystallizes unambiguously in  $Fm-3$  cubic space group with  $a$  unit cell parameter of  $16.2455(1)$  (Å). The detailed information is presented in Table 53 to Table 57 in SI. The composition deduced from the refinement is  $Pb_{14}Ge_8Al_7O_{31}F_{19}$ .

The crystal structure of  $Pb_{14}Ge_8Al_7O_{31}F_{19}$  contains two crystallographically independent lead sites, two – aluminum, and one – germanium. The coordination environment of cations is shown on Figure 125. The anionic part contains both oxygen and fluorine in significant amount as evidenced by the EDS measurement. Monocrystalline diffraction method has some limitations such as separation of oxygen and fluorine in one position because of the similar atomic number. Preliminary bond valance calculations indicated that possible partial substitution on some anionic positions. According to that, the electroneutrality of the formula was achieved by

inserting mixed sites on O1 and O2 sites refined in ratio 0.8542/0.1458 for O1/F1 and 0.4167/0.5833 for O2/F2. In addition, there are two full O3 and F3 sites.

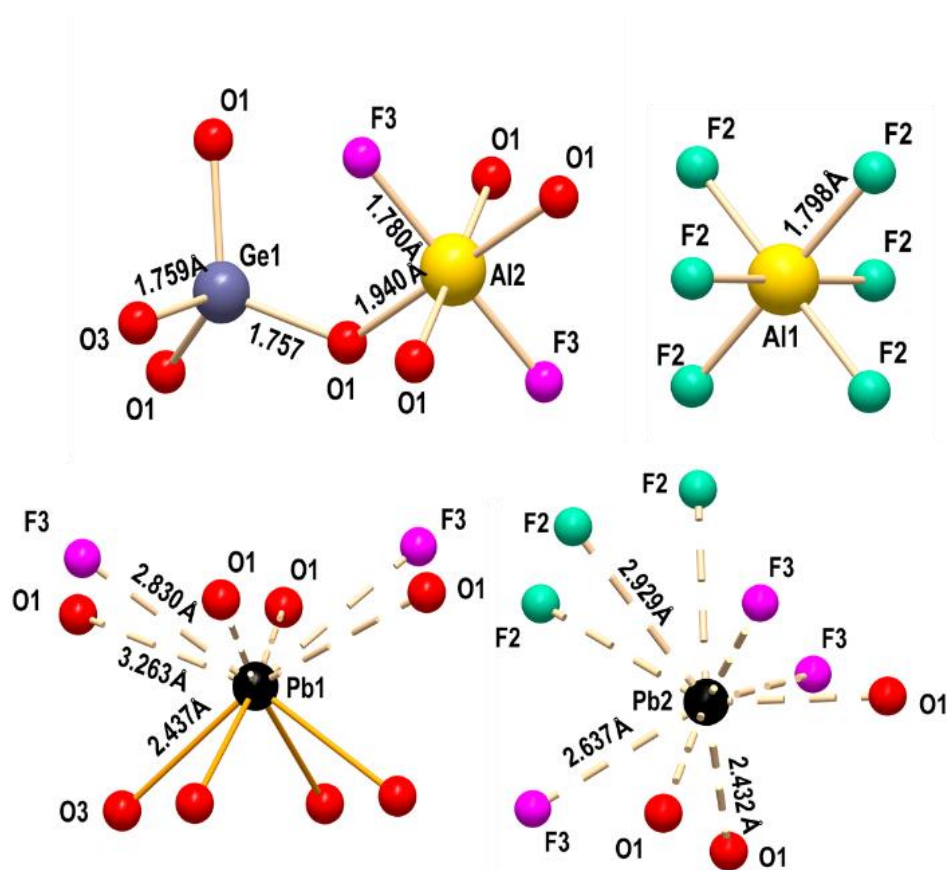
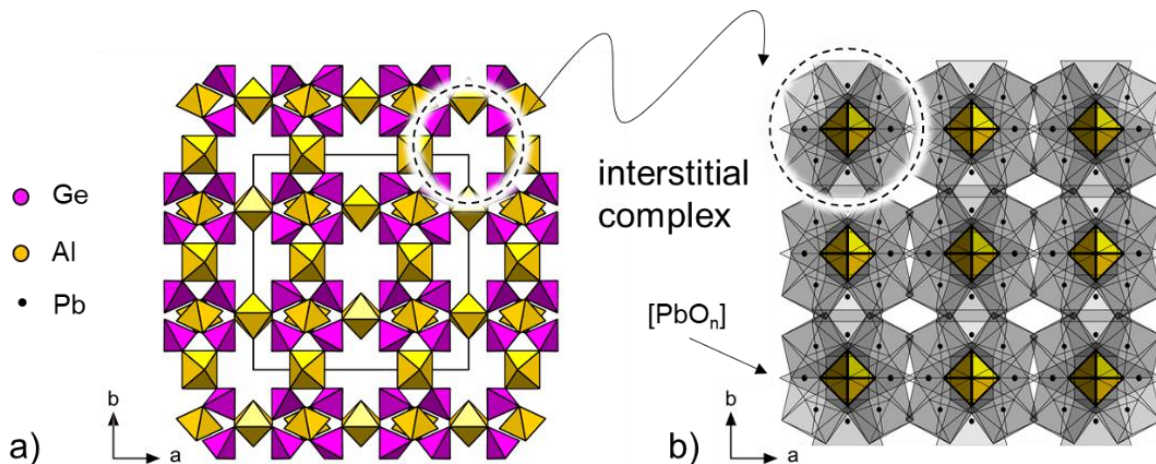


Figure 125. Coordination environment of cations are forming the crystal structure of  $\text{Pb}_{14}\text{Ge}_8\text{Al}_7\text{O}_{31}\text{F}_{19}$ .

Using the idea of Binary Structural Representation, [29] the infinite framework of new compound is, as already stated above, divided in two parts. The strongly bonded structural unit consist of corner shared alumina octahedrons and germanium tetrahedrons, forming a three-dimensional infinite framework. The general projection of the framework is given on Figure 126 (a), where the germanium tetrahedrons are shown in pink color, and alumina polyhedrons in yellow. Existing voids are filled with second structural part - isolated alumina octahedrons surrounded by atoms of lead, that is represented on Figure 126 (b). The irregular polyhedrons  $[\text{Pb}(\text{O}/\text{F})_n]$  are given in light grey color.



**Figure 126.** General projection of crystal structure of  $\text{Pb}_{14}\text{Ge}_8\text{Al}_7\text{O}_{31}\text{F}_{19}$  compound divided on two constituent parts: infinite framework (a) and isolated alumina octahedrons with  $[\text{PbO}_n]$  irregular polyhedrons (b).

This  $[\text{Pb}(\text{O}/\text{F})_n]$  3D framework is interesting because, to the best of our knowledge, it is the first oxyfluoro lead alumino-germanate reported in literature. In a second step, the same initial mixture was heated at  $650^\circ\text{C}$ , leading to the formation of a second new compound.

#### ***b. $[\text{Pb}_{12}\text{O}_6]\text{Ge}_7\text{Al}_4\text{O}_{26}$***

A prismatic transparent crystal was selected for further investigation (Figure 127(b)). This crystal was mounted on nylon loop to provide single crystal X-Ray diffraction. An EDS measurement revealed the presence of number of Pb, Ge, Al, F and O, Si (lines from 1.6 to 1.9 keV) arising from the use of grease, that are shown on Figure 127(a).

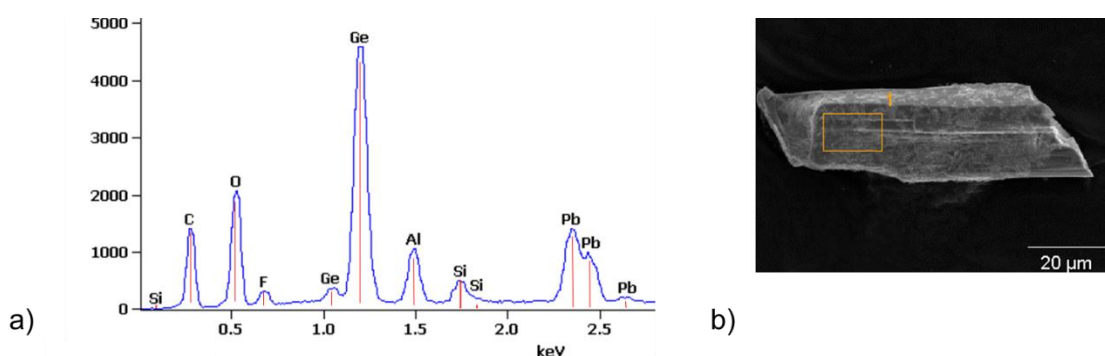


**Figure 127.** (a) EDS measurement and chemical analysis of mixture heated on 650°C. (b) Image of the crystal.

The single crystal diffraction analysis allowed solving and refining the crystal structure. It crystallized in  $C2/c$  monoclinic space group with unit cell parameters of  $a = 10.1055(12)$  (Å),  $b = 17.825(2)$  (Å),  $c = 19.436(2)$  (Å), and  $\beta = 95.572(8)^\circ$ . The detailed information about data collection and structure refinement are given in Table 53. The final formula of new compound is  $[Pb_{12}O_6]Ge_7Al_4O_{26}$ . All atomic parameters are presented in Table 58. The bond valence calculations, presented in confirmed the quality of the refinement. Selected interatomic distances are given in Table 60.

The crystal structure of new compound contains six independent positions of tetrahedrally coordinated sites, four of them are Ge and the rest two are Al atoms. The average bond lengths in  $[GeO_4]$  tetrahedrons vary from 1.661(1) to 1.841(2) Å, whereas in case of  $[AlO_4]$  tetrahedron they vary in a range from 1.693(1) to 1.80(2). These values are well correlated with “Bond-length distributions for ions bonded to oxygen” reported by Gagné, O. C., & Hawthorne, F. C. (2018) [34].

Each tetrahedron shares common vertices with three or four tetrahedrons. In order to describe this structure in terms of Binary Structural Representation [29], some elemental structural units were highlighted. Twelve corner-sharing tetrahedrons form planar twelve-member rings, as is shown on Figure 128 (a). Letters U (up) and D (down) give us an idea about orientation of apical vertices. The rings are presented in two projections to show how U and D oriented tetrahedrons alternate next but one in UDUDUD-sequence.

The identical 12-member rings form infinite single 2D sheet, as is demonstrated on Figure 128 (b). Within this sheet, all  $[GeO_4]$  tetrahedrons are connected to two neighboring tetrahedrons, whereas all  $[AlO_4]$  – to three tetrahedrons. According to Hawthorne’s classification, this type

of sheet corresponds to nets derived from the  $6^3$  net (already discussed for mica crystal structure). Figure 128 (c) demonstrates how 2-connected  $[\text{GeO}_4]$  vertices (in violet) have been inserted into all edges of the  $[\text{AlO}_4]$  (in yellow)  $6^3$  net, forming infinite net.

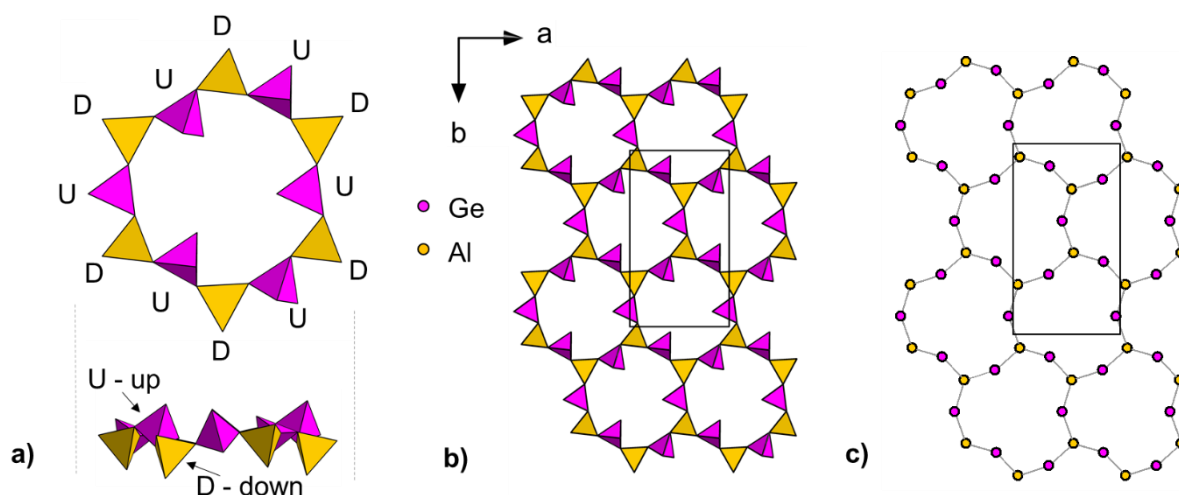


**Figure 128.** (a) 12-member rings and its cross-sectional view, with U – up or D – down orientation of the apical vertical. (b) Infinite 2D sheet and its net (c).

Further description of the crystal structure requires the introduction of Multi-layer phenomena that was also developed by Hawthorne. [31] He proposed a series of topological operations giving rise to another type of nets that can represent more complicated sheet structures. In case of our new compound, the *insertion*, *replication* and *reorientation* operations will be introduced.

There are seven independent sites of lead atoms in the crystal structure. Lead atoms Pb1-Pb6 are surrounded by 6 to 9 oxygen atoms forming highly distorted polyhedrons with two types of Pb-O bond length – short and long. Coordination environment of these lead atoms attributed to *hemidirected* type of bonds distribution. The short bonds are shown in thick dark gray line on Figure 129, whereas long ones – in thin line. The short bonds are typically around  $2.3\text{\AA}$  and located in one hemisphere, while the rest long bond can go from  $2.65$  to  $3.55\text{\AA}$ . The only Pb7 has a more or less regular cubic coordination with a spread in Pb-O distances between  $2.4$  to  $2.8\text{\AA}$ . Coordination environment of Pb7 attributed to *holodirected* geometry of bonds distribution.

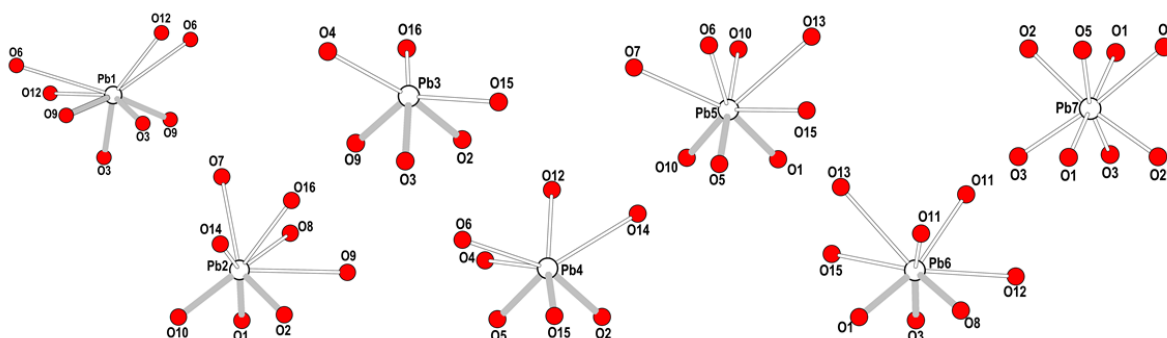


**Figure 129.** Highly distorted coordination environment of lead atom in crystal structure of  $[\text{Pb}_{12}\text{O}_6]\text{Ge}_7\text{Al}_4\text{O}_{26}$ .

The general projection of crystal structure of  $[\text{Pb}_{12}\text{O}_6]\text{Ge}_7\text{Al}_4\text{O}_{26}$  is given on Figure 130 (a). The  $[\text{GeO}_4]$  and  $[\text{AlO}_4]$  tetrahedrons forming infinite framework. It is made up of infinite 2D single-layer sheets (A) that are *replicated* and *reoriented* forming another single-layer sheet (A'). These two single layers are linked together through a common vertical of tetrahedrons, and are forming double-layer sheet of tetrahedra. *Inserted*  $[\text{GeO}_4]$  tetrahedrons in B and B' zones serve as connectors between double-layer sheets.

The framework contains voids that are occupied by oxygen and lead atoms. The use of the oxo-centered approach to describe a crystal structure is efficient due to the presence of short Pb-O bonds. The oxo-centered  $[\text{OPb}_4]$  tetrahedra is a building unit in the crystal structure of this compound. A zero-dimensional isolated  $[\text{Pb}_{12}\text{O}_6]$  clusters formed by six  $[\text{OPb}_4]$  tetrahedra sharing common edges. These clusters are inserted in the tunnels arising from the Ge/Al framework and act as Interstitial Complexes (Figure 130(b)).

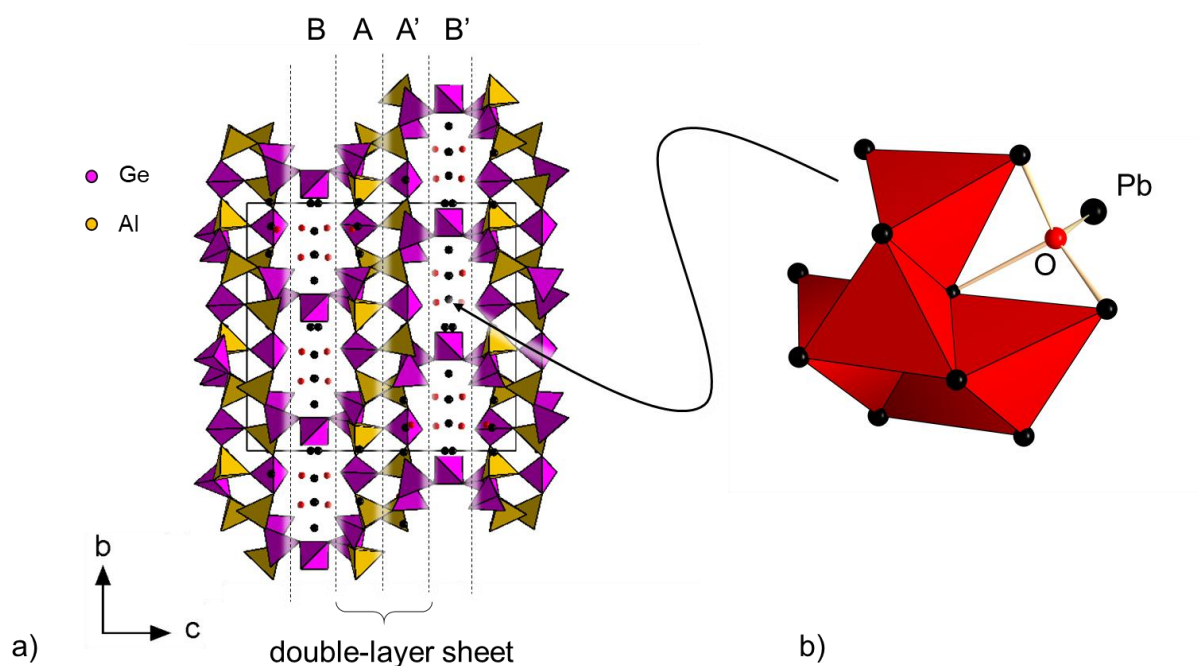


**Figure 130. (a) Infinite framework based on AA' double-layer sheets and BB' linking [GeO<sub>4</sub>] tetrahedrons. (b) [Pb<sub>12</sub>O<sub>6</sub>] cluster consisting of six [OPb<sub>4</sub>] oxo-centered tetrahedrons in crystal structure.**

The additional powder X-Rays experiment was provided to establish the phase composition of powder sample heated at 650°C. It revealed the predominance of the new [Pb<sub>12</sub>O<sub>6</sub>]Ge<sub>7</sub>Al<sub>4</sub>O<sub>26</sub> compound and existence of Al<sub>2</sub>O<sub>5</sub>Si (COD ID 1008755) [37]. The unit cell parameters were refined with a good agreement with inputted data. The pattern matching of this sample is shown on Figure 131.

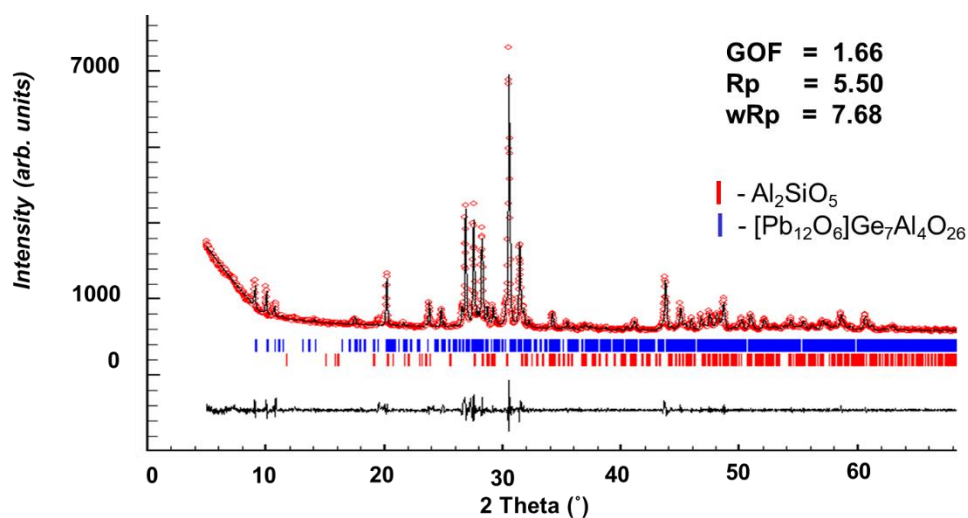


**Figure 131. The fitted XRD pattern using profile matching method for the [Pb<sub>12</sub>O<sub>6</sub>]Ge<sub>7</sub>Al<sub>4</sub>O<sub>26</sub> sample.**

### IV.3.3. Pb – Si – Al – O chemical system

#### a. $[Pb_{13}O_8]Si_8Al_2O_{24}$

Inspired by the first results on obtaining new compounds in previous chemical system, it was decided to replace germanium by silica. The 3:1:1 ratio of  $PbF_2$ ,  $SiO_2$  and  $Al_2O_3$  precursors was also repeated from previous successful experiment presented in paragraph IV.3.2. The initial mixture was well grinded in agate mortar and heated to  $650^\circ C$  in alumina crucible. It resulted in formation of yellow plate-like crystals (Figure 132(b)). They were selected and analyzed via EDS measurements, presented on Figure 132(a).

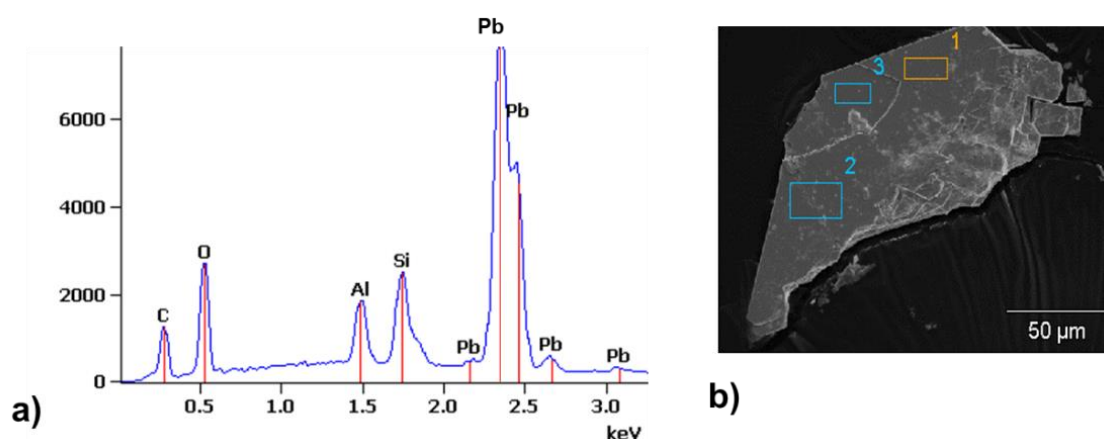
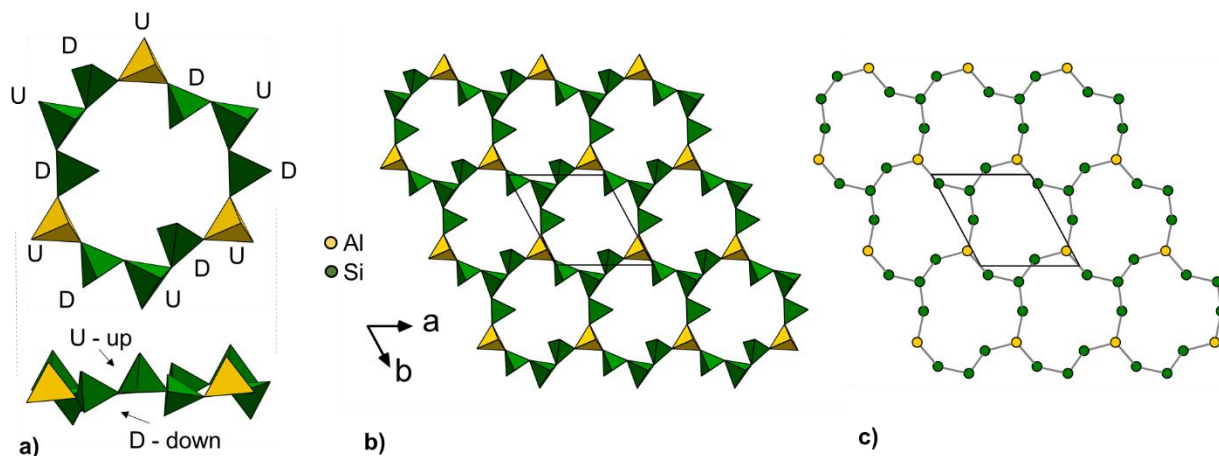


Figure 132. (a) EDS measurement and chemical analysis of mixture heated on  $650^\circ C$ . (b) Image of the crystal.

Single crystal X-Rays experiment allows to solve and refine a crystal structure in triclinic  $P-1$  space group. Detailed information about crystal parameters, data collections etc. is presented in tables from Table 63 to Table 66 in SI. The formula of this compound is  $[Pb_{13}O_8]Si_8Al_2O_{24}$ . The crystal structure contains five symmetrically independent positions of tetrahedrally coordinated atoms. The presence of Si and Al was confirmed by EDS measurement. During the crystal structure investigation, we faced difficulties in Al/Si-ordering of tetrahedrally occupied positions. This ordering plays the principal role in determining the physicochemical properties of zeolites [38]. It also affects the symmetry breaking of monoclinic Na feldspar (albite) structure in the triclinic phase [39]. In our particular case, there is a discrepancy in Si4 position, which demonstrates a lack of bond valence sum, as is shown in Table 66. Having made several unsuccessful attempts to correct this value by mixing site positions, it was decided to leave this question for further neutron scattering lengths and cross sections study.



**Figure 133. (a) 12-member rings and its cross-sectional view, with U – up or D – down orientation of the apical vertical. (b) Infinite 2D sheet and its net (c).**

Following structure hierarchy for silicate minerals by Hawthorne [31], the crystal structure of this compound can also be explained in terms of multi-layer tetrahedron-sheets and isolated interstitial complexes. The Al and Si tetrahedrons share common vertices and form 12 member rings (Figure 133(a)), that are quite similar to reported for previously described crystal structure of  $[\text{Pb}_{12}\text{O}_6]\text{Ge}_7\text{Al}_4\text{O}_{26}$ . It reproduces the UDUDUD-arrangement and planar configuration of sheet (Figure 133(b)). These rings are also associated in zeophyllite-like single layers, that is shown on net representation (Figure 133(c)).

There are seven positions of lead in the crystal structure. Coordination environment of most lead atoms attributed to *hemidirected* type of bonds distribution, except on Pb3 that has *holodirected* geometry of bonds distribution, as is shown on Figure 134.

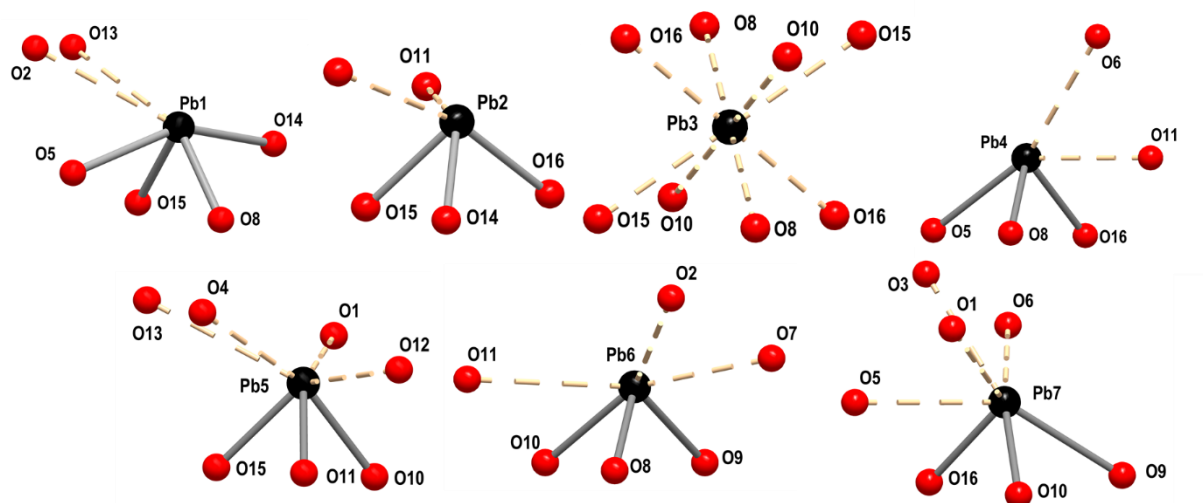


**Figure 134.** Highly distorted coordination environment of lead atom in crystal structure of  $[\text{Pb}_{13}\text{O}_8]\text{Si}_8\text{Al}_2\text{O}_{24}$ .

The general projection of the crystal structure is given on Figure 135(a). Each single-sheet is replicated, reoriented and linked to the original single-layer sheet to produce a double-layer sheet. A sequential alternation of double-layer sheets, parallel to *ab*-plane, resulted in the formation of a layered crystal structure. The interlayered space is filled by interstitial complexes of oxo-centered OD isolated clusters. They are based on  $[\text{OPb}_4]$  oxo-centered tetrahedrons. Eight  $[\text{OPb}_4]$  tetrahedrons share common edges and form zero-dimensional  $[\text{O}_8\text{Pb}_{13}]$  clusters, as is detailed on Figure 135.

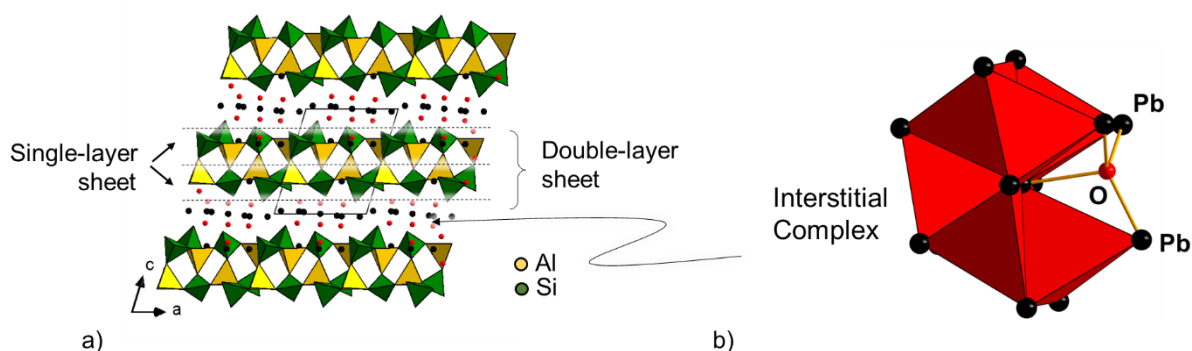


**Figure 135.** (a) Association of two Single-layer sheet in one doubled, forming layered crystal structure. (b)  $[\text{Pb}_{13}\text{O}_8]$  cluster consisting of eight  $[\text{OPb}_4]$  oxo-centered tetrahedrons, inserted as Interstitial Complex.

The additional powder X-Rays experiment was provided to establish the phase composition of powder sample heated at 650°C. It revealed the presence of mainly new  $[\text{Pb}_{13}\text{O}_8]\text{Si}_8\text{Al}_2\text{O}_{24}$  phase with a small quantity of  $\text{Al}_2\text{SiO}_5$  (PDF card № 38-0471) [49] The unit cell parameters

were refined with a good agreement with inputted data. The pattern matching of this sample is shown on Figure 136.

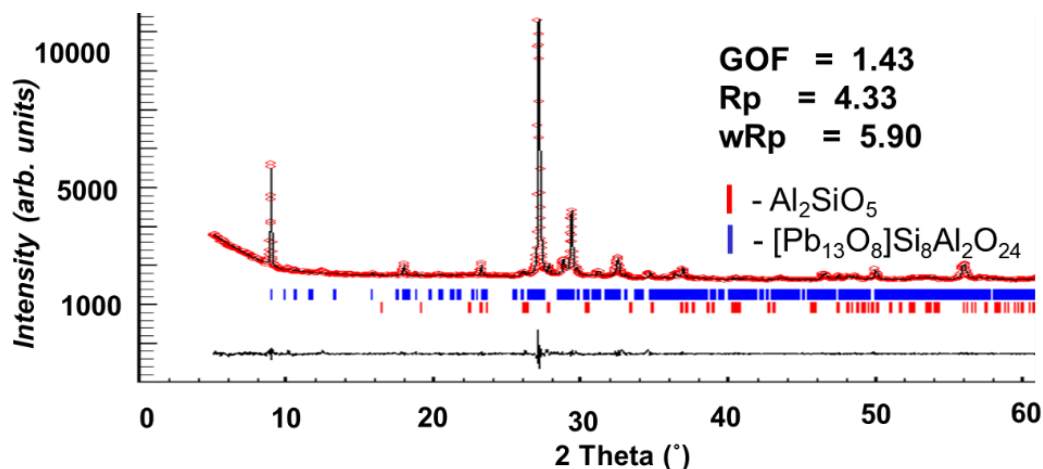


Figure 136. The fitted XRD pattern using profile matching method for the [Pb<sub>13</sub>O<sub>8</sub>]Si<sub>8</sub>Al<sub>2</sub>O<sub>24</sub> sample.

- Structure comparison of [Pb<sub>12</sub>O<sub>6</sub>]Ge<sub>7</sub>Al<sub>4</sub>O<sub>26</sub> and [Pb<sub>13</sub>O<sub>8</sub>]Si<sub>8</sub>Al<sub>2</sub>O<sub>24</sub>

During the study of the crystal structures of two new compounds: [Pb<sub>12</sub>O<sub>6</sub>]Ge<sub>7</sub>Al<sub>4</sub>O<sub>26</sub> and [Pb<sub>13</sub>O<sub>8</sub>]Si<sub>8</sub>Al<sub>2</sub>O<sub>24</sub> the similar 12 member rings are in the base of infinite single 2D sheets. Similar net was described for Zeophyllite mineral with the same UDUDUD-arrangement and planar configuration of sheet. [35] The representation of zeophyllite sheet and its 12<sup>3</sup> net are given on Figure 137 (b) and (c), respectively. It is compared to equal net observed in the crystal structures of new [Pb<sub>12</sub>O<sub>6</sub>]Ge<sub>7</sub>Al<sub>4</sub>O<sub>26</sub> (e) and [Pb<sub>13</sub>O<sub>8</sub>]Si<sub>8</sub>Al<sub>2</sub>O<sub>24</sub> compounds (d).

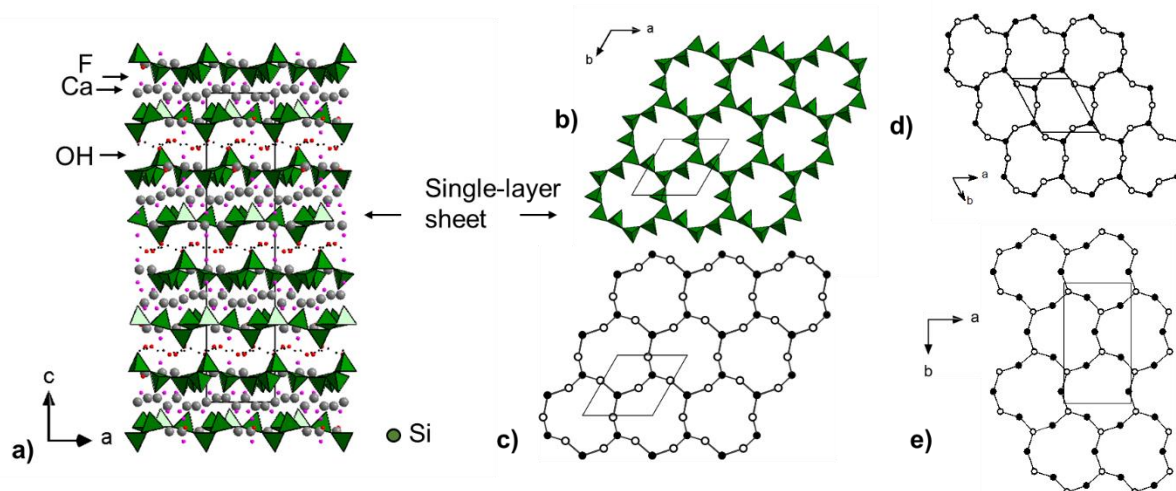
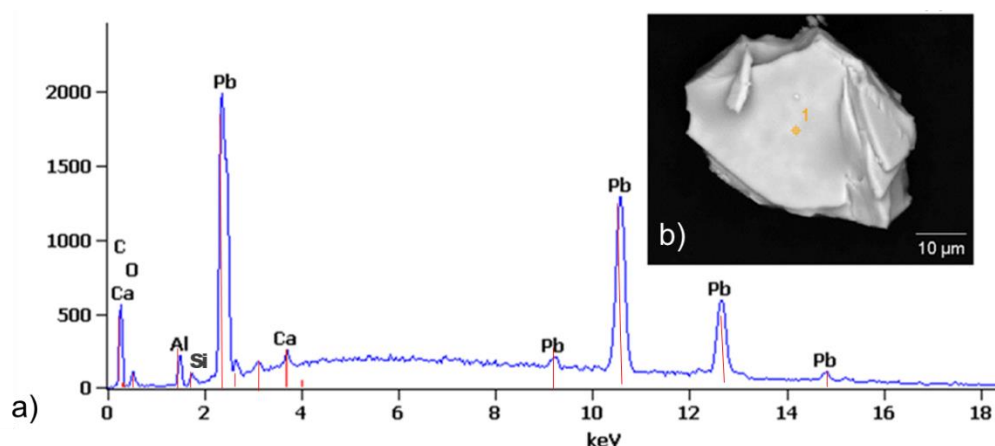


Figure 137. (a) General projection on crystal structure of zeophyllite [31]; (b) Single-layer sheet of Si tetrahedra in zeophyllite; (c) 12<sup>3</sup> net in the structure of zeophyllite [31]; (d) 12<sup>3</sup> net in the structures of new [Pb<sub>12</sub>O<sub>6</sub>]Ge<sub>7</sub>Al<sub>4</sub>O<sub>26</sub> and [Pb<sub>13</sub>O<sub>8</sub>]Si<sub>8</sub>Al<sub>2</sub>O<sub>24</sub> compounds.

Zeophyllite crystal structure is based on single –layered sheets that are not directly connected to each other, whereas the description of our two new compounds is based on multiplication of single –layered sheets.

**b.  $[Pb_6CaO_2](Al/Si)_8O_{17}$**

From the same initial mixture, another temperature of synthesis was successfully tried, leading to another innovative crystal structure. In a second step, the initial mixture was heated to 850°C and slowly cooled with a 1°C/min rate. The sub-amorphous mass was found in the crucible, whereas crystals were obtained on the internal surface of the covering plate. Chemical analysis confirmed the presence of Pb, Al and unexpected Ca, that was most probably exhorsted from the alumina crucible as shown on Figure 138.



**Figure 138. (a) EDS measurement and chemical analysis of mixture heated on 850°C. (b) Image of the crystal.**

The crystal structure of  $[Pb_6CaO_2](Al/Si)_8O_{17}$  was refined in trigonal  $R\bar{3}$  space group. The detailed information about crystal parameters, data collection and structure refinement are given in Table 62. The crystal structure contains only one fully occupied symmetry-independent position of cation that is Pb1. The unique calcium position Ca1 is tenth part occupied by lead Pb2 atom. The remaining positions of Al/Si1 and Al/Si2 are mixed and were settled in equal parts.

The determination of silicon/aluminum and calcium/lead ratio by position was made using the bonds valence calculation. A slight excess of silicon over aluminum was found in the first

position and the inverse ratio in the second. Reliably, it is not possible to determine the exact ratio of cations in the tetrahedral positions. The average bond length in tetrahedron is 1.68(1) Å for Si1/Al1 position and 1.66(1) Å for Si2/Al2, that allowed us to suggest the silicon/alumina ratio as equal that ensures the electroneutrality of the formula. The atomic parameters are given in Table 67.

[TO<sub>4</sub>] tetrahedra, where T1 = Si1/Al1 and Si2/Al2 respectively, share corners to form infinite 2D layers in ab plane (see Figure 139(a)). Such layers are based on two types of six-membered rings. The regular-shaped six-membered ring alternate with distorted ungeometrical rings. Both of them are following the U–D sequences – UDUDUD. The net of 2D layer is 6<sup>3</sup> represented on Figure 139(b). This net is the most common single-layer sheet in silicate minerals.

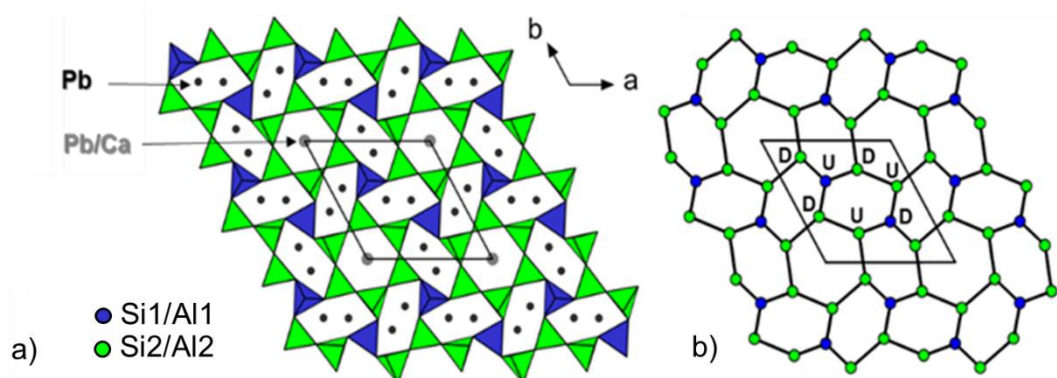


**Figure 139. Elemental 2D building unit (a). Green tetrahedrons correspond to first mixed position of Al/Si atoms, whereas blue – to second one. Black circles correspond to lead atoms and grey – to mixed calcium/lead positions. (b) Net representation of 2D layer, where U corresponds to tetrahedrons in Upper position, whereas D to – down.**

Related planar 6<sup>3</sup> nets are with U and D orientation of tetrahedra have been found in other structures, in gyrolite [40], for example. The detailed examination of sheets was provided by Hawthorne [31]. Figure 140 borrowed from [31] demonstrates two types of rings: six-membered rings close to showing 6-fold rotational symmetry and strongly distorted rings. Less-distorted rings have a U<sup>6</sup> arrangement, where all apical vertices are in the same Up configuration. At the same time the more-distorted rings have a U<sup>2</sup>DU<sup>2</sup>D arrangement. Here is a difference with new [O<sub>2</sub>Pb<sub>6</sub>Ca](Al/Si)<sub>8</sub>O<sub>17</sub> crystal structure – it has UDUDUD sequence in both type of rings.

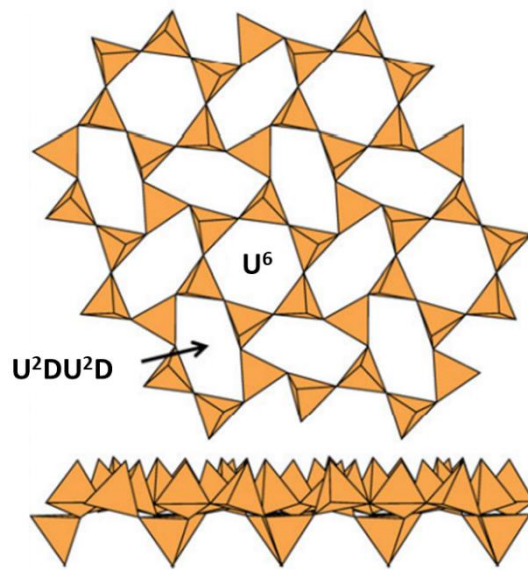


Figure 140. The  $6^3$  sheets of tetrahedra in gyrolite [31].

The interstitial complex in  $[\text{O}_2\text{Pb}_6\text{Ca}](\text{Al}/\text{Si})_8\text{O}_{17}$  consists of lead, calcium and oxygen.

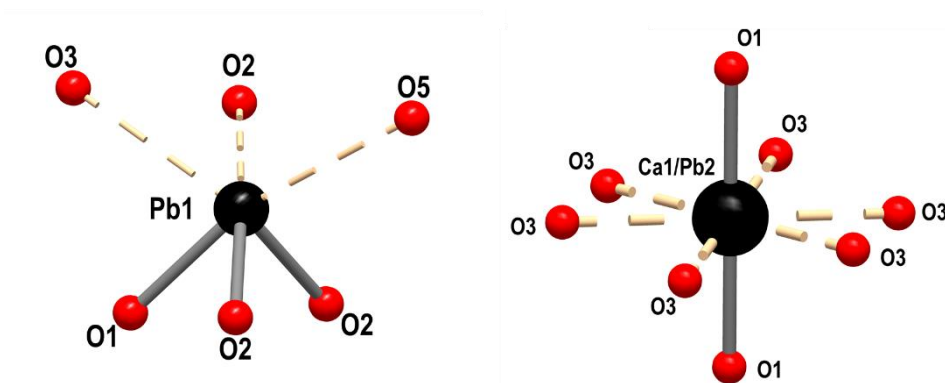


Figure 141. Coordination environment around Pb and mixed Pb/Ca positions in structure of  $[\text{Pb}_6\text{CaO}_2](\text{Al}/\text{Si})_8\text{O}_{17}$ .

Coordination environment of the fully lead occupied site Pb1 is typical to be rather irregular (see Figure 141) and demonstrate strongly distorted *hemidirected* [33] coordination environments.

Finally, the crystal structure of  $[\text{O}_2\text{Pb}_6\text{Ca}](\text{Al}/\text{Si})_8\text{O}_{17}$  is based on planar infinite 2D single-layer sheets of corner-shared Si/Al tetrahedrons. These sheets are replicated and connected via common vertices forming infinite 3D framework (Figure 142(b)). The cavities in 3D framework are filled by interstitial complex described using oxo-centered building unit. In that approach, the oxygen atom O1 is surrounded by four Pb and Pb/Ca atoms forming  $[\text{O}(\text{Pb}/\text{Ca})_4]$  tetrahedron. Two oxo-centered tetrahedra  $[\text{O}(\text{Pb}/\text{Ca})_4]$  share common Pb/Ca vertex and form finite 0D cluster  $[\text{O}_2\text{Pb}_6\text{Ca}]$ .

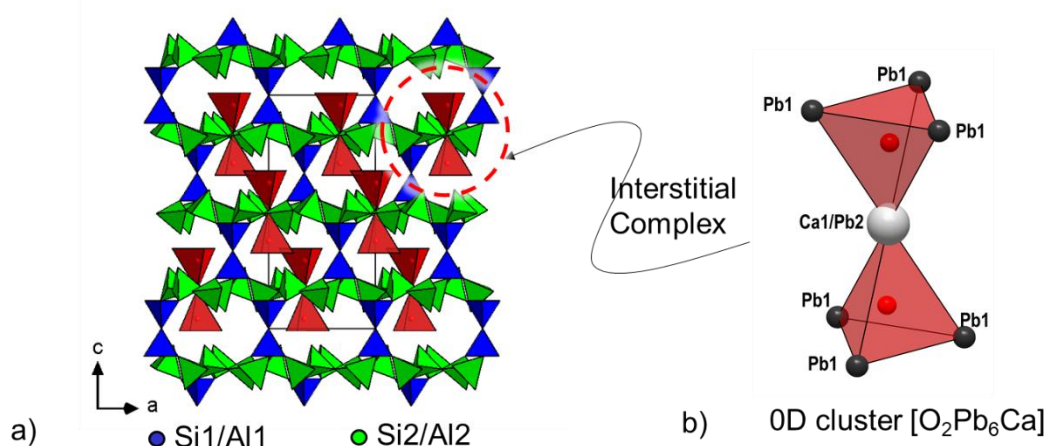


Figure 142. (a) Infinite 3D framework of corner-shared tetrahedrons; (b)  $[\text{O}_2\text{Pb}_6\text{Ca}]$  dimer.

Additional Powder X-Rays investigation was not possible due to insufficient volume of substance.

- Structure comparison of  $\text{Pb}_2[\text{O}_2\text{Pb}_7](\text{Al}_8\text{O}_{19})$

Same type of infinite cluster has been found in the structure of  $\text{Pb}_2[\text{O}_2\text{Pb}_7](\text{Al}_8\text{O}_{19})$ . [32] The crystal structure of that compounds is based on corner-shared  $[\text{AlO}_4]$  tetrahedrons, as is shown

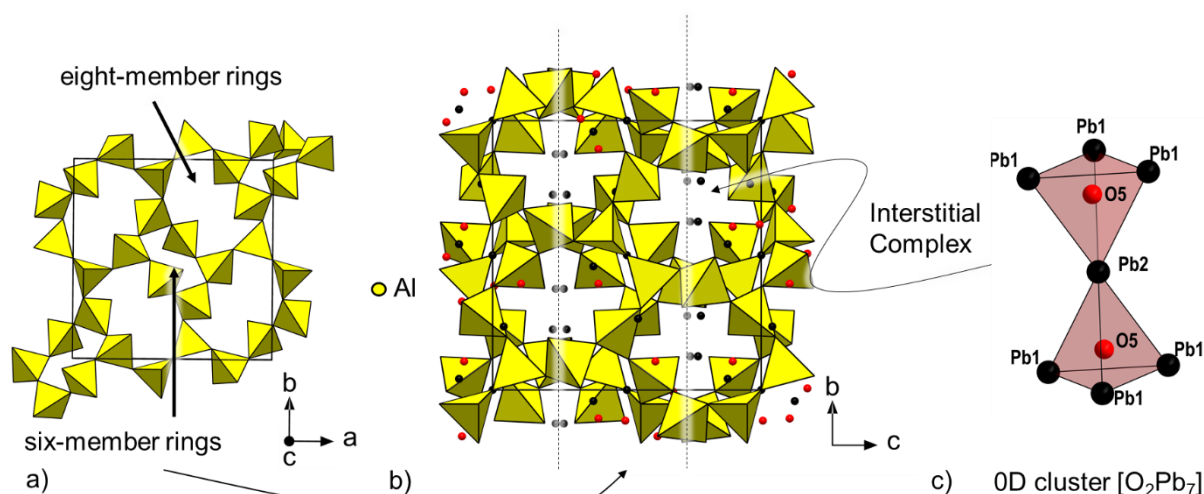


Figure 143. Six- and eight-member rings of alumina tetrahedrons (a) forming infinite 3D framework (b) in crystal structure of  $\text{Pb}_2[\text{Pb}_7\text{O}_2](\text{Al}_8\text{O}_{19})$ . The cavities are filled by OD infinite  $[\text{O}_2\text{Pb}_7]$  clusters (c).

on Figure 143(a). Tetrahedrons are arranged in regular six- and distorted eight-member rings of alumina tetrahedrons. Their alternation leads to formation of infinite 3D framework (Figure 143(b)). The lead and oxygen atoms are in the base of interstitial complex (Figure 143(c)). It contains two oxo-centered  $[\text{OPb}_4]$  tetrahedrons, that are sharing common Pb2 vertice and forming OD  $[\text{O}_2\text{Pb}_7]$  clusters.

## IV.4. Perspectives and conclusion

This part of the work is interesting primarily from a fundamental point of view and the evidence, description and comparison of new topologies. To go further with the physical property's investigation, the next step is the synthesis of the pure powder samples. Within the framework of this work, several attempts were made but did not lead to the desired result. In order to obtain the pure phases, it will be necessary to change the synthesis conditions, probably the initial precursors ( $\text{Al}_2\text{O}_3$  for the moment which is not so reactive...) and optimize or change the way of synthesis. Upon receipt of the pure phase, the HTXRD experiments will be provided to investigate high-temperature behavior and possible phase transitions. The crystal structures of new oxo-centered compounds are rather complicated and demonstrate resemblance in formation of OD clusters. It will be interesting to study, why the formation of these clusters is preferable in both chemical systems.

### IV.4.1. Perspectives

This chapter gives a large overview of several Pb-based oxo-centered materials. The last part is from a crystallographic point of view very interesting and open a wide range of possible investigation. Especially, the addition of transition metals as iron, cobalt, chromium or manganese may give rise to materials with interesting properties, magnetic, electric and eventually magnetoelectric properties which could be of interest for further investigations. In addition, the possibility to describe in the same time the structural units and the interstitial complex is of great interest from a fundamental point of view because, if considering what was done at UCCS concerning the Bi-based family of compounds we could imagine doing some design on these type of materials and been able to formulate and synthesize a great number of new materials.

## IV.5. Supplementary information

**Table 50.** Crystal parameters, data collection and structure refinement details for the crystal of HP-Pb<sub>4</sub>Nd<sub>2</sub>O<sub>7</sub>.

<b>Crystal data</b>	
Formula	Pb <sub>4</sub> Nd <sub>2</sub> O <sub>7</sub>
Formula weight (g/mol)	1229.2
Temperature (K)	293
Crystal system	triclinic
Space group	<i>P</i> -1
<i>a</i> (Å)	7.5913(1)
<i>b</i> (Å)	7.5989(1)
<i>c</i> (Å)	10.4392(1)
$\alpha$ (°)	99.886(1)
$\beta$ (°)	102.024(1)
$\gamma$ (°)	118.482(1)
<i>V</i> (Å <sup>3</sup> )	491.29 (1)Å <sup>3</sup>
<i>Z</i>	2
<b>Data collection</b>	
Diffractometer	DUO Bruker
Radiation; $\lambda$ (Å)	MoK $\alpha$ ; 0.71073
Absorption coefficient, $\mu$ (mm <sup>-1</sup> )	78.661
<i>F</i> (000)	1008
Data range $\theta$ (°); <i>h</i> , <i>k</i> , <i>l</i>	2.1 – 33.15; -11 < <i>h</i> < 11, -11 < <i>k</i> < 11, -15 < <i>l</i> < 15
No. of total reflections	9386
Total unique reflections	3322
Criterion for observed reflections	$I > 3\sigma(I)$
<i>R</i> <sub>int</sub> (%)	3.6
<b>Refinement</b>	
Refinement on	Full-matrix least squares on <i>F</i>
Weight scheme	$1/(\sigma^2  F  + 0.0004 F^2)$
<i>R</i> <sub>gt</sub> , <i>R</i> <sub>all</sub>	2.72, 4.03
w <i>R</i> <sub>gt</sub> , w <i>R</i> <sub>ref</sub>	2.93, 3.13
GOF <sub>gt</sub> , GOF <sub>ref</sub>	1.10, 1.17
Max. /min. residual <i>e</i> density, (eÅ <sup>-3</sup> )	17.53 / -8.21

**Table 51.** Table of atomic parameters for Pb<sub>4</sub>Nd<sub>2</sub>O<sub>7</sub>

Atom	x/a	y/b	z/c	U [Å <sup>2</sup> ]
<b>Pb1</b>	0.75500(5)	0.65870(5)	0.18390(4)	
<b>Pb2</b>	0.23598(5)	0.68521(5)	0.16991(4)	
<b>Pb3</b>	0.27865(5)	0.18531(5)	0.18639(4)	
<b>Pb4</b>	0.77300(5)	1.13548(5)	0.15714(4)	
<b>Nd1</b>	0.73232(7)	0.98158(7)	0.46825(5)	
<b>Nd2</b>	0.76705(7)	0.50678(7)	0.52904(5)	
<b>O1</b>	0.3369(9)	0.8047(9)	0.3924(6)	0.0085(11)
<b>O2</b>	0.8454(9)	1.2867(9)	0.3777(6)	0.0097(12)
<b>O3</b>	0.5745(9)	0.8122(10)	0.2126(7)	0.0123(12)
<b>O4</b>	0.3869(9)	0.2809(9)	0.4135(6)	0.0085(11)
<b>O5</b>	0.152(1)	0.3911(10)	0.2144(7)	0.0138(13)
<b>O6</b>	0.8833(9)	0.7695(9)	0.4092(6)	0.0081(11)
<b>O7</b>	0.955(1)	0.9656(10)	0.1684(7)	0.0170(14)

**Table 52.** Selected interatomic distances in Pb<sub>4</sub>Nd<sub>2</sub>O<sub>7</sub>

Atom 1	Atom 2	d, Å
<b>Pb4</b>	O2	2.2105(60)
	O7	2.2968(92)
	O5	2.4415(60)
	O3	2.4418(71)
<b>Pb3</b>	O7	2.1555(63)
	O5	2.2025(92)
	O4	2.2025(59)
	O7	3.4706(67)
<b>Pb2</b>	O1	2.1623(59)
	O5	2.1766(78)
	O3	2.1782(65)
<b>Pb1</b>	O7	2.1506(67)
	O6	2.1843(58)
	O3	2.2144(87)

Atom 1	Atom 2	d, Å
<b>Nd2</b>	O4	2.4173(52)
	O2	2.4382(56)
	O6	2.4430(68)
	O1	2.4598(69)
	O2	2.4659(76)
	O4	2.4673(82)
	O5	2.5093(71)
	<b>Nd1</b>	O1
	O4	2.4306(68)
	O6	2.4508(82)
	O6	2.4655(50)
	O2	2.4900(69)
	O3	2.4967(65)
	O1	2.4979(61)

**Table 53. Crystal parameters, data collection and structure refinement details for the crystals from Pb – Ge – Al – O chemical system.**

<b>Crystal data</b>	<b>Pb<sub>14</sub>Ge<sub>8</sub>Al<sub>7</sub>O<sub>31</sub>F<sub>19</sub></b>	<b>[Pb<sub>12</sub>O<sub>6</sub>]Ge<sub>7</sub>Al<sub>4</sub>O<sub>26</sub></b>
Formula	Pb <sub>14</sub> Ge <sub>8</sub> Al <sub>7</sub> O <sub>31</sub> F <sub>19</sub>	[Pb <sub>12</sub> O <sub>6</sub> ]Ge <sub>7</sub> Al <sub>4</sub> O <sub>26</sub>
Formula weight (g/mol)	4527.2	481.91
Temperature (K)	293	299(2)
Crystal system	cubic	monoclinic
Space group	<i>Fm</i> -3 (202)	<i>C</i> 2/c (15)
<i>a</i> (Å)	16.2455(1)	10.1055(1)
<i>b</i> (Å)	16.2455(1)	17.8246(2)
<i>c</i> (Å)	16.2455(1)	19.436(1)
$\alpha^\circ$	90	90
$\beta^\circ$	90	95.572(8)
$\gamma^\circ$	90	90
<i>V</i> (Å <sup>3</sup> )	4287.4(5)	3484.4(7)
<i>Z</i>	4	30
<b>Data collection</b>		
Diffractionmeter	Bruker X8 APEX II	Bruker X8 APEX II
Radiation; $\lambda$ (Å)	MoK $\alpha$ ; 0.71073	MoK $\alpha$ ; 0.71073
Absorption coef., $\mu$ (mm <sup>-1</sup> )	60.57	63.875
<i>F</i> (000)	7656	6064
Data range $\theta$ (°); <i>h</i> , <i>k</i> , <i>l</i>	2.17 – 33; -24 < <i>h</i> < 24, -24 < <i>k</i> < 24, -24 < <i>l</i> < 24	2.11 – 30.54; -14 < <i>h</i> < 12, -25 < <i>k</i> < 25, -27 < <i>l</i> < 27
No. of total reflections	755	5330
Total unique reflections	472	2607

Criterion for observed reflections	$I > 3\sigma(I)$	$I > 2\sigma(I)$
<b>Refinement</b>		
Refinement method	Full-matrix least squares on $F$	
Restraints, parameters	39, 755	48, 170
$R_{gt}, R_{all}$	2.64, 4.98	4.84; 13.33
$wR_{gt}, wR_{ref.}$	2.43, 2.68	5.43; 6.10
$GoF_{gt}, GoF_{ref.}$	9.9, 8.5	8.22; 8.20
Max./min. residual $e$ density, ( $e\text{\AA}^{-3}$ )	1.16 / -1.28	3.439 / -3.709

**Table 54. Atomic parameters for  $Pb_{14}Ge_8Al_7O_{31}F_{19}$**

Atom	S.O.F.	x	y	z
<b>Pb1</b>		0.17359(4)	0	0
<b>Pb2</b>		0.37302(2)	0.12698(2)	0.12698(2)
<b>Ge1</b>		0.35129(5)	0.35129(5)	0.14871(5)
<b>Al1</b>		1/2	0	0
<b>Al2</b>		1/4	1/4	0
<b>F3</b>		0.3571(3)	0.2268(4)	0
<b>O1</b>	0.8542	0.2648(3)	0.3300(3)	0.0874(3)
<b>F1</b>	0.1458	0.2648(3)	0.3300(3)	0.0874(3)
<b>F2</b>	0.5833	1/2	0.1107(6)	0
<b>O2</b>	0.4167	1/2	0.1107(6)	0
<b>O3</b>		0.4138(3)	0.4138(3)	0.0862(3)

**Table 55. Anisotropic displacement parameters for  $Pb_{14}Ge_8Al_7O_{31}F_{19}$**

Atom	$U_{11}$	$U_{22}$	$U_{33}$	$U_{12}$	$U_{13}$	$U_{23}$
<b>Pb1</b>	0.0149(3)	0.0192(3)	0.0114(3)	0.00000	0.00000	0.00000
<b>Pb2</b>	0.01190(13)	0.01190(13)	0.01190(13)	-0.00040(11)	-0.00040(11)	0.00040(11)
<b>Ge1</b>	0.0113(3)	0.0113(3)	0.0113(3)	0.0015(3)	-0.0015(3)	-0.0015(3)
<b>Al1</b>	0.014(2)	0.014(2)	0.014(2)	0.00000	0.00000	0.00000
<b>Al2</b>	0.007(2)	0.010(2)	0.012(2)	0.0003(17)	0.00000	0.00000
<b>F3</b>	0.006(3)	0.014(3)	0.013(3)	0.005(2)	0.00000	0.00000
<b>O1</b>	0.015(3)	0.020(3)	0.023(3)	0.002(2)	-0.006(2)	-0.009(2)
<b>F1</b>	0.015(3)	0.020(3)	0.023(3)	0.002(2)	-0.006(2)	-0.009(2)
<b>F2</b>	0.011(5)	0.012(5)	0.015(5)	0.00000	0.00000	0.00000
<b>O2</b>	0.011(5)	0.012(5)	0.015(5)	0.00000	0.00000	0.00000
<b>O3</b>	0.017(2)	0.017(2)	0.017(2)	-0.002(2)	0.002(2)	0.002(2)

**Table 56. Bond parameters for  $Pb_{14}Ge_8Al_7O_{31}F_{19}$**

Atom 1	Atom 2	$d, \text{\AA}$
<b>Pb1</b>	O3 X4	2.4362(49)
	F3 X2	2.8296(28)
	O1 f1 X4	3.2625(49)
<b>Pb2</b>	O1 f1 X3	2.4310(49)
	F3 X3	2.6362(39)
	F2 o2 X3	2.9294(69)
<b>Ge1</b>	O1 f1 X3	1.7566(49)
	O3 X1	1.7593(49)
<b>Al1</b>	F2 o2 X6	1.7985(0)
<b>Al2</b>	O1 f1 X4	1.9397(49)

**Table 57. Table of bond valence sums for cations in Pb<sub>14</sub>Ge<sub>8</sub>Al<sub>7</sub>O<sub>31</sub>F<sub>19</sub>**

<i>Atom</i>	<i>Sum</i>
<i>Pb1</i>	1.751(9)
<i>Pb2</i>	2.041(7)
<i>Ge1</i>	3.81(3)
<i>Al1</i>	3.31(2)
<i>Al2</i>	2.702(16)

**Table 58. Table of atomic parameters for [Pb<sub>12</sub>O<sub>6</sub>][Ge<sub>7</sub>Al<sub>4</sub>O<sub>26</sub>].**

<i>Atom</i>	<i>x/a</i>	<i>y/b</i>	<i>z/c</i>	<i>U [Å<sup>2</sup>]</i>
<b>Pb1</b>	0	0.18803(8)	1/4	
<b>Pb2</b>	0.18369(10)	0.40628(6)	0.08935(5)	
<b>Pb3</b>	0.31559(10)	0.50044(7)	0.26379(5)	
<b>Pb4</b>	0.31388(10)	0.29220(6)	0.24903(5)	
<b>Pb5</b>	0.15757(10)	0.29594(7)	0.41819(5)	
<b>Pb6</b>	0.13451(10)	0.50532(7)	0.41703(5)	
<b>Pb7</b>	0	0.38814(10)	1/4	
<b>Ge1</b>	-0.1640(3)	0.18808(16)	0.40449(13)	
<b>Ge2</b>	0.1535(3)	0.61875(16)	0.11800(13)	
<b>Ge3</b>	0.4615(3)	0.40608(18)	0.41133(13)	
<b>Ge4</b>	0	0.5867(5)	1/4	
<b>Al1</b>	0.4338(7)	0.4277(4)	0.5732(3)	
<b>Al2</b>	-0.0499(7)	0.7402(4)	0.0502(3)	
<b>O1</b>	0.5785(17)	0.4789(11)	0.4032(8)	0.022(4)
<b>O2</b>	0.5440(16)	0.3268(10)	0.4017(8)	0.013(4)
<b>O3</b>	0.1225(17)	0.2815(11)	0.3009(8)	0.022(4)
<b>O4</b>	-0.3179(17)	0.1826(10)	0.4321(8)	0.019(4)
<b>O5</b>	0.3253(17)	0.6188(11)	0.1258(8)	0.023(5)
<b>O6</b>	-0.0575(16)	0.2426(10)	0.4599(8)	0.017(4)
<b>O7</b>	0.0966(17)	0.6330(11)	0.1968(8)	0.020(4)
<b>O8</b>	0.1145(17)	0.5218(10)	0.2996(8)	0.020(4)
<b>O9</b>	0.0942(18)	0.6910(11)	0.0623(9)	0.024(5)
<b>O10</b>	0.3866(17)	0.4079(11)	0.4892(8)	0.019(4)
<b>O11</b>	0.2188(17)	0.4006(11)	0.2028(8)	0.023(4)
<b>O12</b>	0.0328(17)	0.3950(11)	0.3897(8)	0.021(4)
<b>O13</b>	0.3315(16)	0.4142(11)	0.3482(8)	0.019(4)
<b>O14</b>	-0.1678(17)	0.2333(11)	0.3242(8)	0.022(5)
<b>O15</b>	-0.0948(18)	0.1011(11)	0.3984(8)	0.026(5)
<b>O16</b>	0.0916(19)	0.5303(12)	0.0866(9)	0.030(5)

**Table 59. Table of anisotropic displacement parameters for [Pb<sub>12</sub>O<sub>6</sub>][Ge<sub>7</sub>Al<sub>4</sub>O<sub>26</sub>].**

<i>Atom</i>	<i>U<sub>11</sub></i>	<i>U<sub>22</sub></i>	<i>U<sub>33</sub></i>	<i>U<sub>12</sub></i>	<i>U<sub>13</sub></i>	<i>U<sub>23</sub></i>
<b>Pb1</b>	0.0222(8)	0.0067(8)	0.0136(7)	0	0.0056(6)	0
<b>Pb2</b>	0.0181(6)	0.0127(6)	0.0117(5)	0.0001(4)	0.0038(4)	-0.0018(4)
<b>Pb3</b>	0.0150(5)	0.0133(6)	0.0193(5)	-0.0045(5)	0.0027(4)	0.0032(5)
<b>Pb4</b>	0.0129(5)	0.0170(6)	0.0175(5)	0.0012(5)	0.0024(4)	0.0007(5)
<b>Pb5</b>	0.0156(6)	0.0181(6)	0.0164(5)	0.0019(5)	0.0027(4)	-0.0021(5)
<b>Pb6</b>	0.0221(6)	0.0156(6)	0.0163(5)	-0.0034(5)	0.0016(4)	-0.0009(5)
<b>Pb7</b>	0.0225(10)	0.0161(10)	0.0543(12)	0	0.0115(8)	0
<b>Ge1</b>	0.0116(14)	0.0070(15)	0.0110(13)	-0.0011(11)	0.0046(10)	0.0002(11)

<b>Ge2</b>	0.0134(14)	0.0065(15)	0.0155(14)	0.0024(11)	0.0039(11)	0.0012(11)
<b>Ge3</b>	0.0142(15)	0.0113(16)	0.0168(14)	-0.0015(13)	-0.0014(11)	0.0009(13)
<b>Ge4</b>	0.082(6)	0.089(7)	0.104(6)	0	-0.013(5)	0
<b>Al1</b>	0.004(4)	-0.008(3)	0.012(4)	0.006(3)	0.006(3)	0.001(3)
<b>Al2</b>	0.018(4)	-0.002(4)	0.006(3)	-0.009(3)	0.004(3)	0.000(3)

**Table 60.** Table of created bonds for [Pb<sub>12</sub>O<sub>6</sub>]Ge<sub>7</sub>Al<sub>4</sub>O<sub>26</sub>.

<b>Atom 1</b>	<b>Atom 2</b>	<b>d, Å</b>
<b>Pb1</b>	O3	2.247(18)
	O3	2.2472(180)
	O14	2.4658(175)
	O14	2.4663(175)
<b>Pb2</b>	O11	2.2018(154)
	O12	2.2724(175)
	O16	2.3965(211)
<b>Pb3</b>	O1	2.7211(178)
	O13	2.2431(176)
	O8	2.2435(175)
<b>Pb4</b>	O11	2.3033(181)
	O14	2.2138(166)
	O3	2.2742(175)
<b>Pb5</b>	O11	2.3005(186)
	O13	2.8997(179)
	O12	2.2092(186)
	O3	2.2876(155)
<b>Pb6</b>	O6	2.5738(168)
	O9	2.9425(180)
	O12	2.2583(189)
	O8	2.2904(156)
<b>Pb7</b>	O16	2.3220(193)
	O13	2.9851(176)
	O3	2.4264(183)
	O3	2.4266(183)
<b>Ge1</b>	O11	2.4843(175)
	O11	2.4848(175)
	O12	2.7061(154)
	O12	2.7063(154)
	O8	2.7795(174)
	O8	2.7797(174)
	O4	1.6969(177)
	O15	1.7100(196)
<b>Ge2</b>	O6	1.7430(162)
	O14	1.7527(167)
	O7	1.7065(167)
	O5	1.7279(174)
<b>Ge3</b>	O9	1.7498(186)
	O16	1.7821(208)
	O2	1.6611(178)
	O13	1.7143(154)
<b>Ge4</b>	O10	1.7574(168)
	O1	1.7724(189)
	O7	1.7028(183)
	O7	1.7033(183)
<b>Al1</b>	O8	1.8414(175)
	O8	1.8416(175)
	O10	1.6927(165)
	O1	1.7348(206)
	O15	1.7438(190)

Al2	O5	1.7753(190)
	O9	1.6966(197)
	O4	1.7452(190)
	O6	1.7764(167)
	O2	1.8023(185)

**Table 61. List of bond valence sums for [Pb<sub>12</sub>O<sub>6</sub>]Ge<sub>7</sub>Al<sub>4</sub>O<sub>26</sub>**

Atom	Sum
Pb1	2.16(5)
Pb2	2.09(5)
Pb3	2.00(5)
Pb4	2.12(6)
Pb5	1.79(5)
Pb6	1.95(5)
Pb7	2.32(4)
Ge1	4.29(11)
Ge2	4.10(10)
Ge3	4.31(10)
Ge4	3.84(10)
Al1	3.08(7)
Al2	2.95(7)
O1	1.90(6)
O2	1.93(7)
O3	2.39(6)
O4	1.91(7)
O5	1.76(6)
O6	2.00(6)
O7	2.27(8)
O8	2.26(6)
O9	1.96(7)
O10	1.84(6)
O11	2.35(6)
O12	2.29(6)
O13	2.02(6)
O14	2.13(6)
O15	1.87(7)
O16	1.95(6)

**Table 62. Crystal parameters, data collection and structure refinement details for the crystals from Pb – Si – Al – O chemical system.**

Crystal data	[Pb <sub>13</sub> O <sub>8</sub> ]Si <sub>8</sub> Al <sub>2</sub> O <sub>24</sub>	[Pb <sub>6</sub> CaO <sub>2</sub> ](Al/Si) <sub>8</sub> O <sub>17</sub>
Formula	[Pb <sub>13</sub> O <sub>8</sub> ]Si <sub>8</sub> Al <sub>2</sub> O <sub>24</sub>	[Pb <sub>6</sub> CaO <sub>2</sub> ](Al/Si) <sub>8</sub> O <sub>17</sub>
Formula weight (g/mol)	3484.1	464.19
Temperature (K)	293	296
Crystal system	triclinic	Trigonal
Space group	<i>P</i> -1	R-3 (148)
<i>a</i> (Å)	10.003(1)	9.9466(3)
<i>b</i> (Å)	10.034(1)	
<i>c</i> (Å)	10.476(1)	18.7388(7)
$\alpha^\circ$	80.583(1)	90
$\beta^\circ$	70.716(1)	90
$\gamma^\circ$	60.362(1)	120
<i>V</i> (Å <sup>3</sup> )	862.640(2)	1605.54(11)

Z	1	12
<b>Data collection</b>		
Diffractionmeter	Bruker X8 APEX II	SMART APEX DUO
Radiation; $\lambda$ (Å)	MoK $\alpha$ ; 0.71073	MoK $\alpha$ ; 0.71073
Absorption coef., $\mu$ (mm <sup>-1</sup> )	63.604	48.530
F (000)	1460	2383
Data range $\theta$ (°); $h, k, l$	2.06 – 24; -10 < $h$ < 11, -11 < $k$ < 11, -8 < $l$ < 12	2.602 - 27.974; -9 < $h$ < 13, -13 < $k$ < 10, -24 < $h$ < 24
No. of total reflections	2519	865
Total unique reflections	1306	756
Criterion for observed reflections	I > 3 $\sigma$ (I)	I > 2 $\sigma$ (I)
<b>Refinement</b>		
Refinement method	Full-matrix last squares on $F$	
parameters	145	58
R <sub>gt</sub> , R <sub>all</sub>	5.25, 11.99	3.11, 3.84
wR <sub>gt</sub> , wR <sub>ref</sub>	4.77, 5.76	6.37, 6.54
GoF <sub>gt</sub> , GoF <sub>ref</sub>	1.36, 1.16	1.063, 1.065
Max./min. residual $e$ density, ( $e\text{Å}^{-3}$ )	13.93 / -11.51	4.130 / -1.240

**Table 63.** Table of atomic parameters for [Pb<sub>13</sub>O<sub>8</sub>]<sub>3</sub>[Si<sub>8</sub>Al<sub>2</sub>O<sub>24</sub>]

Atom	X	Y	Z	U [Å <sup>2</sup> ]
Pb1	0.31382(16)	0.25345(15)	0.01761(15)	0.0185(7)
Pb2	0.93671(16)	0.32776(16)	-0.02729(16)	0.0234(8)
Pb3	0.5	0.5	0	0.0379(13)
Pb4	0.73950(17)	0.09543(16)	-0.02430(17)	0.0295(8)
Pb5	0.15578(18)	0.51402(18)	0.33664(16)	0.0255(8)
Pb6	0.59756(18)	0.29115(18)	-0.33238(16)	0.0338(9)
Pb7	0.62521(19)	0.27001(20)	0.30935(17)	0.0414(9)
Si1	0.8200(10)	0.5036(10)	0.2755(9)	0.007(2)
Si2	1.4160(10)	0.0700(9)	0.3018(8)	0.0007(19)
Si3	0.9738(10)	0.8993(9)	0.3320(9)	0.0022(19)
Al1	1.0524(12)	0.1621(11)	0.3523(11)	0.014(2)
Si4	1.6995(11)	-0.1765(10)	0.3921(10)	0.013(2)
O1	1.366(2)	0.174(2)	0.424(2)	0.011(5)
O2	1.264(2)	0.071(2)	0.281(2)	0.015(5)
O3	0.791(2)	0.940(2)	0.329(2)	0.009(5)
O4	1.840(2)	-0.368(2)	0.337(2)	0.006(5)
O5	1.499(3)	0.140(2)	0.168(2)	0.026(6)
O6	0.984(2)	1.054(2)	0.300(2)	0.012(5)
O7	1.539(3)	-0.107(2)	0.328(2)	0.020(6)
O8	0.535(3)	0.269(3)	-0.103(3)	0.034(7)
O9	0.655(3)	0.504(3)	0.347(3)	0.038(7)
O10	0.406(2)	0.490(2)	0.275(2)	0.012(5)
O11	1.114(2)	0.768(2)	0.217(2)	0.007(5)
O12	1.004(2)	0.826(2)	0.474(2)	0.012(5)
O13	0.978(3)	0.340(3)	0.282(2)	0.027(6)
O14	0.839(3)	0.536(3)	0.115(3)	0.060(9)
O15	0.236(3)	0.465(2)	0.117(2)	0.026(6)
O16	0.717(3)	0.282(2)	0.085(2)	0.021(6)

**Table 64. Anisotropic displacement parameters for [Pb<sub>13</sub>O<sub>8</sub>]Si<sub>8</sub>Al<sub>2</sub>O<sub>24</sub>**

Atom	U <sub>11</sub>	U <sub>22</sub>	U <sub>33</sub>	U <sub>12</sub>	U <sub>13</sub>	U <sub>23</sub>
<b>Pb1</b>	0.0205(8)	0.0182(8)	0.0217(9)	-0.0106(7)	-0.0095(7)	0.0000(7)
<b>Pb2</b>	0.0122(8)	0.0244(9)	0.0293(10)	-0.0033(7)	-0.0126(7)	0.0057(8)
<b>Pb3</b>	0.0248(14)	0.0145(12)	0.069(2)	-0.0035(11)	-0.0168(13)	0.0005(12)
<b>Pb4</b>	0.0125(8)	0.0178(8)	0.0502(12)	0.0015(7)	-0.0118(8)	-0.0042(8)
<b>Pb5</b>	0.0203(8)	0.0355(9)	0.0187(9)	-0.0118(7)	-0.0034(7)	-0.0049(7)
<b>Pb6</b>	0.0265(10)	0.0466(11)	0.0300(11)	-0.0188(8)	-0.0014(8)	-0.0130(9)
<b>Pb7</b>	0.0281(10)	0.0460(11)	0.0312(11)	-0.0097(9)	-0.0084(9)	0.0194(9)

**Table 65. Bond parameters for [Pb<sub>13</sub>O<sub>8</sub>]Si<sub>8</sub>Al<sub>2</sub>O<sub>24</sub>**

Atom 1	Atom	d, Å			
<b>Pb1</b>	O15	2.1797(22)	<b>Pb6</b>	O4	3.4981(20)
	O8	2.2235(29)		O8	2.2769(29)
	O14	2.4448(26)		O10	2.3505(23)
	O5	2.543(27)		O9	2.3762(23)
	O2	3.0915(19)		O7	2.7767(31)
<b>Pb2</b>	O13	3.3862(21)	O2	3.2075(18)	
	O15	2.2522(19)	O11	3.2426(23)	
	O16	2.3535(28)	O12	3.3910(17)	
	O14	2.3624(31)	<b>Pb7</b>	O16	2.2296(19)
	O11	2.6273(25)		O10	2.2984(15)
O14	3.0014(35)	O9		2.6141(36)	
O4	3.3697(18)	O3		2.8858(17)	
O13	3.4276(26)	O5		2.9964(31)	
<b>Pb3</b>	O16	2.4965(21)	O1	3.0207(22)	
	O16	2.4967(21)	O6	3.1198(17)	
	O8	2.5352(35)	<b>Si1</b>	O9	1.5689(31)
	O8	2.5355(35)		O14	1.6252(32)
	O15	2.6898(29)		O13	1.6325(23)
<b>Pb4</b>	O15	2.6901(29)	<b>Si2</b>	O4	1.6515(29)
	O10	2.7211(19)		O1	1.5736(24)
	O10	2.7213(19)		O2	1.6012(26)
	<b>Pb5</b>	O16	2.2315(26)	O5	1.6229(23)
		O8	2.2404(27)	O7	1.6263(18)
O5		2.4648(21)	<b>Si3</b>	O6	1.5803(241)
O11		2.6882(20)		O12	1.6015(224)
O6		3.2062(16)		O11	1.6521(179)
<b>Pb6</b>	O2	3.4076(24)	<b>Al1</b>	O3	1.6752(241)
	O15	2.2224(20)		O13	1.7035(263)
	O10	2.2644(20)		O12	1.7234(230)
	<b>Pb7</b>	O11	2.5472(19)	O6	1.7666(299)
		O4	2.7698(19)	O2	1.7714(189)
O12		3.0833(20)	<b>Si4</b>	O7	1.7225(314)
O1		3.1708(16)		O3	1.7453(257)
O13		3.2565(37)		O4	1.7769(179)
			O1	1.8186(221)	

**Table 66. Table of bond valence sums for [Pb<sub>13</sub>O<sub>8</sub>]<sub>2</sub>Si<sub>8</sub>Al<sub>2</sub>O<sub>24</sub>**

<b>Atom</b>	<b>Sum</b>
<b>Pb1</b>	2.30(9)
<b>Pb2</b>	1.97(7)
<b>Pb3</b>	2.14(5)
<b>Pb4</b>	2.03(8)
<b>Pb5</b>	1.88(7)
<b>Pb6</b>	1.82(7)
<b>Pb7</b>	1.59(6)
<b>Si1</b>	4.04(16)
<b>Si2</b>	4.20(15)
<b>Si3</b>	4.01(13)
<b>Al1</b>	3.03(10)
<b>Si4</b>	2.73(9)
<b>O1</b>	1.73(9)
<b>O2</b>	1.77(10)
<b>O3</b>	1.59(8)
<b>O4</b>	1.75(8)
<b>O5</b>	1.70(8)
<b>O6</b>	1.84(10)
<b>O7</b>	1.92(8)
<b>O8</b>	2.41(9)
<b>O9</b>	1.90(10)
<b>O10</b>	1.98(7)
<b>O11</b>	1.69(5)
<b>O12</b>	1.87(8)
<b>O13</b>	1.81(8)
<b>O14</b>	1.91(11)
<b>O15</b>	2.47(9)
<b>O16</b>	2.33(8)

**Table 67. Table of Atomic parameters for [Pb<sub>6</sub>CaO<sub>2</sub>](Al/Si)<sub>8</sub>O<sub>17</sub>**

<b>Atom</b>	<b>S.O.F</b>	<b>X</b>	<b>Y</b>	<b>Z</b>
<b>Pb1</b>		0.50101(4)	0.10046(4)	0.65649(2)
<b>Ca1</b>	0.899(5)	2/3	1/3	5/6
<b>Pb2</b>	0.101(5)	2/3	1/3	5/6
<b>Al1</b>	0.5	0.3761(3)	0.2382(3)	0.51160(13)
<b>Si1</b>	0.5	0.3761(3)	0.2382(3)	0.51160(13)
<b>Al2</b>	0.5	2/3	1/3	0.4211(2)
<b>Si2</b>	0.5	2/3	1/3	0.4211(2)
<b>O1</b>		2/3	1/3	0.7092(6)
<b>O2</b>		0.4458(7)	0.2650(8)	0.5962(4)
<b>O3</b>		0.5131(8)	0.3419(8)	0.4514(4)
<b>O4</b>		0.2313(8)	0.2782(8)	0.5076(4)
<b>O5</b>		2/3	1/3	1/3

**Table 68. Table of bond valence calculations for [Pb<sub>6</sub>CaO<sub>2</sub>](Al/Si)<sub>8</sub>O<sub>17</sub>.**

Atom	Pb1	Ca1/Pb2	Si1/Al1	Si2/Al2	∑va
O1	0.51	0.10 + 0.65			1.26
O2	1.11		0.41 + 0.43		1.95
O3	0.10		0.44 + 0.46	1.33 + 1.36	1.90
O4	0.08	0.17 + 1.07	0.86 + 0.88		2.19
O5				0.47 + 0.49	1.92
∑vc	1.80	1.99	3.49	3.65	

**Table 69. Table of Distances for [Pb<sub>6</sub>CaO<sub>2</sub>](Al/Si)<sub>8</sub>O<sub>17</sub>**

Atom 1	Atom 2	d, Å	
<b>Pb1</b>	O2	2.2708(87)	
	O1	2.2889(49)	
	O2	2.3392(69)	
	O2	3.0427(76)	
	O3	3.1016(70)	
	O4	3.2238(75)	
	<b>Ca1 Pb2</b>	O1	2.3254(11)
		O1	2.3261(11)
O4		2.5695(93)	
O4		2.5698(84)	
O4		2.5698(58)	
O4		2.5699(58)	
O4		2.5699(84)	
O4		2.5701(93)	
<b>Al2 Si2</b>	O5	1.6449(37)	
	O3	1.6711(87)	
	O3	1.6713(60)	
	O3	1.6714(90)	
<b>Al1 Si1</b>	O3	1.6698(71)	
	O4	1.6761(10)	
	O4	1.6874(73)	
	O2	1.6969(78)	

## IV.6. References

1. Colmont, M., Lemoine, K., Roussel, P., Kabbour, H., Olchowka, J., Henry, N., ... Mentré, O. (2019). *Identification and optical features of the  $Pb_4Ln_2O_7$  series ( $Ln = La, Gd, Sm, Nd$ ), genuine 2D-van der Waals oxides*. Chemical Communications. doi:10.1039/c8cc07707j;
2. Novoselov, K. S., Mishchenko, A., Carvalho, A., & Castro Neto, A. H. (2016). *2D materials and van der Waals heterostructures*. Science, 353(6298), aac9439. doi:10.1126/science.aac9439;
3. Lee, J. H., Avsar, A., Jung, J., Tan, J. Y., Watanabe, K., Taniguchi, T., ... Özyilmaz, B. (2014). *van der Waals Force: A Dominant Factor for Reactivity of Graphene*. Nano Letters, 15(1), 319–325. doi:10.1021/nl5036012;
4. Qi, H., Wang, L., Sun, J., Long, Y., Hu, P., Liu, F., & He, X. (2018). *Production Methods of Van der Waals Heterostructures Based on Transition Metal Dichalcogenides*. Crystals, 8(1), 35. doi:10.3390/cryst8010035;
5. Zhang, Z., Liu, Y., Yang, Y., & Yakobson, B. I. (2016). *Growth Mechanism and Morphology of Hexagonal Boron Nitride*. Nano Letters, 16(2), 1398–1403. doi:10.1021/acs.nanolett.5b04874;
6. Li, L., Yu, Y., Ye, G. J., Ge, Q., Ou, X., Wu, H., ... Zhang, Y. (2014). *Black phosphorus field-effect transistors*. Nature Nanotechnology, 9(5), 372–377. doi:10.1038/nnano.2014.35;
7. Huvé, M., Colmont, M., Lejay, J., Aschehoug, P., & Mentré, O. (2009). *Building Units and Intergrowths: Toward the Design of an Extended Family of Acentric Bi-Based Materials with Second Harmonic Generacy*. Chemistry of Materials, 21(17), 4019–4029. doi:10.1021/cm901466e;
8. Sucharitakul, S., Ye, G., Lambrecht, W. R. L., Bhandari, C., Gross, A., He, R., ... Gao, X. P. A. (2017).  *$V_2O_5$ : A 2D van der Waals Oxide with Strong In-Plane Electrical and Optical Anisotropy*. ACS Applied Materials & Interfaces, 9(28), 23949–23956. doi:10.1021/acsami.7b05377;
9. Aliev, A., Olchowka, J., Colmont, M., Capoen, E., Wickleder, C., & Mentré, O. (2013). *New  $[PbBi_2O_4][Bi_2O_2]Cl_2$  and  $[Pb_nBi_{10-n}O_{13}][Bi_2O_2]_nCl_{4+n}$  Series by Association of Sizable Subunits: Relationship with Arppe's Compound  $Bi_{24}O_{31}Cl_{10}$  and Luminescence Properties*. Inorganic Chemistry, 52(15), 8427–8435. doi:10.1021/ic4002708;
10. Drache, M., Huve, M., Roussel, P., & Conflant, P. (2003). *Polymorphism of  $Bi_{1-x}Ln_xO_{1.5}$  phases*. Materials Research Bulletin 38(1), 113-124, doi:10.1016/s0025-5408(02)00984-4;
11. Drache, M., Roussel, P., & Wignacourt, J.-P. (2007). *Structures and Oxide Mobility in Bi–Ln–O Materials: Heritage of  $Bi_2O_3$* . Chemical Reviews, 107(1), 80–96. doi:10.1021/cr050977s;
12. Drache, M., Wignacourt, J. P., & Conflant, P. (2000). *Evidence for a New Monoclinic Bi–La Oxide Solid Solution: Identification and Structural Relationship to the Rhombohedral Bi–Sr–O Type*. Journal of Solid State Chemistry, 151(2), 281–285. doi:10.1006/jssc.2000.8654;
13. Van Vleck, J. H. (1965) *The theory of electric and magnetic susceptibilities*. Oxford University Press;
14. Hamaker, H. C., Woolf, L. D., MacKay, H. B., Fisk, Z., & Maple, M. B. (1979). *Coexistence of superconductivity and antiferromagnetic order in  $SmRh_4B_4$* . Solid State Communications, 32(4), 289–294. doi:10.1016/0038-1098(79)90949-9;

15. Yazici, D., White, B. D., Ho, P.-C., Kanchanavatee, N., Huang, K., Friedman, A. J., ... Maple, M. B. (2014). *Investigation of magnetic order in  $\text{SmTr}_2\text{Zn}_{20}$  ( $\text{Tr}=\text{Fe}, \text{Co}, \text{Ru}$ ) and  $\text{SmTr}_2\text{Cd}_{20}$  ( $\text{Tr}=\text{Ni}, \text{Pd}$ )*. *Physical Review B*, 90(14). doi:10.1103/physrevb.90.144406;
16. Palache, C., Berman, H., Frondel C. (1951). *Dana's system of mineralogy*, (7th edition), v. II, 270–271;
17. Marezio, M., Dernier, P.D., Remeika, J.P. (1972). *The crystal structures of orthorhombic  $\text{SmAlO}_3$  and of trigonal  $\text{NdAlO}_3$* . *Journal of Solid State Chemistry* 4, 11–19;
18. Bommer, H. (1939). *Die Gitterkonstanten der C-Formen der Oxyde der seltenen Erdmetalle*, *Zeitschrift fuer Anorganische und Allgemeine Chemie* 241, 273–273;
19. Watanabe, A., Drache, M., Wignacourt, J., Conflant, P., & Boivin, J. (1993). *The dependence of polymorphism on the ionic radius of  $\text{Ln}^{3+}$  ( $\text{Ln}, \text{La}, \text{Er}, \text{Y}$ ) in the oxide ion conductors  $\text{Bi}_{0.775}\text{Ln}_{0.225}\text{O}_{1.5}$* . *Solid State Ionics*, 67(1-2), 25–28. doi:10.1016/0167-2738(93)90304-1;
20. Obbade, S., Drache, M., Conflant, P., & Suard, E. (2001). *Ab Initio Determination of  $\text{Bi}_{4.86}\text{La}_{1.14}\text{O}_9$  Monoclinic Structure from Powder Neutron Diffraction Data. Characterization of the Related Solid Solution*. *Journal of Solid State Chemistry*, 162(1), 10–19. doi:10.1006/jssc.2001.9335;
21. Ahi, A., Mellergård, A., & Eriksson, S.-G. (2006). *Local and average atomic order of ion-conducting  $\text{Bi}_{0.775}\text{La}_{0.225}\text{O}_{1.5}$  studied by neutron scattering and reverse Monte Carlo simulations*. *Solid State Ionics*, 177(3-4), 289–297. doi:10.1016/j.ssi.2005.10.035;
22. Mercurio, D., Farissi, M. E., Champarnaud-Mesjard, J. C., Frit, B., Conflant, P., & Roult, G. (1989). *Etude structurale par diffraction X sur monocristal et diffraction neutronique sur poudre de l'oxyde mixte  $\text{Bi}_{0.7}\text{La}_{0.3}\text{O}_{1.5}$* . *Journal of Solid State Chemistry*, 80(1), 133–143. doi:10.1016/0022-4596(89)90040-6;
23. Jamroz, J., Malys, M., Krok, F., Maier, J., Kyriacou, A., Ahmed, S. J., ... Wrobel, W. (2020). *The influence of defect structure changes at phase transition on electrical properties in the  $\text{Bi}_{0.75}\text{Pr}_{0.25}\text{O}_{1.5}$  oxide ion conductor*. *Solid State Ionics*, 348, 115284. doi:10.1016/j.ssi.2020.115284;
24. Abraham, F., Boivin, J., Mairesse, G., & Nowogrocki, G. (1990). *The bimevov series: A new family of high performances oxide ion conductors*. *Solid State Ionics*, 40-41, 934–937. doi:10.1016/0167-2738(90)90157-m;
25. Krivovichev, S. V., Mentré, O., Siidra, O. I., Colmont, M., & Filatov, S. K. (2013). *Anion-Centered Tetrahedra in Inorganic Compounds*. *Chemical Reviews*, 113(8), 6459–6535. doi:10.1021/cr3004696;
26. Hazen, R. M., Finger, L. W., Velde, D. (1981) *Crystal structure of a silica- and alkali-rich trioctahedral mica*. *American Mineralogist* 66 (5-6), 586–591;
27. Bowen, N.L. (1928) *Evolution of Igneous Rocks*. Princeton University Press, Princeton, New Jersey, USA;
28. Hawthorne, F. C. (1983). *Graphical enumeration of polyhedral clusters*. *Acta Crystallographica Section A Foundations of Crystallography*, 39(5), 724–736. doi:10.1107/s0108767383001452;
29. Hawthorne, F.C. (1985) *Towards a structural classification of minerals: The  $\text{VI}^{\text{M}}\text{IV}^{\text{T}}\text{O}_n$  minerals*. *American Mineralogist*, 70, 455473;
30. Gagné, O. C., & Hawthorne, F. C. (2017). *Mean bond-length variations in crystals for ions bonded to oxygen*. *Acta Crystallographica Section B Structural Science, Crystal Engineering and Materials*, 73(6), 1019–1031. doi:10.1107/s2052520617014548;
31. Hawthorne, F. C., Uvarova, Y. A., & Sokolova, E. (2018). *A structure hierarchy for silicate minerals: sheet silicates*. *Mineralogical Magazine*, 1–138. doi:10.1180/mgm.2018.152;

32. Plotz, K.-B., & Muller-Buschbaum, H. (1981). *Zur Kristallchemie der Oxoplumbate(II). I. Zur Kenntnis von  $Pb_9Al_8O_{21}$* . Zeitschrift Für Anorganische Und Allgemeine Chemie, 480(9), 149–152. doi:10.1002/zaac.19814800918 ;
33. Shimoni-Livny, L., Glusker, J. P., & Bock, C. W. (1998). *Lone Pair Functionality in Divalent Lead Compounds*. Inorganic Chemistry, 37(8), 1853–1867. doi:10.1021/ic970909r;
34. Gagné, O. C., & Hawthorne, F. C. (2018). *Bond-length distributions for ions bonded to oxygen: metalloids and post-transition metals*. Acta Crystallographica Section B Structural Science, Crystal Engineering and Materials, 74(1), 63–78. doi:10.1107/s2052520617017437;
35. Merlino, S. (1972). *The crystal structure of zeophyllite*. Acta Crystallographica Section B Structural Crystallography and Crystal Chemistry, 28(9), 2726–2732. doi:10.1107/s0567740872006855;
36. Pokras, M. A., & Kneeland, M. R. (2008). *Lead Poisoning: Using Transdisciplinary Approaches to Solve an Ancient Problem*. EcoHealth, 5(3), 379–385. doi:10.1007/s10393-008-0177-x;
37. De Rango, C., Tsoucaris, G., Zelwer, C., Devaux, J. (1966). *Comparaison de deux affinements de la structure de la cyanite*, Bulletin de la Societe Francaise de Mineralogie et de Cristallographie 89, 419-424 ;
38. Smith, J. V. (1970). *Physical properties of order-disorder structures with especial reference to feldspar minerals*. Lithos, 3(2), 145–160. doi:10.1016/0024-4937(70)90070-8;
39. Gordillo, M. C., & Herrero, C. P. (1996). *Monte Carlo Simulation of Al, Si Ordering in Albite*. The Journal of Physical Chemistry, 100(21), 9098–9103. doi:10.1021/jp951386g;
40. Merlino, S. (1988). *Gyrolite: Its Crystal Structure and Crystal Chemistry*. Mineralogical Magazine, 52(366), 377–387. doi:10.1180/minmag.1988.052.366.09;
41. Dent Glasser, L. S., Howie, R. A., & Smart, R. M. (1981). *The structure of lead 'orthosilicate',  $2PbO \cdot SiO_2$* . Acta Crystallographica Section B Structural Crystallography and Crystal Chemistry, 37(2), 303–306. doi:10.1107/s0567740881002902;
42. Kato, K. (1982). *Die Kristallstruktur des Bleisilicats  $Pb_{11}Si_3O_{17}$* . Acta Crystallographica Section B Structural Crystallography and Crystal Chemistry, 38(1), 57–62. doi:10.1107/s0567740882002040;
43. Siidra, O. I., Krivovichev, S. V., & Depmeier, W. (2009). *Crystal structure of  $Pb_6O[(Si_6Al_2)O_{20}]$* . Glass Physics and Chemistry, 35(4), 406–410. doi:10.1134/s1087659609040099;
44. Chukanov, N. V., Jonsson, E., Aksenov, S. M., Britvin, S. N., Rastsvetaeva, R. K., Belakovskiy, D. I., & Van, K. V. (2017). *Roymillerite,  $Pb_{24}Mg_9(Si_9AlO_{28})(SiO_4)(BO_3)(CO_3)_{10}(OH)_{14}O_4$ , a new mineral: mineralogical characterization and crystal chemistry*. Physics and Chemistry of Minerals, 44(10), 685–699. doi:10.1007/s00269-017-0893-2;
45. Kato, K., Hirota, K., Kanke, Y., Sato, A., Ohsumi, K., Takase, T., ... Adiwidjaja, G. (1995). *Die Kristallstruktur des Bleigermanats  $Pb_{11}Ge_3O_{17}$* . Zeitschrift Für Kristallographie, 210(3), 188–194. doi:10.1524/zkri.1995.210.3.188 ;
46. Siidra, O. I., Zinyakhina, D. O., Zadoya, A. I., Krivovichev, S. V., & Turner, R. W. (2013). *Synthesis and Modular Structural Architectures of Mineralogically Inspired Novel Complex Pb Oxyhalides*. Inorganic Chemistry, 52(21), 12799–12805. doi:10.1021/ic402066h;

47. Armbruster, T., & Gunter, M. E. (2001). *Crystal Structures of Natural Zeolites*. *Reviews in Mineralogy and Geochemistry*, 45(1), 1–67. doi:10.2138/rmg.2001.45.1;
48. Petříček, V., Dušek, M., & Palatinus, L. (2014). *Crystallographic Computing System JANA2006: General features*. *Zeitschrift Für Kristallographie - Crystalline Materials*, 229(5). doi:10.1515/zkri-2014-1737;
49. Winter, J.K. and S. Ghose (1979) *Thermal expansion and high-temperature crystal chemistry of the  $Al_2SiO_5$  polymorphs*. *Amer. Mineral.*, 64, 573-586;
50. Colmont, M., Mentré, O., Henry, N., Pautrat, A., Leclercq, B., Capet, F., ... Roussel, P. (2018). *Undulated oxo-centered layers in  $PbLn_3O_4(VO_4)$  ( $Ln = La$  and  $Nd$ ) and relationship with  $Nd_4O_4(GeO_4)$* . *Journal of Solid State Chemistry*, 260, 101–105. doi:10.1016/j.jssc.2018.01.016;
51. Arulmozhi, K. T., & Mythili, N. (2013). *Studies on the chemical synthesis and characterization of lead oxide nanoparticles with different organic capping agents*. *AIP Advances*, 3(12), 122122. doi:10.1063/1.4858419;
52. Charkin, D. O., Plokhikh, I. V., Zadoya, A. I., Zaloga, A. N., Depmeier, W., & Siidra, O. I. (2018). *Structural, thermal, and IR studies of  $\beta$ -[ $Nd_2O_2$ ]( $CrO_4$ ), an unexpected analog of a slag phase [ $Ba_2F_2$ ]( $S^{6+}O_3S^{2-}$ )*. *Zeitschrift Für Kristallographie - Crystalline Materials*, 0(0). doi:10.1515/zkri-2018-2065.

---

## V. *Summary and Outlook*

---

This work is dedicated to investigation of crystal structural features and physical properties of Bi –, Ln – or Pb – based oxo-centered compounds obtained or modified under high-pressure conditions. A wide range of synthesis and modification methods was used during this thesis.

In the first chapter, results dedicated to the Bi-based phases were presented. Started with  $\text{BiM}_2\text{XO}_6$  family of compounds, the existence of continuous  $\text{BiCu}_2\text{XO}_6$  ( $\text{X} = \text{P}, \text{V}$ ) solid solution was established under HP-HT conditions. Magnetic measurements provided on several terms of the solid solution revealed the disappearance of the spin gap behavior typical for  $\text{BiCu}_2\text{PO}_6$  as far as the content of vanadium increased. This study was completed by DFT calculations for high-pressure form of  $\text{BiCu}_2\text{VO}_6$ . In a second step, a new high-pressure polymorph of  $\text{BiNiPO}_5$  was isolated. The structure was refined and compared to initial ambient-pressure phase. The role of Lone Pair activity in AP and HP-polymorphs was discussed, as well as their magnetic properties were compared. The third part reported two new phases:  $\text{Bi}_{3.5}\text{O}_4(\text{AsO}_4)\text{H}_{0.5}$  and  $\text{Bi}_3\text{O}_3(\text{VO}_4)$  obtained by using Supercritical Steam conditions. The structural complexity of the two new structures were compared with the phases already referenced in the same chemical systems.

In the second chapter, several new Ln-based materials were evidenced by doing *in situ* Raman spectroscopy using Diamond Anvil Cell (DAC). The high-pressure exploration in the Li – Ln – V – O system resulted in formation of series of new compounds, that were carefully investigated. Preliminary *in situ* Raman spectroscopy demonstrated the existence of a high-pressure polytype of  $\text{LiLa}_5\text{O}_5(\text{VO}_4)_2$ . Subsequent HP-HT experiments were performed using the Piston-cylinder type of press and succeeded in the formation of  $\beta\text{-LiLa}_5\text{O}_5(\text{VO}_4)_2$ , in the stabilization of  $\text{LiNd}_5\text{O}_5(\text{VO}_4)_2$  . impossible to reach working at ambient pressure . and in the formation of the new 2D  $\text{LiLa}_2\text{O}_2(\text{VO}_4)$  compound.

In the last chapter dedicated to Pb-based compounds, single crystal of 2D Van de Waals oxide:  $\text{Pb}_4\text{Ln}_2\text{O}_7$  ( $\text{Ln} = \text{Nd}, \text{Sm}$  and  $\text{Gd}$ ) were grown using HP technique. Preliminary HP Raman investigations of  $\text{Pb}_4\text{Ln}_2\text{O}_7$  series of compounds using DAC equipment are also promising for further research suggesting phase transition. In a second step, the impossibility of solid solution existence between  $\text{Bi}_{4.65}\text{La}_{1.36}\text{O}_9$  and  $\text{Pb}_4\text{La}_2\text{O}_7$  was established. The ionic conductivity measurements revealed no real difference in electrical characteristics at low and high temperatures. In the final part of the chapter, the crystal structures of new Pb- oxo-centered compounds obtained during the thesis are described comparing the structural units and the interstitial complex.

